Advances in Mathematical Physics

Nonlinear Waves and Differential Equations in Applied Mathematics and Physics

Lead Guest Editor: Xin Yu
Guest Editors: Zhi-Yuan Sun, Xiao-Ling Gai, and Yu-Hao Sun

Nonlinear Waves and Differential Equations in Applied Mathematics and Physics

Advances in Mathematical Physics

Nonlinear Waves and Differential Equations in Applied Mathematics and Physics

Lead Guest Editor: Xin Yu
Guest Editors: Zhi-Yuan Sun, Xiao-Ling Gai, and Yu-Hao Sun

Contents

Hindawi
Advances in Mathematical Physics
Volume 2021, Article ID 4614919, 9 pages
https://doi.org/10.1155/2021/4614919

Research Article

The Stochastic Resonance Phenomenon of Different Noises in Underdamped Bistable System

Shan Yang,[1] Zening Fan,[2] and Ruibin Ren[3]

[1]*Department of Computer and Software, Jincheng College of Sichuan University, Chengdu 611731, China*
[2]*College of Mathematics, Sichuan University, Chengdu 610064, China*
[3]*College of Mathematics, Southwest Jiaotong University, Chengdu 610031, China*

Correspondence should be addressed to Ruibin Ren; airy_ren@163.com

Received 27 July 2020; Revised 31 December 2020; Accepted 28 January 2021; Published 11 February 2021

Academic Editor: Xiao-Ling Gai

In this paper, the stochastic resonance (SR) phenomenon of four kinds of noises (the white noise, the harmonic noise, the asymmetric dichotomous noise, and the Lévy noise) in underdamped bistable systems is studied. By applying theory of stochastic differential equations to the numerical simulation of stochastic resonance problem, we simulate and analyze the system responses and pay close attention to stochastic control in the proposed systems. Then, the factors of influence to the SR are investigated by the Euler-Maruyama algorithm, Milstein algorithm, and fourth-order Runge-Kutta algorithm, respectively. The results show that the SR phenomenon can be generated in the proposed system under certain conditions by adjusting the parameters of the control effect with different noises. We also found that the type of the noise has little effect on the resonance peak of the output power spectrum density, which is not observed in conventional harmonic systems driven by multiplicative noise with only an overdamped term. Therefore, the conclusion of this paper can provide experimental basis for the further study of stochastic resonance.

1. Introduction

The concept of stochastic resonance (SR) was firstly proposed by Benzi et al. [1] in the 1980s to explain the periodic recurrence of ice ages on Earth. Since then, much attention has been paid to SR due to its potential applications in many fields [2–6].

In the past few years, many researchers focused the SR phenomenon of the overdamped systems [2, 4], while in recent years, researchers gradually shifted their views to the underdamped systems. The SR phenomenon in underdamped bistable system was firstly studied by Ray and Sengupta [7]; they analyzed the difference of the dependence of noise amplitude between underdamped bistable system and overdamped bistable system.

In fact, the bistable systems are very important on the noise effect of the nonlinear systems. Jia et al. [5] studied SR in bistable systems driven by additive and multiplicative white noise. Guo et al. [8] studied the instability probability density evolution in bistable systems driven by Gaussian noise and white noise, and obtained rich conclusions. Meanwhile, relevant theories have shown practical application significance in chemistry, physics, engineering, and other fields [9, 10]. With the further study of stochastic phenomena, SR is gradually extended to multistable and more complex systems [11, 12]. However, SR in bistable systems is still widely concerned by researchers due to its practical value.

On the other hand, the studies of early SR mechanism mainly focus on Gaussian white noise [13]. In recent years, however, some literatures have begun to focus on the effects of some non-Gaussian noises on SR of bistable systems [11, 14–17]. Wang et al. [11] studied the SR of the bistable system driven by simple harmonic noise. Zhang et al. [14] studied the stochastic resonance in the system driven by the Lévy noise and found interesting dynamic behaviors. Gingl et al. [15] studied the nondynamical SR with arbitrarily coloured noise, and Shen et al. [16] studied system driven by correlated non-Gaussian noise and Gaussian noise, while Neiman and Schimansky-Geier studied the SR in a bistable system driven by the harmonic noise.

However, as the best of our knowledge, there is no detailed horizontal comparison of the dynamical effects among different noises in the available literature, and also there is a lack of simulation analyses of the complex system driven by nonwhite noise. As a matter of fact, most SR are difficult to be expressed in analytic form [17–20], especially for a wide range of situations in nonlinear systems. We noticed that the numerical simulation of SR is essentially numerically solving a stochastic differential equation. Hence, the numerical algorithm suitable for stochastic differential equations is more suitable for SR [21, 22].

Therefore, the main goal of this paper is to focus on the control effects in an underdamped bistable system driven by four kinds of noises (the white noise, the harmonic noise, the asymmetric dichotomous noise, and the Lévy noise); meanwhile, we will provide the vivid numerical simulation analyses. Furthermore, since the harmonic noise can be generated by the white noise through the resonance subsystem, we would like to control the properties of harmonic noise by controlling the parameters of the resonance subsystem. Thus, the control of SR is realized.

The organization of this paper is as follows. Section 2 definitely introduces the system model and the definition of the four kinds of the noises and its parameters. The analyses of the effects of different noises on system output are given in Section 3 where we give the method to determine the number of simulations firstly. Finally, the conclusions are discussed in Section 4.

2. System Model

We consider the undamped bistable system driven by four kinds of noise which is described by the following stochastic differential equation:

$$\frac{d^2x}{dt^2} + \eta\frac{dx}{dt} = -\frac{\partial U(x)}{\partial x} + A\cos(\omega t + \theta) + \xi(t), \quad (1)$$

where η is the coefficient of the damping term, $U(x)$is the system potential field, with $U(x) = -(1/2)ax^2 + (1/4)bx^4$, $a > 0$ and $b > 0$ are the two constants of potential field $U(x)$, A, ω, θ are the amplitude, frequency, and phase of periodic driven force, respectively, and $\xi(t)$ is the noise; in this paper, we consider four types of noises which are the white noise, the harmonic noise, the asymmetric dichotomous noise, and the Lévy noise.

Firstly, we give a brief description of the four kinds of the noises as follows:

2.1. The White Noise. The white noise $\xi(t)$ is a stationary process with zero mean and constant power spectral density, respectively:

$$\begin{aligned} &\langle \xi(t)\rangle = 0, \\ &S(\omega) = \frac{N_0}{2}, \quad \omega \in (-\infty, +\infty). \end{aligned} \quad (2)$$

Besides, the white noise $\xi(t)$ has the following form of the second moment:

$$\left\langle \xi(t)\xi\left(t'\right)\right\rangle = 2\alpha\delta\left(t - t'\right). \quad (3)$$

Here, ω is the frequency of the white noise, N_0 is a constant independent with the frequency ω, α is the noise intensity, and δ is the delta function.

2.2. The Harmonic Noise. The harmonic noise $\varepsilon(t)$ is a monochromatic noise commonly used in stochastic dynamics. It can be regarded as the output response of the resonant subsystem driven by Gaussian white noise $\xi(t)$:

$$\ddot{\varepsilon}(t) + \Gamma\dot{\varepsilon}(t) + \Omega^2\varepsilon(t) = \sqrt{2\Theta\Gamma}\xi(t). \quad (4)$$

Here, Γ, Ω, and Θ are the system parameters. Equation (3) determines the two-dimensional Ornstein-Uhlenbeck process $\varepsilon(t)$ and $\dot{\varepsilon}(t)$ with the power spectrum:

$$S_{\varepsilon\varepsilon}(\omega) = \frac{\Theta\Gamma}{\omega^2\Gamma^2 + \left(\omega^2 - \Omega^2\right)^2}, \quad (5)$$

and the mean square displacements $\langle \varepsilon^2(t)\rangle = \Theta/\Omega^2$. From the expression function of simple harmonic noise power spectrum, it is not hard to know if $\Omega^2 - \Gamma^2/4 \geq 0$; the peak of power spectrum function should be at $\omega_p = \sqrt{\Omega^2 - \Gamma^2/2}$. When $\Omega^2 - \Gamma^2/2 < 0$, the peak of power spectrum function should be at $\omega_p = 0$.

2.3. The Asymmetric Dichotomous Noise. We take $\xi(t)$ as the asymmetric dichotomous noise which consists of jumps between two values: $\{-a, ka\}$ with $a > 0$ and $k > 0$. The jumps follow, in time, according to the Poisson process. k represents the asymmetric degree of the noise. When $k = 1$, the noise becomes a symmetric noise. Let λ and λ' be the transition rate from $-a$ to ka and the reverse transition rate, respectively. Without loss of generality, we assume that

$$\langle \xi(t)\rangle = \frac{ka\lambda - a\lambda'}{\lambda + \lambda'} = 0. \quad (6)$$

Thus, we can obtain $k\lambda = \lambda'$. Moreover, the correlation function of the asymmetric dichotomous noise is given by the following:

$$\langle \xi(t)\xi(s)\rangle = D\gamma\exp\{-\lambda|t - s|\}. \quad (7)$$

Here, $\gamma = \lambda + \lambda'$ is the reverse of the correlation time τ of the asymmetric noise $\xi(t)$, and the definition of the strength of $\xi(t)$ is as follows:

$$D = \frac{1}{2}\int_{-\infty}^{+\infty}\langle \xi(\tau)\xi(0)\rangle d\tau = \frac{ka^2}{\gamma}.. \quad (8)$$

Thus, we know that the noise strength D is not independent, but is connected with the asymmetric degree k, the correlation time τ, and value a.

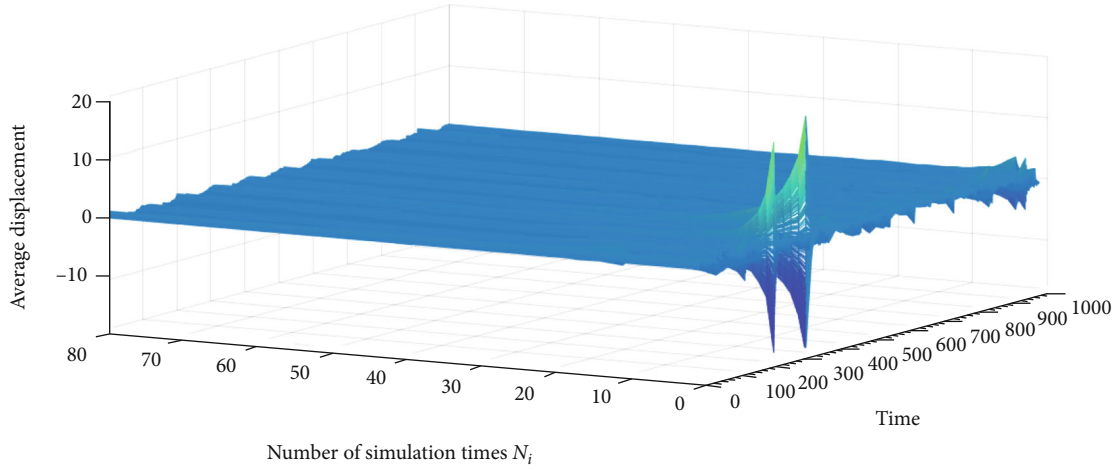

Figure 1: The relationship between the output average displacement and simulation times of the system within time $T = 1000$. The x-axis is the time, the y-axis is the number of simulation times, and the z-axis is the average displacement.

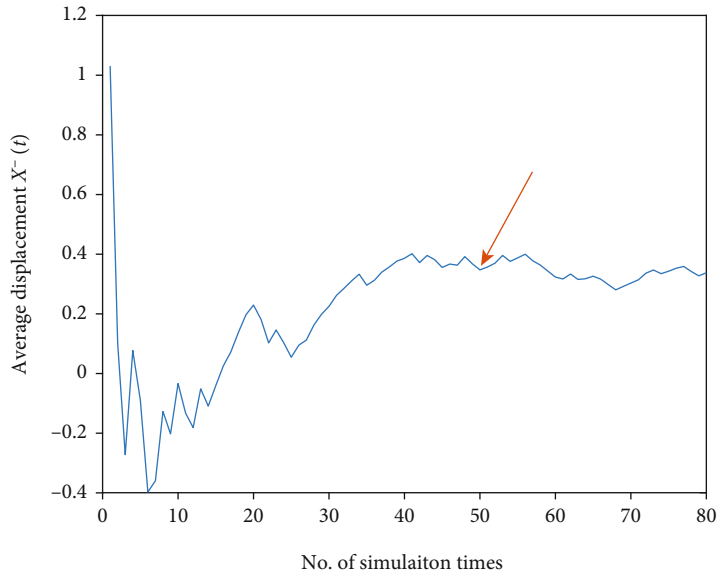

Figure 2: The relationship between the average displacement and the number of simulation time at a certain time. x-axis is the number of simulation time; y-axis is the average displacement.

2.4. The Lévy Noise. Lévy noise is also well known as the alpha stable noise, which was proposed by Lindberg Lévy. Since neither the distribution function nor the probability density function of Lévy noise has an explicit expression, the distribution of Lévy noise is usually expressed by a characteristic function as follows:

$$\varphi(t) = \begin{cases} \exp\left[-\sigma^{\alpha}|t|^{\alpha}\left(1 - i\beta\frac{2}{\pi}\,\mathrm{sign}\,(t)\log|t|\right) + i\mu t\right], & \alpha = 1, \\ \exp\left[-\sigma^{\alpha}|t|^{\alpha}\left(1 - i\beta\frac{2}{\pi}\,\mathrm{sign}\,(t)\tan\frac{\pi\alpha}{2}\right) + i\mu t\right], & \alpha \neq 1. \end{cases} \tag{9}$$

Here, $\alpha \in (0, 2]$ is the stability index, $\beta \in [-1, 1]$ is the skewness parameter, $\sigma > 0$ is the scale parameter, and $\mu \in R$ is the shift.

3. Analyses of the Effects of Different Noises on System Output

We compare the system outputs driven by Gaussian white noise, harmonic noise, asymmetric dichotomous noise, and Lévy noise, which have certain guiding significance for stochastic resonance phenomenon driven by other noises, due to their wide applications.

3.1. The Simulation Number of Times. To obtain a stable state of the system responses, we need to avoid the randomness of

Table 1: The common parameters for numerical simulation of Section 3.

Parameter	Value	Parameter	Value	Parameter	Value	Parameter	Value
T	1000s	TestNum	50	Fs	200	θ	0.03
ω	0.02pi	η	0.5	Ω	1	Γ	1

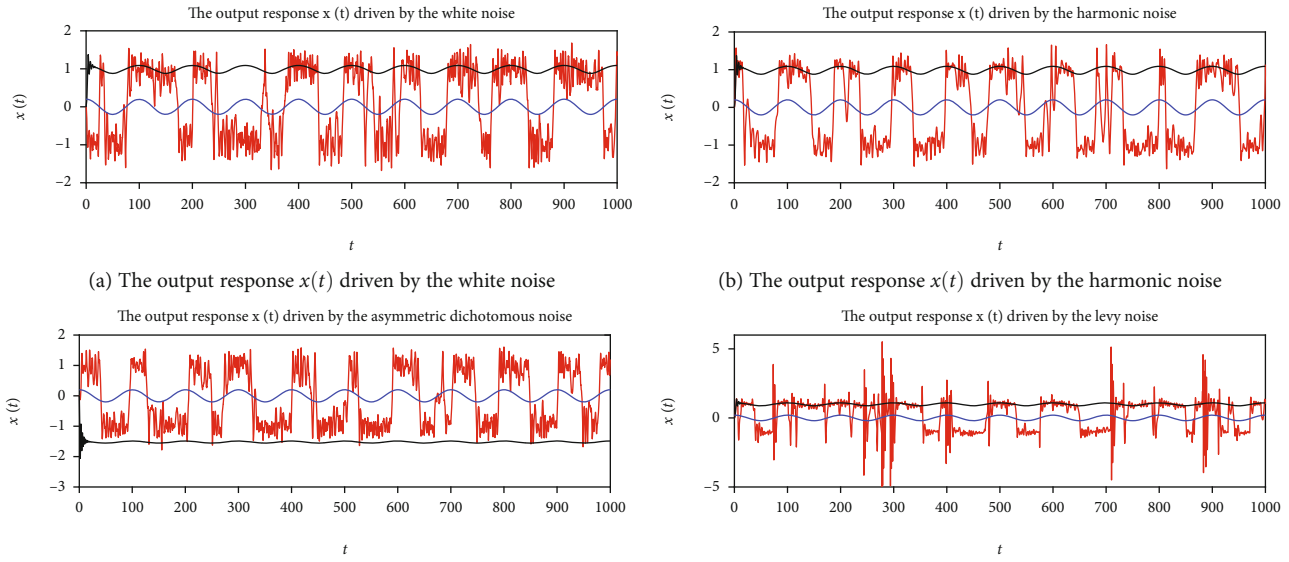

(a) The output response $x(t)$ driven by the white noise

(b) The output response $x(t)$ driven by the harmonic noise

(c) The output response $x(t)$ driven by the asymmetric dichotomous noise

(d) The output response $x(t)$ driven by the Lévy noise

Figure 3: The system responses $x(t)$ for underdamped system under different noises. The values of the parameters for the numerical simulation are shown in Table 1. The blue line is for input sine signal. The black line is for $D = 0$, and red line is for $D = 0.07$.

the noises by considering the statistical average in numerical simulation. Therefore, we will determine the number of simulations in this paper by observing the relationship between the average particle displacement $\bar{X}(t) = \sum_{i=1}^{N_i} X(t)/N_i$ and the number of simulations N_i.

In Figures 1 and 2, it is obvious that the average displacement tends to be stable when the number of simulations is 50, which indicates that when simulation time equals to 50, it can reveal the general rule of the system output. Therefore, it is reasonable for us to use 50 simulations to reveal the rule of the noise-driven dynamical phenomena in the following simulation process.

Furthermore, without a special request, the common simulation parameters will be used in the following table:

3.2. The System Response Driven by Different Noises. We have compared the response of the system driven by Gaussian white noise, harmonic noise, asymmetric binary noise, and Lévy noise, respectively. The simulation values are set as Table 1.

Figure 3 shows the performance of the response of the periodic modulated underdamped system driven by different noises in the time domain, where Figure 3(a) is the situation driven by the white noise, Figure 3(b) is the situation driven by the simple harmonic noise, and Figure 3(c) is the situation driven by the asymmetric dichotomous noise. Figure 3(d) shows the situation driven by Lévy noise. Four kinds of noise can be found that they can cause approximately periodic transitions between two states. And we found that the jump frequencies of the four noise are close to the frequencies of the input periodic forces. In other words, under the simulation conditions with the same parameters as shown in Figure 3, the particles vibrate approximately synchronously with the input periodic force.

Besides, we found that the particles fluctuated in orbit around the noiseless input. At the same time, the output of the system driven by harmonic noise is obviously stronger than the other two damping effects. The vibration of particles is much stronger when they located in the two potential wells during the transition and then decreases significantly. The vibration in the potential wells is more stable than that of harmonic noise and asymmetric binary noise. Finally, the case driven by Lévy noise is the most special. Due to the impulse characteristic of Lévy noise, the particle displacement has great changes in some positions and then quickly returns to orbit.

3.3. The Stochastic Resonance of the System Driven by Different Noises. The power spectral density is the characteristic quantity of signal energy realization in the frequency domain, which reveals the characteristic of signal in the frequency domain. In the next sections, we will observe the influence of noise on system output through the power spectrum of system output at the frequency point of input periodic signal.

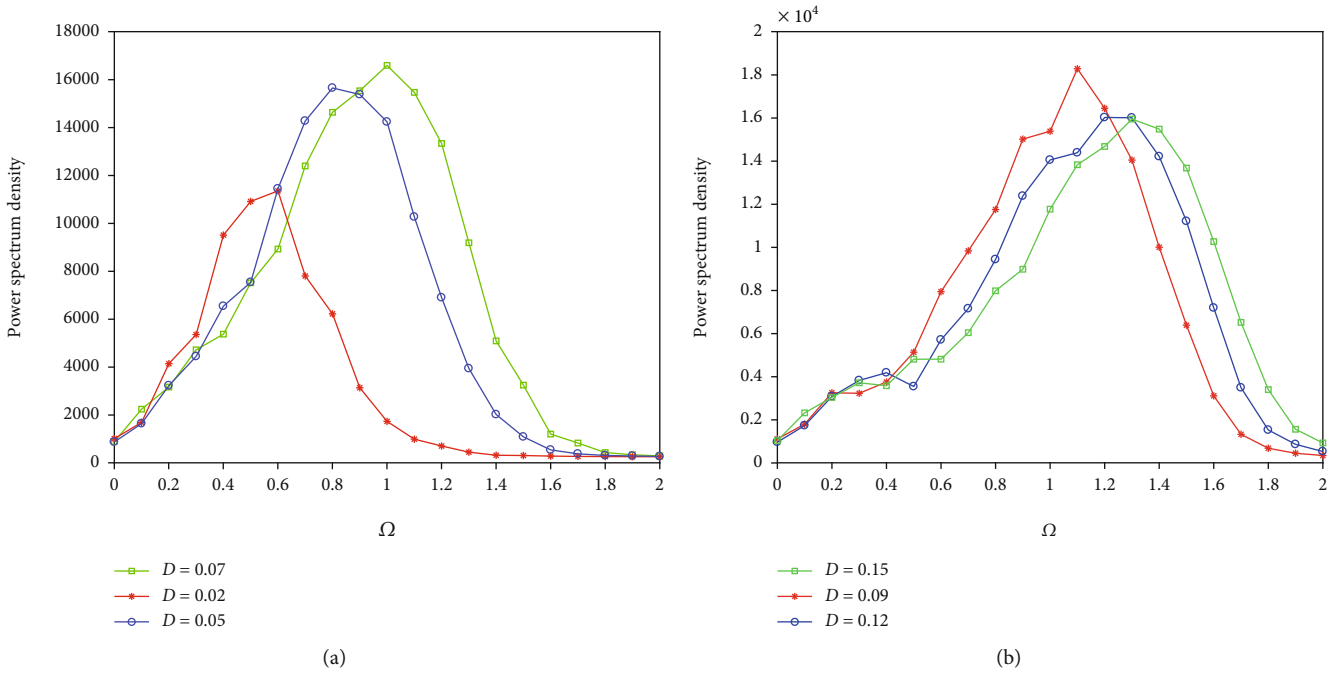

Figure 4: The relationship between Ω and system output PSD of undamped bistable system driven by the harmonic noises. (a) Input white noise intensity $D = 0.02$, 0.05, and 0.07. (b) Input white noise intensity $D = 0.09$, 0.12, and 0.15.

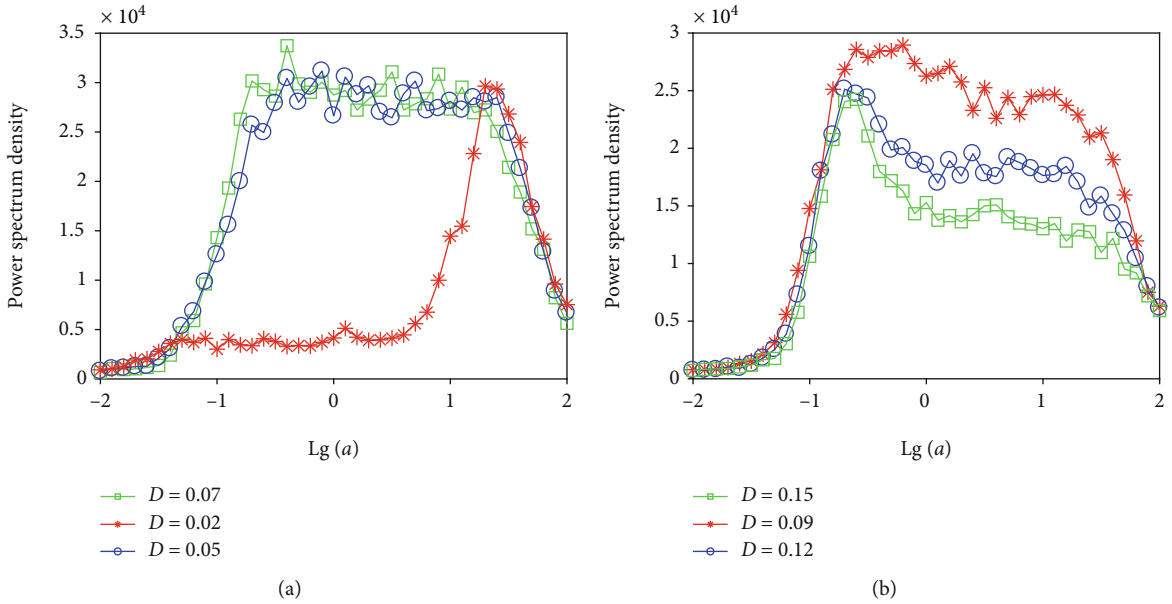

Figure 5: The relationship between lg (a) and system output of undamped bistable system driven by asymmetric dichotomous noise. (a) The output when input white noise intensity is $D = 0.02$, 0.05, and 0.07. (b) The output when input white noise intensity is $D = 0.09$, 0.12, and 0.15.

3.3.1. The System Driven by the Harmonic Noise. In this section, we did the numerical simulation by the Euler-Maruyama method; the results are as follows.

Figure 4 shows the impact of Ω on system response PSD in harmonic noise (Equation (1)) model in the case of different noise intensities. With the increase of Ω, the power spectrum density of the system response is increasing; then, it peaks and then goes down. There are obvious resonance peaks, and there is a random resonance phenomenon. Meanwhile, comparing the two pictures, it can be found that as the noise intensity increases, the power spectrum density of the system response also increases first and then decreases. The value of Ω corresponds to the peak that constantly moves to the right with the increase of noise intensity. Therefore, by adjusting the value of Ω in harmonic noise model, the stochastic resonance phenomenon can be induced by the undamped bistable system.

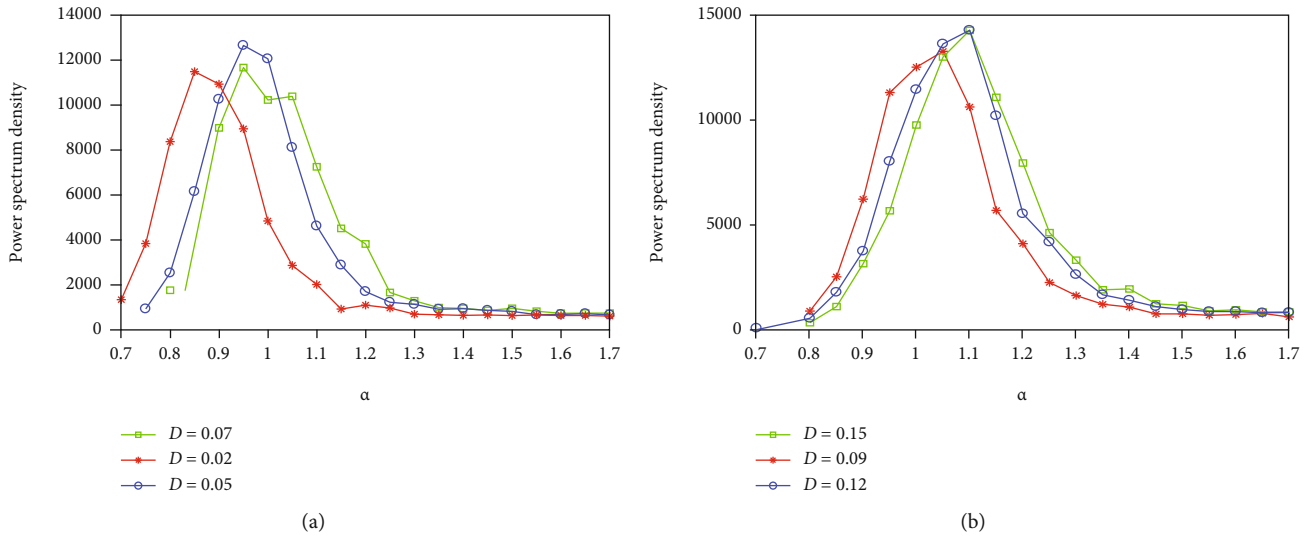

Figure 6: The relationship between characteristic exponent α and system output of undamped bistable system driven by Lévy noise. (a) The output when input is white noise intensity $D = 0.02$, 0.05, and 0.07. (b) The output when input white noise intensity is $D = 0.09$, 0.12, and 0.15.

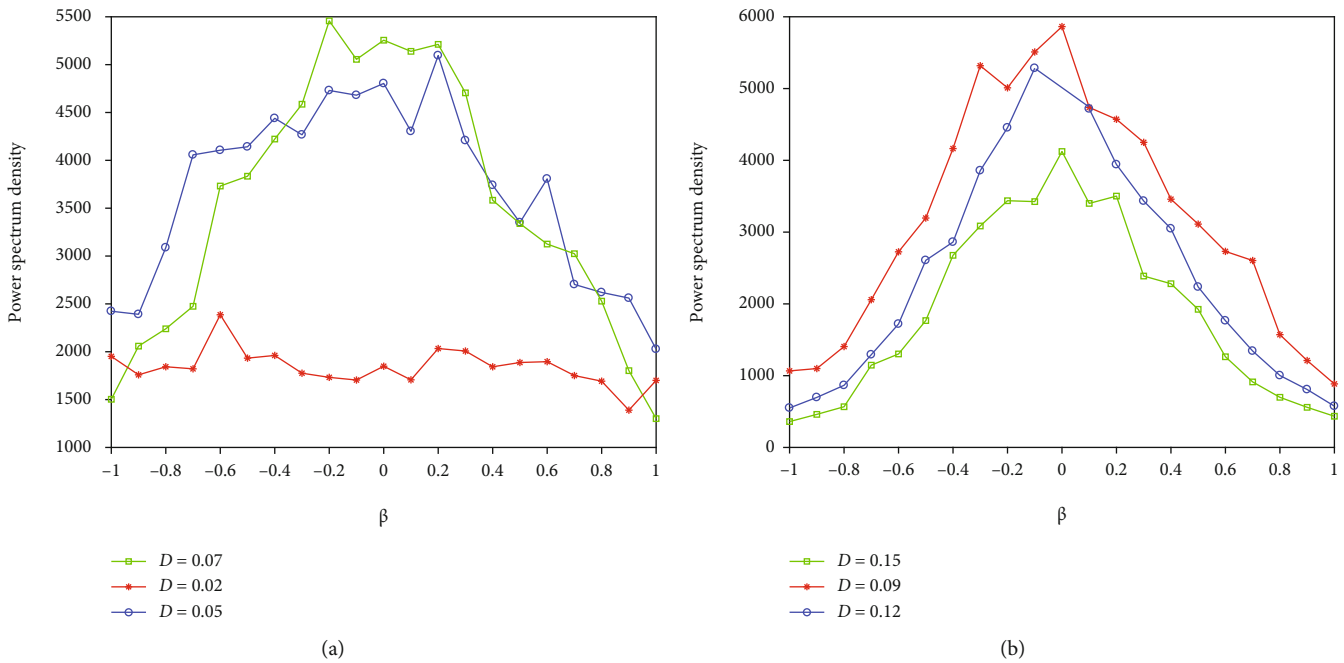

Figure 7: The relationship between symmetric parameter β and system output of undamped bistable system driven by Lévy noise. (a) The output when input white noise intensity is $D = 0.02$, 0.05, and 0.07. (b) The output when input white noise intensity is $D = 0.09$, 0.12, and 0.15.

3.3.2. The System Driven by the Asymmetric Dichotomous Noise. We mainly focused on the relationship between the noise parameter a and the system response PSD, for the two states of random telegraph noise are symmetrical. After the numerical simulation by the Euler-Maruyama method, the results are as follows.

Figure 5 shows the relationship between a and system output of undamped bistable system PSD driven by asymmetric dichotomous noise with b fixed. We find that there is stochastic resonance in this system. When it has low noise intensity, the resonance peak of power spectral density in system responding is narrower. With the increase of noise intensity, the width of the resonant peak is relatively stable, while the height of the resonant peaks goes from low to high.

3.3.3. The System Driven by the Lévy Noise. Due to the complex form of Lévy noise, it is difficult to apply the Euler-Maruyama method and Milstein method to its numerical simulation. Therefore, we will use the fourth-order Runge-Kutta method for numerical simulation, to investigate the control effect of each parameter on stochastic resonance.

In Figure 6, we find there is stochastic resonance in the relational graph. With the increase of the noise intensity, the resonant peak of the power spectral density curve is

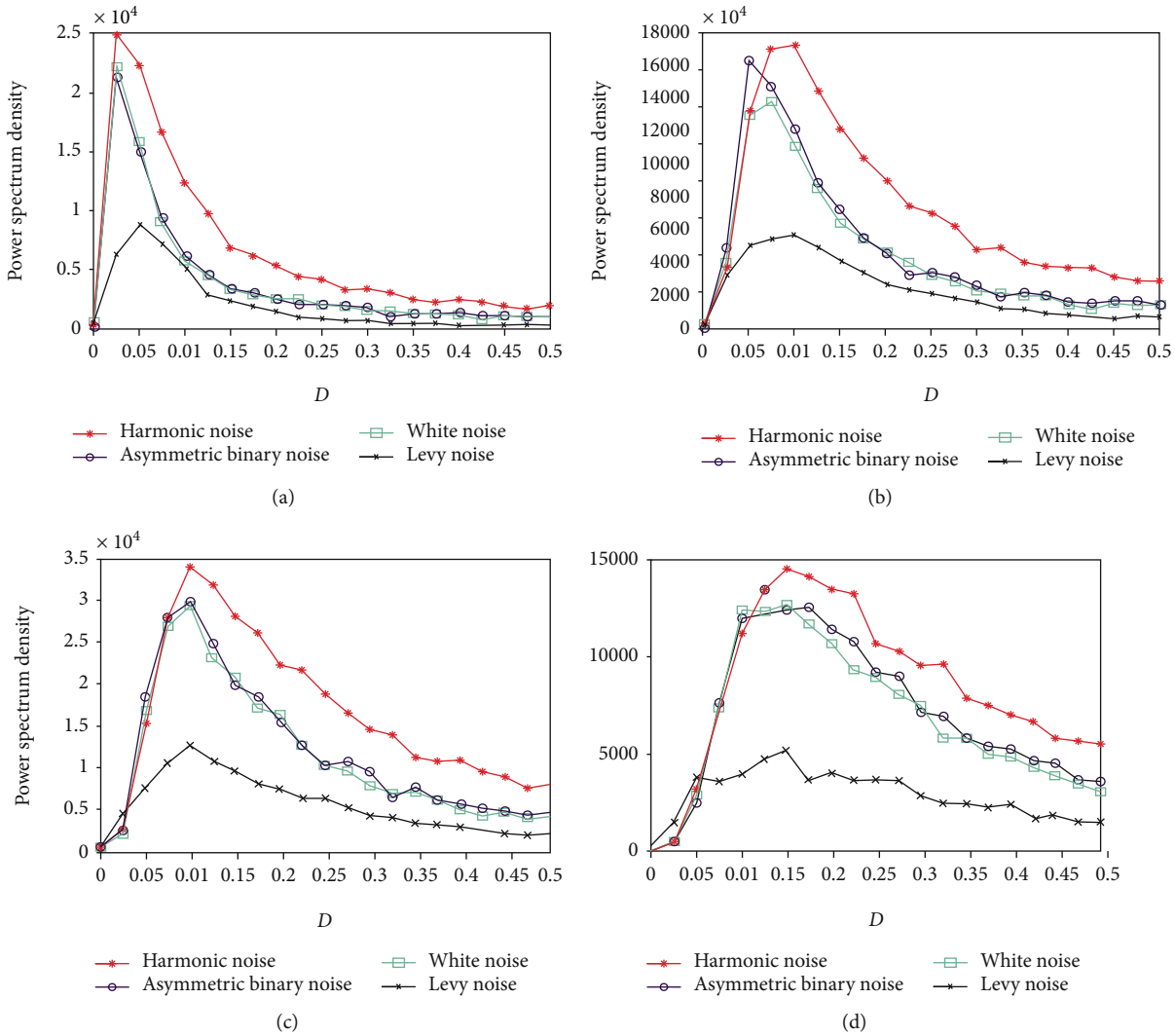

FIGURE 8: The relational graph between noise intensity D and system output of undamped bistable system driven by four noise. (a) The output when the damping coefficient of the bistable system is $\eta = 0.2$. (b) The output when $\eta = 0.5$. (c) The output when $\eta = 0.7$. (d) The output when $\eta = 1.0$.

moving in the positive direction, that is, α reaching resonance peak grows with the increase of the noise intensity.

Comparing Figures 7(a) and 7(b) in Figure 7, we found that the stochastic resonance occurs in this system. With the increase of the noise intensity, the peak value of the resonant peak of the power spectral density curve increases and then decreases. However, the position of the peak is almost unchanged. Hence, by controlling the symmetric parameter $\beta = 0$, we lead to phenomenon of the stochastic resonance of the symmetric parameters of the undamped bistable system driven by Lévy noise.

3.3.4. The Comparison of Different Noises on Stochastic Resonance. It can be found that four kinds of noise can induce the approximate periodic transition between the two states. And the frequency of the four types of jumps is close to the frequency of the input periodic forces. That is, the particle is almost synchronized with the periodic force of the input under the same parameter simulation condition. The particles are all moving up and down in the direction of the noiseless input. At the same time, we also find that the output of system output generated by harmonic noise is significantly stronger than that of other two. The vibration of the particle in two potential well is stronger when the transition occurs and then significantly decreases. Compared with that, the harmonic noise and asymmetric noise are more stable in the potential well. The case driven by Lévy noise is the most special one. Because of the pulse characteristic of steady noise, the displacement of particles varies greatly in some places and then rapidly returns to orbit.

In Figure 8, the noise intensity D can be used to guide the occurrence of random resonance. With the undamped double steady-state damping coefficient increasing, the resonant peaks of noise intensity D are constantly moving to the right. It indicates that damping has an inhibitory effect on random forces. In four kinds of noise, the output power spectral density of the harmonic noise at the signal frequency point is highest, and that from white noise and asymmetric

dichotomous noise takes second place. And that from steady noise is the lowest. When harmonic noise, asymmetric dichotomous noise, and white noise are at low noise intensity, they are very close to the spectral density of the periodic signal. The output power spectrum of the system output in the undamped bistable system is basically coincident with white noise and asymmetric dichotomous noise. The resonant peak of the stochastic resonance of the Lévy noise and the harmonic noise drive is very close to the resonant peak driven by the other two noises. It can be found that the noise type has little influence on the resonance peak of the undamped bistable system on the noise intensity D.

4. Conclusion

In this paper, we mainly study the control effect of four kinds of noise (white noise, harmonic noise, asymmetric dichotomous noise, and Lévy noise) on undamped bistable system. The random resonance phenomenon is generated by adjusting the noise parameters. Since the harmonic noise can be generated by the white noise through the resonance subsystem, we can change the properties of harmonic noise by controlling the parameters of the resonance subsystem and then we can control stochastic resonance. In this paper, the control effect of harmonic noise in undamped bistable system is studied, and the similar random resonance phenomenon is found in the undamped bistable system.

The four kinds of noise used in stochastic resonance research are simulated by numerical algorithms. Here, Euler numerical algorithm and Milstein numerical algorithm are based on stochastic differential equation and fourth-order Runge-Kutta algorithm is based on ODE. The main object of the analysis is the time domain diagram and the power spectral density diagram of the system output.

In this paper, it has indicated that in the undamped bistable system, the stochastic resonance can be controlled by the harmonic noise generated by the resonance subsystem. The four kinds of noise (white noise, harmonic noise, asymmetric dichotomous noise, and Lévy noise) can be used to change the noise parameters and control stochastic resonance under certain conditions. For these four kinds of noise, the power spectrum density of the system output is very close to the horizontal position of the resonant peak of the noise. That is, the noise type has little influence on the horizontal position of the resonant peak of stochastic resonance after full optimization.

Data Availability

The data used to support the findings of this study are included within the article.

Conflicts of Interest

The authors declare that there is no conflict of interests regarding the publication of this paper.

Acknowledgments

This work is supported by the Fundamental Research Funds for the Central Universities (Grant No. 2682018CX65).

References

[1] R. Benzi, A. Sutera, and A. Vulpiani, "The mechanism of stochastic resonance," *Journal of Physics A: Mathematical and General*, vol. 14, no. 11, pp. L453–L457, 1981.

[2] P. Hanggi, P. Jung, C. Zerbe, and F. Moss, "Can colored noise improve stochastic resonance," *Journal of Statistical Physics*, vol. 70, no. 1-2, pp. 25–47, 1993.

[3] L. Gammaitoni, P. Hänggi, P. Jung, and F. Marchesoni, "Stochastic resonance," *Reviews of Modern Physics*, vol. 70, no. 1, pp. 223–287, 1998.

[4] Z. Qiao, Y. Lei, and N. Li, "Applications of stochastic resonance to machinery fault detection: a review and tutorial," *Mechanical Systems and Signal Processing*, vol. 122, pp. 502–536, 2019.

[5] Y. Jia, S.-N. Yu, and J.-R. Li, "Stochastic resonance in a bistable system subject to multiplicative and additive noise," *Physical Review E*, vol. 62, no. 2, pp. 1869–1878, 2000.

[6] S. L. Lu, Q. B. He, and F. R. Kong, "Effects of underdamped step-varying second-order stochastic resonance for weak signal detection," *Digital Signal Processing*, vol. 36, pp. 93–103, 2015.

[7] R. Ray and S. Sengupta, "Stochastic resonance in underdamped, bistable systems," *Physics Letters A*, vol. 353, no. 5, p. 364, 2005.

[8] Y. F. Guo, F. Wei, B. Xi, and J. G. Tan, "The instability probability density evolution of the bistable system driven by Gaussian colored noise and white noise," *Physica A: Statistical Mechanics and its Applications*, vol. 503, pp. 200–208, 2018.

[9] D. Barik, P. K. Ghosh, and D. S. Ray, "Langevin dynamics with dichotomous noise; direct simulation and applications," *Journal of Statistical Mechanics-Theory and Experiment*, vol. 2006, no. 3, Article ID P03010, 2006.

[10] Z. Qiao, Y. Lei, J. Lin, and S. Niu, "Stochastic resonance subject to multiplicative and additive noise: the influence of potential asymmetries," *Physical Review E*, vol. 94, no. 5, article 052214, 2016.

[11] C. J. Wang, F. Long, P. Zhang, and L. R. Nie, "Controlling of stochastic resonance and noise enhanced stability induced by harmonic noises in a bistable system," *Physica A Statistical Mechanics & Its Applications*, vol. 471, p. 288, 2016.

[12] X. Y. Luo, "Stochastic resonance in neuronal network motifs with Ornstein-Uhlenbeck colored noise," *Mathematical Problems in Engineering*, vol. 2014, Article ID 902395, 7 pages, 2014.

[13] G. K. Er, H. T. Zhu, and V. P. Lu, "Nonzero mean PDF solution of nonlinear oscillators under external Gaussian white noise," *Nonlinear Dynamics*, vol. 62, no. 4, p. 743, 2010.

[14] G. Zhang, Y. Song, and T. Q. Zhang, "Stochastic resonance in a single-well system with exponential potential driven by Levy noise," *Chinese Journal of Physics*, vol. 55, no. 1, pp. 85–95, 2017.

[15] Z. Gingl, L. B. Kiss, and F. Moss, "Non-dynamical stochastic resonance: theory and experiments with white and arbitrarily coloured noise," *EPL (Europhysics Letters)*, vol. 29, no. 3, p. 191, 1995.

[16] Y. J. Shen, Y. F. Guo, and B. Xi, "Steady state characteristics in FHN neural system driven by correlated non-Gaussian noise

and Gaussian noise," *Acta Physica Sinica -Chinese Edition*, vol. 65, no. 12, 2016.

[17] L. Zeng, B. Xu, and J. Li, "Dynamical properties of subdiffusion in the bistable system with aperiodic inputs," *Physics Letters A*, vol. 361, no. 6, pp. 455–459, 2007.

[18] A. Neiman and L. Schimansky-Geier, "Stochastic resonance in bistable systems driven by harmonic noise," *Physical Review Letters*, vol. 72, no. 19, pp. 2988–2991, 1994.

[19] B. Ahmad, J. J. Nieto, and A. Alsaedi, "A study of nonlinear Langevin equation involving two fractional orders in different intervals," *Nonlinear Analysis Real World Applications*, vol. 13, no. 2, pp. 599–606, 2012.

[20] R. L. Honeycutt, "Stochastic Runge-Kutta algorithms.1. White noise," *Physical Review A*, vol. 45, no. 2, pp. 600–603, 1992.

[21] R. L. Honeycutt, "Stochastic Runge-Kutta algorithms. II. Colored noise," *Physical Review A*, vol. 45, no. 2, pp. 604–610, 1992.

[22] W. Rumelin, "Numerical treatment of stochastic differential equations," *SIAM Journal on Numerical Analysis*, vol. 19, no. 3, pp. 604–613, 1982.

Hindawi
Advances in Mathematical Physics
Volume 2020, Article ID 2717193, 9 pages
https://doi.org/10.1155/2020/2717193

Research Article

Study of Dust-Acoustic Multisoliton Interactions in Strongly Coupled Dusty Plasmas

Najah Kabalan, Mahmoud Ahmad, and Ali Asad

Department of Physics, Faculty of Science, Tishreen University, Latakia, Syria

Correspondence should be addressed to Ali Asad; ali760633@gmail.com

Received 4 August 2020; Revised 12 October 2020; Accepted 2 November 2020; Published 16 November 2020

Academic Editor: Zhi-Yuan Sun

The effect of the structure parameter on the compressibility of dust grains and soliton behavior in a dusty plasma system consisting of Maxwellian electrons, ions, and dust grains charged with a negative charge has been studied. In the theoretical study, a reductive perturbation technique was used to derive the Korteweg-de Vries (KdV) equation and employ the Hirota bilinear method to obtain multisoliton solution. It is found that coupling and structure parameters have a clear effect on the compressibility. These changes in the compressibility affected the amplitude and width of interactive solitons, in addition to the phase shifts resulting from the interaction. These results can be used to understand the behavior of solitary waves that occur in various natural and laboratory plasma environments with dust impurity situations.

1. Introduction

Study of nonlinear phenomena in dusty plasma had a great deal of interest because of the presence of dust in various space and astrophysical environments, for example, planetary rings, comets, the Earth's ionosphere, and interstellar molecular clouds [1, 2]. Moreover, dusty plasma opened up a new field of research after the possibility of crystallization (whose temperature is low relative to the temperature of other components) in a crystalline structure called a plasma crystal or coulomb crystal was discovered [3, 4].

Dusty plasma is composed of ordinary plasma (electron-ion plasma) and additional solid grains whose radius range from 100 nm-100 μm. These grains are charged with a negative charge because the thermal velocity of electrons is greater than that of ions [2].

The Coulomb coupling parameter is one of the basic properties of the dusty plasma system, which determines the phase state of the system and is a dimensionless parameter which represents the ratio between the electrostatic interaction energy and the thermal energy of the grains, and the first investigations showed that the Coulomb coupling parameter is given as follows [5]:

$$\Gamma_c = \frac{(eZ_d)^2}{4\pi\varepsilon_0 a T_d}, \tag{1}$$

where $a = (3/4\pi n_d)^{1/3}$ interparticle distance, T_d is the temperature of dust grains, n_d is the grain number density, and $Z_d$is the charge number of grains. Later, a new mathematical formula of the coupling parameter was obtained after considering the screening of charges, using the Debye-Hückel or Yukawa potential that is given as follows [6]:

$$\Gamma = \frac{(eZ_d)^2}{4\pi\varepsilon_0 a T_d} \exp(-k), \tag{2}$$

where $k = a/\lambda_D$ is the structural parameter, which represents the ratio between the interparticle distance and the Debye screening length. Vaulina and Khrapak proposed an empirical scaling law of the coupling parameter that is compatible with recent molecular dynamics simulations, which is given as follows [7]:

$$\Gamma = \frac{(eZ_d)^2}{4\pi\varepsilon_0 a T_d}\left(1 + k + \frac{k^2}{2}\right)^{1/2} \exp(-k). \quad (3)$$

The presence of dust of a relatively large mass and charge contributes to modifying the plasma collective behavior and generates new linear and nonlinear modes, for example, dust-ion-acoustic (DIA) waves [8], dust-acoustic waves (DA) [9], dust-lattice (DL) waves [10], DIA solitary waves [11], DA solitary waves [12], and DL solitary waves [13].

Many researchers have studied the interaction of nonlinear waves in dusty plasma systems using many analytical, experimental, and numerical methods. Jaiswal et al. [14] studied dust-acoustic solitary wave (DASW) head-on collision in strongly and weakly coupled dusty plasma, using the extended Poincaré–Lighthill–Kuo perturbation method. Effects of dusty plasma parameters on phase shifts of these solitary waves are studied. They found that the phase shift changes its sign when compressibility of the medium exceeds the critical value for a specific set of dusty plasma parameters. Gao et al. [15] studied the overtaking collision between two dust-acoustic waves in dusty plasmas consisting of Boltzmann electrons and ions, and negative dust grains by the PIC simulation method. They compared their results with previous theoretical studies using the Hirota method and found a significant correlation between the results of the two methods. Boruah et al. [16] experimentally investigated the propagation and interaction of dust-acoustic multisolitons which unmagnetized strongly coupled dusty plasma. By comparing their results with previous theoretical studies, they proved that the evolution of these waves depends on the amplitude of the initial perturbation. Tao et al. [17] studied the head-on collision between two dust-acoustic solitary waves in an unmagnetized strongly coupled dust plasma using the PIC simulation method. By comparing simulation results with an analytical study, they noted that the analytical results are correct if the amplitudes of both of the colliding solitary waves are sufficiently small. Seadawy and Jun [18] obtained The Zakharov–Kuznetsov–Burgers (ZKB) equations that describe the dust-ion-acoustic waves in dusty plasma with high-energy electrons and positrons by applying the modified direct algebraic method. They found that the electric field potential, electric field, and quantum statistical pressure significantly impact in the form of water wave solutions for the three-dimensional ZKB equation. Arnous et al. [19] applied the modified simple equation method to the complex Ginzburg–Landau equation to secure soliton solutions. They studied using this method the Kerr and power laws of nonlinearity. The results of their investigation showed that the limitation of the scheme prevents obtaining bright soliton solutions. Seadawy [20] applied the reductive perturbation procedure method on the fluid system governing plasma, and he got the nonlinear three-dimensional modified Zakharov–Kuznetsov (mZK) equation governing the propagation of ion dynamics of nonlinear ion-acoustic waves in a plasma comprising cold ions and hot isothermal electrons in the presence of a uniform magnetic field. He found that the electrostatic field potential and electric field form traveling wave solutions for the three-dimensional mZK equation.

The Hirota bilinear method differs from the mathematical methods used in previous investigations (for example, the extended modified direct algebraic method and extended mapping method) in that it enables us to obtain multisoliton solutions of nonlinear partial differential equations, which is why we chose this method. Also, previous studies have examined the effect of the coupling parameter on the behavior of the solitons in the strongly coupled dusty plasma but neglected the effect of the structure parameter, as this parameter is expected to play an important role. In this scenario, we relied on the results mentioned in Reference [20], which showed that the internal energy is related to the coupling parameter and the structure parameter together.

In this paper, the overtaking collision between two solitons and three solitons in strongly coupled dusty plasma is studied. The effect of the structure parameter on plasma compressibility and the behavior of the interactive solitons is taken into account. The reductive perturbation method is applied to obtain the Korteweg-de Vries (KdV) equation. The Hirota bilinear method is applied to obtain multisoliton solutions. Computer modeling used the Maple program to show the time development of the propagation and interaction of solitons.

2. Materials and Methods

We consider an unmagnetized strongly coupled dusty plasma system with negatively charged inertial dust grains and inertia-less electrons and the ions that can be described by Boltzmann distributions. The dust fluid equations that can describe this system are given as follows [14, 21]:

$$\frac{\partial n_d}{\partial t} + \frac{\partial (n_d \vartheta_d)}{\partial x} = 0, \quad (4)$$

$$\frac{\partial \vartheta_d}{\partial t} + \vartheta_d \frac{\partial \vartheta_d}{\partial x} = \frac{\partial \Phi}{\partial x} - \frac{\acute{\mu}}{n_d}\frac{\partial n_d}{\partial x}, \quad (5)$$

$$\frac{\partial^2 \Phi}{\partial x^2} = \mu_e n_e + n_d - \mu_i n_i, \quad (6)$$

where n_d is the dust grain number density, $\vartheta_d$is the dust fluid velocity, Φ is the electrostatic potential, n_e is the electron number density, and n_i is the ion number density. The following normalization

$$n_d \to \frac{n_d}{n_{d0}}, \Phi \to \frac{e\varnothing}{K_B T_i}, \vartheta_d \to \frac{\vartheta_d}{C_d}, x \to \frac{x}{\lambda_D}, t \to t\omega_{pd}, \quad (7)$$

where $\lambda_D = (\mathrm{K}_B T_i / n_{d0} Z_d e^2)^{1/2}$ is the dust Debye length, $C_d = (Z_d \mathrm{K}_B T_i / m_d)^{1/2}$ is the dust-acoustic speed, $\omega_{pd} = (n_{d0} {Z_d}^2 e^2 / m_d)^{1/2}$ is the dust plasma frequency, and K_B, n_{d0}, e, and m_d are the Boltzmann constant, the unperturbed dust grain number density, the electron charge, and the dust grain mass, respectively. The contribution due to the compressibility (μ) in the momentum equation, equation (5), is expressed in terms of $\acute{\mu}$ where $\acute{\mu} = \mu T_d / Z_d T_i$ where T_d, T_i, and Z_d denote the dust temperature, the ion temperature, and the

number of electrons residing on the surface of the negatively charged dust grains, respectively. The compressibility μ is defined as [2]

$$\mu = \frac{1}{T_d}\left(\frac{\partial P}{\partial n}\right)_{T_d} = 1 + \frac{u(\Gamma)}{3} + \frac{\Gamma}{9}\frac{\partial u(\Gamma)}{\partial \Gamma}, \tag{8}$$

where Γ is the Coulomb coupling parameter and $u(\Gamma)$ is a measure of the excess internal energy of the system. For a weakly coupled plasma $\Gamma < 1$, $u(\Gamma)$ can be written as $u(\Gamma) \approx -(\sqrt{3}/2)\Gamma^{3/2}$ [22], while in the case of strong coupling (Yukawa fluid) $\Gamma > 100$ excess internal energy can be determined as a function of (k, Γ) by using the following relation [23]:

$$u(k, \Gamma) = a(k)\Gamma + b(k)\Gamma^{1/3} + c(k) + d(k)\Gamma^{-(1/3)}, \tag{9}$$

where parameters $a(k)$, $b(k)$, $c(k)$, and $d(k)$ are defined as follows:

$$\left.\begin{aligned} a(k) &= \frac{k}{2} - 0.899 - 0.103\,k^2 + 0.003\,k^4 \\ b(k) &= 0.565 - 0.026\,k^2 - 0.003\,k^4 \\ c(k) &= -0.207 - 0.086\,k^2 + 0.018\,k^4 \\ d(k) &= -0.031 + 0.042\,k^2 - 0.008\,k^4 \end{aligned}\right\}. \tag{10}$$

The densities of Boltzmann distributed electrons and ions at temperatures T_e and T_i can be written in a normalized form as

$$\begin{aligned} n_e &= \mu_e \exp(\sigma_i \varnothing), \\ n_i &= \mu_i \exp(-\varnothing), \end{aligned} \tag{11}$$

where $\sigma_i = T_i/T_e$ is the ratio of ion temperature and electron temperature, $\mu_e = 1/(\delta - 1)$, and $\mu_i = \delta/(\delta - 1)$, where δ is the ratio of equilibrium ion to electron densities.

3. Derivation of KdV Equation

Now, we derive the KdV equation from equations (4)–(6) by employing the reductive perturbation technique. The independent variables are stretched as

$$\left.\begin{aligned} &\xi = \varepsilon^{1/2}(x - ct), \tau = \varepsilon^{3/2}t \\ &\frac{\partial}{\partial x} = \varepsilon^{1/2}\frac{\partial}{\partial \xi}, \frac{\partial}{\partial t} = -c\varepsilon^{1/2}\frac{\partial}{\partial \xi} + \varepsilon^{3/2}\frac{\partial}{\partial \tau} \end{aligned}\right\}, \tag{12}$$

and the dependent variables are expanded as

$$\left.\begin{aligned} n_d &= 1 + \varepsilon n_1 + \varepsilon^2 n_2 + \cdots \\ \vartheta_d &= \varepsilon\vartheta_1 + \varepsilon^2\vartheta_2 + \cdots \\ \Phi &= \varepsilon\Phi_1 + \varepsilon^2\Phi_2 + \cdots \end{aligned}\right\}. \tag{13}$$

ε is a small parameter proportional to the strength of the perturbation. Substituting (12)–(13) into (4)–(6) and taking the terms in different powers of ε, we obtain in the lowest order of ε:

$$\begin{aligned} n_1 &= -(\mu_e\sigma_i + \mu_i)\Phi_1, \\ \vartheta_1 &= -c(\mu_e\sigma_i + \mu_i)\Phi_1, \end{aligned} \tag{14}$$

where c the phase velocity given as follows:

$$c = \sqrt{\frac{1 + \acute{\mu}(\mu_e\sigma_i + \mu_i)}{(\mu_e\sigma_i + \mu_i)}}. \tag{15}$$

Similarly, we get from the terms of order ε^2 and $\varepsilon^{5/2}$:

$$-c\frac{\partial n_2}{\partial \xi} + \frac{\partial n_1}{\partial \tau} + n_1\frac{\partial \vartheta_1}{\partial \xi} + \frac{\partial \vartheta_2}{\partial \xi} + \vartheta_1\frac{\partial n_1}{\partial \xi} = 0, \tag{16}$$

$$-c\frac{\partial \vartheta_2}{\partial \xi} + \frac{\partial \vartheta_1}{\partial \tau} + \vartheta_1\frac{\partial \vartheta_1}{\partial \xi} = \frac{\partial \Phi_2}{\partial \xi} + \acute{\mu}n_1\frac{\partial n_1}{\partial \xi} - \acute{\mu}\frac{\partial n_2}{\partial \xi}, \tag{17}$$

$$\frac{\partial^2 \Phi_1}{\partial \xi^2} = n_2 + (\mu_e\sigma_i + \mu_i)\Phi_2 + \left(\frac{\mu_e{\sigma_i}^2 - \mu_i}{2}\right)\varnothing_1^2. \tag{18}$$

By common solution to system of equations (15)–(17), we obtain the following Korteweg-de Vries (KdV) equation for the first-order perturbed electrostatic potential Φ_1 as follows:

$$\frac{\partial \Phi_1}{\partial \tau} + A\Phi_1\frac{\partial \Phi_1}{\partial \xi} + B\frac{\partial^3 \Phi_1}{\partial \xi^3} = 0, \tag{19}$$

where the nonlinear coefficient A and the dispersion coefficient B are given by

$$A = -\frac{1}{E}\left\{\left[(\mu_e\sigma_i + \mu_i)^2\left[3 + 2\acute{\mu}(\mu_e\sigma_i + \mu_i)\right] + \left(\mu_e{\sigma_i}^2 - \mu_i\right)\right]\right\}, \tag{20}$$

$$B = \frac{1}{E}, \tag{21}$$

where

$$E = \left\{\frac{(\mu_e\sigma_i + \mu_i)}{c}\left[1 + 2\acute{\mu}(\mu_e\sigma_i + \mu_i)\right]\right\}. \tag{22}$$

4. Multisoliton Solutions

For obtaining the multisoliton solution of equation (16) and to study the interaction between them, to do so, we shall employ the Hirota bilinear method [23].

The first step: using the transformation on equation (19):

$$\Phi_1 = \frac{12B}{A}\frac{\partial^2(\ln(f(\xi, \tau)))}{\partial \xi^2}. \tag{23}$$

We get the following equation:

$$-f_{\xi}f_{\tau} + ff_{\xi\tau} + Bff_{\xi\xi\xi\xi} - 4Bf_{\xi\xi\xi}\cdot f_{\xi} + 3B\left(f_{\xi\xi}\right)^2 = 0. \quad (24)$$

By using the Hirota-D operator, we get

$$D_{\tau}D_{\xi}\{f,f\} = 2\left(ff_{\xi\tau} - f_{\xi}f_{\tau}\right), \quad (25)$$

$$BD_{\xi}{}^4\{f,f\} = 2\left(Bff_{\xi\xi\xi\xi} - 4\mathrm{B}f_{\xi}f_{\xi\xi\xi} + 3B\left(f_{\xi\xi}\right)^2\right). \quad (26)$$

Using (25) and (26) in (24), we get the Hirota bilinear form:

$$\left(D_{\tau}D_{\xi} + BD_{\xi}{}^4\right)\{f,f\} = 0, \quad (27)$$

where D is a binary operator (because it operates on a pair of functions) and is called the Hirota derivative.

We use Hirota's perturbation technique, and we insert $f = 1 + \varepsilon f_1$ where $f_1 = e^{\theta_1}$; substituting $\varepsilon = 1$, we obtain $f = 1 + f_1$; now substituting in equation (23), we get the single-soliton solution as follows:

$$\Phi_1 = \frac{12B}{A}\frac{\partial^2\left\{\ln\left[1 + e^{\left(k_1B^{-(1/3)}\xi - k_1^3\tau\right)}\right]\right\}}{\partial\xi^2}. \quad (28)$$

Same as the previous method, we insert $f = 1 + \varepsilon f_1 + \varepsilon^2 f_2$ where $f_1 = e^{\theta_1} + e^{\theta_2}$ and make some necessary mathematical calculations. We get the relationship $f_2 = a(1,2)e^{\theta_1+\theta_2}$; now substituting in equation (23), we get the two-soliton solution as follows:

$$\Phi_1 = \frac{12B}{A}\frac{\partial^2\left\{\ln\left[1 + e^{\theta_1} + e^{\theta_1} + a(1,2)e^{\theta_1+\theta_2}\right]\right\}}{\partial\xi^2}, \quad (29)$$

where $\theta_i = k_iB^{-(1/3)}\xi - k_i^3\tau - \Delta_i$, $i = 1, 2$, $\Delta_i = \mp(2B^{1/3}/k_i)\ln|\sqrt{a(1,2)}|$ are the phase shifts $a(1,2) = (k_1 - k_2)^2/(k_1 + k_2)^2$ where k_1, k_2 are wave numbers.

In order to get a three-soliton solution, we insert $f = 1 + \varepsilon f_1 + \varepsilon^2 f_2 + \varepsilon^3 f_3 t$ where $f_1 = e^{\theta_1} + e^{\theta_2} + e^{\theta_3}$. f_2 and f_3 are determined by performing some mathematical calculations, and we get the following two relationships:

$$\begin{aligned} f_2 &= a(1,2)e^{\theta_1+\theta_2} + a(1,3)e^{\theta_1+\theta_3} + a(2,3)e^{\theta_2+\theta_3}, \\ f_3 &= be^{\theta_1+\theta_2+\theta_3}. \end{aligned} \quad (30)$$

Substituting in equation (23), we get the two-soliton solution as follows:

$$\begin{aligned} \Phi_1 = \frac{12B}{A}\frac{\partial^2}{\partial\xi^2}\Big\{\ln\Big[1 &+ e^{\theta_1} + e^{\theta_2} + e^{\theta_3} + a(1,2)e^{\theta_1+\theta_2} \\ &+ a(1,3)e^{\theta_1+\theta_3} + a(2,3)e^{\theta_2+\theta_3} + be^{\theta_1+\theta_2+\theta_3}\Big]\Big\}, \end{aligned} \quad (31)$$

where $\theta_1 = k_1B^{-(1/3)}\xi - k_1^3\tau - \Delta_1'$, $\theta_2 = k_2B^{-(1/3)}\xi - k_2^3\tau - \Delta_2'$, and $\theta_3 = k_3B^{-(1/3)}\xi - k_3^3\tau - \Delta_3'$.

The phase shifts are given as follows:

$$\begin{aligned} \Delta_1' &= \mp\frac{2B^{1/3}}{k_1}\ln\left|\frac{b}{a(2,3)}\right|, \quad \Delta_2' = \mp\frac{2B^{1/3}}{k_2}\ln\left|\frac{b}{a(1,3)}\right|, \quad \Delta_3' \\ &= \mp\frac{2B^{1/3}}{k_3}\ln\left|\frac{b}{a(1,2)}\right|, \end{aligned} \quad (32)$$

where $a(1,2) = (k_1 - k_2)^2/(k_1 + k_2)^2$, $a(1,3) = (k_1 - k_3)^2/(k_1 + k_3)^2$, $a(2,3) = (k_2 - k_3)^2/(k_2 + k_3)^2$, and $b = a(1,2)a(1,3)a(2,3)$.

5. Results and Discussion

In this work, we investigated the propagation and interaction of DA multisolitons in strongly coupled dusty plasma consisting of Maxwellian electrons, ions, and inertial negative dust grains. The Korteweg-de Vries (KdV) equation (19) was obtained using a reductive perturbation technique. Soliton solutions are formed due to the balance between the nonlinear coefficient A and the dispersion coefficient B. It is important to indicate the numerical data used in this study obtained from References [24, 25]. The range of structure parameter and the coupling parameter values were chosen based on experimental data, which describes the Yukawa fluid in the case of strong coupling, taken from References [26, 27].

5.1. Compressibility Changes. We plotted the compressibility variations with the coupling parameter for different values of the structure parameter and obtained Figure 1.

In Figure 1, it is shown that the compressibility decreases with the increasing coupling parameter, while the compressibility increases with the increase in the structure parameter value. The increase in the structure parameter means an increase of interparticle distance and a decrease of the Debye screening length; hence, the grains would become more mobile to move. This causes an increase of its compressibility. We compare this result with the result presented in Figure 2 from Reference [17].

In Figure 2, the change of compressibility when the plasma is transferred from the weak coupling state ($\Gamma < 1$) to a strong coupling state ($\Gamma > 1$) while neglecting the effect of the structure parameter ($k = 0$) is shown. By comparing the two shapes (1) and (2), it appears that there is a great agreement between our results and the results of the aforementioned reference when the plasma becomes a strong coupling state where the compressibility values become negative.

5.2. Soliton Shape Changes. We plotted the single-soliton shape relation (28) variations for different values of the structure parameter and obtained Figure 3.

We plotted the single-soliton shape relation (25) variations for different values of the coupling parameter and obtained Figure 4.

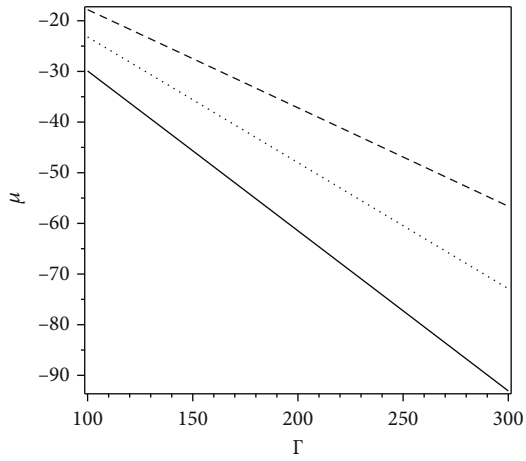

Figure 1: Compressibility variations with the coupling parameter for different values of the structure parameter, $k = 0.4$ (solid line), $k = 0.8$ (dot line), and $k = 1.2$ (dashed line).

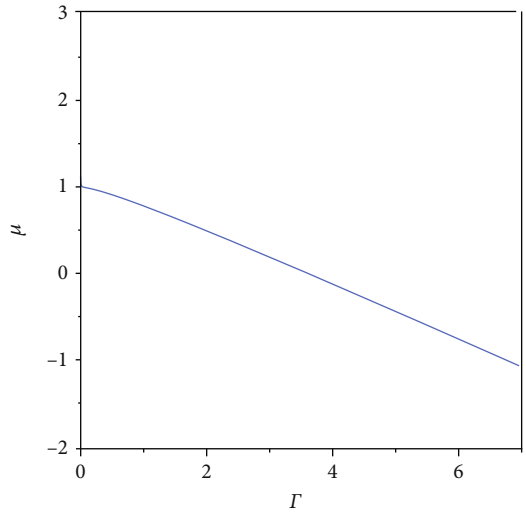

Figure 2: Compressibility variations with the coupling parameter from Reference [17].

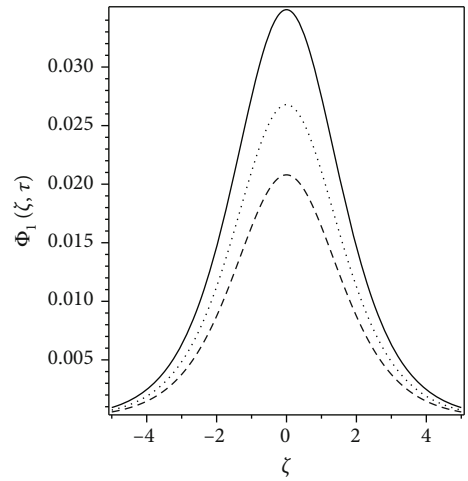

Figure 3: Single-soliton shape variations for different values of the structure parameter, $k = 1.2$ (solid line), $k = 0.8$ (dot line), and $k = 0.4$ (dashed line). $\sigma = 0.1$, $\delta = 10$, and $\Gamma = 170$.

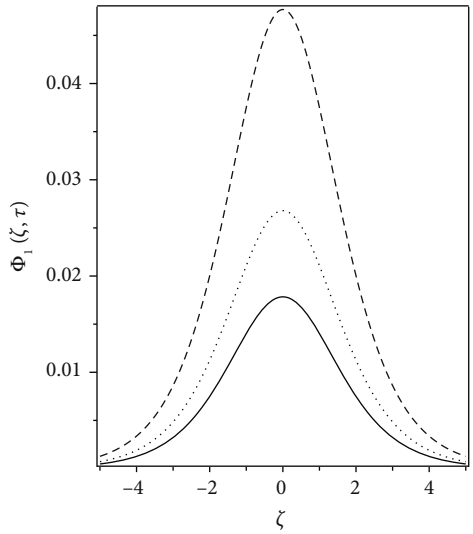

Figure 4: Single-soliton shape variations for different values of the coupling parameter, $\Gamma = 250$ (solid line), $\Gamma = 170$ (dot line), and $\Gamma = 100$ (dashed line). $\sigma = 0.1$, $\delta = 10$, and $k = 0.8$.

Figure 3 shows that the amplitude and width of the soliton increases with the increase of the structure parameter (compressibility increasing) for a constant value of the coupling parameter $\Gamma = 170$. Figure 4 shows that the amplitude and width of the soliton decreases with the increase of the coupling parameter (compressibility decreases) for a constant value of the structure parameter $k = 0.8$. It is observed from Figure 3 that the amplitude of the soliton decreases significantly when the value of the coupling parameter increases from $\Gamma = 100$ (dashed line) to $\Gamma = 170$ (dotted line). It is the critical value of the plasma transmission from the fluid phase to a quasisolid structure called the plasma crystal. These results correspond with the simulation results in Reference [17] and with the theoretical study that did not take into account the effect of the structure parameter on the compressibility (i.e., $k = 0$) in Reference [14].

5.3. Time Evolution of Multisolitons. The mathematical study used in this investigation differs from the previous investigations [18, 19, 28], as they used the Zakharov–Kuznetsov equation (ZK), which is an appropriate equation for studying the (2 + 1)-dimensional systems. But the reason for using the Korteweg-de Vries (KdV) equation in this investigation is that the KdV equation describes multisoliton solutions depending on the initial conditions, as well as the possibility of applying the Hirota direct method to this equation. Thus, this equation fulfills the required purpose of our investigation. The Hirota method is an innovative and powerful method by which we can obtain, in principle, any number of solutions for many nonlinear partial differential equations.

In this section, we used the Mable program to perform a numerical simulation showing the propagation and

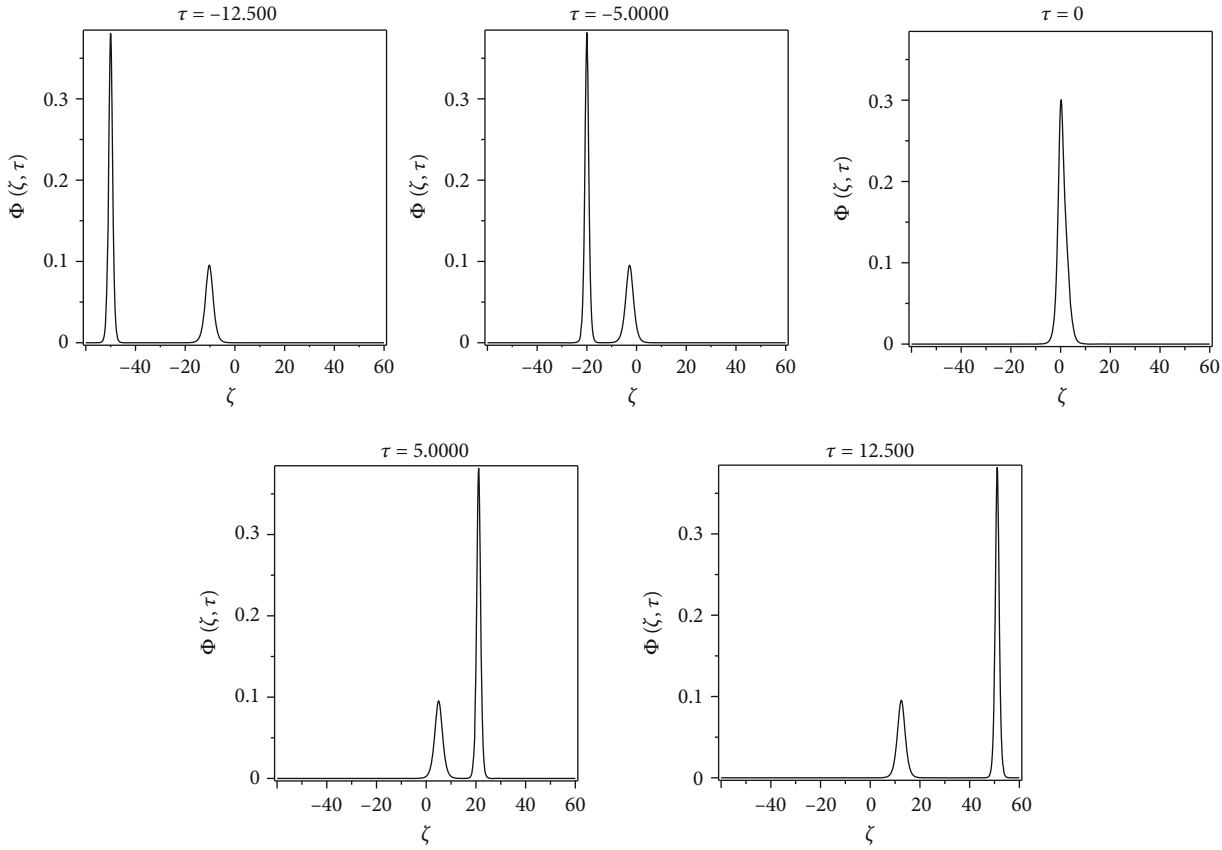

Figure 5: Time evolution of two solitons at different times, $\sigma = 0.1$, $\delta = 10$, $k = 0.8$, $\Gamma = 170$, $k_1 = 1$, and $k_2 = 2$.

interaction of solitons moving in the same direction, and we obtained the following results.

Figure 5 shows the time evolution of two solitons with different amplitudes and widths moving in the same direction from left to right at different times of τ. At $\tau = -12.5$, the larger amplitude soliton is behind the smaller amplitude soliton. With the passage of time, a large soliton approaches a small soliton at $\tau = -5$ because a higher amplitude soliton travels faster than a smaller amplitude soliton. At $\tau = 0$, the two solitons merge and become one soliton where the amplitude of this soliton is less than the amplitude of the large soliton and greater than the amplitude of the small soliton. At $\tau = 5$, they separate from each other again, and each soliton acquires its shape and speed before the reaction, but the large soliton comes in front.

Similarly, the two-soliton interaction scenario was applied on the time evolution of three solitons with different amplitudes and widths moving in the same direction from left to right at different times of τ; the results are shown in Figure 6. It should be noted that the results of simulation of the time evolution of propagation and interaction of solitons in this work correspond with the experimental results in Reference [16].

5.4. Phase Shifts. In this section, we studied the effect of the structure parameter on the phase shifts of interaction solitons, and we obtained the following results.

Figures 7 and 8 show a decrease of phase shift as the structure parameter increases. The reason for the decrease in the phase shift value is due to the phase shift being related to the dispersion coefficient B, which in turn is related to the structure parameter as shown in relation (21). In other words, the phase shifts of solitons after interaction increase as the coupling strength between dust particles increases. This is achieved when the value of the structure parameter is small, that is, the interparticle distance becomes smaller. When we neglect the effect of the structure parameter and study the phase shift changes with compressibility, we get results similar to the theoretical study and PIC simulation in the Figure 5 of Reference [18]. The difference between our study and their study is in the method used, as they used the Poincaré–Lighthill–Kuo (PLK) method in a study of the head-on collision between two dust-acoustic solitary waves. Any waves moving in opposite directions, in which case the effect of the collision is greater, cause an increase in the phase shifts resulting from the collision. In addition, phase shifts are decreasing with the wave number increasing. This corresponds with the results in Reference [29].

6. Conclusions

In this work, the effect of the structure parameter on the compressibility of dust grains and soliton behavior in a dusty plasma system consisting of Maxwellian electrons, ions, and

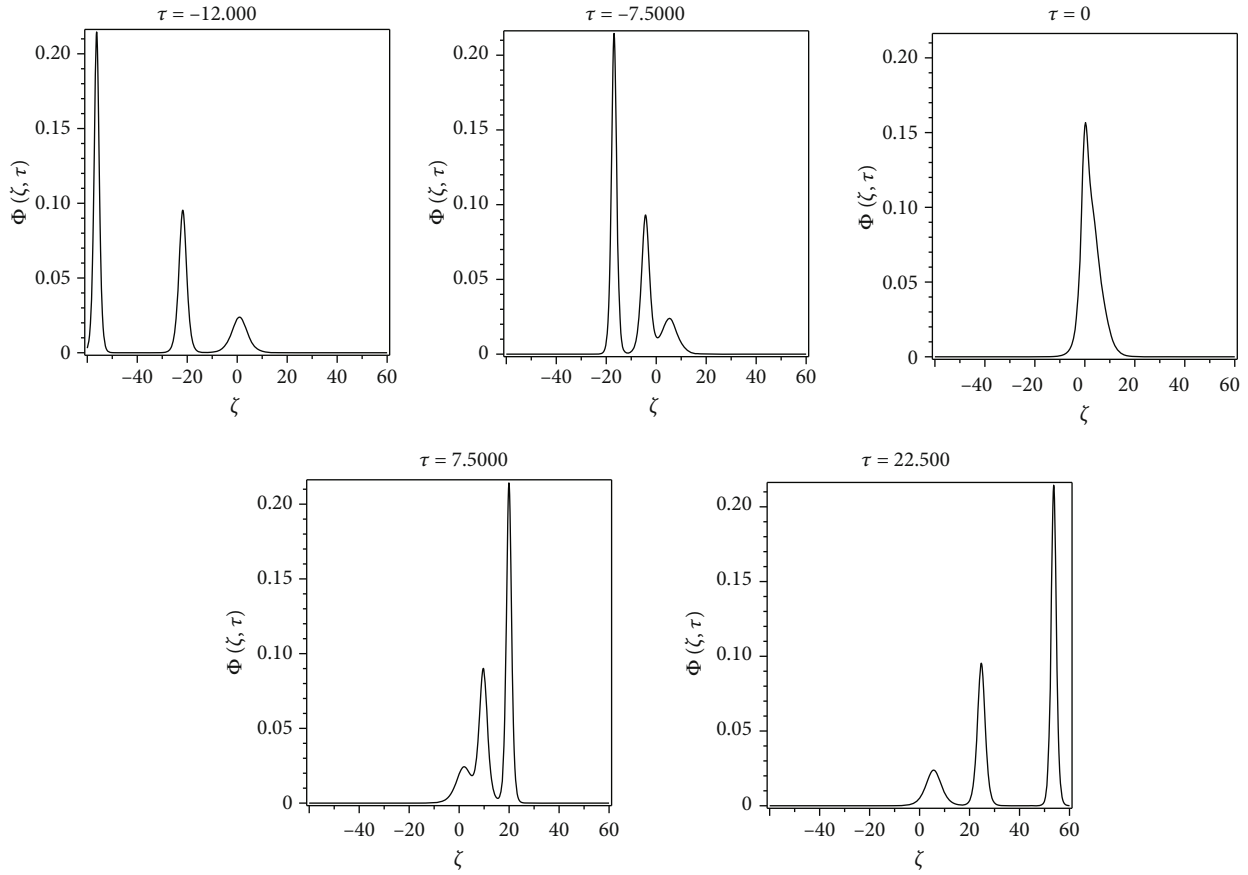

Figure 6: Time evolution of three solitons at different times, $\sigma = 0.1$, $\delta = 10$, $k = 0.8$, $\Gamma = 170$, $k_1 = 0.5$, $k_2 = 1$, and $k_3 = 1.5$.

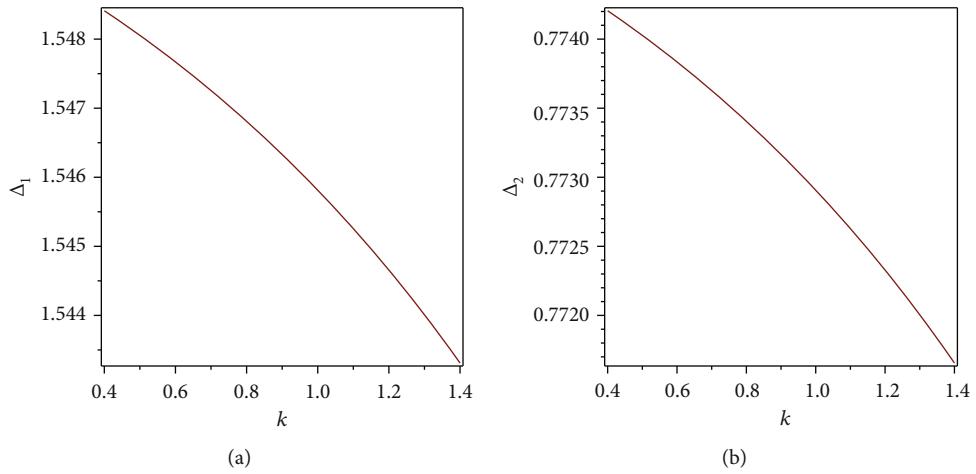

Figure 7: Variation of the phase shift for two solitons against the structure parameter, for small soliton $k_1 = 1$ (a) and for large soliton $k_2 = 2$ (b), for fixed values of $\sigma = 0.1$, $\delta = 10$, and $\Gamma = 170$.

dust grains charged with a negative charge has been studied. In the theoretical study, a reductive perturbation technique was used to derive the Korteweg-de Vries (KdV) equation, employing the Hirota bilinear method for obtaining a multi-soliton solution. The Mable program was used to perform a numerical simulation showing the propagation and interaction of solitons. The results obtained can be summarized as follows:

(i) Coupling and structure parameters have a clear effect on the compressibility, where the compressibility increases with the increase of the structural

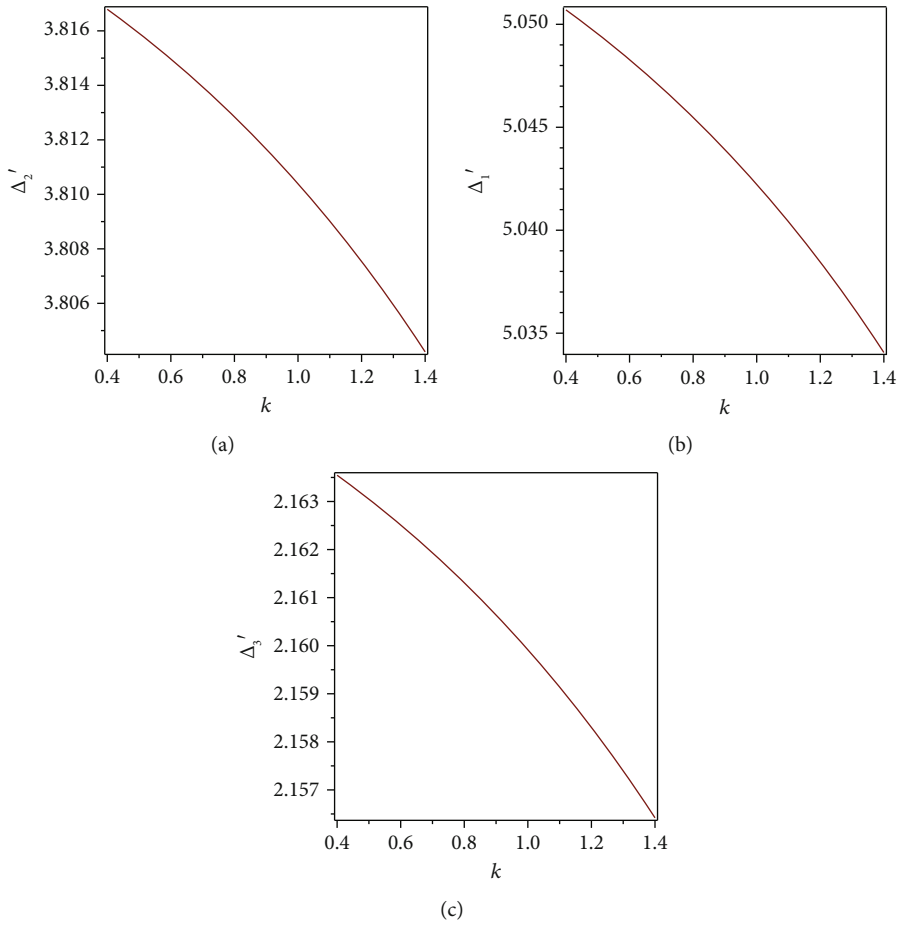

Figure 8: Variation of the phase shift for three solitons against the structure parameter, for the small soliton $k_1 = 0.5$ (a), for the medium soliton $k_2 = 1$ (b), and for the large soliton $k_3 = 1.5$ (c), for fixed values of $\sigma = 0.1$, $\delta = 10$, and $\Gamma = 170$.

parameter and decreases with increase of the coupling parameter

(ii) Compressibility changes contributed to modifying the shape of the soliton, where amplitude and width of the soliton increases with the increase of the structure parameter and decreases with the increase of the coupling parameter

(iii) Numerical simulation of propagation and interaction of solitons showed interest corresponding with previous relevant theoretical and experimental works

(iv) The phase shift of the interactive solitons decreases with structure parameter and wave number increase

Our results showed that the smaller the distance between the grains, the more strongly coupled the dusty plasma, so the structure parameter plays an important role in determining the phase state of the dusty plasma, which clearly affects the behavior of the nonlinear dusty acoustic pattern propagation in this type of plasma.

Analytical and numerical solutions of nonlinear partial differential equations are useful in enabling us to deeply understand the behavior of nonlinear phenomena in complex plasma systems. Moreover, solitons have played a very important and useful role in communication, where optical soliton pulses contributed running over long distances and transmitting high data rate information in optical fiber [30]. In biology, soliton theory has been used to describe signal and energy propagation in biomembranes as occurs, for example, in the nervous system and to low frequency collective pattern proteins and DNA [31].

Data Availability

No data were used to support this study.

Conflicts of Interest

The authors declare that there are no conflicts of interest regarding the publication of this paper.

Acknowledgments

This study was supported by Tishreen University.

References

[1] R. Bingham, U. De Angelis, V. N. Tsytovich, and O. Havnes, "Electromagnetic wave scattering in dusty plasmas," *Physics of Fluids B: Plasma Physics*, vol. 3, no. 3, pp. 811–817, 1991.

[2] P. K. Shukla and A. A. Mamun, *Introduction to Dusty Plasma Physics*, Institute of Physics, Bristol, UK, 2002.

[3] A. Barkan, R. L. Merlino, and N. D'Angelo, "Laboratory observation of the dust-acoustic wave mode," *Physics of Plasmas*, vol. 2, no. 10, pp. 3563–3565, 1995.

[4] R. L. Merlino, A. Barkan, C. Thompson, and N. D'Angelo, "Laboratory studies of waves and instabilities in dusty plasmas," *Physics of Plasmas*, vol. 5, no. 5, pp. 1607–1614, 1998.

[5] E. L. Pollock and J. P. Hansen, "Statistical mechanics of dense ionized matter. II. Equilibrium properties and melting transition of the crystallized one-component plasma," *Physical Review*, vol. 8, no. 6, pp. 3110–3122, 1973.

[6] H. Ikezi, "Coulomb solid of small particles in plasmas," *Physics of Fluids*, vol. 29, no. 6, p. 1764, 1986.

[7] O. S. Vaulina and S. A. Khrapak, "Scaling law for the fluid-solid phase transition in Yukawa systems (dusty plasmas)," *Journal of Experimental and Theoretical Physics*, vol. 90, no. 2, pp. 287–289, 2000.

[8] P. K. Shukla and V. P. Silin, "Dust ion-acoustic wave," *Physica Scripta*, vol. 45, no. 5, pp. 508-509, 1992.

[9] N. N. Rao, P. K. Shukla, and M. Y. Yu, "Dust-acoustic waves in dusty plasmas," *Planetary and Space Science*, vol. 38, no. 4, pp. 543–546, 1990.

[10] F. Melands, "Lattice waves in dust plasma crystals," *Physics of Plasmas*, vol. 3, no. 11, pp. 3890–3901, 1996.

[11] M. R. Amin, G. E. Morfill, and P. K. Shukla, "Modulational instability of dust-acoustic and dust-ion-acoustic waves," *Physical Review*, vol. 58, no. 5, pp. 6517–6523, 1998.

[12] A. A. Mamun and P. K. Shukla, "Linear and nonlinear dust-hydromagnetic waves," *Physics of Plasmas*, vol. 10, no. 11, pp. 4341–4349, 2003.

[13] S. Ghosh and M. R. Gupta, "Solitary waves in two-dimensional dusty plasma crystal: effects of weak magnetic field," *Physics of Plasmas*, vol. 17, no. 3, article 034505, 2010.

[14] S. Jaiswal, P. Bandyopadhyay, and A. Sen, "Theoretical study of head-on collision of dust acoustic solitary waves in a strongly coupled complex plasma," *Physics of Plasmas*, vol. 21, no. 5, article 053701, 2014.

[15] D. N. Gao, H. Zhang, J. Zhang, Z. Z. Li, and W. S. Duan, "Numerical modelling of overtaking collisions of dust acoustic waves in plasmas," *The European Physical Journal D*, vol. 70, no. 11, p. 235, 2016.

[16] A. Boruah, S. K. Sharma, Y. Nakamura, and H. Bailung, "Observation of dust acoustic multi-solitons in a strongly coupled dusty plasma," *Physics of Plasmas*, vol. 23, no. 9, article 093704, 2016.

[17] L. L. Tao, F. P. Wang, D. N. Gao, H. Zhang, and W. S. Duan, "Effect of the pressure of the dust grains in strongly coupled dusty plasma on the head-on collision between two nonlinear waves," *Journal of Plasma Physics*, vol. 86, no. 1, 2020.

[18] Abdullah, A. R. Seadawy, and W. Jun, "Mathematical methods and solitary wave solutions of three-dimensional Zakharov-Kuznetsov-Burgers equation in dusty plasma and its applications," *Results in Physics*, vol. 7, pp. 4269–4277, 2017.

[19] A. H. Arnous, A. R. Seadawy, R. T. Alqahtani, and A. Biswas, "Optical solitons with complex Ginzburg–Landau equation by modified simple equation method," *Optik*, vol. 144, pp. 475–480, 2017.

[20] M. Rosenberg and G. Kalman, "Dust acoustic waves in strongly coupled dusty plasmas," *Physical Review E*, vol. 56, no. 6, pp. 7166–7173, 1997.

[21] H. F. Darweesh, A. M. El-Hanbaly, and E. M. Abulwafa, "Theoretical study of dust acoustic solitary waves interaction in a strongly coupled dusty plasma with nonextensive electrons and ions," *Quantum Physics Letters*, vol. 7, no. 1, pp. 21–28, 2018.

[22] S. Ichimaru, H. Iyetomi, and S. Tanaka, "Statistical physics of dense plasmas: thermodynamics, transport coefficients and dynamic correlations," *Physics Reports*, vol. 149, no. 2-3, pp. 91–205, 1987.

[23] R. Hirota, *The Direct Method in the Soliton Theory*, Cambridge University Press, UK, 2004.

[24] U. Klein and J. Kerp, *Physics of the Interstellar Medium*, Argelander Institute for Astronomy, 1st edition, 2008.

[25] P. Bandyopadhyay, G. Prasad, A. Sen, and P. K. Kaw, "Experimental study of nonlinear dust acoustic solitary waves in a dusty plasma," *Physical Review Letters*, vol. 101, no. 6, 2008.

[26] Z. Donko, P. Hartmann, and J. Goree, "Shear viscosity of strongly-coupled two-dimensional Yukawa liquids: experiment and modeling," *Modern Physics Letters B*, vol. 21, no. 21, pp. 1357–1376, 2011.

[27] V. Nosenko, J. Goree, and A. Piel, "Cutoff wave number for shear waves in a two-dimensional Yukawa system (dusty plasma)," *Physical Review Letters*, vol. 97, no. 11, 2006.

[28] A. R. Seadawy, "Three-dimensional nonlinear modified Zakharov–Kuznetsov equation of ion-acoustic waves in a magnetized plasma," *Computers & Mathematics with Applications*, vol. 71, no. 1, pp. 201–212, 2016.

[29] K. Roy, S. K. Ghosh, and P. Chatterjee, "Two-soliton and three-soliton interactions of electron acoustic waves in quantum plasma," *Pramana*, vol. 86, no. 4, pp. 873–883, 2016.

[30] R. Sharma and G. P. Singh, "Optical soliton & applications thereof," *International Journal of Electronics*, vol. 4, no. 4, pp. 71–76, 2014.

[31] J. H. Geesink and D. K. F. Meijer, "Bio-soliton model that predicts non-thermal electromagnetic radiation frequency bands, that either stabilize or destabilize life conditions," *General Physics*, vol. 36, no. 4, pp. 357–378, 2016.

Hindawi
Advances in Mathematical Physics
Volume 2020, Article ID 1320635, 15 pages
https://doi.org/10.1155/2020/1320635

Research Article

Variational Approach for the Variable-Order Fractional Magnetic Schrödinger Equation with Variable Growth and Steep Potential in $\mathbb{R}^{N*}$

Jianwen Zhou,[1] Bianxiang Zhou,[1] Liping Tian,[1] and Yanning Wang[2]

[1]*Department of Mathematics, Yunnan University, Kunming, Yunnan 650091, China*
[2]*School of Basic Medical Science, Kunming Medical University, Kunming, Yunnan 650500, China*

Correspondence should be addressed to Yanning Wang; wangscanf2004@126.com

Received 4 June 2020; Revised 1 September 2020; Accepted 28 September 2020; Published 28 October 2020

Academic Editor: Zhi-Yuan Sun

In this paper, we show the existence of solutions for an indefinite fractional Schrödinger equation driven by the variable-order fractional magnetic Laplace operator involving variable exponents and steep potential. By using the decomposition of the Nehari manifold and variational method, we obtain the existence results of nontrivial solutions to the equation under suitable conditions.

1. Introduction

In this paper, we investigate the existence of solutions of the following concave-convex fractional elliptic equation driven by the variable-order fractional magnetic Laplace operator involving variable exponents:

$$(-\Delta)_A^{s(\cdot)}u + V_\lambda(x)u = f(x)\left|u\right|^{q(x)-2}u + g(x)\left|u\right|^{p(x)-2}u \text{ in } \mathbb{R}^N, \tag{1}$$

where $N \geq 1, s(\cdot)$: $\mathbb{R}^N \times \mathbb{R}^N \to (0,1)$, is a continuous function, $(-\Delta)_A^{s(\cdot)}$ is the variable-order fractional magnetic Laplace operator, the potential $V_\lambda(x) = \lambda V^+(x) - V^-(x)$ with $V^\pm = \max\{\pm V, 0\}$, $\lambda > 0$ is a parameter, and the magnetic field is $A \in C^{0,\alpha}(\mathbb{R}^N, \mathbb{R}^N)$ with $\alpha \in (0,1], p$, $q \in C(\mathbb{R}^N)$ and u : $\mathbb{R}^N \to \mathbb{C}$. In [1], the fractional magnetic Laplacian has been defined as

$$(-\Delta)_A^s u(x) = \lim_{r\to 0}\int_{B_r^c(x)} \frac{u(x) - e^{i(x-y)\cdot A(x+y/2)}u(y)}{|x-y|^{N+2s}}dy, \tag{2}$$

for $x \in \mathbb{R}^N$. In [2], the variable-order fractional Laplace $(-\Delta)^{s(\cdot)}$ is defined as for each $x \in \mathbb{R}^N$,

$$(-\Delta)^{s(\cdot)}u(x) = 2P.V\int_{\mathbb{R}^N} \frac{u(x) - u(y)}{|x-y|^{N+2s(x,y)}}dy, \tag{3}$$

along any $u \in C_0^\infty(\Omega)$. Inspired by them, we define the variable-order fractional magnetic Laplacian $(-\Delta)_A^{s(\cdot)}$ as for each $x \in \mathbb{R}^N$,

$$(-\Delta)_A^{s(\cdot)}u(x) = \lim_{r\to 0}\int_{B_r^c(x)} \frac{u(x) - e^{i(x-y)\cdot A(x+y/2)}u(y)}{|x-y|^{N+2s(x,y)}}dy. \tag{4}$$

Since $s(\cdot)$ is a function, magnetic field $A \in C^{0,\alpha}(\mathbb{R}^N, \mathbb{R}^N)$ with $\alpha \in (0,1]$, we see that operator $(-\Delta)_A^{s(\cdot)}$ is a variable-order fractional magnetic Laplace operator. Especially, when $s(\cdot) \equiv constant$, $(-\Delta)_A^{s(\cdot)}$ reduces to the usual fractional magnetic Laplace operator. When $s(\cdot) \equiv constant$, $A = 0$, $(-\Delta)_A^{s(\cdot)}$ reduces to the usual fractional Laplace operator. Very recently, when $A = 0$, $V^-(x) = 0$ and $f(x), g(x) \equiv constant$, authors in [2] are given some sufficient conditions to ensure the existence of two different weak solutions, and used the variational method and the mountain pass theorem to obtain the two weak solutions of problem (5) which converge to two

solutions of its limit problems, and the existence of infinitely many solutions to its limit problem:

$$\begin{cases} (-\Delta)^{s(\cdot)}u + \lambda V(x)u = \alpha|u|^{p(x)-2}u + \beta|u|^{q(x)-2}u \text{ in } \Omega, \\ u = 0 \text{ in } \mathbb{R}^N \setminus \Omega. \end{cases} \tag{5}$$

In addition, authors studied the multiplicity and concentration of solutions for a Hamiltonian system driven by the fractional Laplace operator with variable-order derivative in [3]. For $s(\cdot) = 1$, $p(x)$, $q(x) \equiv constant$, and $A = 0$, in [4], authors obtained the multiplicity and concentration of the positive solution of the following indefinite semilinear elliptic equations involving concave-convex nonlinearities by the variational method:

$$\begin{cases} -\Delta u + V_\lambda(x)u = f(x)|u|^{q-2}u + g(x)|u|^{p-2}u \text{ in } \mathbb{R}^N, \\ u \geq 0 \text{ in } \mathbb{R}^N. \end{cases} \tag{6}$$

For $s(\cdot)$, $p(x)$, $q(x) \equiv constant$, and $A = 0$, in [5], under appropriate assumptions, Peng et al. obtained the existence, multiplicity, and concentration of nontrivial solutions for the following indefinite fractional elliptic equation by using the Nehari manifold decomposition:

$$\begin{cases} (-\Delta)^{\alpha}u + V_\lambda(x)u = a(x)|u|^{q-2}u + b(x)|u|^{p-2}u \text{ in } \mathbb{R}^N, \\ u \geq 0 \text{ in } \mathbb{R}^N. \end{cases} \tag{7}$$

In [1], by using the Nehari manifold decomposition, authors studied the concave-convex elliptic equation involving the fractional order nonlinear Schrödinger equation:

$$(-\Delta)_A^s u + V_\lambda(x)u = f(x)|u|^{q-2}u + g(x)|u|^{p-2}u \text{ in } \mathbb{R}^N. \tag{8}$$

Some sufficient conditions for the existence of nontrivial solutions of equation (8) are obtained. Nevertheless, only a few papers see [6–12] deal with the existence and multiplicity of fractional magnetic problems. Some papers see [8, 13–16] deal with the solvability of Kirchhoff problems. Inspired by above, we are interested in the existence and multiplicity of solutions to problem (1) with variable growth and steep potential in $\mathbb{R}^N$. As far as we know, this is the first time to study the multiplicity of nontrivial solutions of the indefinite fractional elliptic equation driven by the variable-order fractional magnetic Laplace operator with variable exponents and steep potential in $\mathbb{R}^N$. This result was improved in the recent paper [1].

It is worth mentioning that in this paper, we not only obtain the existence and multiplicity results of nontrivial solutions of the variable-order fractional magnetic Schrodinger equation with variable growth and steep well potential in $\mathbb{R}^N$ but also our main results are based on the study for the decomposition of Nehari manifolds. On the one hand, relative to [1], we extend the exponent to variable exponent, thus introducing the variable exponent Lebesgue space. In addition, compared with [2], we extend the range of $p(x)$ to $(2, \infty)$ and the research range from the bounded region Ω to the whole space $\mathbb{R}^N$. On the other hand, if we want to find the nontrivial solution of the equation (1) by the variational method, we need some geometry, such as a mountain structure and a link structure. However, the energy functional of equation (1) does not have the mountain structure. In order to overcome this obstacle, we seek another method, the Nehari manifold. By decomposing the Nehari manifold into three parts, we obtain the existence of nontrivial solutions of each part.

Inspired by the above works, we assume

(S_1) There exist two constants $0 < s_0 < s_1 < 1$ such that $s_0 < s(x, y) < s_1$ for all $(x, y) \in \mathbb{R}^N \times \mathbb{R}^N$.

(S_2) $s(\cdot)$ is symmetric, that is, $s(x, y) = s(y, x)$ for all $(x, y) \in \mathbb{R}^N \times \mathbb{R}^N$.

(V_1) V^+ is a continuous function on $\mathbb{R}^N$ and $V^- \in L^{N/2}(\mathbb{R}^N)$.

(V_2) There exists $k > 0$ such that the set $\{V^+ < k\} = \{x \in \mathbb{R}^N : V^+(x) < k\}$ is a nonempty and has finite measure. In addition, $M^2 |\{V^+ < k\}| < 1$, where $|\cdot|$ is the Lebesgue measure and M is the best Sobolev constant (see Lemma 9).

(V_3) $\Omega = \{x \in \mathbb{R}^N, V^+(x) = 0\}$ is nonempty and has a smooth boundary with $\bar{\Omega} = \text{int}\{x \in \mathbb{R}^N, V^+(x) = 0\}$.

(V_4) There exists a constant $\vartheta_0 > 1$ such that

$$\inf_{u \in D_A^{s(\cdot)}(\mathbb{R}^N, \mathbb{C}) \setminus \{0\}} \frac{\int_{\mathbb{R}^{2N}} |u(x) - e^{i(x-y)\cdot A(x+y/2)}u(y)|^2 / |x-y|^{N+2s(x,y)} dxdy + \lambda \int_{\mathbb{R}^N} V^+ u^2 dx}{\int_{\mathbb{R}^N} V^- u^2 dx} \geq \vartheta_0, \tag{9}$$

for all $\lambda > 0$, where $D_A^{s(\cdot),}(\mathbb{R}^N, \mathbb{C})$ is the Hilbert space related to the magnetic field A (see Section 2).

(V_5) $|\{V^+ < k\}| > \max\{A_1, A_2, A_3, A_4\} > 0$ where

$$A_1 = \left(\frac{(p^- - 2)q^-}{2(p^- - q^-)\|f\|_{L\wedge(2/(2-q(x)))}(\mathbb{R}^N)}\right)^{\frac{2}{q^+-2}} \left(\frac{2-q^+}{(p^+-q^+)\|g\|_\infty}\right)^{\frac{2}{2-p^+}} \cdot \left(\frac{(\vartheta_0 - 1)\theta}{\vartheta_0}\right)^{\frac{2(p^+-q^+)}{(p^+-2)(q^+-2)}},$$

$$A_2 = \left(\frac{(p^- - 2)q^-}{2(p^- - q^-)\|f\|_{L\wedge(2/(2-q(x)))}(\mathbb{R}^N)}\right)^{\frac{2(p^- - 2)}{(2-p^+)(2-q^+)}} \left(\frac{\vartheta_0 - 1}{\vartheta_0}\right)^{\frac{2(p^- - q^+)}{(2-p^+)(2-q^+)}} \cdot \left(\frac{2-q^+}{(p^+-q^+)\|g\|_\infty}\right)^{\frac{2}{2-p^+}} \cdot \theta^{\frac{2p^+ - q^+p^+ + q^+p^- - 2q^+}{(2-p^+)(2-q^+)}} M^{\frac{2(p^+-p^-)}{2-p^+}},$$

$$A_3 = \left(\frac{(p^- - 2)q^-}{2(p^- - q^-)\|f\|_{L\wedge(2/(2-q(x)))}(\mathbb{R}^N)}\right)^{\frac{2}{q^+-2}} \left(\frac{(\vartheta_0 - 1)\theta}{\vartheta_0}\right)^{\frac{2(p^+ - q^-)}{(p^+-2)(q^- - 2)}} \cdot \left(\frac{2-q^+}{(p^+-q^+)\|g\|_\infty}\right)^{\frac{2}{2-p^+}},$$

$$A_4 = \left(\frac{(p^- - 2)q^-}{2(p^- - q^-)\|f\|_{L\Lambda(2/(2-q(x)))}(\mathbb{R}^N)}\right)^{\frac{2(p^- - 2)}{(2-p^+)(2-q^-)}} \left(\frac{2-q^+}{(p^+ - q^+)\|g\|_\infty}\right)^{\frac{2}{2-p^+}} \cdot \left(\frac{\vartheta_0 - 1}{\vartheta_0}\right)^{\frac{2(p^- - q^-)}{(2-p^+)(2-q^-)}} \cdot \theta^{\frac{2p^+ - q^- p^+ + q^- p^- - 2q^-}{(2-p^+)(2-q^-)}} M^{\frac{2(p^+ - p^-)}{2-p^+}}. \tag{10}$$

To the best of our knowledge, this type of hypothesis is the first introduced by Bartsch and Wang in [17]. In addition, we recall the potential V_λ satisfied the conditions (V_1)–(V_3) as the steep well potential.

Concerning $p(x), q(x)$ and $f(x), g(x)$, we suppose

(H_1) A measurable function $p : \mathbb{R}^N \to (2, +\infty)$ satisfy

$$2 < p^- \coloneqq essinf_{x\in\mathbb{R}^N} p(x) \le p^+ = esssup_{x\in\mathbb{R}^N} p(x) < \infty. \tag{11}$$

(H_2) A measurable function $q : \mathbb{R}^N \to (1, 2)$ satisfy

$$1 < q^- \coloneqq essinf_{x\in\mathbb{R}^N} q(x) \le q^+ = esssup_{x\in\mathbb{R}^N} q(x) < 2. \tag{12}$$

(H_3) $f \in L^{2/2-q(x)}(\mathbb{R}^N, \mathbb{C})$ and $\|f\|_{L^{2/2-q(x)}(\mathbb{R}^N,\mathbb{C})} > 0$, where $L^{p(x)}(\mathbb{R}^N, \mathbb{C})$ will be given in Section 2.

(H_4) $g \in L^\infty(\mathbb{R}^N, \mathbb{C})$ and $\|g\|_\infty \coloneqq \|g\|_{L^\infty(\mathbb{R}^N,\mathbb{C})} > 0$.(13)

In what follows, it will always be assumed that the hypothesis (S_2) holds. Then, we will give the following definition of weak solutions for problem (1).

Definition 1. We say that $u \in X_\lambda$ is a weak solution of equation (1), if

$$\begin{aligned}&\Re\int_{\mathbb{R}^{2N}} \frac{\left(u(x) - e^{i(x-y)}\cdot A(x+y/2)u(y)\right)\left(v(x)e^{i(xy}\right)\cdot \bar{A}(x+y/2)v(y)\right)}{|x-y|^{N+2s(x,y)}}dxdy \\ &+ \lambda\Re\int_{\mathbb{R}^N} V^+ u\bar{v}dx - \Re\int_{\mathbb{R}^N} V^- u\bar{v}dx - \Re\int_{\mathbb{R}^N}\Big(f(x)|u|^{q(x)-2}u \\ &+ g(x)|u|^{p(x)-2}u\Big)\bar{v}dx = 0,\end{aligned} \tag{13}$$

for any $v \in X_\lambda$, where X_λ will be given in Section 2.

Our main results are as follows.

Theorem 2. *Under (V_1)–(V_4), (H_1)–(H_4), and (H_5), there exists a nonempty open set $\Omega_g \subset \Omega$ such that $g(x) > 0$ in Ω_g. Then, equation (1) allows at least a nontrivial solution for all $\lambda > 1/kM \mid \{V^+ < k\} \mid$.*

Theorem 3. *Suppose that (S_1), (S_2), (V_1)–(V_2), and (H_1)–(H_4) are satisfied. Then, there exists $\lambda^* \ge 0$ such that for every $\lambda > \lambda^*$, equation (1) has at least two nontrivial solutions.*

Remark 4. Generally speaking, if $s(\cdot)$: $\mathbb{R}^N \times \mathbb{R}^N \to (0, 1)$ is a continuous function, magnetic field $A \in C^{0,\alpha}(\mathbb{R}^N, \mathbb{R}^N)$ with $\alpha \in (0, 1]$, then the variable-order fractional magnetic Laplacian can be defined as for each given

$u \in C_0^\infty(\mathbb{R}^N, \mathbb{C})$,

$$\begin{aligned}&\left\langle (-\Delta)_A^{s(\cdot)} u, v\right\rangle \\ &= \Re\int_{\mathbb{R}^{2N}} \frac{\left(u(x) - e^{i(x-y)\cdot A(x+y/2)}u(y)\right)\left(v(x)e^{i(xy)\cdot\bar{A}(x+y/2)}v(y)\right)}{|x-y|^{N+2s(x,y)}}dxdy,\end{aligned} \tag{14}$$

along any $v \in C_0^\infty(\mathbb{R}^N, \mathbb{C})$.

2. Preliminaries and Notations

For the reader's convenience, we first review some necessary definitions that we are later going to use of variable exponent Lebesgue spaces. We refer the reader to [2, 3, 18–20] for details. Furthermore, we give the variational setting for equation (1) and some preliminary results.

Denote

$$p^+ = esssup_{x\in\mathbb{R}^N} p(x), p^- = essinf_{x\in\mathbb{R}^N} p(x). \tag{15}$$

If $p^+ < \infty$, then p is said to be bounded. If $(1/p(x)) + (1/p'(x)) = 1$, then $p'(x) = p(x)/p(x) - 1$ is called the dual variable exponent of $p(x)$. The variable exponent Lebesgue space can be defined as

$$\begin{aligned}L^{p(x)}(\mathbb{R}^N, \mathbb{C}) = \Big\{&u : \mathbb{R}^N \to \mathbb{C} \text{ is a measurable function}; \rho_{p(x)}(u) \\ &= \int_{\mathbb{R}^N} |u(x)|^{p(x)}dx < \infty\Big\}\end{aligned} \tag{16}$$

with the norm

$$\|u\|_{L^{p(\cdot)}(\mathbb{R}^N,\mathbb{C})} = \inf\left\{\mu > 0 : \rho_{p(x)}\left(\mu^{-1}u\right) \le 1\right\}, \tag{17}$$

then $L^{p(x)}(\mathbb{R}^N, \mathbb{C})$ is a Banach space. When p is bounded, we have

$$\begin{aligned}&\min\left\{\|u\|^{p^-}_{L^{p(x)}(\mathbb{R}^N,\mathbb{C})}, \|u\|^{p^+}_{L^{p(x)}(\mathbb{R}^N,\mathbb{C})}\right\} \\ &\le \int_{\mathbb{R}^N} |u(x)|^{p(x)}dx \le \max\left\{\|u\|^{p^-}_{L^{p(x)}(\mathbb{R}^N,\mathbb{C})}, \|u\|^{p^+}_{L^{p(x)}(\mathbb{R}^N,\mathbb{C})}\right\}.\end{aligned} \tag{18}$$

For bounded exponent, the dual space $(L^{p(x)}(\mathbb{R}^N, \mathbb{C}))'$ can be identified with $L^{p'(x)}(\mathbb{R}^N, \mathbb{C})$, where $p'(x)$ is called the dual variable exponent of $p(x)$. Especially,

$$L^2(\mathbb{R}^N, \mathbb{C}) = \left\{u : \mathbb{R}^N \to \mathbb{C} \text{ is a measurable function}; \int_{\mathbb{R}^N} |u(x)|^2 dx < \infty\right\} \tag{19}$$

with the real scalar product $\langle u, v\rangle_{L^2(\mathbb{R}^N,\mathbb{C})} \coloneqq \Re\int_{\mathbb{R}^N} u\bar{v}dx$, for all $u, v \in L^2(\mathbb{R}^N, \mathbb{C})$. By Lemma 11, 20 of [20] and $\|\cdot$

$\|\cdot\|_{L^{p(x)}(\mathbb{R}^N,\mathbb{C})} = \||\cdot|\|_{L^{p(x)}(\mathbb{R}^N,\mathbb{R})}$, we know that in the variable exponent Lebesgue space, the Hölder inequality is still valid. For all $u \in L^{p(x)}(\mathbb{R}^N, \mathbb{C})$, $v \in L^{p'(x)}(\mathbb{R}^N, \mathbb{C})$ with $p(x) \in (1,\infty)$, the following inequality holds

$$\int_{\mathbb{R}^N} |u||v|dx \le \left(\frac{1}{p^-} + \frac{1}{\left(p'\right)^-}\right) \|u\|_{L^{p(x)}\left(\mathbb{R}^N,\mathbb{C}\right)} \|v\|_{L^{p'(x)}\left(\mathbb{R}^N,\mathbb{C}\right)} \le 2\|u\|_{L^{p(x)}\left(\mathbb{R}^N,\mathbb{C}\right)} \|v\|_{L^{p'(x)}\left(\mathbb{R}^N,\mathbb{C}\right)}. \tag{20}$$

Define

$$D^{s(\cdot)}\left(\mathbb{R}^N, \mathbb{C}\right) = \left\{ u \in L^2\left(\mathbb{R}^N, \mathbb{C}\right): \int_{\mathbb{R}^N}\int_{\mathbb{R}^N} \frac{|u(x) - u(y)|^2}{|x-y|^{N+2s(x,y)}} dxdy < \infty \right\}. \tag{21}$$

Equip $D^{s(\cdot)}(\mathbb{R}^N, \mathbb{C})$ with the inner product

$$\langle u, v\rangle_{s(\cdot)} = \int_{\mathbb{R}^N}\int_{\mathbb{R}^N} \frac{(u(x) - u(y))(v(x) - v(y))}{|x-y|^{N+2s(x,y)}} dxdy + \int_{\mathbb{R}^N} u(x)v(x)dx, \tag{22}$$

and the corresponding norm $\|u\|^2_{s(\cdot)} = \langle u, u\rangle_{s(\cdot)}$. Especially, if $s(\cdot) \equiv$ constant, then the space $D^{s(\cdot)}(\mathbb{R}^N, \mathbb{C})$ is the usual fractional Sobolev space $D^s(\mathbb{R}^N, \mathbb{C})$.

Lemma 5 (see [3] Lemma 5). *Let $p \in [2, 2^*_{s_0}]$, $2^*_{s_0} = 2N/N - 2s_0$, if $N > 2$; $2^*_{s_0} = \infty$ if $N \le 2$. The embedding $D^{s_1}(\mathbb{R}^N, \mathbb{R}) \hookrightarrow D^{s(\cdot)}(\mathbb{R}^N, \mathbb{R}) \hookrightarrow D^{s_0}(\mathbb{R}^N, \mathbb{R}) \hookrightarrow L^p(\mathbb{R}^N, \mathbb{R})$ are continuous.*

For each function $u : \mathbb{R}^N \to \mathbb{C}$, set

$$[u]^2_{s(\cdot),A} := \int_{\mathbb{R}^{2N}} \frac{\left|u(x) - e^{i(x-y)\cdot A(x+y/2)}u(y)\right|^2}{|x-y|^{N+2s(x,y)}} dxdy, \tag{23}$$

and the corresponding norm is defined as $\|u\|^2_{s(\cdot),A} = \|u\|^2_{L^2(\mathbb{R}^N,\mathbb{C})} + [u]^2_{s(\cdot),A}$. Set D be the space of measurable functions $u : \mathbb{R}^N \to \mathbb{C}$ such that $\|u\|_{s(\cdot),A} < \infty$; then, $(D, \langle\cdot,\cdot\rangle_{s(\cdot),A})$ is a Hilbert space. If we let $D^{s(\cdot)}_A(\mathbb{R}^N, \mathbb{C})$ as the closure of $C^\infty_c(\mathbb{R}^N, \mathbb{C})$ in D, then $D^{s(\cdot)}_A(\mathbb{R}^N, \mathbb{C})$ is a Hilbert space.

Lemma 6. *For each compact subset $W \subset \mathbb{R}^N$, the embedding $D^{s(\cdot)}_A(\mathbb{R}^N, \mathbb{C}) \hookrightarrow D^{s(\cdot)}(W, \mathbb{C})$ is continuous.*

Proof. Fixed any compact subset $W \subset \mathbb{R}^N$, for any $u \in D^{s(\cdot)}(W, \mathbb{C})$, we have

$$\begin{aligned}
\|u\|^2_{D^{s(\cdot)}(W,\mathbb{C})} &= \int_W |u(x)|^2 dx + \int_W\int_W \frac{|u(x) - u(y)|^2}{|x-y|^{N+2s(x,y)}} dxdy \\
&\le \int_{\mathbb{R}^N} |u(x)|^2 dx + 2\int_W\int_W \frac{\left|u(x) - e^{i(x-y)\cdot A(x+y/2)}u(y)\right|^2}{|x-y|^{N+2s(x,y)}} dxdy \\
&\quad + 2\int_W\int_W \frac{|u(y)|^2\left|e^{i(x-y)\cdot A((x+y)/2)} - 1\right|^2}{|x-y|^{N+2s(x,y)}} dxdy \\
&\le 2\int_{\mathbb{R}^N} |u(x)|^2 dx + 2\int_{\mathbb{R}^N}\int_{\mathbb{R}^N} \frac{\left|u(x) - e^{i(x-y)\cdot A(x+y/2)}u(y)\right|^2}{|x-y|^{N+2s(x,y)}} dxdy \\
&\quad + 2\int_W\int_W \frac{|u(y)|^2\left|e^{i(x-y)\cdot A(x+y/2)} - 1\right|^2}{|x-y|^{N+2s(x,y)}} dxdy \le 2\|u\|^2_{s(\cdot),A} + 2J,
\end{aligned} \tag{24}$$

where

$$\begin{aligned}
J &:= \int_W\int_W \frac{|u(y)|^2\left|e^{i(x-y)\cdot A(x+y/2)} - 1\right|^2}{|x-y|^{N+2s(x,y)}} dxdy \\
&= \int_W |u(y)|^2 \left(\int_{W\cap\{|x-y|>1\}} \frac{\left|e^{i(x-y)\cdot A(x+y/2)} - 1\right|^2}{|x-y|^{N+2s(x,y)}} dx\right) dy \\
&\quad + \int_W |u(y)|^2 \left(\int_{W\cap\{|x-y|\le 1\}} \frac{\left|e^{i(x-y)\cdot A(x+y/2)} - 1\right|^2}{|x-y|^{N+2s(x,y)}} dx\right) dy \\
&= J_1 + J_2.
\end{aligned} \tag{25}$$

Since $|e^{it} - 1| \le 2$, we have

$$\begin{aligned}
J_1 &\le 4\int_W |u(y)|^2 \left(\int_{W\cap\{|x-y|>1\}} \frac{1}{|x-y|^{N+2s(x,y)}} dx\right) dy \\
&\le 4\int_W |u(y)|^2 \left(\int_{W\cap\{|x-y|>1\}} \frac{1}{|x-y|^{N+2s_0}} dx\right) d \\
&= 4\int_W |u(y)|^2 \left(\int_{W\cap\{|z|>1\}} \frac{1}{|z|^{N+2s_0}} dz\right) dy \le C_1\int_W |u(y)|^2 dy \\
&\le C_1\int_{\mathbb{R}^N} |u(y)|^2 dy = C_1\|u\|^2_{L^2\left(\mathbb{R}^N,\mathbb{C}\right)}.
\end{aligned} \tag{26}$$

By Lemma 6 of [21], we know that A is locally bounded, and $W \subset \mathbb{R}^N$ is compact, $\left|e^{i(x-y)\cdot A(x+y/2)} - 1\right|^2 \le$

$C_2|x-y|^2$, for $|x-y| \le 1$, $x, y \in W$. Thus, we obtain

$$\begin{aligned} J_2 &= \int_W |u(y)|^2 \left(\int_{W\cap\{|x-y|\le 1\}} \frac{\left|e^{i(x-y)\cdot A(x+y/2)} - 1\right|^2}{|x-y|^{N+2s(x,y)}} dx \right) dy \\ &\le \int_W |u(y)|^2 \left(\int_{W\cap\{|x-y|\le 1\}} \frac{C_2}{|x-y|^{N+2s(x,y)-2}} dx \right) dy \\ &\le \int_W |u(y)|^2 \left(\int_{W\cap\{|x-y|\le 1\}} \frac{C_2}{|x-y|^{N+2s_1-2}} dx \right) dy \\ &\le C_2 \int_W |u(y)|^2 \left(\int_{W\cap\{|z|\le 1\}} \frac{1}{|z|^{N+2s_1-2}} dz \right) dy \\ &\le C_3 \int_W |u(y)|^2 dy \le C_3 \int_{\mathbb{R}^N} |u(y)|^2 dy = C_3 \|u\|^2_{L^2(\mathbb{R}^N,\mathbb{C})}. \end{aligned} \tag{27}$$

By (24)-(27), we can easily get that

$$\|u\|^2_{D^{s(\cdot)}(W,\mathbb{C})} \le 2\|u\|^2_{s(\cdot),A} + 2C_1\|u\|^2_{L^2(\mathbb{R}^N,\mathbb{C})} + 2C_3\|u\|^2_{L^2(\mathbb{R}^N,\mathbb{C})} \le C_4\|u\|^2_{s(\cdot),A}, \tag{28}$$

which implies that the embedding $D^{s(\cdot)}_A(\mathbb{R}^N,\mathbb{C})$ is continuously embedded into $D^{s(\cdot)}(W,\mathbb{C})$.

Through the above lemma, we know that $D^{s(\cdot)}_A(\mathbb{R}^N,\mathbb{C}) \hookrightarrow D^{s(\cdot)}(W,\mathbb{C})$, and from Theorem 2.1 of [2], we know that for Ω be a bounded subset of $\mathbb{R}^N$ and $p : \bar{\Omega} \to [1,\infty)$ is continuous functions, $D^{s(\cdot)}(\Omega,\mathbb{C})$ is continuously embedded into $L^{p(x)}(\Omega,\mathbb{C})$, so we seek another method to prove the size relationship between $\int_{\mathbb{R}^N}|u(x)|^{p(x)}dx$, $\int_{\mathbb{R}^N}|u(x)|^{q(x)}dx$, and $\|u\|_\lambda$.

Lemma 7 (see [6] Lemma 10). *For every $u \in D^{s(\cdot)}_A(\mathbb{R}^N,\mathbb{C})$, it holds $|u| \in D^{s(\cdot)}(\mathbb{R}^N,\mathbb{R})$. More precisely, °Í*

$$\||u|\|_{s(\cdot)} \le \|u\|_{s(\cdot),A}, \text{for every } u \in D^{s(\cdot)}_A(\mathbb{R}^N,\mathbb{C}). \tag{29}$$

Remark 8 (see [6] Remark 9). There holds

$$|u(x) - e^{i(x-y)\cdot A\left(\frac{x+y}{2}\right)}u(y)| \ge ||u(x)|-|u(y)||, \text{for } a.e.x, y \in \mathbb{R}^N. \tag{30}$$

Lemma 9. *Let $p \in [2, 2^*_{s_0}]$, where $2^*_{s_0} = 2N/N - 2s_0$ if $N > 2$; $2^*_{s_0} = \infty$ if $N \le 2$. $D^{s(\cdot)}_A(\mathbb{R}^N,\mathbb{C})$ is continuously embedded into $L^p(\mathbb{R}^N,\mathbb{C})$. Moreover, if $s_0 \in (1/2, 1)$, then $D^{s(\cdot)}_A(\mathbb{R}^N,\mathbb{C})$ can be continuously embedded into $L^\infty(\mathbb{R}^N,\mathbb{C})$; that is, there exists a constant $M > 0$ such that*

$$\|u\|_\infty \le M\|u\|_{s(\cdot),A}. \tag{31}$$

Proof. By Lemma 7, we know that for every $u \in D^{s(\cdot)}_A(\mathbb{R}^N,\mathbb{C})$, it holds $|u| \in D^{s(\cdot)}(\mathbb{R}^N,\mathbb{R})$. By Lemma 5, we know that for $D^{s(\cdot)}(\mathbb{R}^N,\mathbb{R}) \hookrightarrow L^p(\mathbb{R}^N,\mathbb{R})$ is continuous. In light of Remark 8, one has

$$\begin{aligned} \|u\|_{L^p(\mathbb{R}^N,\mathbb{C})} &= \||u|\|_{L^p(\mathbb{R}^N,\mathbb{R})} \le \tilde{c}\||u|\|_{s(\cdot)} \\ &= \tilde{c}\left(\int_{\mathbb{R}^N} \|u\|^2 dx + \int_{\mathbb{R}^N}\int_{\mathbb{R}^N} \frac{\|u(x)|-|u(y)\|^2}{|x-y|^{N+2s(x,y)}} dxdy \right)^{\frac{1}{2}} \\ &\le \tilde{c}\left(\int_{\mathbb{R}^N} |u|^2 dx + \int_{\mathbb{R}^N}\int_{\mathbb{R}^N} \frac{\left|u(x) - e^{i(x-y)\cdot A(x+y/2)}u(y)\right|^2}{|x-y|^{N+2s(x,y)}} dxdy \right)^{\frac{1}{2}} \\ &= \tilde{c}\|u\|_{s(\cdot),A}. \end{aligned} \tag{32}$$

From the above inequality, we immediately obtain the embedding $D^{s(\cdot)}_A(\mathbb{R}^N,\mathbb{C}) \hookrightarrow L^p(\mathbb{R}^N,\mathbb{C})$ which is continuous.

For $\lambda > 0$, define

$$\begin{aligned} \langle u, v\rangle_\lambda &:= \Re \int_{\mathbb{R}^{2N}} \frac{\left(u(x) - e^{i(x-y)\cdot A(x+y/2)}u(y)\right)\left(v(x)e^{i(xy)\cdot \bar{A}(x+y/2)}v(y)\right)}{|x-y|^{N+2s(x,y)}} dxdy \\ &\quad + \Re\lambda \int_{\mathbb{R}^N} V^+ u\bar{v}dx, \end{aligned}$$

$$\|u\|_\lambda := \langle u, u\rangle^{\frac{1}{2}}_\lambda. \tag{33}$$

Set $E = \{u \in D^{s(\cdot)}_A(\mathbb{R}^N,\mathbb{C}): \int_{\mathbb{R}^N} V^+u^2dx < \infty\}$ be equipped with the inner product $\langle u, v\rangle_E = \langle u, v\rangle_1$ (i.e., $\lambda = 1$ in $\langle u, v\rangle_\lambda$). Obviously, $\|u\|_E \le \|u\|_\lambda$ for $\lambda \ge 1$. Set $X_\lambda = (X, \|\cdot\|_\lambda)$. Combining condition (V_4) and fractional Sobolev inequality, we could get

$$\begin{aligned} \int_{\mathbb{R}^N} |u(x)|^2 dx &= \int_{\{V^+<k\}} |u(x)|^2 dx + \int_{\{V^+\ge k\}} |u(x)|^2 dx \\ &\le \|u\|^2_\infty |\{V^+ < k\}| + \frac{1}{k}\int_{\mathbb{R}^N} V^+(x)|u(x)|^2 dx \\ &\le M^2\|u\|^2_{s(\cdot),A}|\{V^+ < k\}| + \frac{1}{k}\int_{\mathbb{R}^N} V^+u^2dx \\ &= M^2|\{V^+ < k\}|\left(\int_{\mathbb{R}^N} |u(x)|^2 dx + [u]^2_{s(\cdot),A} \right) \\ &\quad + \frac{1}{k}\int_{\mathbb{R}^N} V^+u^2dx, \end{aligned} \tag{34}$$

which shows that

$$\begin{aligned} \int_{\mathbb{R}^N} |u(x)|^2 dx &\le \frac{1}{1 - M^2 \mid \{V^+ < k\} \mid} \left[M^2 \mid \{V^+ < k\} \mid [u]^2_{s(\cdot),A} \right. \\ &\quad \left. + \frac{1}{k}\int_{\mathbb{R}^N} V^+u^2dx \right] \\ &\le \frac{\max\left\{M^2 \mid \{V^+ < k\}\mid, (1/k)\right\}}{1 - M^2 \mid \{V^+ < k\} \mid} \left[[u]^2_{s(\cdot),A} + \int_{\mathbb{R}^N} V^+u^2dx \right] \\ &= \frac{\max\left\{M^2 \mid \{V^+ < k\}\mid, (1/k)\right\}}{1 - M^2 \mid \{V^+ < k\} \mid} \|u\|^2_X. \end{aligned} \tag{35}$$

From the above inequality, it holds that

$$[u]^2_{s(\cdot),A} + \int_{\mathbb{R}^N} |u(x)|^2 dx \le \left(1 + \frac{\max\left\{M^2 \mid \{V^+ < k\}|, (1/k)\right\}}{1 - M^2 \mid \{V^+ < k\} \mid}\right) \|u\|^2_X, \tag{36}$$

which shows that X is continuously embedded into $D^{s(\cdot)}_A(\mathbb{R}^N, \mathbb{C})$. Similarly, for all $\lambda \ge 1/kM^2 \mid \{V^+ < k\} \mid$, there holds

$$\begin{aligned}\int_{\mathbb{R}^N} |u(x)|^2 dx &\le \frac{1}{1 - M^2 \mid \{V^+ < k\} \mid} \\ &\quad \cdot \left[M^2 \mid \{V^+ < k\} \mid [u]^2_{s(\cdot),A} + \lambda M^2 \mid \{V^+ < k\} \mid \int_{\mathbb{R}^N} V^+ u^2 dx\right] \\ &= \frac{M^2 \mid \{V^+ < k\} \mid}{1 - M^2 \mid \{V^+ < k\} \mid} \left[[u]^2_{s(\cdot),A} + \lambda \int_{\mathbb{R}^N} V^+ u^2 dx\right] \\ &= \frac{M^2 \mid \{V^+ < k\} \mid}{1 - M^2 \mid \{V^+ < k\} \mid} \|u\|^2_\lambda = \frac{1}{\theta} \|u\|^2_\lambda,\end{aligned} \tag{37}$$

where $\theta = 1 - M^2|\{V^+ < k\}|/M^2|\{V^+ < k\}|$. In addition, we have

$$\begin{aligned}\int_{\mathbb{R}^N} |u(x)|^{p(x)} dx &= \int_{\mathbb{R}^N} |u(x)|^{p(x)-2} \cdot |u(x)|^2 dx \\ &\le \max\left\{\|u\|^{p^+-2}_{\infty}, \|u\|^{p^--2}_{\infty}\right\} \int_{\mathbb{R}^N} |u(x)|^2 dx \\ &\le \max\left\{M^{p^+-2}\left(\int_{\mathbb{R}^N} |u(x)|^2 dx + [u]^2_{s(\cdot),A}\right)^{\frac{p^+-2}{2}}, M^{p^--2}\right. \\ &\quad \left. \cdot \left(\int_{\mathbb{R}^N} |u(x)|^2 dx + [u]^2_{s(\cdot),A}\right)^{\frac{p^--2}{2}}\right\} \frac{M^2 \mid \{V^+ < k\} \mid}{1 - M^2 \mid \{V^+ < k\} \mid} \|u\|^2_\lambda.\end{aligned} \tag{38}$$

This together $M^2 \mid \{V^+ < k\} \mid < 1$ yields that

$$\begin{aligned}\int_{\mathbb{R}^N} |u(x)|^{p(x)} dx &\le \max\left\{M^{p^+-2}\left(\frac{M^2 \mid \{V^+ < k\} \mid}{1 - M^2 \mid \{V^+ < k\} \mid} \|u\|^2_\lambda + \|u\|^2_\lambda\right)^{\frac{p^+-2}{2}}, M^{p^--2}\right. \\ &\quad \left. \cdot \left(\frac{M^2 \mid \{V^+ < k\} \mid}{1 - M^2 \mid \{V^+ < k\} \mid} \|u\|^2_\lambda + \|u\|^2_\lambda\right)^{\frac{p^--2}{2}}\right\} \\ &\quad \frac{M^2 \mid \{V^+ < k\} \mid}{1 - M^2 \mid \{V^+ < k\} \mid} \|u\|^2_\lambda \le |\{V^+ < k\}| \\ &\quad \cdot \left(\frac{1}{1 - M^2 \mid \{V^+ < k\} \mid}\right)^{\frac{p^+}{2}} \max\left\{M^{p^+} \|u\|^{p^+}_\lambda, M^{p^-} \|u\|^{p^-}_\lambda\right\} \\ &= \frac{1}{\theta^{p^+/2} M^{p^+} |\{V^+ < k\}|^{p^+-2/2}} \max\left\{M^{p^+} \|u\|^{p^+}_\lambda, M^{p^-} \|u\|^{p^-}_\lambda\right\} \\ &= \frac{1}{\theta^{p^+/2} |\{V^+ < k\}|^{p^+-2/2}} \max\left\{\|u\|^{p^+}_\lambda, M^{p^- - p^+} \|u\|^{p^-}_\lambda\right\}.\end{aligned} \tag{39}$$

For the sake of notational simplicity, we let $\|u\|^2_{\lambda,V} := [u]^2_{s(\cdot),A} + \int_{\mathbb{R}^N} V_\lambda u^2 dx$. Hence, by condition (V_4), we have

$$\|u\|^2_\lambda \ge \|u\|^2_{\lambda,V} \ge \frac{\vartheta_0 - 1}{\vartheta_0} \|u\|^2_\lambda, \quad \text{for } all\ \lambda \ge 0. \tag{40}$$

Related to equation (1), we think the functional $\Psi_\lambda : X_\lambda \to \mathbb{R}$,

$$\begin{aligned}\Psi_\lambda(u) &= \frac{1}{2}\|u\|^2_\lambda - \frac{1}{2}\int_{\mathbb{R}^N} V^- u^2 dx - \int_{\mathbb{R}^N} \left(\frac{f(x)}{q(x)} |u|^{q(x)} + \frac{g(x)}{p(x)} |u|^{p(x)}\right) dx \\ &= \frac{1}{2}\|u\|^2_{\lambda,V} - \int_{\mathbb{R}^N} \left(\frac{f(x)}{q(x)} |u|^{q(x)} + \frac{g(x)}{p(x)} |u|^{p(x)}\right) dx.\end{aligned} \tag{41}$$

In fact, we can easily verify that Ψ_λ is well-defined of class C^1 in X_λ and

$$\begin{aligned}\left\langle \Psi'_\lambda(u), v\right\rangle &= \langle u, v\rangle_\lambda - \Re\int_{\mathbb{R}^N} V^- u\bar{v} dx - \Re\int_{\mathbb{R}^N} \left(f(x)|u|^{q(x)-2}u\right. \\ &\quad \left. + g(x)|u|^{p(x)-2}u\right)\bar{v} dx \\ &= \langle u, v\rangle_{\lambda,V} - \Re\int_{\mathbb{R}^N} \left(f(x)|u|^{q(x)-2}u\right. \\ &\quad \left. + g(x)|u|^{p(x)-2}u\right)\bar{v} dx,\end{aligned} \tag{42}$$

for all $u, v \in X_\lambda$. Therefore, if $u \in X_\lambda$ is a critical point of Ψ_λ, then u is a solution of equation (1). Since the energy functional Ψ_λ is unbounded below on X_λ, in order to overcome this problem, we use the Nehari manifold $\mathcal{N}_\lambda = \{u \in X_\lambda \setminus \{0\}: \langle \Psi'_\lambda(u), u\rangle = 0\}$ to study the energy functional. In addition, we also note that $\mathcal{N}_\lambda$ contains every nonzero solution of equation (1). Especially, all critical points of must be located in $\mathcal{N}_\lambda$, and the local minimizers on $\mathcal{N}_\lambda$ are usually critical points of Ψ_λ.

3. Main Results

To start with, we can get an estimate of Ψ_λ. Then, we will discuss some basic properties of $\mathcal{N}_\lambda$. Finally, we prove Theorem 2 and Theorem 3 using the variational methods.

Lemma 10. *Ψ_λ is coercive and bounded below on $\mathcal{N}_\lambda$. Furthermore, one has*

$$\begin{aligned}\Psi_\lambda(u) \ge \max\left\{-\frac{2 - q^+}{2p^-}\left(\frac{\vartheta_0 q^+}{\theta(\vartheta_0 - 1)(p^- - 2)}\right)^{\frac{q^+}{2-q^+}}\right. \\ \cdot \left(\frac{(p^- - q^-)\|f\|_{L^{2/2-q(x)}}}{q^-}\right)^{\frac{2}{2-q^+}}, -\frac{2 - q^-}{2p^- q^-} \\ \left. \cdot \left(\frac{\vartheta_0}{\theta(\vartheta_0 - 1)(p^- - 2)}\right)^{\frac{q^-}{2-q^-}} \left((p^- - q^-)\|f\|_{L^{\frac{2}{2-q(x)}}}\right)^{\frac{2}{2-q^-}}\right\}.\end{aligned} \tag{43}$$

Proof. If $u \in \mathcal{N}_\lambda$, in view of (37), (40), and Hölder inequality, it gains

$$\begin{aligned}\Psi_\lambda(u) &= \Psi_\lambda(u) - \frac{1}{p^-}\left\langle \Psi'_\lambda(u), u\right\rangle \\ &= \left(\frac{1}{2}-\frac{1}{p^-}\right)\|u\|^2_{\lambda,V} - \int_{\mathbb{R}^N}\left(\frac{1}{q(x)}-\frac{1}{p^-}\right)f(x)|u|^{q(x)}dx \\ &\quad - \int_{\mathbb{R}^N}\left(\frac{1}{p(x)}-\frac{1}{p^-}\right)g(x)|u|^{p(x)}dx \geq \left(\frac{1}{2}-\frac{1}{p^-}\right)\|u\|^2_{\lambda,V} \\ &\quad - \left(\frac{1}{q^-}-\frac{1}{p^-}\right)\int_{\mathbb{R}^N} f(x)|u|^{q(x)}dx \geq \left(\frac{1}{2}-\frac{1}{p^-}\right)\|u\|^2_{\lambda,V} \\ &\quad - \left(\frac{1}{q^-}-\frac{1}{p^-}\right)\|f\|_{L^{\frac{2}{2-q(x)}}(\mathbb{R}^N)}\left(\int_{\mathbb{R}^N}|u|^2dx\right)^{\frac{q(x)}{2}} \\ &\geq \left(\frac{1}{2}-\frac{1}{p^-}\right)\|u\|^2_{\lambda,V} - \left(\frac{1}{q^-}-\frac{1}{p^-}\right)\|f\|_{L^{\frac{2}{2-q(x)}}(\mathbb{R}^N)}\frac{1}{\theta^{q(x)/2}}\|u\|^{q(x)}_\lambda \\ &\geq \frac{p^- - 2}{2p^-}\|u\|^2_{\lambda,V} - \left(\frac{1}{q^-}-\frac{1}{p^-}\right)\|f\|_{L^{\frac{2}{2-q(x)}}(\mathbb{R}^N)}\max\left\{\frac{1}{\theta^{q^+/2}}\|u\|^{q^+}_\lambda, \right. \\ &\quad \left.\frac{1}{\theta^{q^-/2}}\|u\|^{q^-}_\lambda\right\} \geq \frac{p^- - 2}{2p^-}\frac{\vartheta_0 - 1}{\vartheta_0}\|u\|^2_\lambda \\ &\quad - \left(\frac{1}{q^-}-\frac{1}{p^-}\right)\|f\|_{L^{\frac{2}{2-q(x)}}(\mathbb{R}^N)}\max\left\{\frac{1}{\theta^{q^+/2}}\|u\|^{q^+}_\lambda, \frac{1}{\theta^{q^-/2}}\|u\|^{q^-}_\lambda\right\} \\ &\geq \max\left\{-\frac{2-q^+}{2p^-}\left(\frac{\vartheta_0 q^+}{\theta(\vartheta_0-1)(p^- - 2)}\right)^{\frac{q^+}{2-q^+}}\right. \\ &\quad \cdot\left(\frac{(p^- - q^-)\|f\|_{L^{2/2-q(x)}(\mathbb{R}^N)}}{q^-}\right)^{\frac{2}{2-q^+}}, -\frac{2-q^-}{2p^-q^-} \\ &\quad \left.\cdot\left(\frac{\vartheta_0}{\theta(\vartheta_0-1)(p^- - 2)}\right)^{\frac{q^-}{2-q^-}}\left((p^- - q^-)\|f\|_{L^{\frac{2}{2-q(x)}}(\mathbb{R}^N)}\right)^{\frac{2}{2-q^-}}\right\}.\end{aligned} \tag{44}$$

Therefore, Ψ_λ is coercive and bounded below on $\mathcal{N}_\lambda$.

We know that $\mathcal{N}_\lambda$ is linked to the behavior of the function of the form $L_u(t)$: $t \to \Psi_\lambda(tu)$ for $t > 0$. This map is called as the fibering map which can be traced back to basic works [1, 22, 23]. If $u \in X_\lambda$, then

$$L_u(t) = \frac{t^2}{2}\|u\|^2_{\lambda,V} - \int_{\mathbb{R}^N}\frac{f(x)}{q(x)}|tu|^{q(x)}dx - \int_{\mathbb{R}^N}\frac{g(x)}{p(x)}|tu|^{p(x)}dx,$$

$$L'_u(t) = t\|u\|^2_{\lambda,V} - \int_{\mathbb{R}^N} f(x)t^{q(x)-1}|u|^{q(x)}dx - \int_{\mathbb{R}^N} g(x)t^{p(x)-1}|u|^{p(x)}dx;$$

$$\begin{aligned}L''_u(t) &= \|u\|^2_{\lambda,V} - \int_{\mathbb{R}^N} f(x)(q(x)-1)t^{q(x)-2}|u|^{q(x)}dx \\ &\quad - \int_{\mathbb{R}^N} g(x)(p(x)-1)t^{p(x)-2}|u|^{p(x)}dx.\end{aligned} \tag{45}$$

After observation, we can get that

$$tL'_u(t) = \|tu\|^2_{\lambda,V} - \int_{\mathbb{R}^N} f(x)|tu|^{q(x)}dx - \int_{\mathbb{R}^N} g(x)|tu|^{p(x)}dx \tag{46}$$

and thus, for $u \in X_\lambda \setminus \{0\}$ and $t > 0$, $L'_u(t) = 0$ if and only if $tu \in \mathcal{N}_\lambda$, i.e., positive critical points of L_u correspond points on the Nehari manifold. Especially, $L'_u(1) = 0$ if and only if $u \in \mathcal{N}_\lambda$. We found that $\mathcal{N}_\lambda$ can be divided into three parts corresponding local minimal, local maximum, and points of inflection. Based on the above, we can define

$$\begin{aligned}\mathcal{N}^+_\lambda &= \left\{u \in \mathcal{N}_\lambda : L''_u(1) > 0\right\}; \\ \mathcal{N}^0_\lambda &= \left\{u \in \mathcal{N}_\lambda : L''_u(1) = 0\right\}; \\ \mathcal{N}^-_\lambda &= \left\{u \in \mathcal{N}_\lambda : L''_u(1) < 0\right\}.\end{aligned} \tag{47}$$

For each $u \in \mathcal{N}_\lambda$, we can find that

$$\begin{aligned}L''_u(1) &= \|u\|^2_{\lambda,V} - \int_{\mathbb{R}^N}(q(x)-1)f(x)|u|^{q(x)}dx \\ &\quad - \int_{\mathbb{R}^N}(p(x)-1)g(x)|u|^{p(x)}dx.\end{aligned} \tag{48}$$

Now, we will deduce some results of $\mathcal{N}^+_\lambda$, $\mathcal{N}^0_\lambda$, and $\mathcal{N}^-_\lambda$.

Lemma 11. *Assume u_0 is a local minimizer of Ψ_λ on $\mathcal{N}_\lambda$ and $u_0 \notin \mathcal{N}^0_\lambda$, then $\Psi'_\lambda(u_0) = 0$ in X^{-1}_λ.*

Proof. If u_0 is a local minimizer of Ψ_λ on $\mathcal{N}_\lambda$, then u_0 is a solution of the optimization problem

$$\text{minimizer}\,\Psi_\lambda(u) \text{ subject to } K(u) = 0, \tag{49}$$

where $K(u) = \|u\|^2_{\lambda,V} - \int_{\mathbb{R}^N} f(x)|u|^{q(x)}dx - \int_{\mathbb{R}^N} g(x)|u|^{p(x)}dx$. Consequently, by the theory of Lagrange multipliers, there exists $\nu \in \mathbb{R}$ such that $\Psi'_\lambda(u_0) = \nu K'(u_0)$. Therefore,

$$\left\langle \Psi'_\lambda(u_0), u_0\right\rangle = \nu\left\langle K'(u_0), u_0\right\rangle. \tag{50}$$

It follows from $u_0 \in \mathcal{N}_\lambda$ that

$$\|u_0\|^2_{\lambda,V} - \int_{\mathbb{R}^N} f(x)|u_0|^{q(x)}dx - \int_{\mathbb{R}^N} g(x)|u_0|^{p(x)}dx = 0. \tag{51}$$

Thus,

$$\begin{aligned}\left\langle K'(u_0), u_0\right\rangle &= 2\|u_0\|^2_{\lambda,V} - \int_{\mathbb{R}^N} q(x)f(x)|u_0|^{q(x)}dx \\ &\quad - \int_{\mathbb{R}^N} p(x)g(x)|u_0|^{p(x)}dx = \|u_0\|^2_{\lambda,V} \\ &\quad - \int_{\mathbb{R}^N}(q(x)-1)f(x)|u_0|^{q(x)}dx - \int_{\mathbb{R}^N}(p(x) \\ &\quad - 1)g(x)|u_0|^{p(x)}dx.\end{aligned} \tag{52}$$

If $u_0 \notin \mathcal{N}^0_\lambda$, then $\langle K'(u_0), u_0\rangle \neq 0$. In view of (50), it gains $\nu = 0$.

Lemma 12.

(1) $\forall u \in \mathcal{N}_\lambda^+ \cup \mathcal{N}_\lambda^0$, *one has* $\int_{\mathbb{R}^N} f(x)|u|^{q(x)}dx > 0$

(2) $\forall u \in \mathcal{N}_\lambda^-$, *one has* $\int_{\mathbb{R}^N} g(x)|u|^{p(x)}dx > 0$

Proof. By the definitions of $\mathcal{N}_\lambda^+$ and $\mathcal{N}_\lambda^0$, we can obtain

$$\begin{aligned} 0 \le L_u''(1) &= \|u\|_{\lambda,V}^2 - \int_{\mathbb{R}^N} (q(x)-1)f(x)|u|^{q(x)}dx \\ &\quad - \int_{\mathbb{R}^N} (p(x)-1)g(x)|u|^{p(x)}dx = \|u\|_{\lambda,V}^2 \\ &\quad - \int_{\mathbb{R}^N} (q^- - 1)f(x)|u|^{q(x)}dx \\ &\quad - \int_{\mathbb{R}^N} (p^- - 1)g(x)|u|^{p(x)}dx < (2-p^-)\|u\|_{\lambda,V}^2 \\ &\quad - (q^- - p^-)\int_{\mathbb{R}^N} f(x)|u|^{q(x)}dx. \end{aligned} \tag{53}$$

It is easy to get that $\int_{\mathbb{R}^N} f(x)|u|^{q(x)}dx > p^- - 2/p^- - q^-\|u\|_{\lambda,V}^2 \ge 0$. It follows from the definition of $\mathcal{N}_\lambda^-$ that

$$\begin{aligned} 0 > L_u''(1) &= \|u\|_{\lambda,V}^2 - \int_{\mathbb{R}^N} (q(x)-1)f(x)|u|^{q(x)}dx \\ &\quad - \int_{\mathbb{R}^N} (\mathrm{p}(x)-1)g(x)|u|^{p(x)}dx \ge \|u\|_{\lambda,V}^2 \\ &\quad - \int_{\mathbb{R}^N} (q^+ - 1)f(x)|u|^{q(x)}dx \\ &\quad - \int_{\mathbb{R}^N} (p^+ - 1)g(x)|u|^{p(x)}dx \\ &= (2-q^+)\|u\|_{\lambda,V}^2 - (p^+ - q^+)\int_{\mathbb{R}^N} g(x)|u|^{p(x)}dx, \end{aligned} \tag{54}$$

which implies that $\int_{\mathbb{R}^N} g(x)|u|^{p(x)}dx > 2 - q^+/p^+ - q^+\|u\|_{\lambda,V}^2 \ge 0$.

Lemma 13. *Let the condition* (H_3), (H_4), *and* (V_1)-(V_5) *are satisfied. Then, for all* $\lambda \ge 1/kM^2 \mid \{V^+ < k\} \mid$, *one has* $\mathcal{N}_\lambda^0 = \varnothing$.

Proof. If the conclusion does not hold, then there exists $\lambda \ge 1/kM^2 \mid \{V^+ < k\} \mid$, such that $\mathcal{N}_\lambda^0 \ne \varnothing$. Then, for $u \in \mathcal{N}_\lambda^0$, by (40), (48), and the Hölder inequality, we have

$$\begin{aligned} 0 = L_u''(1) &= \|u\|_{\lambda,V}^2 - \int_{\mathbb{R}^N} (q(x)-1)f(x)|u|^{q(x)}dx \\ &\quad - \int_{\mathbb{R}^N} (p(x)-1)g(x)|u|^{p(x)}dx < (2-p^-)\|u\|_{\lambda,V}^2 \\ &\quad - (q^- - p^-)\int_{\mathbb{R}^N} f(x)|u|^{q(x)}dx. \end{aligned} \tag{55}$$

This means that

$$\begin{aligned} \frac{q^-}{2}\frac{\vartheta_0 - 1}{\vartheta_0}\|u\|_\lambda^2 \le \frac{\vartheta_0 - 1}{\vartheta_0}\|u\|_\lambda^2 \le \|u\|_{\lambda,V}^2 &< \frac{p^- - q^-}{p^- - 2}\int_{\mathbb{R}^N} f(x)|u|^{q(x)}dx \\ &< \frac{p^- - q^-}{p^- - 2}\|f\|_{L^{\frac{2}{2-q(x)}}(\mathbb{R}^N)}\int_{\mathbb{R}^N}|u|^{q(x)}dx \\ &< \frac{p^- - q^-}{p^- - 2}\|f\|_{L^{\frac{2}{2-q(x)}}(\mathbb{R}^N)} \max\left\{\frac{1}{\theta^{q^+/2}}\|u\|_\lambda^{q^+}, \frac{1}{\theta^{q^-/2}}\|u\|_\lambda^{q^-}\right\}. \end{aligned} \tag{56}$$

Thus, we have

$$\begin{aligned} \|u\|_\lambda \le \min\Bigg\{ &\left(\frac{2\vartheta_0(p^- - q^-)\|f\|_{L^{2/2-q(x)}(\mathbb{R}^N)}}{q^-(\vartheta_0 - 1)(p^- - 2)\theta^{q^+/2}}\right)^{\frac{1}{2-q^+}}, \\ &\cdot \left(\frac{2\vartheta_0(p^- - q^-)\|f\|_{L^{2/2-q(x)}(\mathbb{R}^N)}}{q^-(\vartheta_0 - 1)(p^- - 2)\theta^{q^-/2}}\right)^{\frac{1}{2-q^-}}\Bigg\}. \end{aligned} \tag{57}$$

From (48), we seem to easily get that

$$\begin{aligned} &(2-q^+)\|u\|_{\lambda,V}^2 - (p^+ - q^+)\int_{\mathbb{R}^N} g(x)|u|^{p(x)}dx \le \|u\|_{\lambda,V}^2 \\ &- \int_{\mathbb{R}^N} (q(x)-1)f(x)|u|^{q(x)}dx - \int_{\mathbb{R}^N} (p(x)-1)g(x)|u|^{p(x)}dx \\ &= L_u''(1) = 0, \end{aligned} \tag{58}$$

which implies that

$$\frac{2-q^+}{p^+ - q^+}\|u\|_{\lambda,V}^2 \le \int_{\mathbb{R}^N} g(x)|u|^{p(x)}dx. \tag{59}$$

Combining (39) and (40) with the Sobolev inequality, we have

$$\begin{aligned} \frac{(\vartheta_0 - 1)(2-q^+)}{\vartheta_0(p^+ - q^+)}\|u\|_\lambda^2 \le \frac{2-q^+}{p^+ - q^+}\|u\|_{\lambda,V}^2 &\le \int_{\mathbb{R}^N} g(x)|u|^{p(x)}dx \\ &\le \frac{\|g\|_\infty}{\theta^{p^+/2}|\{V^+ < k\}|^{p^+ - 2/2}} \max \\ &\quad \cdot \left\{\|u\|_\lambda^{p^+}, M^{p^- - p^+}\|u\|_\lambda^{p^-}\right\}. \end{aligned} \tag{60}$$

This means that

$$\begin{aligned} \|u\|_\lambda \ge \max\Bigg\{ &\left[\frac{(\vartheta_0 - 1)(2-q^+)\theta \wedge (p\wedge +/2) \mid \{V^+ < k\} \mid \wedge((p\wedge +-2)/2)}{\vartheta_0(p^+ - q^+)\|g\|_\infty}\right]^{\frac{1}{p^+ - 2}}, \\ &\cdot \left[\frac{(\vartheta_0 - 1)(2-q^+)\theta \wedge (p\wedge +/2) \mid \{V^+ < k\} \mid \wedge((p\wedge +-2)/2)}{\vartheta_0(p^+ - q^+)\|g\|_\infty M^{p^- - p^+}}\right]^{\frac{1}{p^- - 2}}\Bigg\}. \end{aligned} \tag{61}$$

Hence, combining (57) and (61), we have

$$|\{V^+ < k\}| < \min\{A_1, A_2, A_3, A_4\} \le \max\{A_1, A_2, A_3, A_4\}, \tag{62}$$

which is a contradictive with (V_5). Therefore, for all $\lambda \ge 1/k M^2 |\{V^+ < k\}|$, one has $\mathcal{N}_\lambda^0 = \varnothing$.

By Lemma 13, $\lambda \ge 1/kM^2 |\{V^+ < k\}|$, we can easily get that $\mathcal{N}_\lambda = \mathcal{N}_\lambda^+ \cup \mathcal{N}_\lambda^-$ and define

$$c_\lambda^+ = \inf_{u \in \mathcal{N}_\lambda^+} \Psi_\lambda(u) \text{ and } c_\lambda^- = \inf_{u \in \mathcal{N}_\lambda^-} \Psi_\lambda(u). \tag{63}$$

Furthermore, we derive the following results.

Lemma 14. *Under the condition (H_3), (H_4), and (V_1)-(V_5). Then, for all $\lambda \ge 1/kM^2 |\{V^+ < k\}|$, there exists C_5 such that $c_\lambda^+ < 0 < C_5 < c_\lambda^-$. Particularly, $c_\lambda^+ = \inf_{u \in \mathcal{N}_\lambda} \Psi_\lambda(u)$.*

Proof. Our proof is decoupled in the following two steps:

Step 1. We claim that there exist $u \in \mathcal{N}_\lambda^+$ such that $\Psi_\lambda(u) < 0$. Indeed, let $tv_0 \in \mathcal{N}_\lambda^+ \subset \mathcal{N}_\lambda$, where $t \in (0, 1)$ small enough. It is follows from (48) that

$$\begin{aligned} 0 < L''_{tv_0}(1) &= \|tv_0\|_{\lambda,V}^2 - \int_{\mathbb{R}^N} (q(x) - 1) f(x) |tv_0|^{q(x)} dx \\ &\quad - \int_{\mathbb{R}^N} (p(x) - 1) g(x) |tv_0|^{p(x)} dx < (2 - p^-) \|tv_0\|_{\lambda,V}^2 \\ &\quad - (q^- - p^-) \int_{\mathbb{R}^N} f(x) |tv_0|^{q(x)} dx. \end{aligned} \tag{64}$$

This shows that

$$0 \le \frac{p^- - 2}{p^- - q^-} \|tv_0\|_{\lambda,V}^2 < \int_{\mathbb{R}^N} f(x) \left| tv_0 \right|^{q(x)} dx < t^{q^-} \int_{\mathbb{R}^N} f(x) \left| v_0 \right|^{q(x)} dx. \tag{65}$$

This yields at once that

$$\int_{\mathbb{R}^N} f(x) |v_0|^{q(x)} dx > 0. \tag{66}$$

Similarly,

$$\begin{aligned} 0 < L''_{tv_0}(1) &= \|tv_0\|_{\lambda,V}^2 - \int_{\mathbb{R}^N} (q(x) - 1) f(x) |tv_0|^{q(x)} dx \\ &\quad - \int_{\mathbb{R}^N} (p(x) - 1) g(x) |tv_0|^{p(x)} dx < (2 - q^-) \|tv_0\|_{\lambda,V}^2 \\ &\quad - (p^- - q^-) \int_{\mathbb{R}^N} g(x) |tv_0|^{p(x)} dx. \end{aligned} \tag{67}$$

From (67), we can easily get that

$$\frac{2 - q^-}{p^- - q^-} \|tv_0\|_{\lambda,V}^2 > \int_{\mathbb{R}^N} g(x) |tv_0|^{p(x)} dx. \tag{68}$$

Consequently, it derives from (67) and (68) that

$$\begin{aligned} \Psi_\lambda(tv_0) &= \Psi_\lambda(tv_0) - \frac{1}{p^-} \left\langle \Psi'_\lambda(tv_0), tv_0 \right\rangle < \frac{1}{2} \|tv_0\|_{\lambda,V}^2 \\ &\quad - \frac{1}{q^+} \int_{\mathbb{R}^N} f(x) |tv_0|^{q(x)} dx - \frac{1}{p^+} \int_{\mathbb{R}^N} g(x) |tv_0|^{p(x)} dx \\ &\quad - \frac{1}{p^-} \|tv_0\|_{\lambda,V}^2 + \frac{1}{p^-} \int_{\mathbb{R}^N} f(x) |tv_0|^{q(x)} dx \\ &\quad + \frac{1}{p^-} \int_{\mathbb{R}^N} g(x) |tv_0|^{p(x)} dx = \left(\frac{1}{2} - \frac{1}{p^-} \right) \|tv_0\|_{\lambda,V}^2 \\ &\quad - \int_{\mathbb{R}^N} \left(\frac{1}{q^+} - \frac{1}{p^-} \right) f(x) |tv_0|^{q(x)} dx \\ &\quad + \left(\frac{1}{p^-} - \frac{1}{p^+} \right) \int_{\mathbb{R}^N} g(x) |tv_0|^{p(x)} dx \\ &< \left(\frac{1}{2} - \frac{1}{p^-} \right) \|tv_0\|_{\lambda,V}^2 - \int_{\mathbb{R}^N} \left(\frac{1}{q^+} - \frac{1}{p^-} \right) f(x) |tv_0|^{q(x)} dx \\ &\quad + \left(\frac{1}{p^-} - \frac{1}{p^+} \right) \frac{2 - q^-}{p^- - q^-} \|tv_0\|_{\lambda,V}^2 = \left[\left(\frac{1}{2} - \frac{1}{p^-} \right) \right. \\ &\quad \left. + \left(\frac{1}{p^-} - \frac{1}{p^+} \right) \frac{2 - q^-}{p^- - q^-} \right] \|tv_0\|_{\lambda,V}^2 \\ &\quad - \int_{\mathbb{R}^N} \left(\frac{1}{q^+} - \frac{1}{p^-} \right) f(x) |tv_0|^{q(x)} dx < t^2 \left[\left(\frac{1}{2} - \frac{1}{p^-} \right) \right. \\ &\quad \left. + \left(\frac{1}{p^-} - \frac{1}{p^+} \right) \frac{2 - q^-}{p^- - q^-} \right] \|v_0\|_{\lambda,V}^2 - t^{q^+} \int_{\mathbb{R}^N} \\ &\quad \cdot \left(\frac{1}{q^+} - \frac{1}{p^-} \right) f(x) |v_0|^{q(x)} dx. \end{aligned} \tag{69}$$

Hence, $c_\lambda^+ < 0$.

Step 2. We assert that there exist $u \in \mathcal{N}_\lambda^-$ such that $\Psi_\lambda(u) > 0$. In fact, let $u \in \mathcal{N}_\lambda^- \subset \mathcal{N}_\lambda$. From (48), we seem to easily get that

$$\begin{aligned} &(2 - q^+) \|u\|_{\lambda,V}^2 - (p^+ - q^+) \int_{\mathbb{R}^N} g(x) |u|^{p(x)} dx \le \|u\|_{\lambda,V}^2 \\ &\quad - \int_{\mathbb{R}^N} (q(x) - 1) f(x) |u|^{q(x)} dx - \int_{\mathbb{R}^N} (p(x) - 1) g(x) |u|^{p(x)} dx \\ &\quad = L''_u(1) < 0, \end{aligned} \tag{70}$$

which implies that

$$\frac{2 - q^+}{p^+ - q^+} \|u\|_{\lambda,V}^2 < \int_{\mathbb{R}^N} g(x) |u|^{p(x)} dx. \tag{71}$$

Combining (39), (40), and (71) with Sobolev inequality, we have

$$\frac{(\vartheta_0-1)(2-q^+)}{\vartheta_0(p^+-q^+)}\|u\|_\lambda^2 \le \frac{2-q^+}{p^+-q^+}\|u\|_{\lambda,V}^2 < \int_{\mathbb{R}^N} g(x)|u|^{p(x)}dx \le \frac{\|g\|_\infty}{\theta^{p^+/2}|\{V^+<k\}|^{p^+-2/2}} \max\left\{\|u\|_\lambda^{p^+}, M^{p^--p^+}\|u\|_\lambda^{p^-}\right\} \tag{72}$$

and so

$$\|u\|_\lambda \ge \max\left\{\left[\frac{(\vartheta_0-1)(2-q^+)\theta\wedge(p\wedge+/2)\mid\{V^+<k\}\mid\wedge((p\wedge+-2)/2)}{\vartheta_0(p^+-q^+)\|g\|_\infty}\right]^{\frac{1}{p^+-2}}, \cdot\left[\frac{(\vartheta_0-1)(2-q^+)\theta\wedge(p\wedge+/2)\mid\{V^+<k\}\mid\wedge((p\wedge+-2)/2)}{\vartheta_0(p^+-q^+)\|g\|_\infty M^{p^--p^+}}\right]^{\frac{1}{p^+-2}}\right\} := C_6. \tag{73}$$

It follows from (44) that

$$\Psi_\lambda(u) \ge \frac{p^--2}{2p^-}\frac{\vartheta_0-1}{\vartheta_0}\|u\|_\lambda^2 - \left(\frac{1}{q^-}-\frac{1}{p^-}\right)\|f\|_{L^{\frac{2}{2-q(x)}}(\mathbb{R}^N)} \max \cdot\left\{\frac{1}{\theta^{q^+/2}}\|u\|_\lambda^{q^+}, \frac{1}{\theta^{q^-/2}}\|u\|_\lambda^{q^-}\right\} > \max \cdot\left\{C_6^{q^+}\left[\frac{p^--2}{2p^-}\frac{\vartheta_0-1}{\vartheta_0}C_6^{2-q^+} - \left(\frac{1}{q^-}-\frac{1}{p^-}\right)\|f\|_{L^{\frac{2}{2-q(x)}}(\mathbb{R}^N)}\frac{1}{\theta^{q^+/2}}\right], C_6^{q^-} \cdot\left[\frac{p^--2}{2p^-}\frac{\vartheta_0-1}{\vartheta_0}C_6^{2-q^-} - \left(\frac{1}{q^-}-\frac{1}{p^-}\right)\|f\|_{L^{\frac{2}{2-q(x)}}(\mathbb{R}^N)}\frac{1}{\theta^{q^-/2}}\right]\right\}. \tag{74}$$

Consequently, if $\lambda > 1/kM^2 \mid \{V^+<k\} \mid$, then $c_\lambda^- > C_5$ for some $C_5 > 0$.

We note that if f, g and V_λ satisfy the hypotheses in Theorem 3, we can choose $\varphi \in C_0^\infty(\Omega_g, \mathbb{C})$, such that $L_\varphi(t) = \Psi_\lambda(t\varphi) = t^2/2\|\varphi\|_{\lambda,V}^2 - \int_{\Omega_g}(f(x)/q(x))|t\varphi|^{q(x)}dx - \int_{\Omega_g}(g(x)/p(x))|t\varphi|^{p(x)}dx$ have $t_0 > 0$ and C_0 which are independent of λ that satisfy $t_0\varphi \in \mathcal{N}_\lambda^-$ for all $\lambda > \lambda^*$ and

$$\sup_{t\ge0} L_\varphi(t) = L_\varphi(t_0) = C_0 > 0, \tag{75}$$

which shows $c_\lambda^- \le C_0$ for all $\lambda > \lambda^*$.

Lemma 15. *Assume that the conditions (H_1)-(H_5) and (V_1)-(V_5) hold, then there exists $\lambda^* \ge 1/kM^2 \mid \{V^+<k\} \mid$ such that Ψ_λ satisfies the $(PS)_c$ condition in X_λ for all $c < C_0$ and $\lambda > \lambda^*$.*

Proof. First, we assume $\{u_n\}$ is a $(PS)_c$ sequence with $c < C_0$. In view of Lemma 10, there exists a positive constant $\widehat{C}$ related to λ such that $\|u_n\|_\lambda \le \widehat{C}$. Consequently, there is a subsequence which is still denote as $\{u_n\}$ and u_0 in X_λ such that

$$\begin{aligned} u_n &\rightharpoonup u_0 \text{ in } X_\lambda, \\ u_n &\to u_0 \text{ in } L_{loc}^r(\mathbb{R}^N, \mathbb{C}), \text{ for } 2 \le r \le \infty, \\ g(x)|u_n|^{p(x)-2}u_n &\rightharpoonup g(x)|u_0|^{p(x)-2}u_0 \text{ in } L^{p'(x)}(\mathbb{R}^N, \mathbb{C}). \end{aligned} \tag{76}$$

Besides, $\Psi_\lambda'(u_0) = 0$. Let $v_n = u_n - u_0$. Making use of the Vitali theorem, it holds that

$$\lim_{n\to\infty}\int_{\mathbb{R}^N} f(x)|v_n|^{q(x)}dx = 0. \tag{77}$$

In fact, note that $f \in L^{2/2-q(x)}(\mathbb{R}^N, \mathbb{C})$, for any $0 < \varepsilon < 1$; then, there exists $r(\varepsilon) > 0$ such that for $\zeta \in \mathbb{R}^N$ and $r > r(\varepsilon)$,

$$\int_{\mathbb{R}^N\setminus B_r(\zeta)} |f(x)|^{\frac{2}{2-q(x)}}dx < \varepsilon^{\frac{2}{2-q^+}}. \tag{78}$$

For each $\Omega_0 \subset B_r(\zeta)$, one has

$$\int_{\Omega_0} f(x)|v_n|^{q(x)}dx \le \max\left\{\left(\int_{\Omega_0}|f(x)|^{\frac{2}{2-q(x)}}dx\right)^{\frac{2-q^-}{2}}, \cdot\left(\int_{\Omega_0}|f(x)|^{\frac{2}{2-q(x)}}dx\right)^{\frac{2-q^+}{2}}\right\} \max \cdot\left\{\left(\int_{\Omega_0}|v_n|^2dx\right)^{\frac{q^-}{2}}, \left(\int_{\Omega_0}|v_n|^2dx\right)^{\frac{q^+}{2}}\right\} \le \widehat{C}\max\left\{\left(\int_{\Omega_0}|f(x)|^{\frac{2}{2-q(x)}}dx\right)^{\frac{2-q^-}{2}}, \cdot\left(\int_{\Omega_0}|f(x)|^{\frac{2}{2-q(x)}}dx\right)^{\frac{2-q^+}{2}}\right\}. \tag{79}$$

It is easy to get that $\{f(x)|v_n|^{q(x)}\}$ is a equi-integrable on $B_r(\zeta)$. Besides, $f(x)|v_n|^{q(x)} \to 0$, a.e., in $B_r(\zeta)$. It follows from the Vitali theorem that

$$\lim_{n\to\infty}\int_{B_r(\zeta)} f(x)|v_n|^{q(x)}dx = 0. \tag{80}$$

Hence, there holds

$$\int_{\mathbb{R}^N} f(x)|v_n|^{q(x)}dx = \int_{B_r(\zeta)} f(x)|v_n|^{q(x)}dx + \int_{\mathbb{R}^N\setminus B_r(\zeta 0)} f(x)|v_n|^{q(x)}dx \le \widehat{C}\varepsilon + \int_{B_r(\zeta)} f(x)|v_n|^{q(x)}dx, \tag{81}$$

which implies that $\lim_{n\to\infty}\int_{\mathbb{R}^N} f(x)|v_n|^{q(x)}dx = 0$.

Next, we assert that $u_n \to u_0$ in X_λ. In fact, by (V_2), we obtain

$$\int_{\mathbb{R}^N} v_n^2 dx = \int_{\{V^+\ge k\}} v_n^2 dx + \int_{\{V^+<k\}} v_n^2 dx \le \frac{1}{\lambda k}\int_{\{V^+\ge k\}} \lambda V^+ v_n^2 dx + \int_{\{V^+<k\}} v_n^2 dx \le \frac{1}{\lambda k}\|v_n\|_\lambda^2 + o(1). \tag{82}$$

In light of the Hölder inequality with the Sobolev inequality, we have

$$\begin{aligned}\int_{\mathbb{R}^N}|v_n|^{p(x)}dx &= \int_{\mathbb{R}^N}|v_n|^{p(x)-2}\cdot|v_n|^2dx \le \max \cdot\left\{\|v_n\|_\infty^{p^+-2},\ \|v_n\|_\infty^{p^--2}\right\}\int_{\mathbb{R}^N}|v_n|^2dx \le \max \cdot\left\{M^{p^+-2}\|v_n\|_{s(\cdot),A}^{p^+-2},\ M^{p^--2}\|v_n\|_{s(\cdot),A}^{p^--2}\right\}\int_{\mathbb{R}^N}|v_n|^2dx \\ &\le \max\left\{M^{p^+-2}\left(\|v_n\|_{L^2(\mathbb{R}^N)}^2 + [v_n]_{s(\cdot),A}^2\right)^{\frac{p^+-2}{2}},\ M^{p^--2}\cdot\left(\|v_n\|_{L^2(\mathbb{R}^N)}^2 + [v_n]_{s(\cdot),A}^2\right)^{\frac{p^--2}{2}}\right\}\int_{\mathbb{R}^N}|v_n|^2d \le \max \cdot\left\{M^{p^+-2}\left(\frac{1}{\lambda k}\|v_n\|_\lambda^2+\|v_n\|_\lambda^2 + o(1)\right)^{\frac{p^+-2}{2}},\ M^{p^--2}\cdot\left(\frac{1}{\lambda k}\|v_n\|_\lambda^2+\|v_n\|_\lambda^2 + o(1)\right)^{\frac{p^--2}{2}}\right\}\int_{\mathbb{R}^N}|v_n|^2dx \le \max \cdot\left\{M^{p^+-2}\left(\frac{\lambda k+1}{\lambda k}\right)^{\frac{p^+-2}{2}}\|v_n\|_\lambda^{p^+-2} + o(1), M^{p^--2}\cdot\left(\frac{\lambda k+1}{\lambda k}\right)^{\frac{p^--2}{2}}\|v_n\|_\lambda^{p^--2} + o(1)\right\}\int_{\mathbb{R}^N}|v_n|^2dx \\ &\le \frac{1}{\lambda k}\max\left\{M^{p^+-2}\|v_n\|_\lambda^{p^+-2},\ M^{p^--2}\|v_n\|_\lambda^{p^--2}\right\}\cdot\left(\frac{\lambda k+1}{\lambda k}\right)^{\frac{p^+-2}{2}}\|v_n\|_\lambda^2 + o(1).\end{aligned} \tag{83}$$

By Bre′is-Lieb Lemma, we have

$$\|u_n\|_{\lambda,V}^2 = \|u_n-u_0\|_{\lambda,V}^2 + \|u_0\|_{\lambda,V}^2 + o(1). \tag{84}$$

By applying a Bre′is-Lieb type result on variable exponent Lebesgue space (see [24]) and (H_3)-(H_4), it is easy to obtain that

$$\int_{\mathbb{R}^N} f(x)|u_n|^{q(x)}dx = \int_{\mathbb{R}^N} f(x)|u_n-u_0|^{q(x)}dx + \int_{\mathbb{R}^N} f(x)|u_0|^{q(x)}dx + o(1). \tag{85}$$

Similarly,

$$\int_{\mathbb{R}^N} g(x)|u_n|^{p(x)}dx = \int_{\mathbb{R}^N} g(x)|u_n-u_0|^{p(x)}dx + \int_{\mathbb{R}^N} g(x)|u_0|^{p(x)}dx + o(1). \tag{86}$$

Then, overall, we can get that $\Psi_\lambda(v_n) = \Psi_\lambda(u_n) - \Psi_\lambda(u_0) + o(1)$ and $\Psi'_\lambda(v_n) = o(1)$. Then, by virtue of (77) and Lemma 10, we get that

$$\begin{aligned}C_0 + C_7 + o(1) > c - \Psi_\lambda(u_0) + o(1) &= \Psi_\lambda(v_n) - \frac{1}{p^-}\left\langle\Psi'_\lambda(v_n), v_n\right\rangle + o(1) \ge \frac{p^--2}{2p^-}\|v_n\|_{\lambda,V}^2 - \left(\frac{1}{q^-}-\frac{1}{p^-}\right)\int_{\mathbb{R}^N} f(x)|v_n|^{q(x)}dx + o(1) \\ &\ge \frac{p^--2}{2p^-}\|v_n\|_{\lambda,V}^2 - \left(\frac{1}{q^-}-\frac{1}{p^-}\right)\|f\|_{L^{\frac{2}{2-q(x)}}}\max\left\{\frac{1}{\theta^{q^+/2}}\|u\|_\lambda^{q^+}, \frac{1}{\theta^{q^-/2}}\|u\|_\lambda^{q^-}\right\} + o(1) \ge \frac{p^--2}{2p^-}\frac{\vartheta_0-1}{\vartheta_0}\|v_n\|_\lambda^2 \\ &\quad - \left(\frac{1}{q^-}-\frac{1}{p^-}\right)\|f\|_{L^{\frac{2}{2-q(x)}}}\max\left\{\frac{1}{\theta^{q^+/2}}\|u\|_\lambda^{q^+}, \frac{1}{\theta^{q^-/2}}\|u\|_\lambda^{q^-}\right\} + o(1),\end{aligned} \tag{87}$$

where

$$C_7 = \min\left\{\frac{2-q^+}{2p^-}\left(\frac{\vartheta_0 q^+}{\theta(\vartheta_0-1)(p^--2)}\right)^{\frac{q^+}{2-q^+}}\left(\frac{(p^--q^-)\|f\|_{L^{2/2-q(x)}}}{q^-}\right)^{\frac{2}{2-q^+}}, \frac{2-q^-}{2p^-q^-}\left(\frac{\vartheta_0}{\theta(\vartheta_0-1)(p^--2)}\right)^{\frac{q^-}{2-q^-}}\left((p^--q^-)\|f\|_{L^{\frac{2}{2-q(x)}}}\right)^{\frac{2}{2-q^-}}\right\}. \tag{88}$$

Suppose by contradiction that $\{v_n\}$ is not bounded in X_λ. Then, there exists a subsequence still denoted by $\{v_n\}$ such that $\|v_n\|_\lambda \to \infty$ as $n\to\infty$. Hence, by virtue of (87), we have

$$\frac{C_0+C_7}{\|v_n\|_\lambda^2} + o(1)\frac{1}{\|v_n\|_\lambda^2} \ge \frac{p^--2}{2p^-}\frac{\vartheta_0-1}{\vartheta_0} - \left(\frac{1}{q^-}-\frac{1}{p^-}\right)\|f\|_{L^{\frac{2}{2-q(x)}}}\max\cdot\left\{\frac{1}{\theta^{q^+/2}}\|v_n\|_\lambda^{q^+-2}, \frac{1}{\theta^{q^-/2}}\|v_n\|_\lambda^{q^--2}\right\} + o(1)\frac{1}{\|v_n\|_\lambda^2}, \tag{89}$$

which is contradictory since $1 < q^- \le q^+ < 2 < p^-$. Thus, $\{v_n\}$ is bounded in X_λ for all $\lambda > \lambda^* \ge 1/kM^2 \mid \{V^+ < k\}\mid$. That is, there exist a constant $M_1 > 0$ such that $\|v_n\|_\lambda \le M_1$. From

(83), we can get that

$$\int_{\mathbb{R}^N} |v_n|^{p(x)} dx \le \frac{1}{\lambda k} \max\left\{(MM_1)^{p^+-2}, (MM_1)^{p^--2}\right\} \cdot \left(\frac{\lambda k+1}{\lambda k}\right)^{\frac{p^+-2}{2}} \|v_n\|_\lambda^2 + o(1). \tag{90}$$

Together $\langle \Psi'_\lambda(v_n), v_n\rangle = o(1)$ with (77)-(90), there holds

$$\begin{aligned} o(1) = \left\langle \Psi'_\lambda(v_n), v_n \right\rangle &= \|v_n\|_{\lambda,V}^2 - \int_{\mathbb{R}^N} g(x)|v_n|^{p(x)} dx \\ &\ge \frac{\vartheta_0 - 1}{\vartheta_0}\|v_n\|_\lambda^2 - \|g\|_\infty \int_{\mathbb{R}^N} |v_n|^{p(x)} dx \ge \frac{\vartheta_0 - 1}{\vartheta_0}\|v_n\|_\lambda^2 \\ &\quad - \frac{\|g\|_\infty}{\lambda k} \max\left\{(MM_1)^{p^+-2}, (MM_1)^{p^--2}\right\} \\ &\quad \cdot \left(\frac{\lambda k+1}{\lambda k}\right)^{\frac{p^+-2}{2}} \|v_n\|_\lambda^2 + o(1). \end{aligned} \tag{91}$$

We find that there exists $\lambda^* \ge 1/kM^2 \mid \{V^+ < k\} \mid$ large enough such that

$$\frac{\|g\|_\infty}{\lambda_k} \max\left\{(MM_1)^{p^+-2}, (MM_1)^{p^--2}\right\} \left(\frac{\lambda k+1}{\lambda k}\right)^{\frac{p^+-2}{2}} < \frac{\vartheta_0 - 1}{\vartheta_0}, \tag{92}$$

for all $\lambda > \lambda^*$. It follows from (91) that $v_n \to 0$ in X_λ for all $\lambda > \lambda^*$.

Theorem 16. *Assume that (H_1)-(H_5) and (V_1)-(V_5) hold, then there exists $\lambda^* \ge 0$ such that for every $\lambda > \lambda^*$, Ψ_λ has a minimizer u_λ^+ in $\mathcal{N}_\lambda^+$ satisfying that*

$$\Psi_\lambda(u_\lambda^+) = c_\lambda^+ = \inf_{u\in\mathcal{N}_\lambda^+} \Psi_\lambda(u), \tag{93}$$

(1) u_λ^+ is a nontrivial solution of equation (1).

Proof. Combining Lemma 14 and the Ekeland variational principle in [25], there exists $\{u_n\} \subset \mathcal{N}_\lambda^+$ such that $\{u_n\}$ is a $(PS)_{c_\lambda^+}$ sequence for Ψ_λ. Furthermore, using Lemma 10, we can get that $\{u_n\}$ is bounded in X_λ. Consequently, there exists a subsequence of $\{u_n\}$ (we still denote as $\{u_n\}$) and u_λ^+ in X_λ such that

$$\begin{aligned} u_n &\rightharpoonup u_\lambda^+ \text{ in } X_\lambda, \\ u_n &\to u_\lambda^+ \text{ in } L^r_{loc}(\mathbb{R}^N, \mathbb{C}), \text{ for } 2 \le r \le \infty. \end{aligned} \tag{94}$$

Besides, $\Psi'_\lambda(u_\lambda^+) = 0$. In view of Lemma 15, we know that $u_n \to u_\lambda^+$ in X_λ and $\Psi_\lambda(u_\lambda^+) = c_\lambda^+$. In other words, u_λ^+ is a solution of equation (1).

Now, we will check that $u_\lambda^+ \ne 0$. On the contrary, by combining (40), (H_3), the Egoroff theorem and the Hölder inequality, there holds $\int_{\mathbb{R}^N} f(x)|u_n|^{q(x)} dx \to 0$ as $n \to \infty$, which shows that

$$\|u_n\|_{\lambda,V}^2 = \int_{\mathbb{R}^N} g(x)|u_n|^{p(x)} dx + o(1)$$

$$\begin{aligned} \Psi_\lambda(u_n) &= \frac{1}{2}\|u_n\|_{\lambda,V}^2 - \int_{\mathbb{R}^N} \frac{f(x)}{q(x)}|u_n|^{q(x)} dx - \int_{\mathbb{R}^N} \frac{g(x)}{p(x)}|u_n|^{p(x)} dx \\ &\ge \frac{1}{2}\|u_n\|_{\lambda,V}^2 - \frac{1}{q^-}\int_{\mathbb{R}^N} f(x)|u_n|^{q(x)} dx - \frac{1}{p^-}\int_{\mathbb{R}^N} g(x)|u_n|^{p(x)} dx \\ &= \frac{1}{2}\|u_n\|_{\lambda,V}^2 - \frac{1}{p^-}\|u_n\|_{\lambda,V}^2 + o(1) = \frac{p^- - 2}{2p^-}\|u_n\|_{\lambda,V}^2 + o(1) \\ &\ge \frac{(p^- - 2)(\vartheta_0 - 1)}{2p^-\vartheta_0}\|u_n\|_\lambda^2 + o(1) \ge 0. \end{aligned} \tag{95}$$

This is contradictive with $\lim_{n\to\infty} \Psi_\lambda(u_n) = c_\lambda^+ < 0$. Hence, $u_\lambda^+ \ne 0$; that is, u_λ^+ is a nontrivial solution of equation (1).

Proof of Theorem 17. The result of Theorem 2 is immediately available from Theorem 20.

Theorem 18. *Assume that the conditions (H_3), (H_4), and (V_1)-(V_5) are satisfied, then there exists $\lambda^* \ge 0$ such that for every $\lambda > \lambda^*$, Ψ_λ has a minimizer u_λ^- in $\mathcal{N}_\lambda^-$ satisfying that*

$$\Psi_\lambda(u_\lambda^-) = c_\lambda^-, \tag{96}$$

(1) u_λ^- is a nontrivial solution of equation (1).

Proof. According to Lemma 14 and the Ekeland variational principle in [25], there exists $\{u_n\} \subset \mathcal{N}_\lambda^-$ such that $\{u_n\}$ is a $(PS)_{c_\lambda^-}$ sequence for Ψ_λ. Furthermore, using Lemma 10, we can get that $\{u_n\}$ is bounded in X_λ. Consequently, there exists a subsequence of $\{u_n\}$ (we still denote as $\{u_n\}$) and u_λ^- in X_λ such that

$$\begin{aligned} u_n &\rightharpoonup u_\lambda^- \text{ in } X_\lambda, \\ u_n &\to u_\lambda^- \text{ in } L^r_{loc}(\mathbb{R}^N), \text{ for } 2 \le r \le \infty. \end{aligned} \tag{97}$$

Besides, $\Psi'_\lambda(u_\lambda^-) = 0$. In view of Lemma 15, we know that $u_n \to u_\lambda^-$ in X_λ and $\Psi_\lambda(u_\lambda^-) = c_\lambda^-$. In other words, u_λ^- is a solution of equation (1).

Now, we will check that $u_\lambda^- \ne 0$. Suppose the contrary, combining (39), (40), Egoroff theorem, and (H_4), there holds $\int_{\mathbb{R}^N} g(x)|u_n|^{p(x)} dx \to 0$ as $n \to \infty$, which shows that

$$\|u_n\|_{\lambda,V}^2 = \int_{\mathbb{R}^N} f(x)|u_n|^{q(x)} dx + o(1)$$

$$\begin{aligned}\Psi_\lambda(u_n) &= \frac{1}{2}\|u_n\|^2_{\lambda,V} - \int_{\mathbb{R}^N}\frac{f(x)}{q(x)}|u_n|^{q(x)}dx - \int_{\mathbb{R}^N}\frac{g(x)}{p(x)}|u_n|^{p(x)}dx \\ &\le \frac{1}{2}\|u_n\|^2_{\lambda,V} - \frac{1}{q^+}\int_{\mathbb{R}^N} f(x)|u_n|^{q(x)}dx - \frac{1}{p^+}\int_{\mathbb{R}^N} g(x)|u_n|^{p(x)}dx \\ &= \frac{1}{2}\|u_n\|^2_{\lambda,V} - \frac{1}{q^+}\|u_n\|^2_{\lambda,V} + o(1) = \frac{q^+-2}{2q^+}\|u_n\|^2_{\lambda,V} + o(1) \\ &\le \frac{(q^+-2)(\vartheta_0-1)}{2q^+\vartheta_0}\|u_n\|^2_\lambda + o(1) \le 0.\end{aligned} \tag{98}$$

This is contradictive with $\lim_{n\to\infty}\Psi_\lambda(u_n) = c^-_\lambda > 0$. Hence, $u^-_\lambda \neq 0$; that is, u^-_λ is a nontrivial solution of equation (1).

Proof of Theorem 19. It derives from Theorem 20, Theorem 22, and Lemma 14 that equation (1) has two nontrivial solutions u^+_λ and u^-_λ such that $u^+_\lambda \in \mathcal{N}^+_\lambda$ and $u^-_\lambda \in \mathcal{N}^-_\lambda$ with $\Psi_\lambda(u^+_\lambda) = c^+_\lambda < 0 < C_5 < \Psi_\lambda(u^-_\lambda) = c^-_\lambda$.

Theorem 20. *Assume that (H_3), (H_4), and (V_1)-(V_5) hold, then for all $\lambda \ge 1/kM^2 \mid \{V^+ < k\} \mid$, Ψ_λ has a minimizer u^+_λ in $\mathcal{N}^+_\lambda$ satisfying that*

$$\Psi_\lambda(u^+_\lambda) = c^+_\lambda = \inf_{u\in\mathcal{N}^+_\lambda}\Psi_\lambda(u); \tag{99}$$

(1) u^+_λ is a nontrivial solution of equation (1).

Proof. Combining Lemma 14 and the Ekeland variational principle in [25], there exists $\{u_n\} \subset \mathcal{N}^+_\lambda$ such that $\{u_n\}$ is a $(PS)_{c^+_\lambda}$ sequence for Ψ_λ. Furthermore, using Lemma 10, we can get that $\{u_n\}$ is bounded in X_λ. Consequently, there exists a subsequence of $\{u_n\}$ (we still denote as $\{u_n\}$) and u^+_λ in X_λ such that

$$\begin{aligned} u_n &\rightharpoonup u^+_\lambda \text{ in } X_\lambda, \\ u_n &\to u^+_\lambda \text{ in } L^r_{loc}(\mathbb{R}^N), \text{ for } 2 \le r \le \infty. \end{aligned} \tag{100}$$

Besides, $\Psi'_\lambda(u^+_\lambda) = 0$. In view of Lemma 15, we know that $u_n \to u^+_\lambda$ in X_λ and $\Psi_\lambda(u^+_\lambda) = c^+_\lambda$. In other words, u^+_λ is a solution of equation (1).

Now, we will check that $u^+_\lambda \neq 0$. On the contrary, by combining (40), (H_3), the Egoroff theorem, and the Hölder inequality, there holds $\int_{\mathbb{R}^N} f(x)|u_n|^{q(x)}dx \to 0$ as $n \to \infty$, which shows that

$$\|u_n\|^2_{\lambda,V} = \int_{\mathbb{R}^N} g(x)|u_n|^{p(x)}dx + o(1)$$

$$\begin{aligned}\Psi_\lambda(u_n) &= \frac{1}{2}\|u_n\|^2_{\lambda,V} - \int_{\mathbb{R}^N}\frac{f(x)}{q(x)}|u_n|^{q(x)}dx - \int_{\mathbb{R}^N}\frac{g(x)}{p(x)}|u_n|^{p(x)}dx \\ &\ge \frac{1}{2}\|u_n\|^2_{\lambda,V} - \frac{1}{q^-}\int_{\mathbb{R}^N} f(x)|u_n|^{q(x)}dx - \frac{1}{p^-}\int_{\mathbb{R}^N} g(x)|u_n|^{p(x)}dx \\ &= \frac{1}{2}\|u_n\|^2_{\lambda,V} - \frac{1}{p^-}\|u_n\|^2_{\lambda,V} + o(1) = \frac{p^--2}{2p^-}\|u_n\|^2_{\lambda,V} + o(1) \\ &\ge \frac{(p^--2)(\vartheta_0-1)}{2p^-\vartheta_0}\|u_n\|^2_\lambda + o(1) \ge 0.\end{aligned} \tag{101}$$

This is contradictive with $\lim_{n\to\infty}\Psi_\lambda(u_n) = c^+_\lambda < 0$. Hence, $u^+_\lambda \neq 0$; that is, u^+_λ is a nontrivial solution of equation (1).

Proof of Theorem 21. The result of Theorem 2 is immediately available from Theorem 20.

We note that if f, g and V_λ satisfy the hypotheses in Theorem 3, we can choose $\varphi \in C^\infty_0(\Omega_g)$, such that $L_\varphi(t) = \Psi_\lambda(t\varphi) = t^2/2\|\varphi\|^2_{\lambda,V} - \int_{\Omega_g}(f(x)/q(x))|t\varphi|^{q(x)}dx - \int_{\Omega_g}(g(x)/p(x))|t\varphi|^{p(x)}dx$ have $t_0 > 0$ and C_8 which are independent of λ that satisfy $t_0\varphi \in \mathcal{N}^-_\lambda$ for all $\lambda > \lambda^*$ and

$$\sup_{t\ge 0} L_\varphi(t) = L_\varphi(t_0) = C_8 > 0, \tag{102}$$

which shows $c^-_\lambda \le C_8$ for all $\lambda > \lambda^*$.

Theorem 22. *Assume that the conditions (H_3), (H_4), and (V_1)-(V_5) are satisfied, then for all $\lambda > 1/kM^2 \mid \{V^+ < k\} \mid$, Ψ_λ has a minimizer u^-_λ in $\mathcal{N}^-_\lambda$ satisfying that*

$$\Psi_\lambda(u^-_\lambda) = c^-_\lambda; \tag{103}$$

(1) u^-_λ is a nontrivial solution of equation (1).

Proof. According to Lemma 14 and the Ekeland variational principle in [25], there exists $\{u_n\} \subset \mathcal{N}^-_\lambda$ such that $\{u_n\}$ is a $(PS)_{c^-_\lambda}$ sequence for Ψ_λ. Furthermore, using Lemma 10, we can get that $\{u_n\}$ is bounded in X_λ. Consequently, there exists a subsequence of $\{u_n\}$ (we still denote as $\{u_n\}$) and u^-_λ in X_λ such that

$$\begin{aligned} u_n &\rightharpoonup u^-_\lambda \text{ in } X_\lambda, \\ u_n &\to u^-_\lambda \text{ in } L^r_{loc}(\mathbb{R}^N), \text{ for } 2 \le r \le \infty. \end{aligned} \tag{104}$$

Besides, $\Psi'_\lambda(u^-_\lambda) = 0$. In view of Lemma 15, we know that $u_n \to u^-_\lambda$ in X_λ and $\Psi_\lambda(u^-_\lambda) = c^-_\lambda$. In other words, u^-_λ is a solution of equation (1).

Now, we will check that $u^-_\lambda \neq 0$. Suppose the contrary, combining (39), (40), Egoroff theorem, and (H_4), there holds

$\int_{\mathbb{R}^N} g(x)|u_n|^{p(x)}dx \to 0$ as $n \to \infty$, which shows that

$$\|u_n\|^2_{\lambda,V} = \int_{\mathbb{R}^N} f(x)|u_n|^{q(x)}dx + o(1)$$

$$\begin{aligned}\Psi_\lambda(u_n) &= \frac{1}{2}\|u_n\|^2_{\lambda,V} - \int_{\mathbb{R}^N}\frac{f(x)}{q(x)}|u_n|^{q(x)}dx - \int_{\mathbb{R}^N}\frac{g(x)}{p(x)}|u_n|^{p(x)}dx\\ &\le \frac{1}{2}\|u_n\|^2_{\lambda,V} - \frac{1}{q^+}\int_{\mathbb{R}^N} f(x)|u_n|^{q(x)}dx - \frac{1}{p^+}\int_{\mathbb{R}^N} g(x)|u_n|^{p(x)}dx\\ &= \frac{1}{2}\|u_n\|^2_{\lambda,V} - \frac{1}{q^+}\|u_n\|^2_{\lambda,V} + o(1) = \frac{q^+-2}{2q^+}\|u_n\|^2_{\lambda,V} + o(1)\\ &\le \frac{(q^+-2)(\vartheta_0-1)}{2q^+\vartheta_0}\|u_n\|^2_{\lambda,V} + o(1) \le 0.\end{aligned} \tag{105}$$

This is contradictive with $\lim_{n\to\infty}\Psi_\lambda(u_n) = c^-_\lambda > 0$. Hence, $u^-_\lambda \neq 0$; that is, u^-_λ is a nontrivial solution of equation (1).

Proof of Theorem 23. It derives from Theorem 20, Theorem 22, and Lemma 14 that equation (1) has two nontrivial solutions u^+_λ and u^-_λ such that $u^+_\lambda \in \mathcal{N}^+_\lambda$ and $u^-_\lambda \in \mathcal{N}^-_\lambda$ with $\Psi_\lambda(u^+_\lambda) = c^+_\lambda < 0 < C_5 < \Psi_\lambda(u^-_\lambda) = c^-_\lambda$.

Data Availability

Not applicable data and material.

Conflicts of Interest

The authors declare that there is no conflict of interests regarding the publication of this paper.

Authors' Contributions

All authors contributed equally to the manuscript and typed, read, and approved the final manuscript.

Acknowledgments

The authors expresses their gratitude to the referees for their valuable comments and suggestions which have led to a significant improvement on the presentation and quality of this paper. This work is supported by the Natural Science Foundation of Yunnan Province under grants 2018FE001(-136) and 2017zzx199, the National Natural Science Foundation of People's Republic of China under grants 11961078 and 11561072, the Yunnan Province, Young Academic and Technical Leaders Program (2015HB010), and the Natural Science Foundation of Yunnan Province under grant 2016FB011.

References

[1] S. Z. Mao and A. Xia, "Multiplicity results of nonlinear fractional magnetic Schrödinger equation with steep potential," *Applied Mathematics Letters*, vol. 97, pp. 73–80, 2019.

[2] M. Q. Xiang, B. L. Zhang, and D. Yang, "Multiplicity results for variable-order fractional Laplacian equations with variable growth," *Nonlinear Analysis*, vol. 178, pp. 190–204, 2019.

[3] M. Q. Xiang, D. Yang, and B. Zhang, "Homoclinic solutions for Hamiltonian systems with variable-order fractional derivatives," *Complex Variables and Elliptic Equations*, vol. 65, pp. 1412–1432, 2019.

[4] Y.-h. Cheng and T.-F. Wu, "Multiplicity and concentration of positive solutions for semilinear elliptic equations with steep potential," *Communications on Pure and Applied Analysis*, vol. 15, no. 6, pp. 2457–2473, 2016.

[5] S. Peng and A. Xia, "Multiplicity and concentration of solutions for nonlinear fractional elliptic equations with steep potential," *Communications on Pure & Applied Analysis*, vol. 17, no. 3, pp. 1201–1217, 2018.

[6] P. d'Avenia and M. Squassina, "Ground states for fractional magnetic operators," *ESAIM: Control, Optimisation and Calculus of Variations*, vol. 24, no. 1, pp. 1–24, 2018.

[7] V. Ambrosio and P. d'Avenia, "Nonlinear fractional magnetic Schrödinger equation: existence and multiplicity," *Journal of Differential Equations*, vol. 264, no. 5, pp. 3336–3368, 2018.

[8] M. Xiang, P. Pucci, M. Squassina, and B. Zhang, "Nonlocal Schrodinger-Kirchhoff equations with external magnetic field," *Discrete & Continuous Dynamical Systems - A*, vol. 37, pp. 1631–1649, 2017.

[9] A. Pinamonti, M. Squassina, and E. Vecchi, "The Maz'ya¨C-Shaposhnikova limit in the magnetic setting," *Journal of Mathematical Analysis and Applications*, vol. 449, no. 2, pp. 1152–1159, 2017.

[10] H.-M. Nguyen, A. Pinamonti, M. Squassina, and E. Vecchi, "Some characterizations of magnetic Sobolev spaces," *Complex Variables and Elliptic Equations*, vol. 65, no. 7, pp. 1104–1114, 2020.

[11] A. Pinamonti, M. Squassina, and E. Vecchi, "Magnetic BV-functions and the Bourgain-Brezis-Mironescu formula," *Advances in Calculus of Variations*, vol. 12, no. 3, pp. 225–252, 2019.

[12] H.-M. Nguyen, A. Pinamonti, M. Squassina, and E. Vecchi, "New characterizations of magnetic Sobolev spaces," *Advances in Nonlinear Analysis*, vol. 7, no. 2, pp. 227–245, 2018.

[13] X. Mingqi, V. D. Radulescu, and B. Zhang, "Fractional Kirchhoff problems with critical Trudinger Moser nonlinearity," *Calculus of Variations and Partial Differential Equations*, vol. 58, no. 2, p. 57, 2019.

[14] C. Ji, F. Fang, and B. L. Zhang, "A multiplicity result for asymptotically linear Kirchhoff equations," *Advances in Nonlinear Analysis*, vol. 8, pp. 267–277, 2019.

[15] X. Mingqi, V. D. Rădulescu, and B. Zhang, "Nonlocal Kirchhff problems with singular exponential nonlinearity," *Applied Mathematics and Optimization*, 2020.

[16] A. Fiscella, "A fractional Kirchhoff problem involving a singular term and a critical nonlinearity," *Advances in Nonlinear Analysis*, vol. 8, pp. 645–660, 2019.

[17] T. Bartsch and Z. Q. Wang, "Existence and multiplicity results for some superlinear elliptic problems on $\mathbb{R}^N$, Comm," *Partial Differential Equations*, vol. 20, no. 9-10, pp. 1725–1741, 1995.

[18] O. Kovacik and J. Bakosnik, "On spaces $L^{p(x)}$ and $W^{m,p(x)}$," *Czechoslovak Mathematical Journal*, vol. 41, pp. 592–618, 1991.

[19] X. Fan and D. Zhao, "On the spaces $L^{p(x)}(\Omega)$ and $W^{m,p(x)}(\Omega)$," *Journal of Mathematical Analysis and Applications*, vol. 263, pp. 424–446, 2001.

[20] L. Diening, P. Harjulehto, P. Hästö, and M. Růžička, *Lebesgue and Sobolev Spaces with Variable Exponents*, Springe-Verlag, Heidelberg, 2011.

[21] A. Fiscella, A. Pinamonti, and E. Vecchi, "Multiplicity results for magnetic fractional problems," *Journal of Differential Equations*, vol. 263, no. 8, pp. 4617–4633, 2017.

[22] S. I. Pohozaev, "An approach to nonlinear equations," *Proceedings of the USSR Academy of Sciences*, vol. 247, no. 6, pp. 1327–1331, 1979.

[23] P. Drabek and S. Pohozaev, "Positive solutions for thep-Laplacian: application of the fibrering method," *Proceedings of the Royal Society of Edinburgh*, vol. 127, no. 4, pp. 703–726, 1997.

[24] C. O. Alves and M. C. Ferreira, "Existence of solutions for a class of $p(x)$-Laplacian equations involving a concave-convex nonlinearity with critical growth in $\mathbb{R}^N$," *Topological Methods in Nonlinear Analysis*, vol. 45, no. 2, pp. 399–422, 2015.

[25] I. Ekeland, "On the variational principle," *Journal of Mathematical Analysis and Applications*, vol. 17, pp. 324–353, 1974.

Hindawi
Advances in Mathematical Physics
Volume 2020, Article ID 9708649, 10 pages
https://doi.org/10.1155/2020/9708649

Research Article

Hidden Multistability in a Memristor-Based Cellular Neural Network

Birong Xu,[1] **Hairong Lin**,[2] **and Guangyi Wang**[3]

[1]*College of Mechanic and Electronic Engineering, Wuyi University, Wuyishan 354300, China*
[2]*College of Computer Science and Electronic Engineering, Hunan University, Changsha 410082, China*
[3]*Institute of Modern Circuits and Intelligent Information, Hangzhou Dianzi University, Hangzhou 310018, China*

Correspondence should be addressed to Birong Xu; xubirong1@163.com

Received 18 July 2020; Revised 8 September 2020; Accepted 24 September 2020; Published 27 October 2020

Academic Editor: Zhi-Yuan Sun

In this paper, we report a novel memristor-based cellular neural network (CNN) without equilibrium points. Dynamical behaviors of the memristor-based CNN are investigated by simulation analysis. The results indicate that the system owns complicated nonlinear phenomena, such as hidden attractors, coexisting attractors, and initial boosting behaviors of position and amplitude. Furthermore, both heterogeneous multistability and homogenous multistability are found in the CNN. Finally, Multisim circuit simulations are performed to prove the chaotic characteristics and multistability of the system.

1. Introduction

The cellular neural network (CNN) was proposed by Chua and Yang in 1988 for processing signals in real time, which is constituted of an array of the basic circuit units called cells [1]. The CNN has received widespread attention in academia because of its extensive applications, such as image processing, parallel computation, and complicated optimization problems [2, 3]. Chua and Yang used CNN to realize image processing and pattern recognition [2]. For solving the constrained optimization problem, Shen et al. designed the utility-based radio resource scheduler by employing CNN [3]. Ref. [4] proposed a random weight change (RWC) algorithm to construct CNN weight and to make the hardware-based learning on CNN templates feasible. Based on a fuzzy cellular neural network (FCNN), an image encryption method was put forward in Ref. [5].

Ref. [6] further presented a state-controlled cellular neural network (SC-CNN), and a generalized Chua's circuit is constructed by three SC-CNN cells. A Colpitts-like oscillator also is implemented by SC-CNN [7]. An SC-CNN-based circuit could produce strange nonchaotic attractors in Ref. [8].

With the advent of memristors, many types of artificial neural networks have been improved by memristors, such as Cellular neural network (CNN) and Hopfield neural network (HNN) [9–20]. The research on CNN mainly lies in its application [10–12]. A memristor-based CNN was presented in Ref. [9], which could generate chaotic attractors and whose chaotic behaviors were studied. However, a memristor-based CNN without equilibrium points is never proposed. Therefore, a memristor-based CNN without equilibrium points is introduced in this paper, and its dynamical behaviors are investigated. The memristor-based CNN not only has chaotic features but also shows multistability.

To explore multistability, initial boosting behaviors and attractor coexistence are investigated. Since the memory devices depend on its history, initial boosting behaviors were found in some memristor-based or meminductor-based systems [21–23]. Ref. [21] employed a memristor with sine memductance to construct a memristive jerk system. This novel memristive jerk system had four line equilibrium sets and periodical initial boosting. In Ref. [22], a memristor-meminductor system was presented, which produced the amplitude, frequency, and position boosting. These systems have infinitely many equilibrium points. The initial boosting behaviors of a memristor-based system without equilibrium points are not put forward. Hence, we study the initial boosting behaviors in this memristor-based CNN. Moreover,

multistability is divided into heterogeneous multistability and homogenous multistability [22, 24]. This multistability is heterogeneous multistability if there exist coexisting attractors with different shapes. In contrast, the system owns homogenous multistability if it generates the same shape coexisting attractors with different positions and amplitudes or even frequencies.

This paper is organized as follows: Section 2 proposes the model of a novel memristive neural network. Its nonlinear dynamics is presented in Section 3, while its circuital implementation is completed in Section 4. Finally, conclusions are drawn in the last section.

2. A Memristor-Based Cellular Neural Network

The standard SC-CNN cell is defined as [6]

$$\dot{x}_i = -x_i + \sum_{k=1}^{n} a_{ik} y_k + \sum_{k=1}^{n} s_{ik} x_k + i_k, \tag{1}$$

where x_i and x_k are the state variables and always are the voltage of capacitors, y_k is the output variable, i_k is the independent current source, a_{ik} and s_{ik} are the feedback coefficient and state coefficient, respectively. A memristor-based cellular neural network is presented, which consists of one memristor-based CNN cell and two standard SC-CNN cells. The memristor-based CNN cell is shown as Figure 1, from which the state equation is obtained as

$$\begin{aligned} \dot{x}_i &= -M(\varphi) x_i + \sum_{k=1}^{n} s_{ik} x_k, \\ \dot{\varphi} &= x_i, \end{aligned} \tag{2}$$

where a memristor is select as [25]

$$\begin{aligned} M(\varphi) &= \frac{dq(\varphi)}{d\varphi} = a\varphi^2 + b\varphi + c, \\ \varphi &= v. \end{aligned} \tag{3}$$

The memristor-based CNN cell is selected as the first cell, while the second and third ones are the standard SC-CNN cells. The state variables of two standard SC-CNN cells are independent of the output variable, and the state variable of the second cell does not relate to the independent current source. Therefore, the proposed CNN can be expressed as

$$\begin{aligned} \dot{x}_1 &= -\left(a\varphi^2 + b\varphi + c\right) x_1 + s_{11} x_1 + s_{12} x_2 + s_{13} x_3, \\ \dot{x}_2 &= -x_2 + s_{21} x_1 + s_{22} x_2 + s_{23} x_3, \\ \dot{x}_3 &= -x_3 + s_{31} x_1 + s_{32} x_2 + s_{33} x_3 + i_3, \\ \varphi &= x_1. \end{aligned} \tag{4}$$

In order to better explore the feature of the memristor-based CNN, we let three cells own different numbers of state variables. Set $s_{11} = s_{12} = s_{21} = 0$, Equation (4) can be simplified as

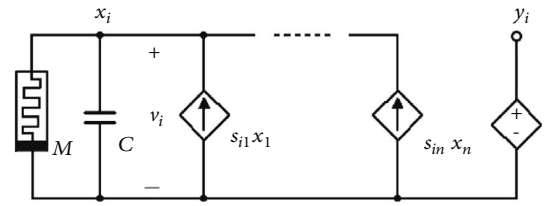

Figure 1: A memristor-based CNN cell.

$$\begin{aligned} \dot{x}_1 &= -\left(a\varphi^2 + b\varphi + c\right) x_1 + s_{13} x_{32}, \\ x_2 &= -x_2 + s_{22} x_2 + s_{23} x_3, \\ x_3 &= -x_3 + s_{31} x_1 + s_{32} x_2 + s_{33} x_3 + i_3, \\ \varphi &= x_1. \end{aligned} \tag{5}$$

Obviously, if $i_3 = 0$, the equilibrium point of the CNN is a line equilibrium set $O(0, 0, 0, \varphi)$. When $s_{11} = s_{12} = s_{21} = 0$, $s_{13} = 7$, $s_{22} = 1.75$, $s_{23} = -1.1$, $s_{31} = -1.3$, $s_{32} = 1.1$, $s_{33} = 0.85$, $a = 20$, $b = -10$, $c = -6$, and the initial condition is $(0.1,0, 0.1,0.3)$, the eigenvalues are $\lambda_1 = 0$, $\lambda_{2.3} = 1.0455 \pm j1.2192$, and $\lambda_4 = 5.7089$. Thereby, the equilibrium of the CNN is an unstable saddle-focus equilibrium.

If $i_3 \neq 0$ and $s_{22} \neq 1$, it is easy to see that the neural network is a system without equilibrium. This case will be analyzed below. When $s_{11} = s_{12} = s_{21} = 0$, $s_{13} = 7$, $s_{22} = 1.75$, $s_{23} = -1.1$, $s_{31} = -1.3$, $s_{32} = 1.1$, $s_{33} = 0.85$, $a = 20$, $b = -10$, $c = -6$, $i_3 = -0.0001$, and the initial condition is chosen as $(0.1,0, 0.1,0.3)$; the Lyapunov exponent is obtained as LE 1 = 0.16, LE2 = 0, LE3 = 0, and LE4 = −27.23. The CNN is in a chaotic state, whose chaotic attractor and Poincaré mapping are exhibited in Figures 2 and 3, respectively. Since the memristor-based CNN in this case has no equilibrium points, this chaotic attractor is a hidden attractor.

3. Dynamics of the Memristor-Based Neural Network

3.1. Influence of the Parameter of the System. In a survey of the dynamical behaviors of the memristor-based CNN, with the parameter a increasing from 9 to 50, and the other parameters and the initial condition set as in Section 2, the Lyapunov exponent spectrum is shown in Figure 4(a), where LE1-3 represent the first three Lyapunov exponents, and the fourth Lyapunov exponent is neglected owing to its large negative value; the corresponding bifurcation diagram is depicted in Figure 4(b). From Figure 4(a), it is easy to observe that the memristor-based CNN keeps a chaotic state. Figure 4(b) shows that the amplitude of x_1 reduces nonlinearly with the increase of a.

3.2. Attractor Coexistence of the Memristor-Based CNN. The memristor-based CNN not only possesses hidden chaotic attractors but also exhibits the phenomenon of attractor coexistence. Setting $s_{11} = s_{12} = s_{21} = 0$, $s_{22} = 1.75$, $s_{23} = -1.1$, $s_{31} = -1.3$, $s_{32} = 1.1$, $s_{33} = 0.85$, $a = 20$, $b = -10$, $c = -6$ and $i_3 = -0.0001$, and varying s_{13}, the phenomenon of attractor coexistence is depicted in Figure 5, where the blue orbits start

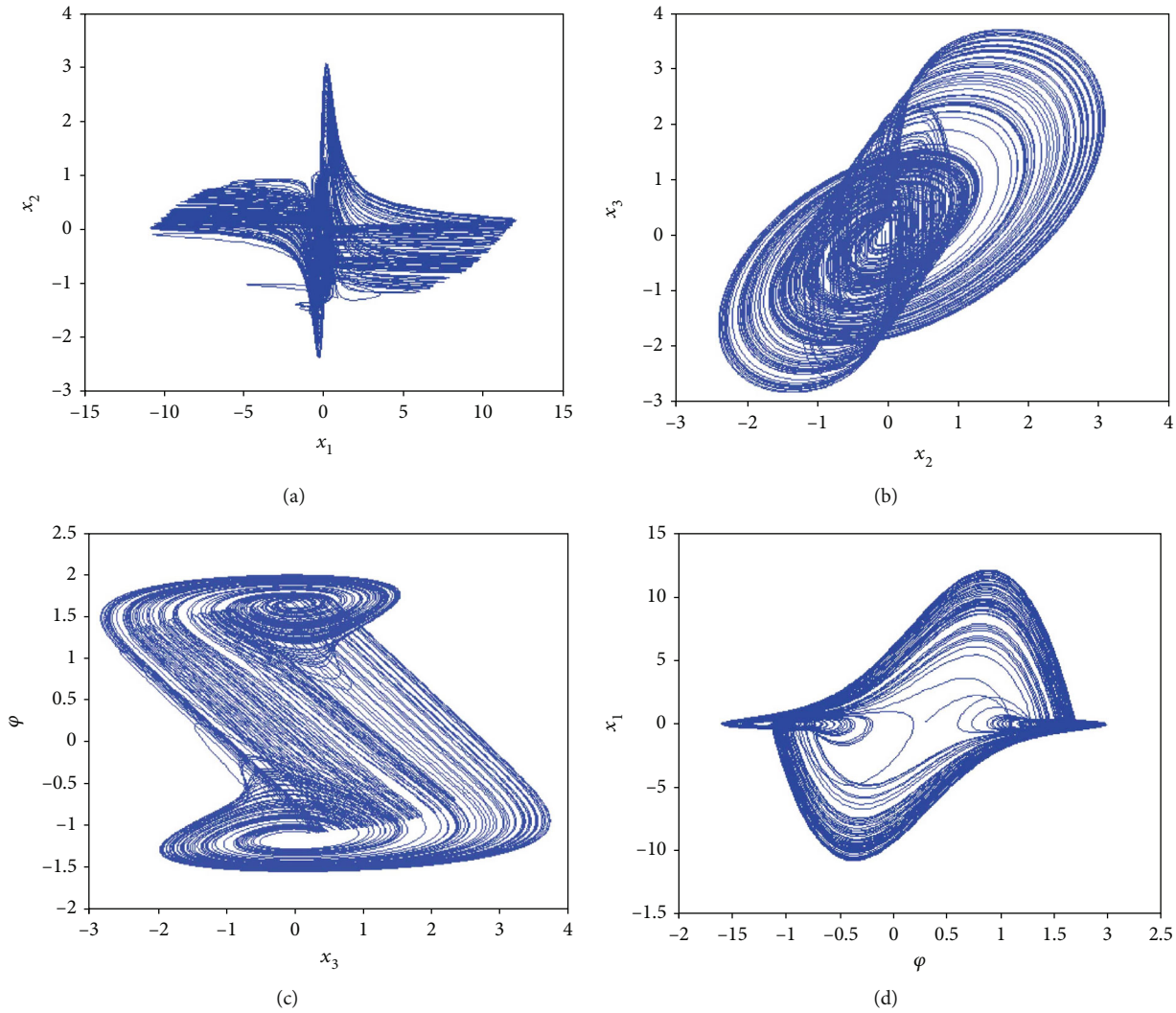

Figure 2: Chaotic attractors of the memristor-based CNN. (a) x_1-x_2 phase diagram, (b) x_2-x_3 phase diagram, (c) x_3-φ phase diagram, and (d) φ-x_1 phase diagram.

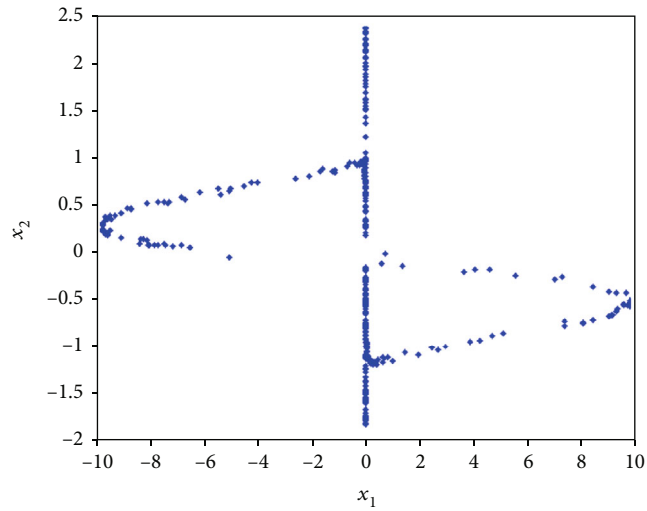

Figure 3: Poincaré map on $x_3 = 0$.

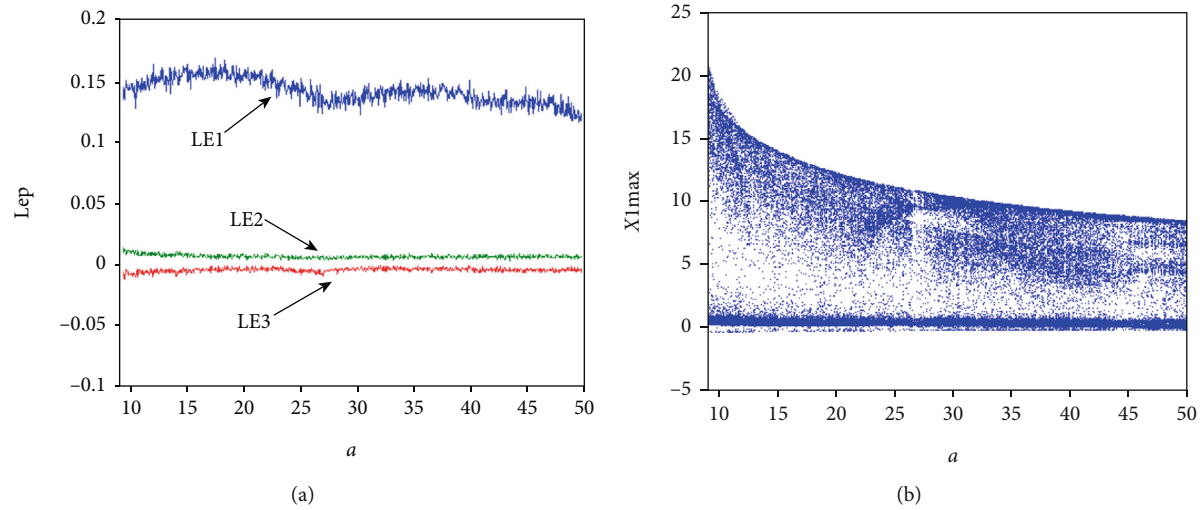

Figure 4: Lyapunov exponent spectrum and bifurcation diagram with respect to a: (a) Lyapunov exponent spectrum and (b) bifurcation diagram.

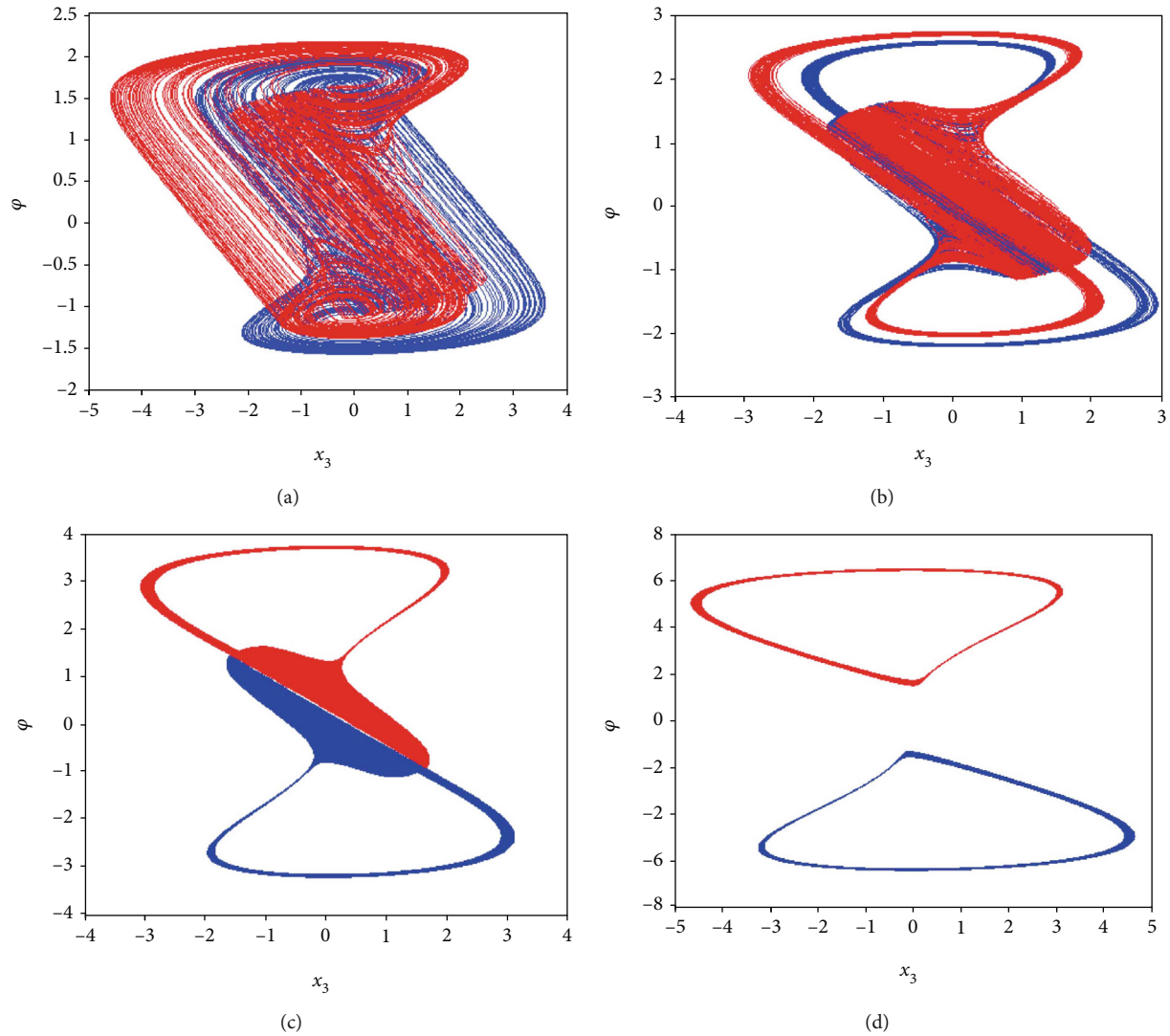

Figure 5: Coexisting attractors on the x_3-φ plane with different s_{13} under the initial conditions of (0.1,0, 0.1, 0.3) (blue) and (0, 0, 0.3,0) (red): (a) coexisting chaotic attractors with $s_{13} = 7$, (b) coexisting chaotic attractors with $s_{13} = 20$, (c) coexisting periodic attractors with $s_{13} = 50$, and (d) coexisting periodic attractors with $s_{13} = 200$.

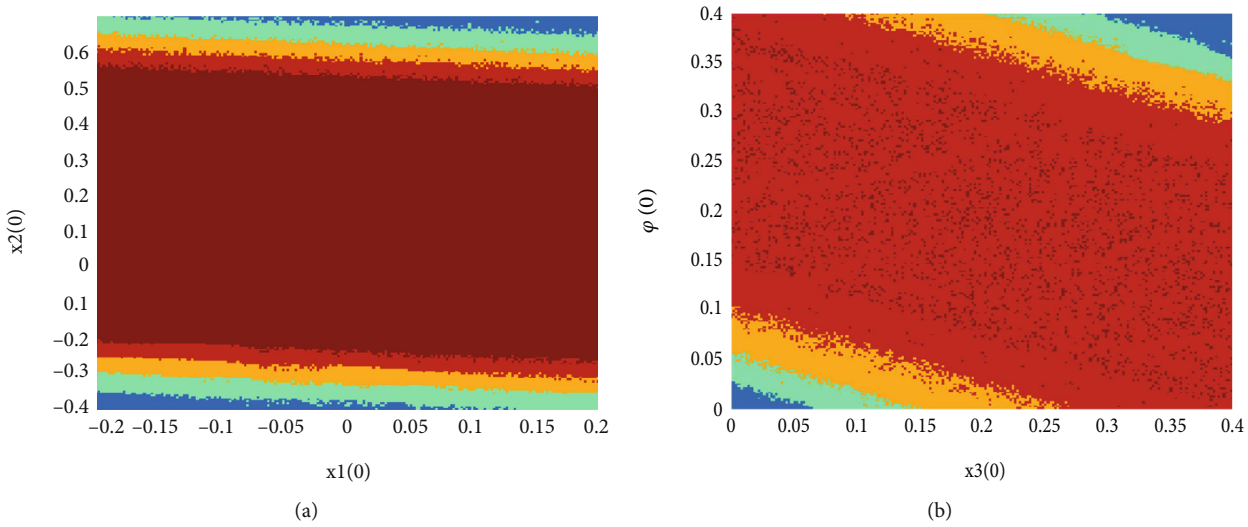

Figure 6: Attractive basins on the cross-section of $s_{11} = s_{12} = s_{21} = 0$, $s_{13} = 7$, $s_{22} = 1.75$, $s_{23} = -1.1$, $s_{31} = -1.3$, $s_{32} = 1.1$, $s_{33} = 0.85$, $a = 20$, $b = -10$, $c = -6$, and $i_3 = -0.0001$: (a) the attractive basin in the cross-section of $x_3(0) = 0.1$ and $\varphi(0) = 0.3$ and (b) the attractive basin in the cross-section of $x_1(0) = 0.1$ and $x_2(0) = 0$.

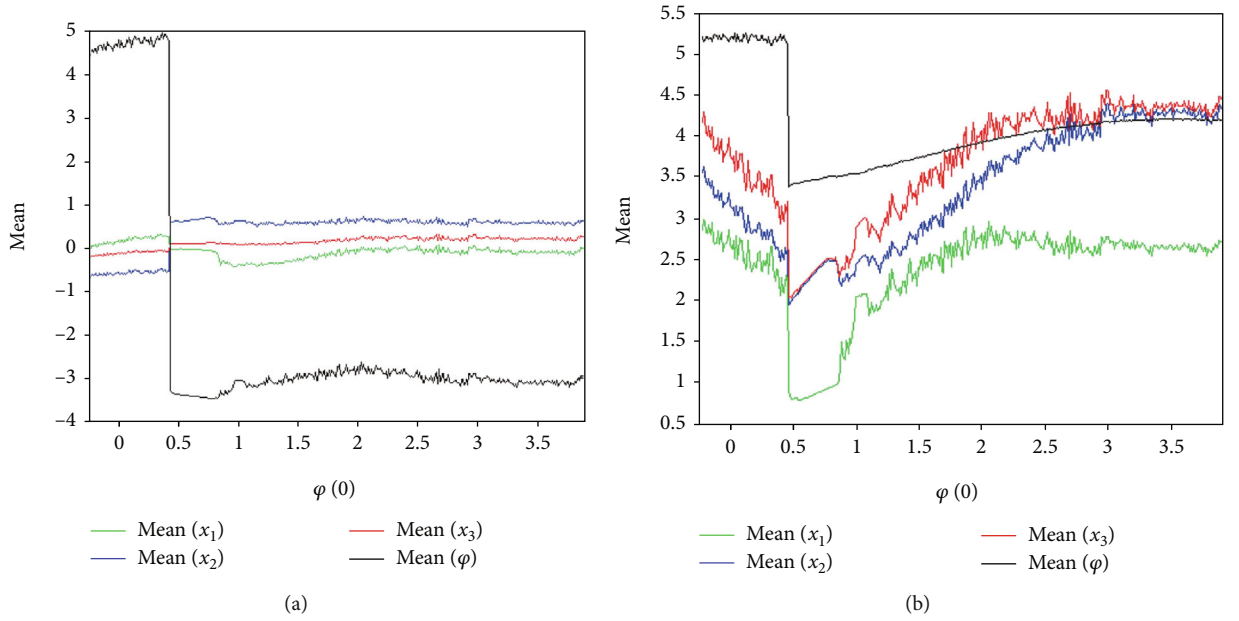

Figure 7: Initial boosting behaviors of position and amplitude with respect to $\varphi(0)$: (a) initial boosting behaviors of position and (b) initial boosting behaviors of amplitude.

from the initial condition of $(0.1, 0, 0.1, 0.3)$, the red ones from the initial condition of $(0, 0, 0.3, 0)$. The coexisting chaotic attractors are observed at $s_{13} = 7$ and 20, whereas the coexisting attractors are periodic at $s_{13} = 50$ and 200. The distance of the periodic attractors increases with the increase of s_{13}. Moreover, since the memristor-based CNN has coexisting attractors with different shapes, it owns heterogeneous multistability.

Coexisting attractors illustrate that the memristor-based CNN has multistability. To explore its multistability nature, the attractive basins are drawn in Figure 6. Figure 6(a) is the attractive basin in the cross-section of $x_3(0) = 0.1$ and $\varphi(0) = 0.3$, and the other is in the cross-section of $x_1(0) = 0.1$ and $x_2(0) = 0$. There are multiple colors in the given value region, which implies several different types of attractors.

3.3. Initial Boosting Behaviors of Position and Amplitude. Initial boosting behavior is a kind of special phenomenon of multistability. Initial boosting behaviors of position and amplitude reveal the attractor's position and amplitude changing with the initial conditions, respectively. When the parameters are chosen as $s_{11} = s_{12} = s_{21} = 0$, $s_{13} = 8$, $s_{22} = 1.6$, $s_{23} = -1.1$, $s_{31} = -1.3$, $s_{32} = 1.1$, $s_{33} = 0.85$, $a = 1.9$, $b = -3.5$, $c = -6$, and $i_3 = -0.0001$, the initial boosting behaviors are depicted in Figure 7, where the initial conditions are$(0, -0.1, 0, \varphi(0))$. From Figure 7(a), the initial boosting

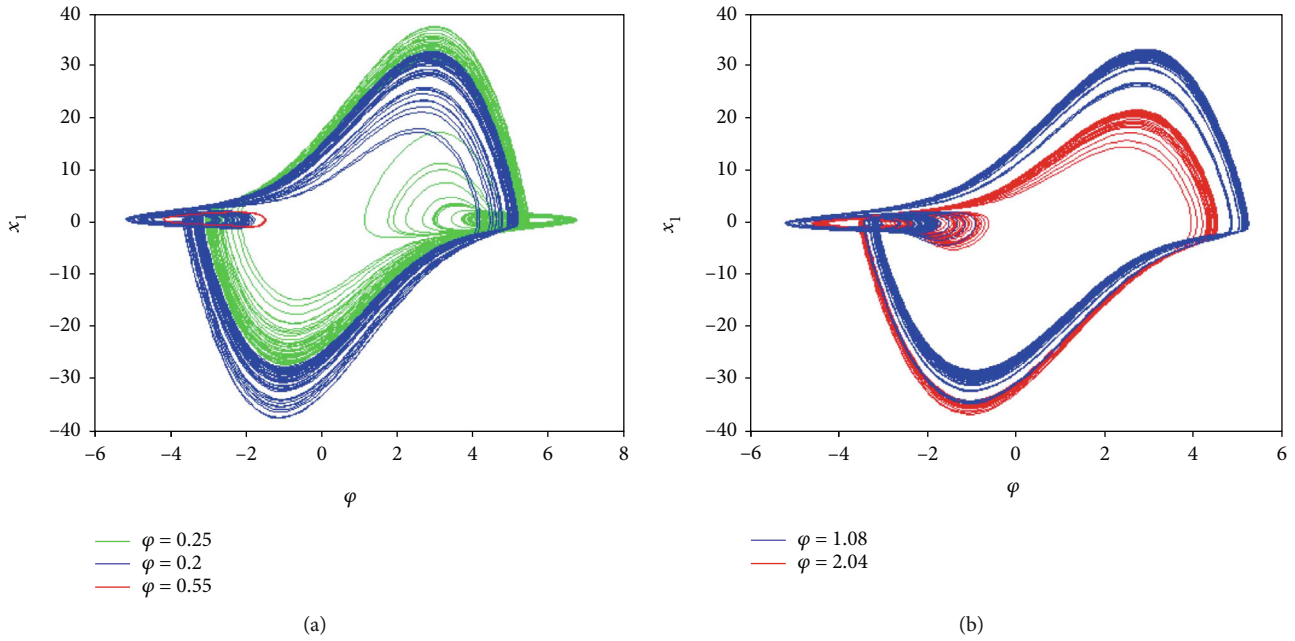

Figure 8: Multistability of the memristor-based CNN: (a) heterogeneous multistability and (b) homogenous multistability.

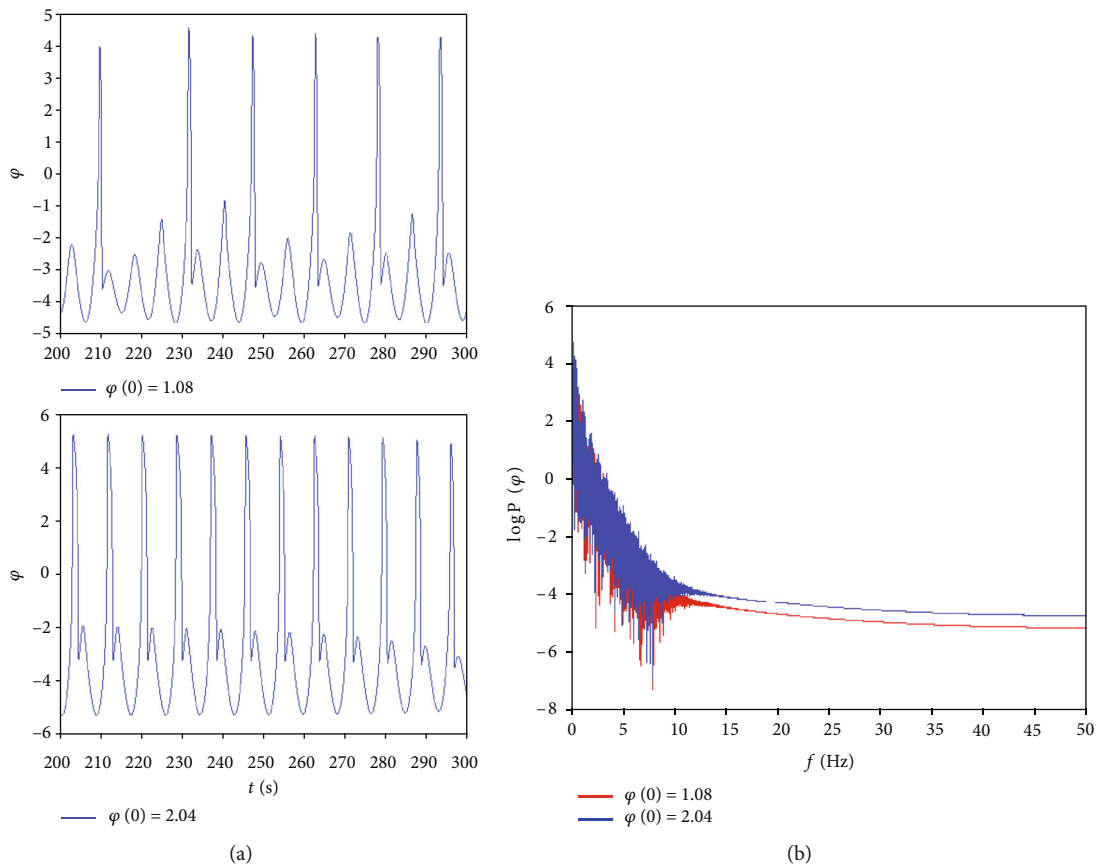

Figure 9: Time-domain waveforms and frequency spectra of the chaotic signals with $\varphi(0) = 1.08$ and 2.04: (a) time-domain waveforms and (b) frequency spectra.

behaviors of position can be observed. The mean values of the variables x_1 and φ nonlinearly increase, while the other mean values almost do not change, in the range of $\varphi(0) \in [-0.25, 0.44]$. When the offset boosting controller is $\varphi(0) = 0.44$, there exists a jump for all the mean values. In the region of $\varphi(0) \in (0.44, 3.9]$, the mean values of the

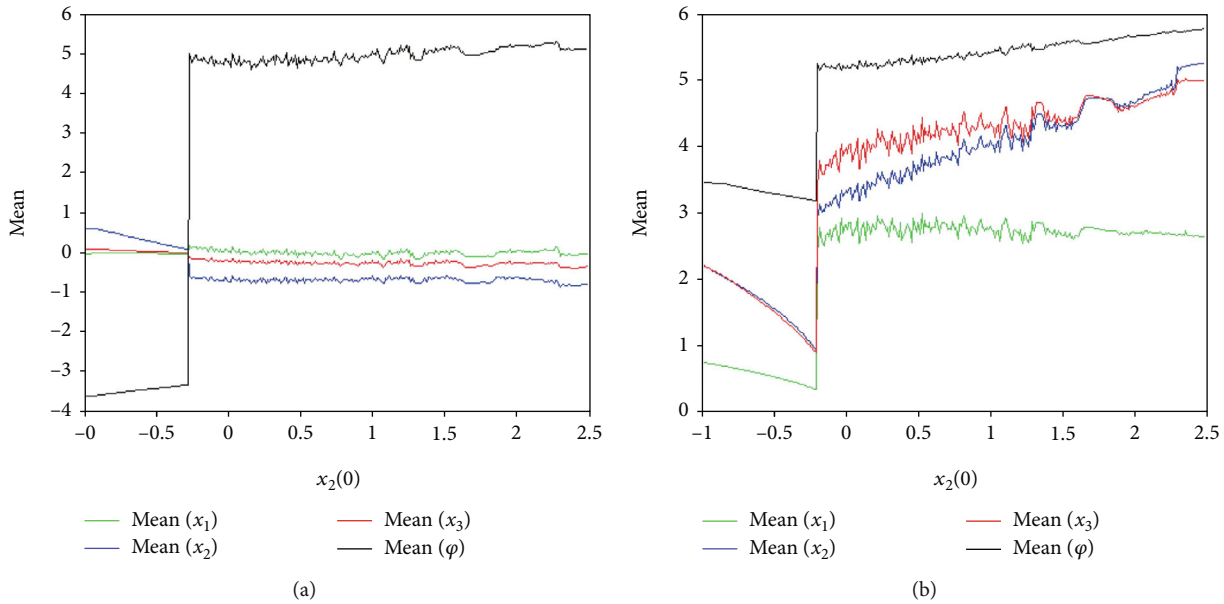

FIGURE 10: Initial boosting behaviors of position and amplitude with respect to $x_2(0)$: (a) initial boosting behaviors of position induced by $x_2(0)$ and (b) initial boosting behaviors of amplitude induced by $x_2(0)$.

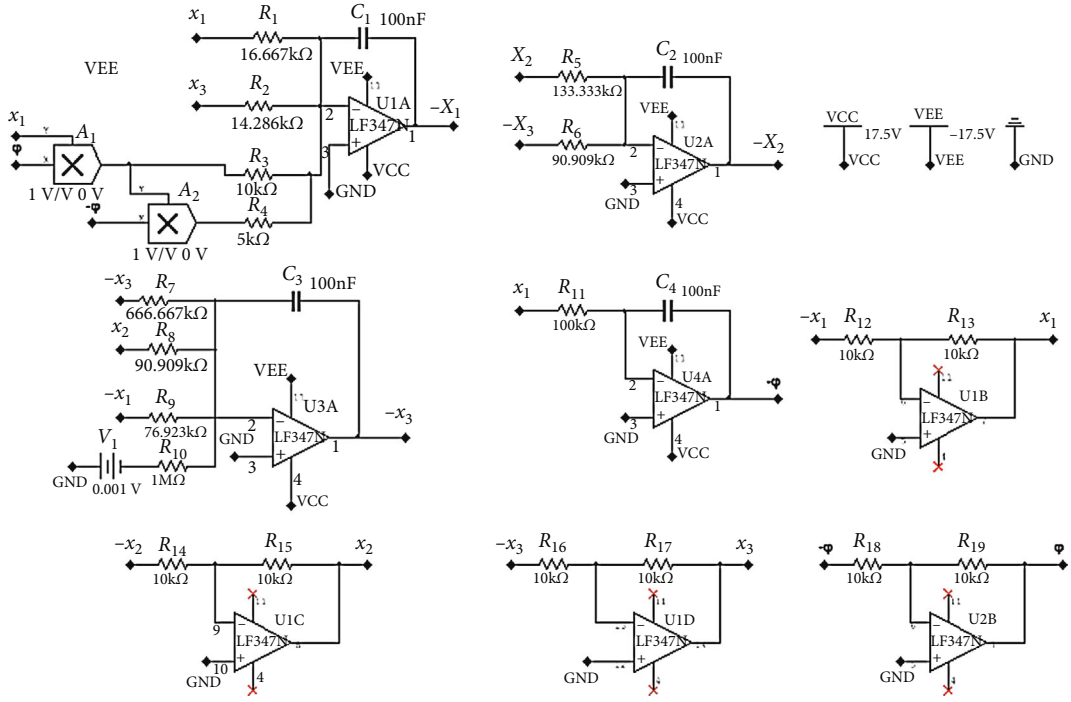

FIGURE 11: Equivalent circuit of the memristor-based CNN without equilibrium points.

variables $x(1)$ and φ irregularly change, whereas the mean values of the variables x_2 and x_3 still hardly change. Obviously, the route differs from Refs. [21–23].

Moreover, the initial variable $\varphi(0)$ is not only the booster of position but also of amplitude. The initial boosting behaviors of amplitude are shown in Figure 7(b). We can divide the figure into two parts. In the first part $(-0.25, 0.44]$, the mean absolute value of the variable φ almost keeps unchanged, but the other values nonlinearly decrease; in the second part $(0.44, 2.5]$, all the mean absolute values increase. When the initial value $\varphi(0)$ is 0.44, all the mean absolute values have a jump, which is the same as the mean values.

For better illustrating the offset boosting, several coexisting attractors are plotted in Figure 8, whose positions and amplitudes are related to the initial variable $\varphi(0)$. From Figure 8(a), three attractors with different shapes are observed, including two chaotic attractors and one periodic attractor, and thus, this system has heterogeneous

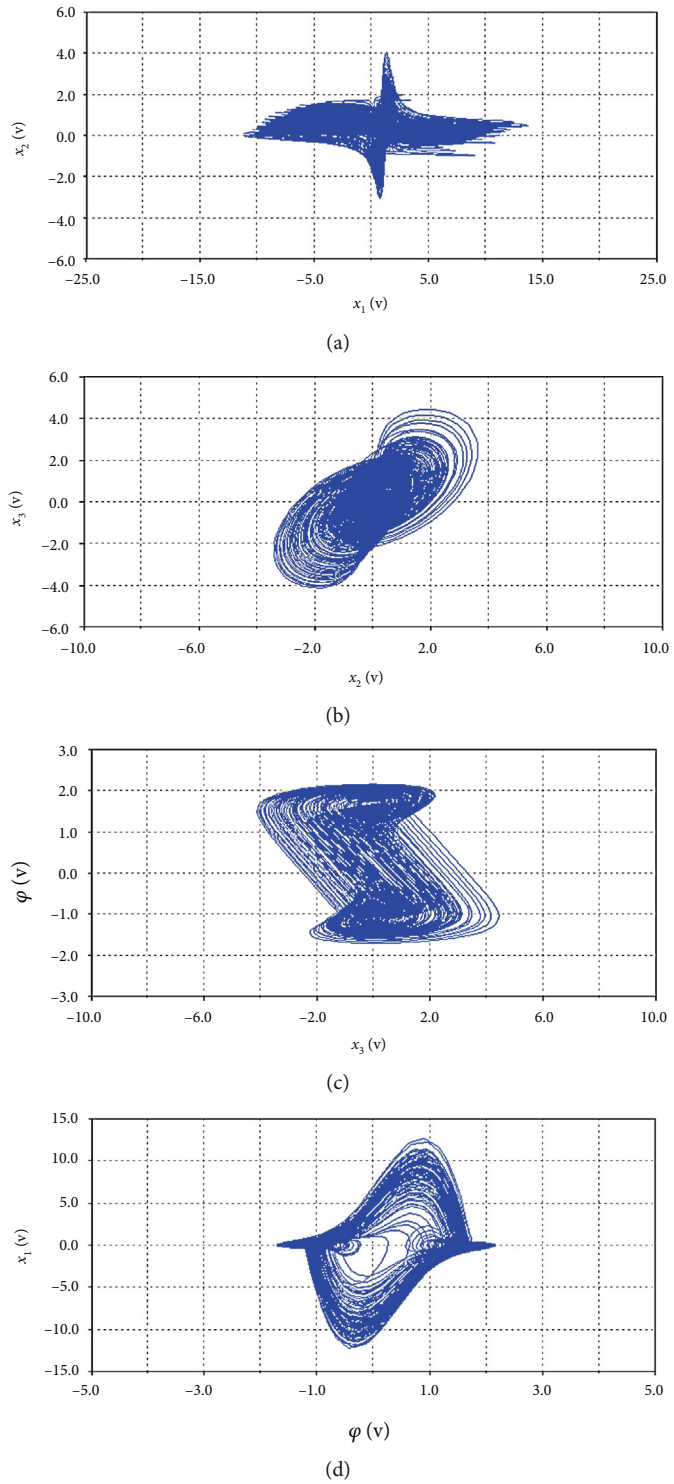

Figure 12: Experimental chaotic orbit: (a) x_1-x_2 phase diagram, (b) x_2-x_3 phase diagram, (c) x_3-φ phase diagram, and (d) φ-x_1 phase diagram.

multistability. Comparing with Figure 8(a), Figure 8(b) shows the same shape attractors with different positions and amplitudes as shown in Figure 7. Furthermore, if the ODE45 method with the time span [0,500] is used to solve Equation (5), the time-domain waveforms of $\varphi(t)$ are shown in Figure 9(a), illustrating different frequencies with different initial variable $\varphi(0)$. The corresponding frequency spectra of the chaotic signals are depicted in Figure 9(b). Therefore, the multistability is homogenous multistability. This memristor-based CNN owns not only heterogeneous multistability but also homogenous multistability.

The initial variable $\varphi(0)$ is an offset impact factor, but not only. Fixing the parameters, when the initial conditions are set as $(0, x_2(0), 0, 0)$, the initial boosting behaviors of position

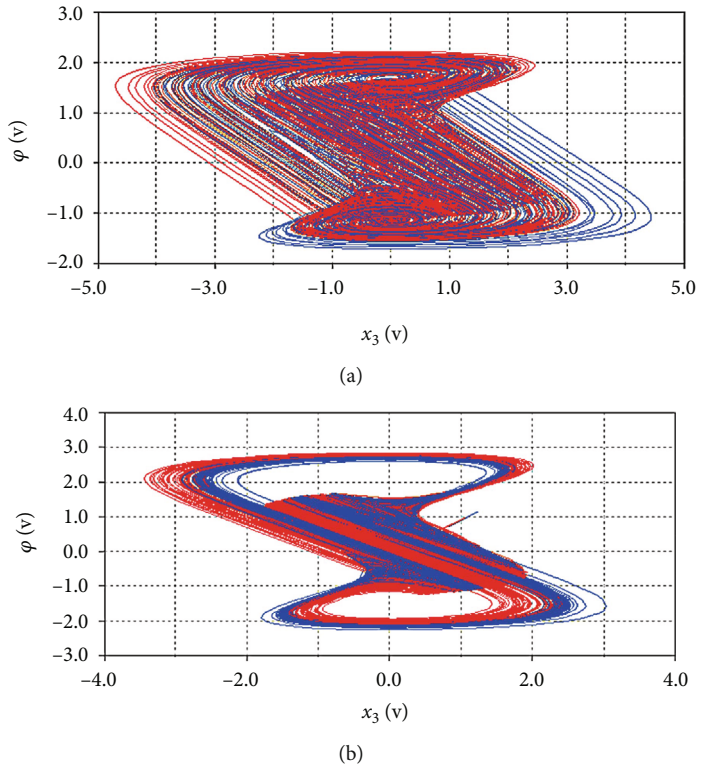

Figure 13: Experimental coexisting attractors: (a) $R_2 = 14.286\,\text{k}\Omega$ and (b) $R_2 = 5\,\text{k}\Omega$.

and amplitude are shown in Figure 10. From Figure 10, it is clear to see that the offset adjuster $x_2(0)$ also can control the attractor's position and amplitude, but this change process is different from the offset adjuster $\varphi(0)$.

4. Circuit Design and Experiment Result

The memristive CNN can be implemented by the circuit. When the parameters are chosen as $s_{11} = s_{12} = s_{21} = 0$, $s_{13} = 7$, $s_{22} = 1.75$, $s_{23} = -1.1$, $s_{31} = -1.3$, $s_{32} = 1.1$, $s_{33} = 0.85$, $a = 20$, $b = -10$, $c = -6$, and $i_3 = -0.0001$, and as we introduce the time scale factor $K = 100$, the circuit is established as Figure 11. Let $R = 100\,\text{k}\Omega$, and the state equations are yielded as

$$\begin{cases} \dot{x}_1 = \dfrac{1}{RC_1}\left[-\left(\dfrac{R}{R_4}\varphi^2 + \dfrac{R}{R_3}\varphi + c\right)x_1 + \left(\dfrac{R}{R_1} + c\right)x_1 + \dfrac{R}{R_2}x_3\right], \\ \dot{x}_2 = \dfrac{1}{RC_2}\left[\dfrac{R}{R_5}x_2 - \dfrac{R}{R_6}x_3\right], \\ \dot{x}_3 = \dfrac{1}{RC_3}\left[\dfrac{R}{R_9}x_1 + \dfrac{R}{R_8}x_2 - \dfrac{R}{R_7}x_1 - \dfrac{R}{R_{10}}V_1\right], \\ \dot{\varphi} = \dfrac{1}{R_1C_4}x_1. \end{cases} \tag{6}$$

Employing Multisim to simulate the circuit, the experimental results show that the circuit is in chaos as Figure 12. By giving different initial values and changing the value of the resistor R_2, the phenomenon of coexisting attractors is obtained as shown in Figure 13. With the resistor $R_2 = 14.286\,\text{k}\Omega$, the coexisting attractors in Figure 13(a) are caught by the oscilloscope of Multisim. The red orbit comes from the initial value of $(0.1\,\text{V}, 0, 0.1\,\text{V}, 0.5\,\text{V})$, while the blue one comes from the initial value of $(0, 0, 0.1\,\text{V}, 0)$. When the resistor R_2 is selected as $5\,\text{k}\Omega$, Figure 13(b) demonstrates the other phenomenon of attractor coexistence.

5. Conclusions

In this paper, we introduce a memristor-based CNN without equilibrium points, which contains a memristor-based CNN cell and two standard SC-CNN cells. By analyzing its dynamical behaviors, the coexisting hidden attractors are found. More interestingly, heterogeneous multistability and homogenous multistability are observed in the CNN. The presented system owns initial boosting behaviors of position and amplitude. Then, the equivalent circuit of the memristor-based CNN is designed, with which its chaotic and multistable characteristic is verified. Owing to its rich dynamical characteristics, the memristor-based CNN can be utilized in the information encryption field.

Data Availability

The data used to support the findings of this study are included within the article.

Conflicts of Interest

The authors declare no potential conflicts of interest with respect to the research, authorship, and/or publication of this article.

Acknowledgments

This work is supported in part by the National Natural Science Foundation of China (Grant Nos. 61771176 and 61271064), the Natural Science Foundation of Fujian Province (Grant No. 2016J01761), and the Natural Science Foundation of Zhejiang Province (Grant No. LY18F010012).

References

[1] L. O. Chua and L. Yang, "Cellular neural networks: theory," *IEEE Transactions on circuits and systems*, vol. 35, no. 10, pp. 1257–1272, 1988.

[2] L. O. Chua and L. Yang, "Cellular neural networks: applications," *EEE Transactions on Circuits and Systems*, vol. 35, no. 10, pp. 1273–1290, 1988.

[3] S. Shen, C. Chang, and L. Wang, "A cellular neural network and utility-based radio resource scheduler for multimedia CDMA communication systems," *IEEE transactions on wireless communications*, vol. 8, no. 11, pp. 5508–5519, 2009.

[4] S. P. Adhikari, H. Kim, C. Yang, and L. O. Chua, "Building cellular neural network templates with a hardware friendly learning algorithm," *Neurocomputing*, vol. 312, pp. 276–284, 2018.

[5] K. Ratnavelu, M. Kalpana, P. Balasubramaniam, K. Wong, and P. Raveendran, "Image encryption method based on chaotic fuzzy cellular neural networks," *Signal Processing*, vol. 140, pp. 87–96, 2017.

[6] P. Arena, L. Fortuna, S. Baglio, and G. Manganaro, "Simplified scheme for realisation of Chua oscillator by using SC-CNN cells," *Electronics Letters*, vol. 31, no. 21, pp. 1794-1795, 1995.

[7] P. Arena, S. Baglio, L. Fortuna, and G. Manganaro, "How state controlled CNN cells generate the dynamics of the Colpitts-like oscillator," *IEEE Transactions on Circuits and Systems I: Fundamental Theory and Applications*, vol. 43, no. 7, pp. 602–605, 1996.

[8] P. M. Ezhilarasu, M. Inbavalli, K. Murali, and K. Thamilmaran, "Strange non-chaotic attractors in a state controlled-cellular neural network-based quasiperiodically forced MLC circuit," *Pramana – Journal of Physics*, vol. 91, no. 1, 2018.

[9] Z. Li, Y. Zeng, and Z. Li, "Memristive chaotic circuit based on modified SC-CNNs," *Acta Physica Sinica*, vol. 63, no. 1, article 010502, 2014.

[10] S. Duan, X. Hu, Z. Dong, L. Wang, and P. Mazumder, "Memristor-based cellular nonlinear/neural network: design, analysis, and applications," *IEEE transactions on neural networks and learning systems*, vol. 26, no. 6, pp. 1202–1213, 2015.

[11] S. Duan, X. Hu, L. Wang, S. Gao, and C. Li, "Hybrid memristor/RTD structure-based cellular neural networks with applications in image processing," *Neural Computing and Applications*, vol. 25, no. 2, pp. 291–296, 2014.

[12] X. Hu, G. Feng, S. Duan, and L. Liu, "A memristive multilayer cellular neural network with applications to image processing," *IEEE transactions on neural networks and learning systems*, vol. 28, no. 8, pp. 1889–1901, 2017.

[13] M. Zheng, L. Li, H. Peng et al., "Finite-time stability and synchronization of memristor-based fractional-order fuzzy cellular neural networks," *Communications in Nonlinear Science and Numerical Simulation*, vol. 59, pp. 272–291, 2018.

[14] C. Chen, J. Chen, H. Bao, M. Chen, and B. Bao, "Coexisting multi-stable patterns in memristor synapse-coupled Hopfield neural network with two neurons," *Nonlinear Dynamics*, vol. 95, no. 4, pp. 3385–3399, 2019.

[15] F. Parastesh, S. Jafari, H. Azarnoush, B. Hatef, H. Namazi, and D. Dudkowski, "Chimera in a network of memristor-based Hopfield neural network," *The European Physical Journal Special Topics*, vol. 228, no. 10, pp. 2023–2033, 2019.

[16] J. Yang, L. Wang, Y. Wang, and T. Guo, "A novel memristive Hopfield neural network with application in associative memory," *Neurocomputing*, vol. 227, pp. 142–148, 2017.

[17] A. Wu, J. Zhang, and Z. Zeng, "Dynamic behaviors of a class of memristor-based Hopfield networks," *Physics Letters A*, vol. 375, no. 15, pp. 1661–1665, 2011.

[18] H. Lin and C. Wang, "Influences of electromagnetic radiation distribution on chaotic dynamics of a neural network," *Applied Mathematics and Computation*, vol. 369, article 124840, 2020.

[19] H. Lin, C. Wang, W. Yao, and Y. Tan, "Chaotic dynamics in a neural network with different types of external stimuli," *Communications in Nonlinear Science and Numerical Simulation*, vol. 90, article 105390, 2020.

[20] H. Lin, C. Wang, Y. Tan, and Y. Tan, "Hidden extreme multistability with hyperchaos and transient chaos in a Hopfield neural network affected by electromagnetic radiation," *Nonlinear Dynamics*, vol. 99, no. 3, pp. 2369–2386, 2020.

[21] H. Wu, Y. Ye, M. Chen, Q. Xu, and B. Bao, "Periodically switched memristor initial boosting behaviors in memristive hypogenetic jerk system," *IEEE Access*, vol. 7, pp. 145022–145029, 2019.

[22] F. Yuan, Y. Deng, Y. Li, and G. Wang, "The amplitude, frequency and parameter space boosting in a memristor meminductor-based circuit," *Nonlinear Dynamics*, vol. 96, no. 1, pp. 389–405, 2019.

[23] H. Wu, Y. Ye, B. Bao, M. Chen, and Q. Xu, "Memristor initial boosting behaviors in a two-memristor-based hyperchaotic system," *Chaos, Solitons & Fractals*, vol. 121, pp. 178–185, 2019.

[24] C. Li, W. Joo-Chen Thio, H. Ho-Ching Iu, and T. Lu, "A memristive chaotic oscillator with increasing amplitude and frequency," *IEEE Access*, vol. 6, pp. 12945–12950, 2018.

[25] W. Liu, F. Q. Wang, and X. K. Ma, "A unified cubic flux-controlled memristor: theoretical analysis, simulation and circuit experiment," *International Journal of Numerical Modelling: Electronic Networks, Devices and Fields*, vol. 28, no. 3, pp. 335–345, 2015.

Hindawi
Advances in Mathematical Physics
Volume 2020, Article ID 1289316, 11 pages
https://doi.org/10.1155/2020/1289316

Research Article

On Analytical Solution of a Plasma Flow over a Moving Plate under the Effect of an Applied Magnetic Field

Taha Zakaraia Abdel Wahid[1] **and Adel M. Morad**[1,2]

[1]*Department of Mathematics and Computer Science, Faculty of Science, Menoufia University, Shebin El-Kom 32511, Egypt*
[2]*Department of Computational Mathematics and Mathematical Physics, Institute of Mathematics, Mechanics and Computer Science, Southern Federal University, Rostov on Don 344090, Russia*

Correspondence should be addressed to Taha Zakaraia Abdel Wahid; taha_zakaraia@yahoo.com

Received 10 July 2020; Accepted 29 September 2020; Published 22 October 2020

Academic Editor: Xin Yu

Our objective of this investigation is to mainly focus on the behavior of a plasma gas that is bounded by a moving rigid flat plate; its motion is damping with time. The effects of an external magnetic field on the electrons collected with each other, with positive ions, and with neutral atoms in the plasma fluid are studied. The BGK type of the Boltzmann kinetic equation is used to study the gas dynamics various regimes with Maxwellian velocity distribution functions. An analytical solution of the model equations for the unsteady flow was given using the moment and the traveling wave methods. The manner of the mean velocity of plasmas is illustrated, which is compatible with the variation of the shear stress, viscosity coefficient, and the initial and boundary conditions. Besides, the thermodynamic prediction is investigated by applying irreversible thermodynamic principles and extended Gibbs formula. Finally, qualitative agreements with previous related papers were demonstrated using 3-dimensional graphics for calculating the variables. The significance of this study is due to its vast applications in numerous fields such as in physics, engineering, commercial, and industrial applications.

1. Introduction

From basic research in plasma science to manufacturing, rapid developments in that field have often been preceded by revolutions in new technologies, such as low-temperature plasmas, or novel applications, such as plasma medicine, plasma biological systems, and microelectronics [1]. For example, Miller et al. [2] have used the nonequilibrium plasma to induce immunogenic cell death in tumors as a therapeutic way for diseases of body systems exposed to the plasma. Plasma–surface interactions have gained immense interest in the last few decades in the context of promising industrial applications in the world's global commercial products, manufacturing processes, and, more recently, microelectronics, medical, and biotechnologies, which are discussed elsewhere in [3].

It is well known that there are two kinetic methods for mathematical modeling of the behavior of a particle population. These methods deal with differential equations that describe the variations of the phase space distribution function $\varphi(t, \mathbf{r}, \mathbf{v})$.. In the case of collisionless plasma, this model equation is the "Vlasov-equation" [4]. In the collisional case, Boltzmann's kinetic equation describes the collisional plasma motion considering microscopic effects. To treat the difficulty of studying the collision term in Boltzmann's kinetic equation, we should use approximate modeling. One of the essential approximate models is the Bhatnagar-Gross-Krook (BGK) model, which saves the computational cost of the collision term of Boltzmann's kinetic equation [5].

Many theoretical and numerical contributions are interested in developing the methods to obtain reasonable solutions to the Boltzmann equation [6, 7]. Also, many approximations have suggested solving the kinetic equation based on the moment method [8–10]. For larger values of Knudsen number (Kn), the Boltzmann kinetic equations and the popular methods depend on the kinetic theory that has to be applied [8–10]. The high magnitude of Kn occurs in rarified gases for the high values of the mean free path or

of the minimal value of the identified length that occurs in the micro-electro-mechanical system (MEMS) or nano-electro-mechanical system (NEMS) devices [11–13]. That property donates the Boltzmann equation a fantastic advantage and many commercial applications [14, 15]. Several papers were treated with Boltzmann equation and its applications in many physical severe situations such as thermal field and microgas sensor [16, 17], irreversible thermodynamics and plasma with kinetic regime [18–22], oscillating flow [23, 24], thermal radiation [25–27], plasma [28], ultrarelativistic heavy-ion collisions [29], photon gas [30], granular fluids [31], and electron energy distribution function [32, 33].

In the Chapman–Enskog method, transport equations are constructed at successive levels of approximation by expanding the distribution function for the parameters around the equilibrium distribution function, while in Grad's method, the transport equations for macroscopic molecular averages are carried out by taking velocity moments of the distribution function, which is approximated by an expansion in orthonormal polynomials [34, 35].

Interaction between moving plasmas and solid surfaces in modern technological applications has a rich history throughout plasma technologies. For example, Chang and Chang [36] have studied the kinetic problem for plasma boundary layer flow in an incompressible viscous case under the effect of an applied magnetic field. Wahid [25] presented an exact solution of the Boltzmann kinetic equation with 4 collision frequency terms. The plasma flow characteristics of a rarefied electron gas generated by neutral atoms have been identified and explained in [27]. Further, they explained the behavior of the gas system but with an approximate solution and an inaccurate collision frequency formula. Abourabia and Tolba [37] investigated the behavior of a rarefied electron gas generated from noble gases using the method of moments in case of a discontinuous distribution function. They obtained an approximate solution for the shear stress and the mean flow velocity.

Furthermore, they considered that the immobile ions are kept as uniform and neutralizing background. Yan [38] designed a hybrid method with deviational particles using three methods (Monte Carlo, particle in cell, and macro-microdecomposition) for the inhomogeneous Vlasov–Poisson–Landau model in plasma. He divides the distribution function into a Maxwellian part generated by a grid-based fluid solver and a deviation part modeled by numerical deviational and coarse particles. A new model was proposed by Juno et al. [23] for the discretization of the kinetic Vlasov–Maxwell equations in a plasma with time using the FEM and Runge–Kutta method. They derived accurate solutions for the distribution function of the plasma. Pan et al. [19] used the charged particle transport by the electric field in the electric acceleration term of Boltzmann's equation in the BGK regime of the collision term. They discovered that, in discrete velocity space, once the nonequilibrium distribution function is produced, the probability distribution functions of the gas are discretized using the finite volume method. Using the discrete unified gas kinetic scheme, Liu et al. [39] developed a novel method for the Vlasov–Poisson equations with the BGK approximation at a wide range of Kn and Debye length. They simulated multiscale plasma using an asymptotic preserving scheme to investigate the electrical potential in all regimes. In our work, we obtain an exact solution for the model equations and study the problem thoroughly, considering the influence of electron-ion and electron-atom collisions in the Boltzmann equation collision term. In this study, we treat the complete collision frequencies of the Boltzmann kinetic equation and introduce a particular form of the model solution to avoid the discontinuity of the solutions. Also, we deal with the full values of variables without any cutoff caused by the small parameters' method implemented in [28]. The great advantage of our study is the consideration of the displacement current terms in the Maxwell equations, which are ignored in all mentioned papers previously (see [24–28, 37]), where they solved the differential equation system using this approximation, whereas in the current study, the term of the displacement current was taken into account because of the applied unsteady external magnetic field that gave this term great importance in our calculations. It cannot be ignored at all. The analytical results provided good agreement with the movement of helium plasma on a moving plate introduced by Wahid and Morad in Ref. [40].

The benefit of treating the Boltzmann kinetic equation enables us to consider the concepts of the linear nonequilibrium irreversible thermodynamics [10]. Besides, the use of Gibbs formulae with the distribution functions gives researchers the possibility to determine the entropy and entropy production of the plasma systems and illustrate the physical interpretation of the nonequilibrium thermodynamic properties [10, 38].

1.1. The Physical Situation and Mathematical Formulation. Assume that the upper half of the space at $y \geq 0$ is bounded by an illimitable plane plate at $y = 0$. The space is filled with a plasma gas under the influence of an unsteady nonuniform external magnetic field (B_{zE}) normal to the direction of the flow. The plasma gas is initially in equilibrium. Considering this plasma in an applied magnetic field, we utilize the customary geometry. The electric field direction is along the x -axis, and the applied magnetic field direction is along the z -axis. The plane plate suddenly moves in its plane with a damping velocity ($V_0 e^{-\alpha t}$) along the x-axis.

Moreover, the plane plate is considered an insulator, uncharged, and impermeable. The system components (the plane plate +electrons + positive ions + neutral atoms) are kept at a constant temperature. We treated a frequency regime such that we can neglect ion currents compared to electron currents. Therefore, one can neglect the motion of ions and pay his attention to the electron motion.

The Lorentz force $\vec{F}_e$ acting on each electron can be acquired by the following:

$$\vec{F}_e = -e\vec{E} - (e/c)\left(\vec{\xi} \wedge \vec{B}\right), \tag{1}$$

where $\vec{B} = B_z \vec{k} = (B_{zE} + B_{zI})\vec{k}$, as$B_{zE} = B_0 e^{\phi(ky-\omega t)}$.

Here, B_{zE} is the applied nonuniform unsteady external magnetic field, and B_{zI} is the induced magnetic field. They are functions of y, and t while $\phi, \omega,$ and κ are constants. Here,

$$\vec{V} \equiv (V_x, 0, 0), \tag{2}$$

$$\vec{J} \equiv (qnV_x, 0, 0), \tag{3}$$

$$\vec{E} \equiv (E_x, 0, 0), \tag{4}$$

$$\vec{B} \equiv (0, 0, B_z), \tag{5}$$

as V_x, E_x, B_z, and J_x are functions of y and t. In particular, this preference satisfies Maxwell's equations. In our model, the distribution function $\varphi_e(\vec{r}, \vec{\xi}, t)$ of the electrons in the plasma gas can be acquired by the Boltzmann kinetic equation that can be written in the BGK model in the form [5]

$$\begin{aligned}
&\frac{\partial \varphi_e\left(\vec{r}, \vec{\xi}, t\right)}{\partial t} + \vec{\xi} \cdot \frac{\partial \varphi_e\left(\vec{r}, \vec{\xi}, t\right)}{\partial \vec{r}} + \frac{\vec{F}_e}{m_e} \cdot \frac{\partial \varphi_e\left(\vec{r}, \vec{\xi}, t\right)}{\partial \vec{\xi}} \\
&= \left(\frac{\varphi_{0e}\left(\vec{r}, \vec{\xi}, t\right) - \varphi_e\left(\vec{r}, \vec{\xi}, t\right)}{\tau_{ee}} \right) \\
&\quad + \left(\frac{\varphi_{0i}\left(\vec{r}, \vec{\xi}, t\right) - \varphi_e\left(\vec{r}, \vec{\xi}, t\right)}{\tau_{ei}} \right) + \left(\frac{\varphi_{0n} - \varphi_e}{\tau_{en}} \right) \text{as } \varphi_{\alpha 0} \\
&= n_\alpha (2\pi R T_\alpha)^{-(3/2)} \exp\left(\frac{-\left(\vec{\xi} - \vec{V}_\alpha\right)^2}{2RT_\alpha} \right).
\end{aligned} \tag{6}$$

The primary arguments n_α, $\vec{V}_\alpha$, and T_α that possess the character of the fundamental equations of motion can be obtained by taking moments of the kinetic equation for the distribution functions. Particles are reflected in full velocity accommodation from the plate, which means that the plasma particles are reflected from the plate with its velocity. Thus, the boundary conditions are [28] $V_{x2}(0, t) = V_0 e^{-\Omega t}$ for $t > 0$, as $V_x = V_{x2}$ as $\xi_y > 0$, and V_x is finite as $y \to \infty$.

Substituting from Equations (1) and (2)–(5) inside Equation (6), one gets

$$\begin{aligned}
&\frac{\partial \varphi_e}{\partial t} + \xi_y \frac{\partial \varphi_e}{\partial y} - \frac{eB_{ez}}{m_e c}\left(\xi_y \frac{\partial \varphi_e}{\partial \xi_x} - \xi_x \frac{\partial \varphi_e}{\partial \xi_y} \right) + \frac{eE_{ex}}{m_e} \frac{\partial \varphi_e}{\partial \xi_x} \\
&\quad = \left(\frac{\varphi_{0e} - \varphi_e}{\tau_{\text{ee}}} \right) + \left(\frac{\varphi_{0i} - \varphi_e}{\tau_{\text{ei}}} \right) + \left(\frac{\varphi_{0n} - \varphi_e}{\tau_{\text{en}}} \right),
\end{aligned} \tag{7}$$

as τ_{ee},τ_{ei}, and τ_{en} are electron-electron, electron-ion, and electron-neutral relaxation times, respectively, that are acquired by [41, 42]

$$\begin{aligned}
\tau_{\text{ee}} &= \left(\frac{3\sqrt{m_e} K_B{}^{3/2} T_e{}^{3/2}}{4\sqrt{\pi} n_e e^4 Log[\Lambda_{\text{ee}}]} \right), \\
\tau_{\text{ei}} &= \left(\frac{3\sqrt{m_e} K_B{}^{3/2} T_e{}^{3/2}}{4\sqrt{2\pi} n_i e^4 Z^2 Log[\Lambda_{\text{ei}}]} \right), \\
\tau_{\text{en}} &= \left(\frac{3 m_e K_B{}^{3/2} T_e{}^{3/2}}{4\sqrt{\pi m_n} n_e e^4 Log[\Lambda_{\text{en}}]} \right).
\end{aligned} \tag{8}$$

Here, $\text{Log}[\Lambda] = \text{Log}[4\pi n \lambda^3{}_D]$ and Z are the Coulomb Logarithm and the degree of ionization, respectively, and $\lambda_{De} = \lambda_{Di} = \lambda_D$ is the Debye length.

The pattern of the cone of influence suggested by Lee [42, 43] for the solution of the Boltzmann kinetic equation is used. The solution of Equation (7) can be written in the form

$$\varphi = \begin{cases} \varphi_1 = n(2\pi \text{RT})^{-(3/2)} \left(1 + \dfrac{\xi_x V_{x1}}{\text{RT}}\right) \exp\left(\dfrac{-\xi^2}{2\text{RT}}\right) & \text{for } \xi_y < 0 \downarrow, \\ \varphi_2 = n(2\pi \text{RT})^{-\frac{3}{2}} \left(1 + \dfrac{\xi_x V_{x2}}{\text{RT}}\right) \exp\left(\dfrac{-\xi^2}{2\text{RT}}\right) & \text{for } \xi_y > 0 \uparrow. \end{cases} \tag{9}$$

Here, V_{x1} and V_{x2} are two underdetermined functions of time t and the single space variable y. Utilizing Grad's moment method in Ref. [7], multiplying Equation (7) by ψ_j $(\vec{\xi})$, and integrating overall values of $\vec{\xi}$, we get the significant transfer equations for electrons in the following form:

$$\begin{aligned}
&\frac{\partial}{\partial t} \int \psi_j \varphi_e d\underline{\xi} + \frac{\partial}{\partial y} \int \xi_y \psi_j \varphi_e d\underline{\xi} + \frac{eE_{xe}}{m_e} \int \varphi_e \frac{\partial \psi_j}{\partial \xi_x} d\underline{\xi} - \frac{eB_{ze}}{m_e c} \int \\
&\quad \cdot \left(\xi_x \frac{\partial \psi_j}{\partial \xi_y} - \xi_y \frac{\partial \psi_j}{\partial \xi_x} \right) d\underline{\xi} = \nu_{\text{ee}} \int (\varphi_{0e} - \varphi_e) \psi_j d\underline{\xi} \\
&\quad + \nu_{\text{ei}} \int (\varphi_{0i} - \varphi_e) \psi_j d\underline{\xi} + \nu_{\text{en}} \int (\varphi_{0n} - \varphi_e) \psi_j d\underline{\xi}.
\end{aligned} \tag{10}$$

All integrals over the velocity dimension are evaluated using the relations below [7]:

$$\int \psi_j \left(\vec{C}\right) \varphi d\underline{\xi} = \int_{-\infty}^{\infty} \int_{-\infty}^{0} \int_{-\infty}^{\infty} \psi_j \varphi_1 d\underline{\xi} + \int_{-\infty}^{\infty} \int_{0}^{\infty} \int_{-\infty}^{\infty} \psi_j \varphi_2 d\underline{\xi}, \tag{11}$$

where $\psi_j = \psi_j(\vec{\xi})$, $j = 1, 2$ and $d\underline{\xi} = d\xi_x d\xi_y d\xi_z$ and ξ_x, ξ_y and ξ_z are the particle velocities components along x, y, and z -axes, respectively. The electric and magnetic fields E and B can also get from Maxwell's equations for electrons as follows:

$$\frac{\partial E_{xe}}{\partial y} - \frac{1}{c}\frac{\partial B_{ze}}{\partial t} = 0,$$

$$\frac{\partial B_{ze}}{\partial y} - \frac{1}{c}\frac{\partial E_{xe}}{\partial t} - \frac{4\pi e n_e}{c_0} V_{xe} = 0. \tag{12}$$

Here, $n = \int \varphi d\underline{\xi}$, $nV_x = \int \xi_x \varphi d\underline{\xi}$,and the initial and boundary conditions

$$\left.\begin{aligned} &E_x(y,0) = 0,\\ &B_z(y,0) = B_0,\\ &E_x(y,t),\\ &B_z(y,t) \text{ are finite as } y \to \infty. \end{aligned}\right\} \tag{13}$$

We offered the nondimensional variables defined by

$$\left.\begin{aligned} t &= t^* \tau_{ee},\\ y &= y^* (\tau_{ee} c),\\ V_x &= V_x^* c,\\ \tau_{xy} &= \tau_{xy}^* c,\\ M &= \frac{V_0}{c},\\ E_x &= E_x^* \left(\frac{m_e c}{e\tau_{ee}}\right),\\ \rho &= nm,\\ B_z &= B_z^* \left(\frac{m_e c}{e\tau_{ee}}\right),\\ \gamma &= \frac{m_e}{m_i},\\ dU &= dU^* (K_B T_e),\\ \varphi_j &= \varphi_j^* n_e (2\pi R T_e)^{-(3/2)}, \quad j = 0, 1, 2. \end{aligned}\right\} \tag{14}$$

The change in density and temperature is negligible for small values of Mach number, i.e., at $M^2 = 1$; therefore, we can assume that $n_\alpha = 1 + O(M^2)$ and $T_\alpha = 1 + O(M^2)$. Then, we can write the mean velocity and shear stress in the following form:

$$V_x = \frac{1}{2}(V_{x1} + V_{x2}),$$

$$\tau_{xy} = \frac{P_{xy}}{\rho V_0 \sqrt{RT_e/2\pi}} = (V_{x2} - V_{x1}). \tag{15}$$

Here, P_{xy} is defined by the relation $P_{xy} = m\int(\xi_x - V_x)\xi_y \phi d\underline{\xi}$ [42].

Utilizing the nondimensional variable, Equation (10) with $\psi_1 = \xi_x$ and $\psi_2 = \xi_x\xi_y$ becomes

$$\frac{\partial V_{ex}^*}{\partial t^*} + \frac{\partial \tau_{exy}^*}{\partial y^*} - E_{ex}^* = 0 \tag{16}$$

$$\frac{\partial \tau_{exy}^*}{\partial t^*} + 2\pi \frac{\partial V_{ex}^*}{\partial y^*} + \tau_{exy}^* = 0. \tag{17}$$

Moreover, the initial and boundary conditions take the form

$$\left.\begin{aligned} &V_{ex}^*(y^*,0) = \tau_{exy}^*(y^*,0) = 0,\\ &2V_{ex}^*(0,t^*) + \tau_{ex}^*(0,t^*) = 2Me^{-\varepsilon t^*},\\ &V_{ex}^* \text{ and } \tau_{exy}^* \text{ are finite as } y \to \infty,\\ &\varepsilon = \omega\tau_{ee}. \end{aligned}\right\} \tag{18}$$

Henceforth, for the sake of notational simplicity, we will drop the star on the non-dimensional variables. Thus, we have the next system of equations representing the boundary value problem for electrons:

$$\frac{\partial V_{ex}}{\partial t} + \frac{\partial \tau_{exy}}{\partial y} - E_{ex} = 0, \tag{19}$$

$$\frac{\partial \tau_{exy}}{\partial t} + 2\pi \frac{\partial V_{ex}}{\partial y} + \left(1 + \frac{\nu_{ei}}{\nu_{ee}} + \frac{\nu_{en}}{\nu_{ee}}\right)\tau_{exy} = 0, \tag{20}$$

$$\frac{\partial E_{ex}}{\partial y} - \frac{\partial B_{ez}}{\partial t} = 0, \tag{21}$$

$$\frac{\partial B_{ez}}{\partial y} - \frac{\partial E_{ex}}{\partial t} - \omega_{e0} V_{ex} = 0, \quad \omega_{e0} = \left(\frac{n_e e^2}{m_e \nu_{ee}^2}\right). \tag{22}$$

The traveling wave solution method [44–46] was utilized considering the new variable θ as

$$\theta = ky - \omega t. \tag{23}$$

This procedure will transform the dependent variables as functions of the new variable θ. Also, the transformation constants k and ω can be measured from the boundary and initial conditions [45, 46].

The partial derivatives of Equations (19)–(22) can be determined from Equation (23) as follows:

$$\left.\begin{aligned} \frac{\partial}{\partial t} &= -\omega \frac{\partial}{\partial \theta},\\ \frac{\partial}{\partial y} &= k \frac{\partial}{\partial \theta},\\ \frac{\partial^n}{\partial t^n} &= (-1)^n \omega^n \frac{\partial^n}{\partial \theta^n},\\ \frac{\partial^n}{\partial y^n} &= k^n \frac{\partial^n}{\partial \theta^n} \end{aligned}\right\} \tag{24}$$

Substituting from Equations (23) and (24) into Equations (19)–(22), after various calculus manipulations, the obtained equations can be reduced to one equation:

$$\left(\left(\omega^2-k^2\right)\left(\frac{2\pi k^2}{\omega}-\omega\right)\right)\frac{d^3V_{ex}(\theta)}{d\theta^3}+w_c\left(\omega^2-k^2\right)\frac{d^2V_{ex}(\theta)}{d\theta^2}+w_{e0}\omega\frac{dV_{ex}(\theta)}{d\theta}+w_{e0}w_cV_{ex}(\theta)=0,\quad w_c=\left(1+\frac{\nu_{ei}}{\nu_{ee}}+\frac{\nu_{en}}{\nu_{ee}}\right). \tag{25}$$

The initial and boundary conditions after dropping the stars from the nondimensional variables are introduced:

$$\left.\begin{aligned}&E_{ex}(\theta=0)=\tau_{exy}(\theta=0)=0,\\&B_{ez}(\theta=0)=B_0,\\&2V_{ex}(\theta=-\omega)+\tau_{exy}(\theta=-\omega)=2Me^{-\varepsilon}\text{ at }y=0,\text{ e.g.,}t=1,\\&V_{ex},\tau_{exy},E_{ex},\text{ and }B_{ez}\text{ are finite as }\theta\to-\infty.\end{aligned}\right\} \tag{26}$$

As a result of calculations on the model equations, we get the differential equation (25) with the conditions in Equation (26). This model equation is a third-order ordinary homogeneous differential equation that can be solved precisely with any symbolic software using the initial and boundary conditions Equation (26). When using these solutions, a more detailed description can be provided for the flows of laboratory argon plasma.

1.2. The Nonequilibrium Thermodynamic Investigations. The problem of the nonequilibrium thermodynamics of irreversible processes is fundamental when modeling any gas flow, and it continues to present considerable significance in the plasma dynamics. As a result of intensive research efforts in this field, scientists have found that the theoretical major of that theory and its applications in numerous branches of science starts from the thermodynamic laws and H-theorem essentials. Now, we can evaluate the entropy per unit mass S in a nondimensional form as in the following relation (see, e.g., Refs. [24–26, 47, 48]):

$$\begin{aligned}S&=-\int\varphi_e\ln\varphi_e d\underline{\xi}\\&=-\left(\int\varphi_{e1}\ln\varphi_{e1}d\underline{\xi}+\int\varphi_{e2}\ln\varphi_{e2}d\underline{\xi}\right)\\&=-\pi^{\frac{3}{2}}\left[\left({V_{x1}}^2+{V_{x2}}^2\right)-0.66\right].\end{aligned} \tag{27}$$

As a consequence, we can get the entropy flux component in the y-direction:

$$\begin{aligned}{J_y}^{(S)}&=-\int\xi_y\varphi_e\ln\varphi_e d\underline{\xi}\\&=-\left(\int\xi_y\varphi_{e1}\ln\varphi_{e1}d\underline{\xi}+\int\xi_y\varphi_{e2}\ln\varphi_{e2}d\underline{\xi}\right)\\&=\left[\pi\left({V_{x1}}^2+{V_{x2}}^2\right)\right].\end{aligned} \tag{28}$$

From the entropy balance relation, one can define the entropy production in a local form [47, 48]:

$$\sigma=\frac{\partial S}{\partial t}+\vec{\nabla}\bullet\overrightarrow{J^{(S)}}. \tag{29}$$

Taking into account the electromagnetic field energy, we can investigate the internal energy change of the entire system using the extended Gibbs formula [49] that includes the entire energy balance. The plasma gas magnetization's main types are paramagnetic and diamagnetic. Now, we can use the 1st law of thermodynamics to formulate the total energy change for both kinds of magnetization. This includes the electromagnetic field energy balance as follows:

(i) In the paramagnetic case: the internal energy change can be written in terms of the entropy, S; polarization, P; and specific magnetization, M, which are the thermodynamic coordinates due to the temperature, T; electric field, E; and magnetic field, B, respectively. As a consequence, the extensive three participants of the internal energy change in the Gibbs relation: $dU=dU_S+dU_{\text{pol}}+dU_{\text{para}}$, in which $dU_S=TdS$ is the internal energy change according to the change in entropy. $dU_{\text{pol}}=E\,dP$ is the internal energy change according to change in polarization. Moreover, $dU_{\text{para}}=B\,dM$ is the internal energy change according to the change in magnetization, where M is calculated from the equation [37, 49]: $\partial S/\partial M_B=-(B/T)\Rightarrow M_B=-\int((T/B)(\partial S/\partial y))_t dy$. Using the nondimensional variables $U^*=U/m_ec^2$, $M_B^*=M_B(\nu_{ee}/ec)$, and $p^*=p(\nu_{ee}/ec)$ in the Gibbs relation, we can get (after dropping the star) $dU=dS_e+f_1E_xdp+f_1B_zdM_B$

(ii) In the diamagnetic case: the internal energy change can be written in terms of the extensive thermodynamic quantities S and P and the induced magnetic field, B, which symbolize the thermodynamic coordinates due to the intensive quantities T, E, and M_B, respectively; thus, we have three participants in the internal energy modified in the Gibbs formula acquired by

$$dU=dU_S+dU_{\text{pol}}+dU_{\text{dia}}, \tag{30}$$

as $dU_{\text{dia}}=-M_BdB$ is the internal energy change according to the change in the generated magnetic field induction, as $M_B=T(\partial S/\partial B)$ [37, 49]. In the present case, the internal energy dU, in a nondimensional form, is written in the compact form as $dU=dS+Edp-M_BdB$ and $dS=(\partial S/\partial r)\,\delta y+(\partial S/\partial t)\delta t$.

2. Discussion

In the present study, we have investigated the unsteady manner of plasma gas based on the Boltzmann's kinetic theory and irreversible thermodynamics using the Boltzmann equation's exact traveling wave solution with the accurate values

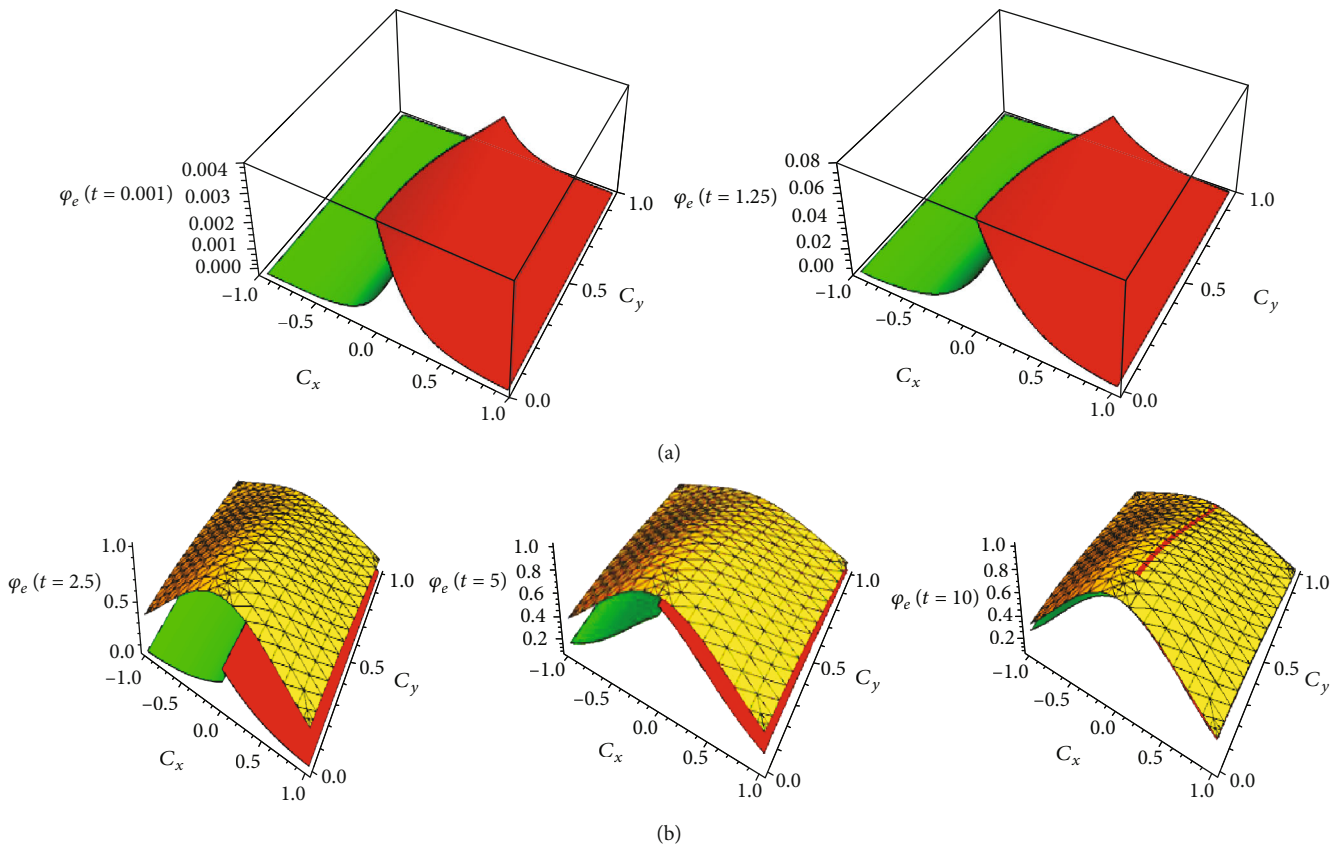

FIGURE 1: (a) The perturbed electron velocity distribution functions φ_e [φ_1 (green), φ_2 (red)] at (t = 0.001 and 1.25) for a fixed y value (y = 1) with the Mach number of the plate M = 0.01. (b) The combination of the perturbed electron velocity distribution functions φ_e: φ_1 (green) and φ_2 (red) compared to the equilibrium velocity distribution function φ_o (grid) at t = 2.5, 5, and 10 with the Mach number of the plate M = 0.01 at y = 1.

of electron-electron, electron-ion, and electron-atom collision frequencies in the BGK technique of the collision terms. The results are clarified in figures for dilute plasma argon gas. It is shown that the computations due to the methods of solution are well performed using standardized data for electron gas in an argon plasma. The analytical results fit very well with the plasma laboratory [28, 41] in the following two cases: in the paramagnetic medium, based on the ionizing potential of the atoms, the argon gas loses single electrons, while in the diamagnetic case, the argon gas loses electron pairs.

We present the solutions of the model equation using the idea of the shooting numerical calculation method to estimate the transformation constants $k = 0.85$ and $\omega = 0.1$ and the Mach number of the plate $M = 1.0 \times 10^{-2}$ as presented in [15]. The calculations are carried out for the problem according to the following plasma fluid properties and conditions: Boltzmann constant, initial temperature, electron concentration, and diameter of the argon atom are given by $k_B = 1.3807 \times 10^{-16}$erg/K,$T_0 = 200$ K, $n_e = 10^{17}$cm^{-3}, and $d = 3.84 \times 10^{-8}$cm. The electron rest mass and electron charge are given by $m_e = 9.093 \times 10^{-28}$g and $e = 4.8\ 10^{-10}$ esu, which are used to determine the dimensionless control parameter $\alpha_0 = 1.6 \times 10^{-12}$. Besides, the electron-ion, electron-electron, and electron-neutral atom collision frequency values are $\nu_{ei} = 1.46 \times 10^{15}$ sec^{-1}, $\nu_{ee} = 1.033 \times 10^{15}$ sec^{-1}, and $\nu_{en} = 1.199 \times 10^{4}$ sec^{-1}, respectively. Finally, the plasma's mean free path $\lambda = (\sqrt{2}\pi n_e d^2)^{-1} = 1.526 \times 10^{-3}$ cm, which is large compared with one of the most fundamental properties, which is the electron Debye length $\lambda_{De} = \sqrt{K_B T_0 / 4\pi n_e e^2} = 3.086 \times 10^{-7}$ cm.

The behavior of solutions that appear in Figures 1(a) and 1(b) reveals that the effect of the plate motion on the electron velocity distribution function is very considerable. Figure 1(b) displays the perturbed electron velocity distribution function in the nearby area of the flat plate that suddenly sets in motion with Mach number equals to 0.01. As shown in Figure 1(b), the deviation from equilibrium decreases with time as the system tries to reach an equilibrium state as expected from Le Chatelier's principle. Therefore, the electron velocity distribution function F_e approaches to equilibrium velocity distribution function F_0 as $t = 10$, a result that strengthens the interpretation of the equilibrium principle. According to Le Chatelier, the position of equilibrium at a certain point in time for the perturbed electron velocity distribution functions F_1 and F_2 approaches to the equilibrium distribution function F_0, which is of interest to our problem (see Figure 1(b)).

Figures 2–6 show, respectively, the graphics of the velocity, shear stress, viscosity, applied magnetic field, and the

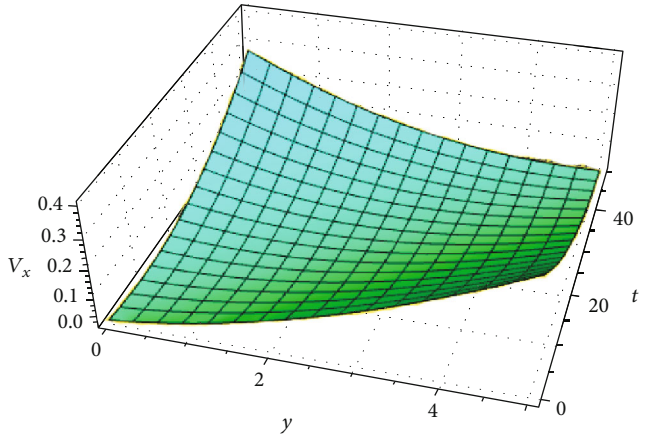

Figure 2: Spatiotemporal velocity profile V_x.

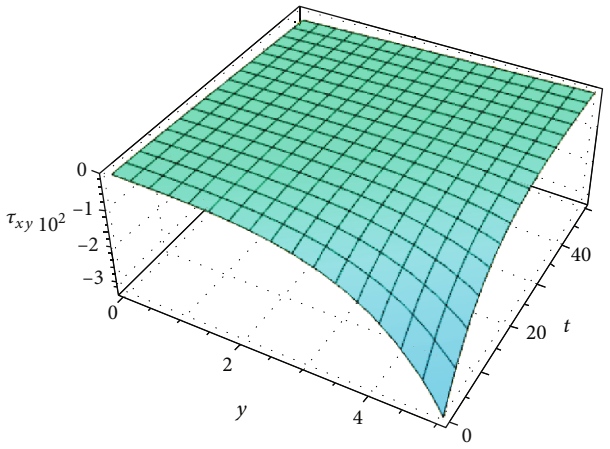

Figure 3: The shear stress τ_{xy} vs. space y and time t.

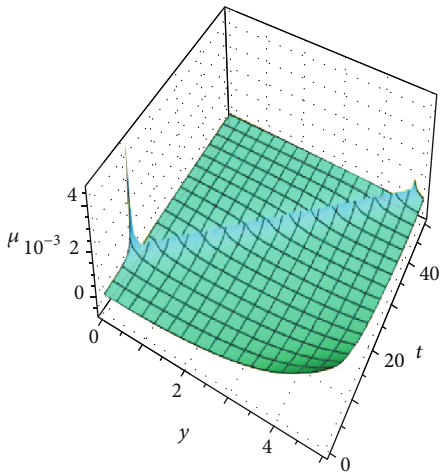

Figure 4: The viscosity coefficient μ vs. space y and time t.

induced electric field according to it. We see that near the moving plate, the mean velocity of the electrons in Figure 2 has a value equal to Mach number $M = 0.01$ of the flat plate as $(y, t) = (0, 0)$. It decreases exponentially with time, which gives a good agreement with the results presented in [28, 37]. The shear stress decreases with time, as shown in Figure 3. The viscosity coefficient follows the equilibrium law by counteracting the change such that the system tends to equilibrate with increasing viscosity, as seen in Figure 4. We shed light upon the behavior of the generated electric and applied magnetic fields in Figures 5 and 6. They illustrate that the electric and magnetic fields are decreasing in magnitudes that tend to zero value over time. That is due to our assumption of the applied external magnetic field and due to the dependency of the generated electric field to the external magnetic field as they connected by Maxwell's equations. Away from the plate, the generated electric field increases with time (see Figure 5). However, the magnetic field has the maximum value at the beginning of time, and then, it decreases nonlinearly towards zero for all y values, as shown in Figure 6. In such a way, the effects of the electromagnetic fields are dominant compared with dynamic effects in the plasma flow model.

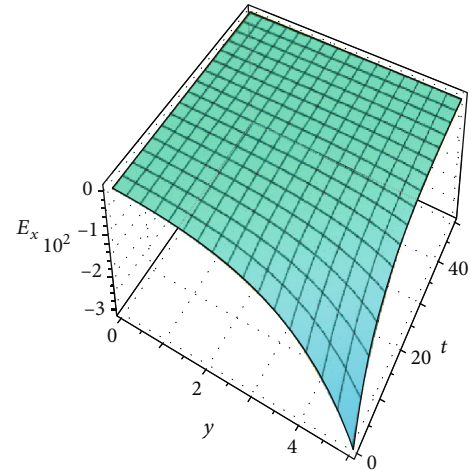

Figure 5: The induced electric field E_x vs. space y and time t.

From the results for velocity, density, and temperature, which were obtained from the solution of the mathematical model, we can demonstrate the nonlinear behavior of the entropy, as seen in Figure 7. The entropy S increases for argon plasma with time, which gives a good agreement with the 2nd law of thermodynamics [38]. The entropy production σ decreases once the system goes towards the equilibrium till it reaches the state of equilibrium, i.e., σ=0 and S is maximum (see Figures 7 and 8). The entropy production of the plasma model satisfies the fundamental laws of thermodynamics and the Boltzmann H-theorem as $\sigma \geq 0$ for all values of the position y and the time t, as shown in Figure 8.

As shown in Figure 9, the change in the internal energy due to the variation of entropy nonlinearly decreases with time and space. For the paramagnetic plasma cases of $dU_{\text{pol}} = E\,dP$ and $dU_{\text{para}} = B\,dM$, the internal energy changes are plotted in Figures 10 and 11. We note that the internal energy polarization and magnetization change is nonlinearly increased.

An investigation of the stability requires to study the time rate of change (time derivatives) of the internal energy $U(\lim_{\Delta t \to 0}(\Delta U/\Delta t) = \lim_{\Delta t \to 0}(\Delta U_S/\Delta t) + \lim_{\Delta t \to 0}(\Delta U_{\text{pol}}/\Delta t) + \lim_{\Delta t \to 0}(\Delta$

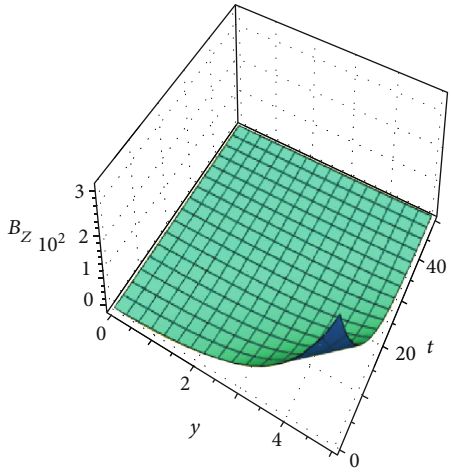

Figure 6: The applied magnetic field B_z vs. space y and time t.

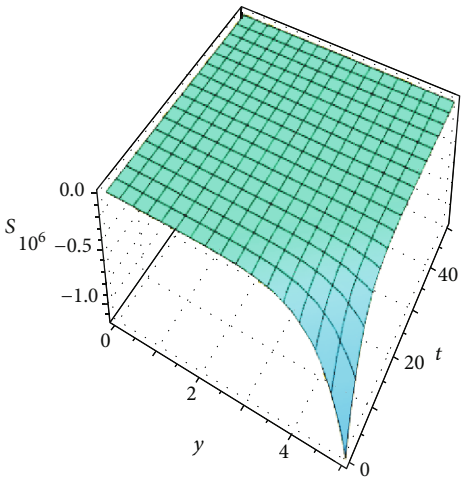

Figure 7: The spatiotemporal entropy profile S.

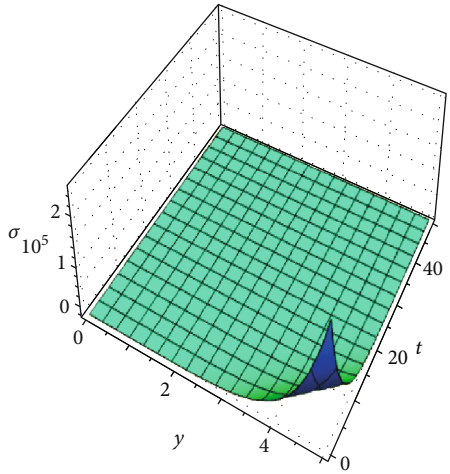

Figure 8: The entropy production σ vs. space y and time t.

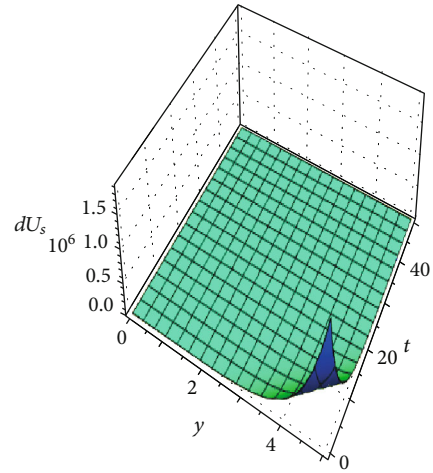

Figure 9: The internal energy change dU_S vs. space y and time t.

$U_{\text{para}}/\Delta t)$). The right-hand side terms can be positive, negative, or null. The positive values indicate an increase in time of internal energy, whereas negative values indicate a decrease in internal energy. On the other side, if the sum of the terms is equal to null, then the rate of change in the internal energy vanishes. Besides, the necessary and sufficient condition for the system to be in the equilibrium state is $\sigma = 0$ and $dU = 0$, which is indicated in Figures 8–11.

The electron gyrofrequency, which is the angular frequency of the circular motion of a charged particle in the plane perpendicular to the applied magnetic field, gradually decreases with time for argon plasma and increases away from the plate (see Figure 12), whereas in plate vicinity, electron Larmor radius or gyroradius, which is the radius of the circular motion of an electron in the plane perpendicular to the applied magnetic field, has the maximum value for argon. Then, it vanishes away from the vicinity of the plate, as shown in Figure 13.

3. Conclusions

In this paper, a detailed calculation of the effect of the collisions of the electrons with positive ions and neutral atoms operating with argon plasma has been made. Further, the current displacement term in the Maxwell equations is taken into consideration, which was ignored in the previous works (see [24–28, 37]). We have elaborated a model to calculate the distribution functions, velocities, and electromagnetic fields of the plasma flow under the effect of an external magnetic field.

All graphics presented in the text have shown excellent agreement within the investigated ranges of the governing parameters and initial and boundary conditions. This fact supports the following idea: based on the BGK model, the collisionless plasma flow problem can be studied in the framework of the Boltzmann kinetic equation supplemented by the Maxwell equations. Also, we can investigate the behavior of electron gas, which is generated from noble gases under the effect of a nonuniform unsteady external magnetic field using the method of moments of the kinetic equation for

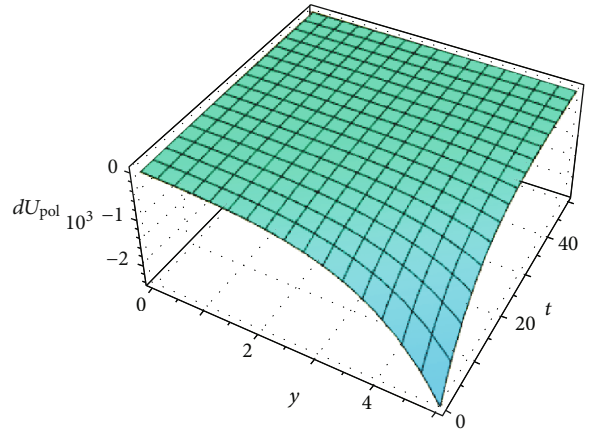

Figure 10: The internal energy change dU_{pol} vs. space y and time t.

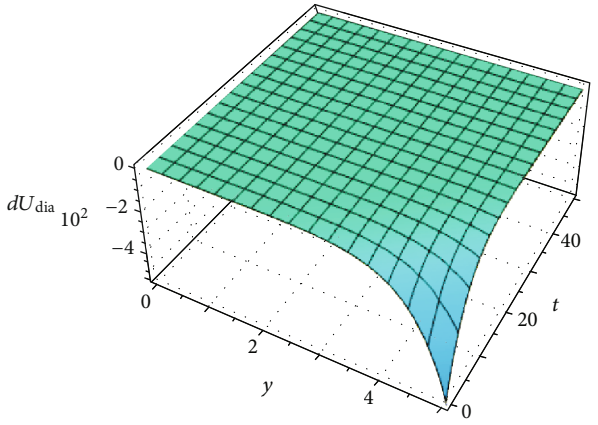

Figure 11: The internal energy change dU_{dia} vs. space y and time t.

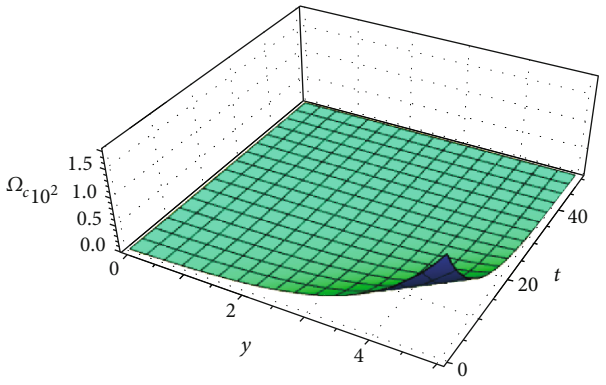

Figure 12: The gyrofrequency Ω_c vs. space y and time t.

the two-sided distribution functions of the velocity. From a thermodynamic viewpoint, collisions between plasma components (ions, electrons, and atoms) are characterized by the fluctuation between loss and gain part of the energy of the charged particles (electrons).

The calculated distribution functions are used to estimate entropy and entropy production that are compatible with the nonequilibrium thermodynamic laws. These properties are

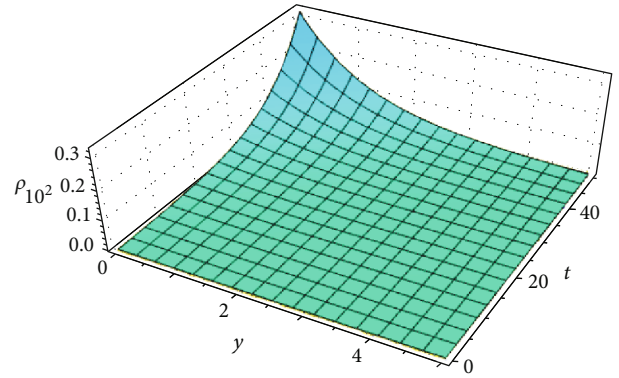

Figure 13: The gyroradius ⊠ versus space y and time t.

deeply discussed. After drawing the solutions, a good consistency between them was found with the thermodynamic laws. Finally, it should be added that the discovered behavior of the collision processes between electrons and ions in argon plasma based on the BGK technique of the Boltzmann kinetic equation might depend on the velocity of the moving plate in the rarefied gas dynamics. This point has been examined minutely in this paper.

Data Availability

The data used to support the findings of this study are included within the article.

Conflicts of Interest

The authors declare that there is no conflict of interest regarding the publication of this paper.

Acknowledgments

This study is supported by the Egyptian Academy of Scientific Research and Technology by the associated grant number (No. 6508), under the program of Science UP Faculties of Science.

References

[1] C. G. N. Lee, K. J. Kanarik, and R. A. Gottscho, "The grand challenges of plasma etching: a manufacturing perspective," *Journal of Physics D: Applied Physics*, vol. 47, no. 27, p. 273001, 2014.

[2] V. Miller, A. Lin, and A. Fridman, "Why target immune cells for plasma treatment of cancer," *Plasma Chemistry and Plasma Processing*, vol. 36, no. 1, pp. 259–268, 2016.

[3] K. Weltmann, J. Kolb, M. Holub et al., "The future for plasma science and technology," *Plasma Processes and Polymers*, vol. 16, article e1800118, 2019.

[4] G. Belmont, R. Grappin, F. Mottez, F. Pantellini, and G. Pelletier, *Collisionless Plasmas in Astrophysics*, WILEY-VCHVerlag GmbH & Co. KGaA, Boschstr, Weinheim, Germany, 2014.

[5] P. L. Bhatnagar, E. P. Gross, and M. Krook, "A model for collision processes in gases. I. Small amplitude processes in

charged and neutral one-component systems," *Physical review*, vol. 94, no. 3, pp. 511–525, 1954.

[6] Z. Donko and N. Dyatko, "First-principles particle simulation and Boltzmann equation analysis of negative differential conductivity and transient negative mobility effects in xenon," *European Physical Journal D: Atomic, Molecular, Optical and Plasma Physics*, vol. 70, no. 6, p. 135, 2016.

[7] H. Struchtrup, "Grad's moment method," in *Macroscopic Transport Equations for Rarefied Gas Flows*, Interaction of Mechanics and Mathematics, Springer, Berlin, Heidelberg, 2005.

[8] A. M. Abourabia and T. Z. A. Wahid, "Solution of the Krook kinetic equation model and non-equilibrium thermodynamics of a rarefied gas affected by a nonlinear thermal radiation field," *Journal of Non-Equilibrium Thermodynamics*, vol. 36, pp. 75–98, 2011.

[9] A. M. Abourabia and T. Z. A. Wahid, "Kinetic and thermodynamic treatment for the Rayleigh flow problem of an inhomogeneous charged gas mixture," *Journal of Non-Equilibrium Thermodynamics*, vol. 37, no. 1, pp. 1–25, 2012.

[10] T. A. Wahid, *Kinetic Irreversible Thermodynamic Study of Plasma and Neutral Gases*, LAP LAMBERT Academic Publishing, Germany, 2014.

[11] V. Shahabi, T. Baier, E. Roohi, and S. Hardt, "Thermally induced gas flows in ratchet channels with diffuse and specular boundaries," *Scientific Reports*, vol. 7, no. 1, p. 41412, 2017.

[12] J. Zhao, J. Yao, M. Zhang et al., "Study of gas flow characteristics in tight porous media with a microscale lattice Boltzmann model," *Scientific Reports*, vol. 6, no. 1, p. 32393, 2016.

[13] H. Xiao and K. Tang, "A unified framework for modeling continuum and rarefied gas flows," *Scientific Reports*, vol. 7, no. 1, p. 13108, 2017.

[14] B.-Y. Cao, J. Sun, M. Chen, and Z.-Y. Guo, "Molecular momentum transport at fluid-solid interfaces in MEMS/NEMS a review," *International Journal of Molecular Sciences*, vol. 10, no. 11, pp. 4638–4706, 2009.

[15] T. Z. A. Wahid, "Kinetic and thermodynamic treatment for the exact solution of the unsteady Rayleigh flow problem of a rarefied homogeneous charged gas," *Journal of Non-Equilibrium Thermodynamics*, vol. 37, no. 2, pp. 119–141, 2012.

[16] H. A. Tighchi, M. Sobhani, and J. A. Esfahani, "Effect of volumetric radiation on natural convection in a cavity with a horizontal fin using the lattice Boltzmann method," *The European Physical Journal Plus*, vol. 133, no. 1, p. 8, 2018.

[17] M. Barzegar Gerdroodbary, D. D. Ganji, M. Taeibi-Rahni, and S. Vakilipour, "Effect of Knudsen thermal force on the performance of low-pressure micro gas sensor," *The European Physical Journal Plus*, vol. 132, no. 7, p. 315, 2017.

[18] M. Lesur, "Method- and scheme-independent entropy production in turbulent kinetic simulations," *Computer Physics Communications*, vol. 200, pp. 182–189, 2016.

[19] D. Pan, C. Zhong, C. Zhuo, and W. Tan, "A unified gas kinetic scheme for transport and collision effects in plasma," *Applied Sciences*, vol. 8, no. 5, p. 746, 2018.

[20] K. Tang and H. Xiao, "Entropy conditions involved in the nonlinear coupled constitutive method for solving continuum and rarefied gas flows," *Entropy*, vol. 19, no. 12, p. 683, 2017.

[21] L. Ferrari, "Comparing Boltzmann and Gibbs definitions of entropy in small systems," *The European Physical Journal Plus*, vol. 132, no. 11, p. 487, 2017.

[22] D. Kalempa and F. Sharipov, "Sound propagation through a binary mixture of rarefied gases at arbitrary sound frequency," *European Journal of Mechanics-B/Fluids*, vol. 57, pp. 50–63, 2016.

[23] J. Juno, A. Hakim, J. TenBarge, E. Shi, and W. Dorland, "Discontinuous Galerkin algorithms for fully kinetic plasmas," *Journal of Computational Physics*, vol. 353, pp. 110–147, 2018.

[24] T. Z. A. Wahid and S. K. Elagan, "Kinetic treatment for the exact solution of the unsteady Rayleigh flow problem of a rarefied homogeneous charged gas bounded by an oscillating plate," *Canadian Journal of Physics*, vol. 90, pp. 987–998, 2012.

[25] T. Z. A. Wahid, "Travelling waves solution of the unsteady flow problem of a rarefied nonhomogeneous charged gas bounded by an oscillating plate," *Mathematical Problems in Engineering*, vol. 2013, Article ID 503729, 13 pages, 2013.

[26] A. M. Abourabia and T. Z. A. Wahid, "Kinetic and thermodynamic treatments of a neutral binary gas mixture affected by a nonlinear thermal radiation field," *Canadian Journal of Physics*, vol. 90, no. 2, pp. 137–149, 2012.

[27] T. Z. A. Wahid, "Travelling wave solution of the unsteady BGK model for a rarefied gas affected by a thermal radiation field," *Sohag Journal of Mathematics*, vol. 2, no. 2, pp. 75–87, 2015.

[28] T. Z. A. Wahid, "Travelling waves solution of the unsteady flow problem of a collisional plasma bounded by a moving plate," *Fluid Mechanics*, vol. 4, no. 1, pp. 27–37, 2018.

[29] L. Oliva, "Impact of the pre-equilibrium stage of ultra-relativistic heavy ion collisions: isotropization and photon production," *The European Physical Journal Plus*, vol. 134, no. 6, p. 306, 2019.

[30] P. Ma, Y. Zheng, and G. Qi, "The nonextensive Bose-Einstein condensation and photon gas with parameter transformation," *The European Physical Journal Plus*, vol. 134, no. 10, p. 502, 2019.

[31] A. M. Abourabia and A. M. Morad, "Exact traveling wave solutions of the van der Waals normal form for fluidized granular matter," *Physica A*, vol. 437, pp. 333–350, 2015.

[32] Ž. Mladenović, S. Gocić, D. Marić, and Z. L. Petrović, "Influence of space charge density on electron energy distribution function and on composition of atmospheric pressure He/O2/air plasmas," *The European Physical Journal Plus*, vol. 133, no. 8, p. 344, 2018.

[33] T. Z. A. Wahid, "Exact solution of the unsteady Krook kinetic model and nonequilibrium thermodynamic study for a rarefied gas affected by a nonlinear thermal radiation field," *Canadian Journal of Physics*, vol. 91, no. 3, pp. 201–210, 2013.

[34] W. Marques and A. R. Méndez, "On the kinetic theory of vehicular traffic flow: Chapman–Enskog expansion versus Grad's moment method," *Physica A*, vol. 392, no. 16, pp. 3430–3440, 2013.

[35] G. M. Kremer, *An Introduction to the Boltzmann Equation and Transport Processes in Gases*, Springer-Verlag, Berlin Heidelberg, 2010.

[36] T. S. Chang and C. M. Chang, "Rayleigh's problem in collisionless plasmas," *Plasma Physics*, vol. 13, no. 9, pp. 695–714, 1971.

[37] A. M. Abourabia and R. E. Tolba, "On the irreversible thermodynamics of an electron gas in the vicinity of a suddenly moving rigid plate," *The European Physical Journal Plus*, vol. 127, no. 58, pp. 1–11, 2012.

[38] B. Yan, "A hybrid method with deviational particles for spatial inhomogeneous plasma," *Journal of Computational Physics*, vol. 309, no. 18–36, pp. 18–36, 2016.

[39] H. Liu, F. Shi, J. Wan, X. He, and Y. Cao, "Discrete unified gas kinetic scheme for a reformulated BGK–Vlasov–Poisson system in all electrostatic plasma regimes," *Computer Physics Communications*, vol. 255, no. 107400, p. 107400, 2020.

[40] T. Z. A. Wahid and A. M. Morad, "Unsteady plasma flow near an oscillating rigid plane plate under the influence of an unsteady nonlinear external magnetic field," *IEEE Access*, vol. 8, pp. 76423–76432, 2020.

[41] J. D. Huba, *NRL Plasma Formulary*, Naval Research Laboratory, Washington, DC, 2019.

[42] S. I. Braginskii, *Transport processes in a plasma. Reviews of Plasma Physics, Volume 1. Authorized translation from Russian by Herbert Lashinsky, University of Maryland, USA*, M. A. Leontovich, Ed., Published by Consultants Bureau, New York, 1965.

[43] L. Lees, "Kinetic theory description of rarefied gas flow," *Journal of the Society for Industrial and Applied Mathematics*, vol. 13, no. 1, pp. 278–311, 1965.

[44] A. M. Abourabia, T. S. El-Danaf, and A. M. Morad, "Exact solutions of the hierarchical Korteweg–de Vries equation of microstructured granular materials," *Chaos, Solitons & Fractals*, vol. 41, no. 2, pp. 716–726, 2009.

[45] J. Gratton, S. M. Mahajan, and F. Minotti, *Non-Newtonian gravity creeping flow*, International Centre for Theoretical Physics, Trieste (Italy), 1988.

[46] G. Nugroho, A. M. S. Ali, and Z. A. Abdul Karim, "Towards a new simple analytical formulation of Navier-Stokes equations," *World Academy of Science, Engineering and Technology*, vol. 39, pp. 197–201, 2009.

[47] G. Lebon, D. Jou, and J. Casas-Vàzquez, *Understanding Non-equilibrium Thermodynamics: Foundations, Applications, Frontiers*, Springer-Verlag, Berlin, Heidelberg, Germany, 2008.

[48] T. Z. Abdel Wahid, *The Effect of Lorentz and Centrifugal Forces on Gases and Plasma*, LAMBERT Academic Publishing, Germany, 2017.

[49] P. Van der Linde, "Thermodynamic stability of dia-and paramagnetic materials," *Periodica Polytechnica Chemical Engineering*, vol. 12, p. 97, 1998.

Hindawi
Advances in Mathematical Physics
Volume 2020, Article ID 8323148, 7 pages
https://doi.org/10.1155/2020/8323148

Research Article

Fractal Ion Acoustic Waves of the Space-Time Fractional Three Dimensional KP Equation

M. A. Abdou,[1,2] Saud Owyed,[3] S. Saha Ray,[4] Yu-Ming Chu,[5,6] Mustafa Inc,[7,8] and Loubna Ouahid[1]

[1]*Physics Department, College of Science, University of Bisha, Bisha 61922, P.O. Box 344, Saudi Arabia*
[2]*Theoretical Research Group, Physics Department, Faculty of Science, Mansoura University, 35516 Mansoura, Egypt*
[3]*Mathematics Department, College of Science, University of Bisha, Bisha 61922, P.O. Box 344, Saudi Arabia*
[4]*Department of Mathematics, National Institute of Technology, Rourkela, 769008 Odisha, India*
[5]*Department of Mathematics, Huzhou University, Huzhou 313000, China*
[6]*Hunan Provincial Key Laboratory of Mathematical Modeling and Analysis in Engineering, Changsha University of Science and Technology, Changsha 410114, China*
[7]*Department of Mathematics, Science Faculty, Firat University, 23119 Elazig, Turkey*
[8]*Department of Medical Research, China Medical University Hospital, China Medical University, Taichung, Taiwan*

Correspondence should be addressed to Yu-Ming Chu; chuyuming2005@126.com and Mustafa Inc; minc@firat.edu.tr

Received 3 August 2020; Revised 29 August 2020; Accepted 22 September 2020; Published 17 October 2020

Academic Editor: Xiao-Ling Gai

Methods known as fractional subequation and sine-Gordon expansion (FSGE) are employed to acquire new exact solutions of some fractional partial differential equations emerging in plasma physics. Fractional operators are employed in the sense of conformable derivatives (CD). New exact solutions are constructed in terms of hyperbolic, rational, and trigonometric functions. Computational results indicate the power of the method.

1. Introduction

Nonlinear propagation of electrostatic excitations in electron-positron ion plasmas and nonthermal distribution of electrons is an important research area in astrophysical and space plasmas [1–6].

Many important phenomena such as the effective behavior of the ionized matter, magnetic field near the surfaces of the sun and stars, emission mechanisms of pulsars, the origin of cosmic rays and radio sources, dynamics of magnetosphere, and propagation of electromagnetic radiation through the upper atmosphere required the study of plasma physics. Equations such as Korteweg de Vries (KdV), Burgers, KdV-Burgers, and Kadomtsev-Petviashvili (KP) were highly used models in the description of plasma systems.

We study the physical phenomena for space-time fractional KP equation with the aid of fractional calculus and examine the resulting solutions in detail. The factional calculus [7–13] has a wide range of applications and is deeply rotted in the field of probability, mathematical physics, differential equations, and so on. Very recently, fractional differential equations have got a lot of consideration as they define many complex phenomena in various fields. Several fractional-order models play very important roles in different areas including physics, engineering, mechanics and dynamical systems, signal and image processing, control theory, biology, and materials [14–18].

The paper is summarized as follows. Definitions and properties of conformable derivatives are discussed. In Section 2, a discussion about the two algorithms method,

namely, fractional subequation method and sine-Gordon expansion method for solving FPDEs arising in plasma physics are given. In Section 3, two schemes are employed for some new exact solutions for the FKPE. We presented a graphical description of some of the solutions with a fixed value of fractal order α in a brief conclusion at the end of the article.

Definition 1. Let $\psi : (0,\infty) \longrightarrow R$. Some definitions, useful properties, and a theorem about conformable derivatives are given as follows:

$$\begin{aligned} U_\alpha(\psi)(t) &= \lim_{\varepsilon \longrightarrow 0} \frac{\psi\left(t + \varepsilon t^{1-\alpha}\right) - \psi(t)}{\varepsilon}, \quad t > 0, \quad 0 < \alpha < 1, \\ U_\alpha(b\psi + ch) &= BU_\alpha(\psi) + CU_\alpha(h), B, C \in R, \\ U_\alpha t^\lambda &= \lambda t^{\lambda-\alpha}, \quad \lambda \in R, \\ U_\alpha(\psi h) &= \psi U_\alpha(h) + hU_\alpha(\psi), \\ U_\alpha\left(\frac{\psi}{h}\right) &= \frac{hU_\alpha(\psi) - \psi U_\alpha(h)}{h^2}. \end{aligned} \tag{1}$$

If ψ is differentiable, then $U_\alpha(\psi)(t) = t^{1-\alpha}(d\psi/dh)$.

Theorem 2. *Let $\psi : (0,\infty) \longrightarrow R$ be a differentiable function. Then,*

$$U_\alpha(\psi * h) = t^{1-\alpha} h'(t) \psi'(h(t)). \tag{2}$$

2. Solution Method

2.1. Extended Fractional Subequation Method. For a given nonlinear FPDE as

$$\chi\left(u_1\, u_k, D_t^\alpha u_1\, D_t^\alpha u_k, D_{x_1}^\alpha u_1\, D_{x_1}^\alpha u_k\right) = 0, \quad 0 < \alpha < 1. \tag{3}$$

in which χ is a polynomial of u. Using wave transformation as

$$u_i(t, x_1, x_2, \cdots x_n) = U_i(\xi), \xi = ct + \cdots + k_n x_n, \tag{4}$$

Eq. (3) reads

$$\phi\left(U_1 \cdots U_k, c^\alpha D_\xi^\alpha U_1 \cdots c^\alpha D_\xi^\alpha U_k, k_1^\alpha D_\xi^\alpha U_1 \cdots k_1^\alpha D_\xi^\alpha U_k \cdots, k_n^\alpha D_\xi^\alpha U_1\right) = 0, \quad 0 < \alpha < 1. \tag{5}$$

Thus,

$$U_i(\xi) = \sum_{i=0}^{M} a_i \left(\frac{D_\xi^\alpha w(\xi)}{w(\xi)}\right)^i, \tag{6}$$

where $w = w(\xi)$ satisfies

$$Aw(\xi) D_\xi^{2\alpha} w(\xi) - Bw(\xi) D_\xi^\alpha w(\xi) - C\left[D_\xi^\alpha w(\xi)\right]^2 - Ew(\xi)^2 = 0, \tag{7}$$

where $D_\xi^\alpha w(\xi)$ is a RL fractional operator of order α. To solve Eq. (7), assume $w(\xi) = z(\eta)$, with the fractional complex transformation, then

$$Az((\eta))z''(\eta) - Bz(\eta)z'(\eta) - C\left[z'(\eta)\right]^2 - Ez^2(\eta) = 0. \tag{8}$$

Since $D_\xi^\alpha w(\xi) = D_\xi^\alpha z(\eta) = z'(\eta)$. The general solutions Eq. (7) is as follows:where $\nu_1 = B^2 + 4E(A - C)$, $\nu_2 = E(A - C)$, L_1, and L_2 are arbitrary constants and $\eta = \xi^\alpha/\Gamma(1 + \alpha)$. Inserting Eq. (6) into (5) knowing Eq.(7), collecting the same order terms $(D_\xi^\alpha w(\xi)/w(\xi))$, then equating it to zero, k and c are obtained. As long as the solutions are obtained with the general expression $[D_\xi^\alpha w(\xi)/w(\xi)]$, admits several solutions of Eq. (3).

Family 1. As long as $B \neq 0$, $\nu_1 > 0$, admits to

$$\left[\frac{D_\xi^\alpha w(\xi)}{w(\xi)}\right] = \frac{B}{2(A-C)} + \frac{\sqrt{\nu_1}}{2(A-C)}\left[\frac{L_1 \sin h\left(\sqrt{\nu_1}\eta/2(A-C)\right) + L_2 \cos h\left(\sqrt{\nu_1}\eta/2(A-C)\right)}{L_1 \cos h\left(\sqrt{\nu_1}\eta/2(A-C)\right) + L_2 \sin h\left(\sqrt{\nu_1}\eta/2(A-C)\right)}\right]. \tag{9}$$

Family 2. Limiting case $B \neq 0$, $\nu_1 < 0$ gains

$$\left[\frac{D_\xi^\alpha w(\xi)}{w(\xi)}\right] = \frac{B}{2(A-C)} + \frac{\sqrt{-\nu_1}}{2(A-C)}\left[\frac{-L_1 \sin\left(\sqrt{-\nu_1}\eta/2(A-C)\right) + L_2 \cos\left(\sqrt{-\nu_1}\eta/2(A-C)\right)}{L_1 \cos\left(\sqrt{-\nu_1}\eta/2(A-C)\right) + L_2 \sin\left(\sqrt{-\nu_1}\eta/2(A-C)\right)}\right]. \tag{10}$$

Family 3. For $B \neq 0$, $\nu_1 = 0$,

$$\left[\frac{D_\xi^\alpha w(\xi)}{w(\xi)}\right] = \frac{B}{2(A-C)} + \frac{L_2}{L_1 + L_2\eta}. \tag{11}$$

Family 4. When $B = 0$, $\nu_2 > 0$,

$$\left[\frac{D_\xi^\alpha w(\xi)}{w(\xi)}\right] = \frac{\sqrt{\nu_2}}{2(A-C)}\left[\frac{L_1 \sin h\left(\sqrt{\nu_2}\eta/2(A-C)\right) + L_2 \cos h\left(\sqrt{\nu_2}\eta/2(A-C)\right)}{L_1 \cos h\left(\sqrt{\nu_2}\eta/2(A-C)\right) + L_2 \sin h\left(\sqrt{\nu_2}\eta/2(A-C)\right)}\right]. \tag{12}$$

Family 5. When $B = 0$, $\nu_2 < 0$, then

$$\left[\frac{D_\xi^\alpha w(\xi)}{w(\xi)}\right] = \frac{\sqrt{-\nu_2}}{2(A-C)}\left[\frac{-L_1 \sin\left(\sqrt{-\Delta_2}\eta/2(A-C)\right) + L_2 \cos\left(\sqrt{-\nu_2}\eta/2(A-C)\right)}{L_1 \cos\left(\sqrt{-\nu_2}\eta/2(A-C)\right) + L_2 \sin\left(\sqrt{-\nu_2}\eta/2(A-C)\right)}\right], \tag{13}$$

2.2. Analysis of the Fractional Sine-Gordon Expansion (FSGE) Method. Let us first consider the fractional sine-Gordon equation as

$$V_{xx} - D_t^{2\alpha} V = m^2 \sin(V), \tag{14}$$

m is constant.

By using the transformation $V = V(\xi), \xi = a(x - \nu(t^\alpha/\alpha))$. Then Eq. (14) yields

$$\frac{d^2(V/2)}{d\xi^2} = \frac{m^2}{a^2(1-\nu^2)}\sin^2(V/2) + C, \tag{15}$$

where C is an integration constant to be zero. Setting $\chi(\xi) = V(\xi)/2$, $b^2 = m^2/a^2(1-\nu^2)$. Then Eq. (15) reads

$$\frac{d(\chi w(\xi)}{d\xi} = b\sin(\chi), \tag{16}$$

Setting $b = 1$, we have

$$\sin(\chi(\xi)) = \frac{2de^{\xi}}{d^2e^{2\xi}+1} = \sec h(\xi), \quad \cos(\chi(\xi)) = \frac{d^2e^{2\xi}-1}{d^2e^{2\xi}+1} = \tan h(\xi), \tag{17}$$

$$\sin(\chi(\xi)) = i\csc h(\xi), \quad \cos(\chi(\xi)) = \cot h(\xi), d = 1. \tag{18}$$

In view of this method, we assume the trail solutions by

$$V(\xi) = \sum_{j=1}^{N} \tan h^{j-1}(\xi)\left[B_j \sec h(\xi) + A_j \sec h(\xi)\right] + A_0, \tag{19}$$

$$V(\xi) = \sum_{j=1}^{N} \cot h^{j-1}(\xi)\left[jB_j \csc h(\xi) + A_j \cot h(\xi)\right] + A_0. \tag{20}$$

Making use of Eq. (18), then Eq. (19) can be rewritten as follows

$$V(\xi) = \sum_{j=1}^{N} \cos^{j-1}(\xi)\left[B_j \sin(\xi) + A_j \cos(\xi)\right] + A_0, \tag{21}$$

where N can be obtained by balancing principle. Inserting Eq. (21) into (15) and the collecting the same power of $\cos^i(\xi)\sin^j(\xi)$, admitting the system of algebraic equation, by solving them by Maple, the coefficient values A_j, B_j, ν can be determined. Inserting these values into Eq. (19), the exact solutions of Eq. (14) are determined.

3. New Applications

In this part of our research, we apply a novel computational approach mentioned above to illustrate the advantages for finding analytical solutions of (3 + 1)-dimension space-time FKPE which is as follows

$$\begin{aligned} &D_x^\alpha D_t^\alpha u(x,y,z,t) + dD_x^\alpha[u(x,y,z,t)D_x^\alpha u(x,y,z,t)] \\ &\quad + \nu D_y^{\alpha\alpha\alpha\alpha} u(x,y,z,t) + \beta D_z^{\alpha\alpha} u(x,y,z,t) \\ &\quad + \nu D_x^{\alpha\alpha} u(x,y,z,t) = 0, \end{aligned} \tag{22}$$

where $u(\xi) = U(x,y,z,t)$ is the field function, ν, δ, d, and $\beta \in \mathbb{R}$. Let $u(x,y,z,t) = U(\xi)$, where $\xi = kx + ct + ly + mz + \xi_0$, k, l, c, m, ξ_0 then

$$\begin{aligned} D_x^\alpha U &= D_x^\alpha U(\xi) = \left(D_\xi^\alpha U\right)\left(\xi_x'\right)^\alpha = k^\alpha D_\xi^\alpha U, \\ D_t^\alpha U &= D_t^\alpha U(\xi) = \left(D_\xi^\alpha U\right)\left(\xi_t'\right)^\alpha = c^\alpha D_\xi^\alpha U. \end{aligned} \tag{23}$$

Then, Eq. (22) reduces to

$$\begin{aligned} &c^\alpha k^\alpha D_\xi^{\alpha\alpha} U(\xi) + dk^{2\alpha} D_\xi^\alpha\left[U(\xi)D_\xi^\alpha U(\xi)\right] + \nu k^{4\alpha} D_\xi^{\alpha\alpha\alpha\alpha} U(\xi) \\ &\quad + \delta l^{2\alpha} D_\xi^{\alpha\alpha} U(\xi) + m^{2\alpha}\beta D_\xi^{\alpha\alpha} U(\xi) = 0. \end{aligned} \tag{24}$$

Now, we assume the solution of Eq. (24) as

$$U(\xi) = \sum_{i=0}^{M} a_i \left(\frac{D_\xi^\alpha w(\xi)}{w(\xi)}\right)^i, \tag{25}$$

where $w = w(\xi)$. Using the proposed algorithm for Eq. (24), we have $M = 2$.

Then,

$$U(\xi) = a_0 + a_1\left(\frac{D_\xi^\alpha w(\xi)}{w(\xi)}\right) + a_2\left(\frac{D_\xi^\alpha w(\xi)}{w(\xi)}\right)^2. \tag{26}$$

Inserting (26) into (24) and collecting the terms with a similar degree of $(D_\xi^\alpha w(\xi)/w(\xi))$, equating it to zero, we have two values of a_i, $(i = 0, 1, 2..)$, k, c, l, and m

$$a_0 = \frac{-\left(k^{-2\alpha}A^2m^{2\alpha}\beta + k^{-2\alpha}A^2\delta l^{2\alpha} + k^{-2\alpha}A^2c^\alpha k^\alpha - 8k^{2\alpha}\nu EA + k^{2\alpha}\nu B^2 + 8k^{2\alpha}\nu EC\right)}{dA^2}, \tag{27}$$

$$\begin{aligned} a_1 &= \frac{12(-C+A)\nu k^{4\alpha}B}{dk^{2\alpha}A^2}, \\ a_2 &= \frac{-12\left(C^2 - 2AC + A^2\right)\nu k^{4\alpha}}{dk^{2\alpha}A^2}, \\ c^\alpha &= c^\alpha, k^\alpha = k^\alpha. \end{aligned} \tag{28}$$

From Eqs. (28) and (26), we gain

$$\begin{aligned} U(\xi) = &\frac{-\left(k^{-2\alpha}A^2m^{2\alpha}\beta + k^{-2\alpha}A^2\delta l^{2\alpha} + k^{-2\alpha}A^2c^\alpha k^\alpha - 8k^{2\alpha}\nu EA + k^{2\alpha}\nu B^2 + 8k^{2\alpha}\nu EC\right)}{dA^2}, \\ &+\left[\frac{12(-C+A)\nu k^{4\alpha}B}{dk^{2\alpha}A^2}\right]\left(\frac{D_\xi^\alpha w(\xi)}{w(\xi)}\right) + \left[\frac{-12\left(C^2-2AC+A^2\right)\nu k^{4\alpha}}{dk^{2\alpha}A^2}\right]\left(\frac{D_\xi^\alpha w(\xi)}{w(\xi)}\right)^2. \end{aligned} \tag{29}$$

In view of Family 1–5 in (26), we obtain the following

Family 6. When $B \neq 0$, $\nu_1 > 0$

$$U_1(\xi) = \frac{-\left(k^{-2\alpha}A^2m^{2\alpha}\beta + k^{-2\alpha}A^2\delta l^{2\alpha} + k^{-2\alpha}A^2c^{\alpha}k^{\alpha} - 8k^{2\alpha}\nu EA + k^{2\alpha}\nu B^2 + 8k^{2\alpha}\nu EC\right)}{dA^2} + \left[\frac{12(-C+A)\nu k^{4\alpha}B}{dk^{2\alpha}A^2}\right]\left[\frac{B}{2(A-C)} + \frac{\sqrt{\nu_1}}{2(A-C)}\left[\frac{L_1 \sin h\left(\sqrt{\nu_1}\eta/2(A-C)\right) + L_2 \cos h\left(\sqrt{\nu_1}\eta/2(A-C)\right)}{L_1 \cos h\left(\sqrt{\nu_1}\eta/2(A-C)\right) + L_2 \sin h\left(\sqrt{\nu_1}\eta/2(A-C)\right)}\right]\right] + \left[\frac{-12\left(C^2-2AC+A^2\right)\nu k^{4\alpha}}{dk^{2\alpha}A^2}\right]\left[\frac{B}{2(A-C)} + \frac{\sqrt{\nu_1}}{2(A-C)}\left[\frac{L_1 \sin h\left(\sqrt{\nu_1}\eta/2(A-C)\right) + L_2 \cos h\left(\sqrt{\nu_1}\eta/2(A-C)\right)}{L_1 \cos h\left(\sqrt{\nu_1}\eta/2(A-C)\right) + L_2 \sin h\left(\sqrt{\nu_1}\eta/2(A-C)\right)}\right]\right]^2. \tag{30}$$

Family 7. When $B \neq 0$, $\nu_1 < 0$

$$U_2(\xi) = \frac{-\left(k^{-2\alpha}A^2m^{2\alpha}\beta + k^{-2\alpha}A^2\delta l^{2\alpha} + k^{-2\alpha}A^2c^{\alpha}k^{\alpha} - 8k^{2\alpha}\nu EA + k^{2\alpha}\nu B^2 + 8k^{2\alpha}\nu EC\right)}{dA^2} + \left[\frac{12(-C+A)\nu k^{4\alpha}B}{dk^{2\alpha}A^2}\right]\left[\frac{B}{2(A-C)} + \frac{\sqrt{-\nu_1}}{2(A-C)}\left[\frac{-L_1 \sin\left(\sqrt{-\nu_1}\eta/2(A-C)\right) + L_2 \cos\left(\sqrt{-\nu_1}\eta/2(A-C)\right)}{L_1 \cos\left(\sqrt{-\nu_1}\eta/2(A-C)\right) + L_2 \sin\left(\sqrt{-\nu_1}\eta/2(A-C)\right)}\right]\right] + \left[\frac{-12\left(C^2-2AC+A^2\right)\nu k^{4\alpha}}{dk^{2\alpha}A^2}\right]\left[\frac{B}{2(A-C)} + \frac{\sqrt{-\nu_1}}{2(A-C)}\left[\frac{-L_1 \sin\left(\sqrt{-\nu_1}\eta/2(A-C)\right) + L_2 \cos\left(\sqrt{-\nu_1}\eta/2(A-C)\right)}{L_1 \cos\left(\sqrt{-\nu_1}\eta/2(A-C)\right) + L_2 \sin\left(\sqrt{-\nu_1}\eta/2(A-C)\right)}\right]\right]^2. \tag{31}$$

Family 8. When $B \neq 0$, $\nu_1 = 0$

$$U_3(\xi) = \frac{-\left(k^{-2\alpha}A^2m^{2\alpha}\beta + k^{-2\alpha}A^2\delta l^{2\alpha} + k^{-2\alpha}A^2c^{\alpha}k^{\alpha} - 8k^{2\alpha}\nu EA + k^{2\alpha}\nu B^2 + 8k^{2\alpha}\nu EC\right)}{dA^2} + \left[\frac{12(-C+A)\nu k^{4\alpha}B}{dk^{2\alpha}A^2}\right]\left[\frac{B}{2(A-C)} + \frac{L_2}{L_1+L_2\eta}\right] + \left[\frac{-12\left(C^2-2AC+A^2\right)\nu k^{4\alpha}}{dk^{2\alpha}A^2}\right]\left[\frac{B}{2(A-C)} + \frac{L_2}{L_1+L_2\eta}\right]^2. \tag{32}$$

Family 9. For $B = 0$, $\nu_2 > 0$

$$U_4(\xi) = \frac{-\left(k^{-2\alpha}A^2m^{2\alpha}\beta + k^{-2\alpha}A^2\delta l^{2\alpha} + k^{-2\alpha}A^2c^{\alpha}k^{\alpha} - 8k^{2\alpha}\nu EA + 8k^{2\alpha}\nu EC\right)}{dA^2} + \left[\frac{-12\left(C^2-2AC+A^2\right)\nu k^{4\alpha}}{dk^{2\alpha}A^2}\right]\left[\frac{\sqrt{\nu_2}}{2(A-C)}\left[\frac{L_1 \sin h\left(\sqrt{\nu_2}\eta/2(A-C)\right) + L_2 \cos h\left(\sqrt{\nu_2}\eta/2(A-C)\right)}{L_1 \cos h\left(\sqrt{\Delta_2}\eta/2(A-C)\right) + L_2 \sin h\left(\sqrt{\nu_2}\eta/2(A-C)\right)}\right]\right]^2. \tag{33}$$

Family 10. In case of $B = 0$, $\nu_2 < 0$

$$U_5(\xi) = \frac{-\left(k^{-2\alpha}A^2m^{2\alpha}\beta + k^{-2\alpha}A^2\delta l^{2\alpha} + k^{-2\alpha}A^2c^{\alpha}k^{\alpha} - 8k^{2\alpha}\nu EA + 8k^{2\alpha}\nu EC\right)}{dA^2} + \left[\frac{-12\left(C^2 - 2AC + A^2\right)\nu k^{4\alpha}}{dk^{2\alpha}A^2}\right]\left[\frac{\sqrt{-\nu_2}}{2(A-C)}\left[\frac{-L_1\sin\left(\sqrt{-\Delta_2}\eta/2(A-C)\right) + L_2\cos\left(\sqrt{-\nu_2}\eta/2(A-C)\right)}{L_1\cos\left(\sqrt{-\nu_2}\eta/2(A-C)\right) + L_2\sin\left(\sqrt{-\nu_2}\eta/2(A-C)\right)}\right]\right]^2, \tag{34}$$

where $\nu_1 = 4E(A-C)$, $\nu_2 = E(A-C)$, $\eta = \xi^{\alpha}/\Gamma(\alpha+1)$, and $\xi = kx + ct + mz + ly + \xi_0$. It is clearly seen that the solutions depend on α, and when $\alpha = 1$, we have the solutions that are obtained for normal derivative. The results introduce free parameters. Hence, five solutions are essential in handling initial and boundary problems. To solve the reduced Eq. (24) by the sine-Gordon expansion (FSGE) method, assume the solution of Eq. (24) as

$$U(\xi) = A_0 + B_1\sin(\xi) + A_1\cos(\xi) + A_2\cos^2(\xi) + B_2\cos(\xi)\sin(\xi). \tag{35}$$

Inserting Eq. (35) into (24) and the collecting the same power of $\cos^i(\chi(xi))\sin^j(\chi(xi))$, admitting the system of algebraic equation, by solving them by Maple, admits to

Set 1.

$$k^{\alpha} = k^{\alpha},\quad c^{\alpha} = c^{\alpha},\quad A_1 = 0,\quad B_1 = 0,\quad B_2 = \pm\frac{6ik^{2\alpha}\nu}{d},\quad A_2 = -\frac{6\nu k^{4\alpha}}{dk^{2\alpha}},\quad A_0 = \frac{\left(5k^{2\alpha}\nu - k^{-2\alpha}\delta L^{2\alpha} - k^{-2\alpha}c^{\alpha}k^{\alpha} - k^{-2\alpha}m^{2\alpha}\beta\right)}{d}, \tag{36}$$

Set 2.

$$k^{\alpha} = k^{\alpha},\quad c^{\alpha} = c^{\alpha},\quad A_1 = 0,\quad B_1 = 0,\quad B_2 = 0,\quad A_2 = \frac{-12\nu k^{4\alpha}}{dk^{2\alpha}},\quad A_0 = \frac{8k^{2\alpha}\nu - k^{-2\alpha}c^{\alpha}k^{\alpha} - k^{-2\alpha}\delta L^{2\alpha} - k^{-2\alpha}m^{2\alpha}\beta}{d}. \tag{37}$$

Inserting Set 1 into (35), we obtain the exact solution of Eq. (22) as

$$u_1(\xi) = \left[\frac{\left(5k^{2\alpha}\nu - k^{-2\alpha}\delta L^{2\alpha} - k^{-2\alpha}c^{\alpha}k^{\alpha} - k^{-2\alpha}m^{2\alpha}\beta\right)}{d}\right] - \left[\frac{6\nu k^{4\alpha}}{dk^{2\alpha}}\right]\tan h^2(\xi) \pm \left[\frac{6ik^{2\alpha}\nu}{d}\right]\tan h(\xi)\,\mathrm{sech}\,(\xi), \tag{38}$$

$$u_2(\xi) = \left[\frac{\left(5k^{2\alpha}\nu - k^{-2\alpha}\delta L^{2\alpha} - k^{-2\alpha}c^{\alpha}k^{\alpha} - k^{-2\alpha}m^{2\alpha}\beta\right)}{d}\right] - \left[\frac{6\nu k^{4\alpha}}{dk^{2\alpha}}\right]\cot \mathrm{h}^2(\xi) \pm \left[\frac{6ik^{2\alpha}\nu}{d}\right] i\coth(\xi)\,\mathrm{csc}\,h(\xi), \tag{39}$$

where $\xi = kx + ct + ly + mz + \xi_0$. Knowing Set 2 and Eq. (35), we gain the exact solution of Eq. (22) as follows:

$$u_3(\xi) = \left[\frac{\left(8k^{2\alpha}\nu - k^{-2\alpha}c^{\alpha}k^{\alpha} - k^{-2\alpha}\delta L^{2\alpha} - k^{-2\alpha}m^{2\alpha}\beta\right)}{d}\right] - \left[\frac{12\nu k^{4\alpha}}{d\left(k^{2\alpha}\right.}\right]\tan h^2(\chi(\xi)), \tag{40}$$

$$u_4(\xi) = \left[\frac{\left(8k^{2\alpha}\nu - k^{-2\alpha}c^{\alpha}k^{\alpha} - k^{-2\alpha}\delta L^{2\alpha} - k^{-2\alpha}m^{2\alpha}\beta\right)}{d}\right] - \left[\frac{12\nu k^{4\alpha}}{dk^{2\alpha}}\right]\cot \mathrm{h}^2(\chi(\xi)), \tag{41}$$

where $\xi = kx + ct + ly + mz + \xi_0$. It is to be noted that, the 3*D* graph represent the obtained solutions with fixed $y = z = 1$ of Eqs. (38) and (40) are shown graphically (see Figures 1–7) for fixed parameter with a different choice of fractal order α.

4. Concluding Remarks

In this article, the extended fractional subequation method and sine-Gordon expansion (FSGE) method have been proposed for finding exact solutions of fractional partial differential equations (FPDEs) in the sense of conformable derivative. This paper studies $(3+1)$-dimensions space-time FKPE which appears in plasma physics in the sense of conformable derivatives via two algorithms, namely, the extended fractional subequation method and FSGE method to obtain sets of exact solutions. Using suitable wave transform, the equations are reduced to some ODEs. Then, the admissible solutions are substituted into the resultant ODE. Equating the coefficients of $(D_{\xi}^{\alpha}w(\xi)/w(\xi))$ in extended

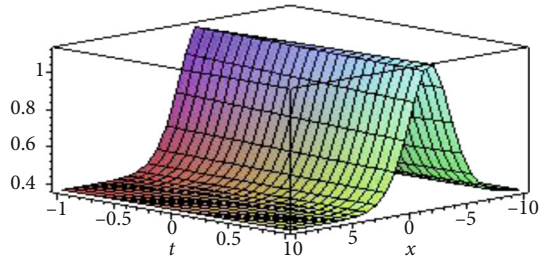

Figure 1: The 3D graph represents of Eq. (38) via sine-Gordon expansion method under the fixed values $m = 0.05, l = 1\,; k = 0.5, v = 1, y = z = 1, c = 0.05, d = 1, \beta = 1, \delta = 1, L = 0.5, 10 < x < 10, 10 < t < 10$ with fractal order $\alpha = 1$.

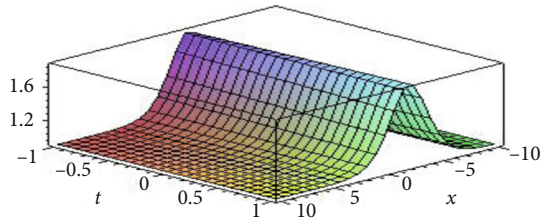

Figure 2: The 3D graph represents of Eq. (38) via sine-Gordon expansion method with a fixed values $m = 0.05, l = 1\,; k = 0.5, v = 1, y = z = 1, c = 0.05, d = 1, \beta = 1, \delta = 1, L = 0.5, 10 < x < 10, 10 < t < 10$ with fractal order $\alpha = 0.55$

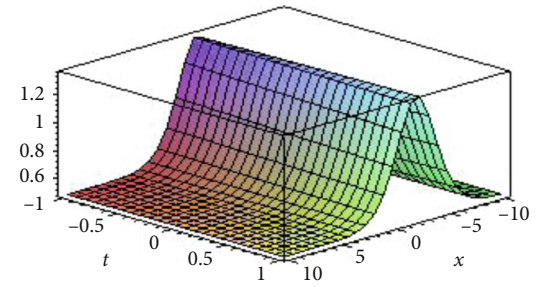

Figure 3: The 3D graph represents of Eq. (38) via sine-Gordon expansion method with a fixed values $m = 0.05, l = 1\,; k = 0.5, v = 1, y = z = 1, c = 0.05, d = 1, \beta = 1, \delta = 1, L = 0.5, 10 < x < 10, 10 < t < 10$ with fractal order $\alpha = 0.85$

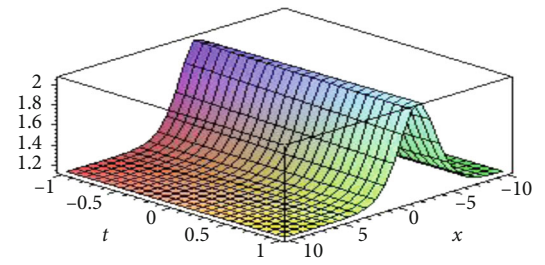

Figure 4: The 3D graph represents of Eq. (38) via sine-Gordon expansion method under the values $m = 0.05, l = 1\,; k = 0.5, v = 1, y = z = 1, c = 0.05, d = 1, \beta = 1, \delta = 1, L = 0.5, 10 < x < 10, 10 < t < 10$ with fractal order $\alpha = 0.45$

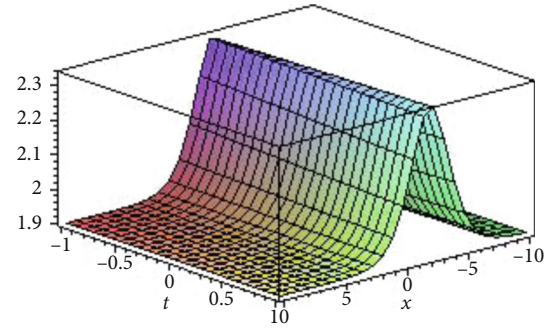

Figure 5: The 3D graph represents of the wave solutions of Eq. (40) via sine-Gordon expansion method with a fixed values $m = 0.05, l = 1\,; k = 0.5, v = 1, y = z = 1, c = 0.05, d = 1, \beta = 1, \delta = 1, L = 0.5, 10 < x < 10, 10 < t < 10$ with fractal order $\alpha = 1$

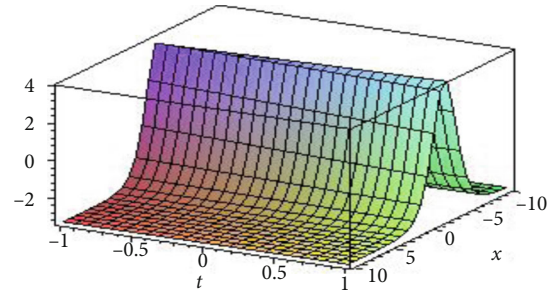

Figure 6: The 3D graph represents of Eq. (40) via sine-Gordon expansion method with a fixed values $m = 0.05, l = 1\,; k = 0.5, v = 1, y = z = 1, c = 0.05, d = 1, \beta = 1, \delta = 1, L = 0.5, 10 < x < 10, 10 < t < 10$ with fractal order $\alpha = 0.35$

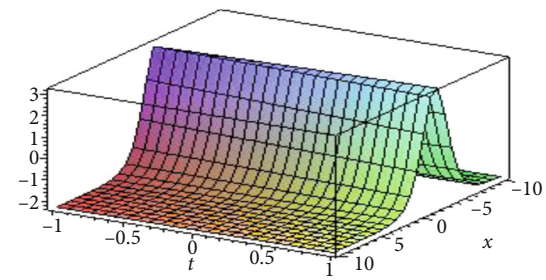

Figure 7: The 3D graph represents of Eq. (40) via sine-Gordon expansion method with a fixed values $m = 0.05, l = 1\,; k = 0.5, v = 1, y = z = 1, c = 0.05, d = 1, \beta = 1, \delta = 1, L = 0.5, 10 < x < 10, 10 < t < 10$ with fractal order $\alpha = 0.55$

fractional subequation method and cosine and sine functions and their multiplications in FSGE method to zero leads to some algebraic system of equations. Solving this system gives the relations among the parameters. Some 3-D solution graphs are presented in some finite domains to comprehend the effects of α.

The presence of parameters makes our results useful for the IVBVP with fractional order. For $\alpha = 1$, our solutions go back to that previously obtained solution. The performance

of these approaches shows the ability for applying on various space-time fractional nonlinear equations in nonlinear science.

Data Availability

No any data availability

Conflicts of Interest

The authors declare that they have no known competing financial interests or personal relationships that could have appeared to influence the work reported in this paper.

Acknowledgments

The work was supported by the Natural Science Foundation of China (Grant Nos. 61673169, 11301127, 11701176, 11626101, and 11601485).

References

[1] R. Sabry, W. M. Moslem, P. K. Shukla, and H. Saleem, "Cylindrical and spherical ion-acoustic envelope solitons in multicomponent plasmas with positrons," *Physical Review E*, vol. 79, no. 5, article 056402, 2009.

[2] H. Schamel, "Stationary solitary, snoidal and sinusoidal ion acoustic waves," *Journal of Plasma Physics*, vol. 14, no. 10, pp. 905–924, 1972.

[3] M. A. Zahran, E. K. El-Shewy, and H. G. Abdelwahed, "Dust-acoustic solitary waves in a dusty plasma with dust of opposite polarity and vortex-like ion distribution," *Journal of Plasma Physics*, vol. 79, no. 5, pp. 859–865, 2013.

[4] E. K. El-Shewy, "Linear and nonlinear properties of electron-acoustic solitary waves with non-thermal electrons," *Chaos, Solitons and Fractals*, vol. 31, no. 4, pp. 1020–1023, 2007.

[5] A. A. Kilbas, H. M. Srivastava, and J. J. Trujillo, *Theory and Applications of Fractional Differential Equations*, vol. 204, Elsevier, Amsterdam, The Netherlands, 2006.

[6] D. Baleanu, K. Diethelm, E. Scalas, and J. J. Trujillo, *Fractional Calculus Models and Numerical Methods*, World Scientific, Series on Complexity Nonliearity and Chaos. Boston, 2012.

[7] A. Jajarmi, A. Yusuf, D. Baleanu, and M. Inc, "Theory and application for the system of fractional Burger equations with Mittag leffler kernel," *Physica A*, vol. 547, p. 123860, 2020.

[8] R. Khalil, M. Al Forani, A. Yousef, and M. Sababheh, "A new definition of fractional derivative," *Journal of Computational Apllied Mathematics*, vol. 264, pp. 65–70, 2014.

[9] R. Cimpoiasu and R. Constantinescu, "The inverse symmetry problem for a 2D generalized second order evolutionary equation," *Nonlinear Analysis: Theory, Methods & Applications*, vol. 57, pp. 147–154, 2010.

[10] S. Saha Ray, "New exact solutions of nonlinear fractional acoustic wave equations in ultrasound," *Computers and Mathematics with Applications*, vol. 71, no. 3, pp. 859–868, 2016.

[11] Z. Korpinar, M. Inc, and M. Bayram, "Theory and application for the system of fractional Burger equations with Mittag leffler kernel," *Applied Mathematics and Computation*, vol. 367, p. 124781, 2020.

[12] S. Sahoo and S. S. Ray, "Improved fractional sub-equation method for (3+1) -dimensional generalized fractional KdV–Zakharov–Kuznetsov equations," *Computers and Mathematics with Applications*, vol. 70, no. 2, pp. 158–166, 2015.

[13] M. A. Abdou and A. A. Soliman, "New exact travelling wave solutions for space-time fractional nonlinear equations describing nonlinear transmission lines," *Results in Physics*, vol. 9, pp. 1497–1501, 2018.

[14] M. A. Abdou, "An analytical method for space time fractional nonlinear differential equations arising in plasma physics," *Journal of Ocean Engineering and Science*, vol. 2, no. 4, pp. 288–292, 2017.

[15] S. Sahoo and S. S. Ray, "New exact solutions of fractional Zakharov—Kuznetsov and modified Zakharov—Kuznetsov equations using fractional sub-equation method," *Communications in Theoretical Physics*, vol. 63, no. 1, pp. 25–30, 2015.

[16] Z. Odibat and D. Baleanu, "Numerical simulation of initial value problems with generalized Caputo-type fractional derivatives," *Applied Numerical Mathematics*, vol. 156, pp. 94–105, 2020.

[17] J. Singh, D. Kumar, Z. Hammouch, and A. Atangana, "A fractional epidemiological model for computer viruses pertaining to a new fractional derivative," *Applied Mathematics and Computation*, vol. 316, pp. 504–515, 2018.

[18] S. Uçar, E. Uçar, N. Özdemir, and Z. Hammouch, "Mathematical analysis and numerical simulation for a smoking model with Atangana-Baleanu derivative," *Chaos, Solitons and Fractals*, vol. 118, pp. 300–306, 2019.

Hindawi
Advances in Mathematical Physics
Volume 2020, Article ID 7849035, 10 pages
https://doi.org/10.1155/2020/7849035

Research Article

Coherently Driven N Number of Degenerate Three-Level Atoms with Parametric Amplifier

Tamirat Abebe, Chimdessa Gashu, and Nebiyu Gemechu

Department of Physics, Jimma University, P. O. Box 378, Jimma, Ethiopia

Correspondence should be addressed to Tamirat Abebe; tam1704@gmail.com

Received 23 May 2020; Accepted 22 September 2020; Published 12 October 2020

Academic Editor: Yu-Hao Sun

We have analyzed the squeezing and statistical properties of the cavity light beam produced by a coherently driven degenerate three-level laser with a degenerate parametric amplifier (DPA) in an open cavity and coupled to a vacuum reservoir via a single-port mirror. We have carried out our analysis by putting the noise operators associated with the vacuum reservoir in normal order. Applying the solutions of the equations of evolution for the expectation values of the atomic operators and the quantum Langevin equation for the cavity mode operator, the mean photon number and the quadrature squeezing of the cavity light are calculated. And a large part of the mean photon number is confined in a relatively small frequency interval. Furthermore, we also obtain the antinormally ordered characteristic function defined in the Heisenberg picture. With the aid of the resulting characteristic function, we determine the Q function which is then used to calculate the photon number distribution.

1. Introduction

Three-level cascade lasers have received considerable interest in connection with its potential as a source of light with interesting nonclassical features [1–22]. The quantum properties of the light, in this device, are attributed to atomic coherence that can be induced either by preparing the atoms initially in a coherent superposition of the top and bottom levels [3, 12, 13, 22] or coupling these levels by an external radiation [7, 8, 10] or using these mechanisms together [23].

Moreover, some authors have studied quantum properties of light generated by the three-level laser whose cavity contains parametric amplifier [10, 11]. Parametric amplifier involves three different modes of the radiation fields the signal, the idler, and the pump which are coupled by a nonlinear medium. In this device a pump photon interacts with a nonlinear crystal inside a cavity and is down converted into two highly correlated photons of different frequencies [12]. These works indicated the cavity radiation is found to be in a squeezed and entangled states under certain conditions. In addition, the mean and variance of the photon number for a degenerate [11, 12, 17] and nondegenerate [13–16] three-level cascade laser whose cavity contains parametric amplifier have been determined for different cases.

In the paper, we wish to study the squeezing and statistical properties of the light generated by a degenerate parametric amplifier (DPA) and coherently driven degenerate three-level laser with an open cavity coupled to a vacuum reservoir via a single-port mirror. We carry out our calculation by putting the noise operators associated with the vacuum reservoir in normal order [6, 8, 24, 25]. We thus first determine the master equation for a coherently driven degenerate three-level laser in an open cavity coupled to a vacuum reservoir and the quantum Langevin equation for the cavity mode operator. In addition, employing the master equation and the large-time approximation scheme, we obtain equations of evolution of the expectation values of atomic operators. Moreover, we determine the solutions of the equations of evolution of the expectation values of the atomic operators and the quantum Langevin equation for cavity mode operator. Then, applying the resulting solutions, we calculate the photon statistics and the quadrature squeezing of the two-mode light beams. Furthermore, applying the same solutions, we determine the antinormally ordered characteristic

function defined in the Heisenberg picture [17, 24, 26]. With the aid of the resulting characteristic function, we determine the Q function which is then used to calculate the photon number distribution.

2. The Model

We consider a coherently pumped degenerate three-level laser with DPA coupled to a vacuum reservoir whose cavity contains N three-level atoms in cascade configuration as shown in Figure 1. The interaction of a degenerate three-level atom with the cavity mode a can be described by the Hamiltonian.

$$\widehat{H}_1 = ig\left[\left(\widehat{\sigma}_a^{\dagger k} + \widehat{\sigma}_b^{\dagger k}\right)\widehat{a} - a\Lambda^{\dagger}\left(\widehat{\sigma}_a^{k} + \widehat{\sigma}_b^{k}\right)\right], \tag{1}$$

where g is the coupling constant between the atom and cavity mode a, and $\widehat{a}(a\Lambda^{\dagger})$ are the annihilation (creation) operators for cavity light mode. We also define that $\Omega = 2\mu\lambda$, in which μ considered to be real and constant, is the amplitude of the driving coherent light, and λ is the coupling constant between the driving coherent light and the three-level atom. We also define that

$$\widehat{\sigma}_a^k = |b\rangle_{kk}\langle a|, \tag{2}$$

$$\widehat{\sigma}_b^k = |c\rangle_{kk}\langle b|, \tag{3}$$

are lowering atomic operators.

On the other hand, a pump mode photon of frequency, $\omega' = 2\omega$, directly interacts with a parametric amplifier (DPA) to produce two signal photons having the same frequency. Furthermore, we consider the case for which the pump mode emerging from a DPA does not couple the top and bottom levels. This could be realized by putting on the right-hand side of the DPA a screen which absorbs the pump mode. With the pump mode treated classically, the process of a single-mode subharmonic generation can be described by the Hamiltonian [22, 26].

$$\widehat{H}_2 = \frac{i\varepsilon}{2}\left[a\Lambda^2 - a\Lambda^{\dagger 2}\right], \tag{4}$$

in which $\varepsilon = 2\beta\lambda_0$ with λ_0 is the coupling constant between the pump mode and nonlinear crystal, and β is proportional to the amplitude of the coherent light driving pump mode. The coupling of the top and bottom levels of a three-level atom by coherent light can be described by the Hamiltonian [7, 8, 24].

$$\widehat{H}_3 = \frac{i\Omega}{2}\left[\widehat{\sigma}_c^{\dagger k} - \widehat{\sigma}_c^{k}\right]. \tag{5}$$

Here, $\Omega = 2\mu\lambda_1$ where μ, considered to be real and constant, is the amplitude of the driving coherent light, and λ_1 is the coupling constant between the driving coherent light with the three-level atom and $\widehat{\sigma}_c^k = |c\rangle_{kk}\langle a|$. Thus, upon combining Eqs. (1), (4), and (5), we have

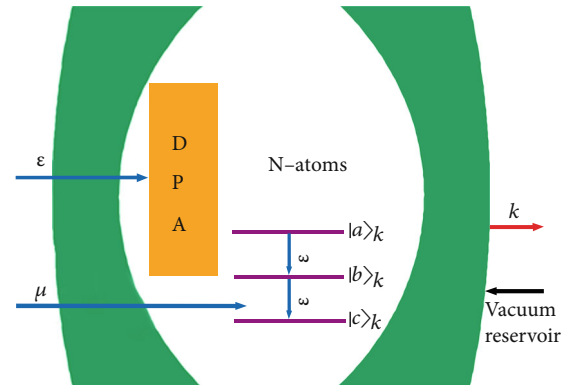

Figure 1: Schematic representation of a degenerate three-level laser with a degenerate parametric amplifier (DPA) and coupled to a two-mode vacuum reservoir. Here, ε, considered to be real and constant, is proportional to the amplitude of the pump mode that drives the nonlinear crystal (NLC), and μ is the amplitude of the driving coherent light that couples the top and bottom levels of the atom. And also κ is the cavity damping constant, and it is assumed the same for both transitions. The top, middle, and bottom levels of the three-level atom are denoted by $|a\rangle_k$, $|b\rangle_k$, and $|c\rangle_k$, respectively, where as $k = 1, 2, \cdots N$ are the number of atoms inside the cavity. When the atom makes a transition from level $|a\rangle_k \rightarrow \langle b|_k$ and from levels $|b\rangle_k \rightarrow \langle c|_k$ two photons with the same frequencies, ω, are emitted.

$$\begin{aligned}\widehat{H} = {} & ig\left[\left(\widehat{\sigma}_a^{\dagger k} + \widehat{\sigma}_b^{\dagger k}\right)\widehat{a} - a\Lambda^{\dagger}\left(\widehat{\sigma}_a^{k} + \widehat{\sigma}_b^{k}\right)\right] \\ & + \frac{i\varepsilon}{2}\left[a\Lambda^2 - a\Lambda^{\dagger 2}\right] + \frac{i\Omega}{2}\left[\widehat{\sigma}_c^{\dagger k} - \widehat{\sigma}_c^{k}\right].\end{aligned} \tag{6}$$

In addition, the master equation for a coherently driven degenerate three-level laser with a one-mode subharmonic generator coupled to a vacuum reservoir in an open cavity, following the procedure described in Ref. [7, 24], is found to be

$$\begin{aligned}\frac{d}{dt}\widehat{\rho}(t) = {} & -i\left[\widehat{H}_S, \widehat{\rho}(t)\right] + \frac{\gamma}{2}\left[2\widehat{\sigma}_a^k\widehat{\rho}\widehat{\sigma}_a^{\dagger k} - \widehat{\sigma}_a^{\dagger k}\widehat{\sigma}_a^k\widehat{\rho} - \widehat{\rho}\widehat{\sigma}_a^{\dagger k}\widehat{\sigma}_a^k\right] \\ & + \frac{\gamma}{2}\left[2\widehat{\sigma}_b^k\widehat{\rho}\widehat{\sigma}_b^{\dagger k} - \widehat{\sigma}_b^{\dagger k}\widehat{\sigma}_b^k\widehat{\rho} - \widehat{\rho}\widehat{\sigma}_b^{\dagger k}\widehat{\sigma}_b^k\right],\end{aligned} \tag{7}$$

where γ, considered to be the same for all the three levels, is the spontaneous emission decay constant. In view of Eq. (6), Eq. (7) turns out to be

$$\begin{aligned}\frac{d}{dt}\widehat{\rho}(t) = {} & g\left[\widehat{\sigma}_a^{\dagger k}\widehat{a}\widehat{\rho} - a\Lambda^{\dagger}\widehat{\sigma}_a^k\widehat{\rho} + \widehat{\sigma}_b^{\dagger k}\widehat{a}\widehat{\rho} - a\Lambda^{\dagger}\widehat{\sigma}_b^k\widehat{\rho} - \widehat{\rho}\widehat{\sigma}_a^{\dagger k}\widehat{a}\right. \\ & \left. + \widehat{\rho}a\Lambda^{\dagger}\widehat{\sigma}_a^k - \widehat{\rho}\widehat{\sigma}_b^{\dagger k}\widehat{a} + \widehat{\rho}a\Lambda^{\dagger}\widehat{\sigma}_b^k\right] \\ & + \frac{\gamma}{2}\left[2\widehat{\sigma}_a^k\widehat{\rho}\widehat{\sigma}_a^{\dagger k} - \widehat{\sigma}_a^{\dagger k}\widehat{\sigma}_a^k\widehat{\rho} - \widehat{\rho}\widehat{\sigma}_a^{\dagger k}\widehat{\sigma}_a^k\right] \\ & + \frac{\gamma}{2}\left[2\widehat{\sigma}_b^k\widehat{\rho}\widehat{\sigma}_b^{\dagger k} - \widehat{\sigma}_b^{\dagger k}\widehat{\sigma}_b^k\widehat{\rho} - \widehat{\rho}\widehat{\sigma}_b^{\dagger k}\widehat{\sigma}_b^k\right] \\ & + \frac{\varepsilon}{2}\left[a\Lambda^2\widehat{\rho} - \widehat{\rho}a\Lambda^2 + \widehat{\rho}a\Lambda^{\dagger 2} - a\Lambda^{\dagger 2}\widehat{\rho}\right] \\ & + \frac{\Omega}{2}\left[\widehat{\sigma}_c^{\dagger k}\widehat{\rho} - \widehat{\sigma}_c^k\widehat{\rho} + \widehat{\rho}\widehat{\sigma}_c^{\dagger k} - \widehat{\rho}\widehat{\sigma}_c^k\right].\end{aligned} \tag{8}$$

We recall that the laser cavity is coupled to a single-mode vacuum reservoir via a single-port mirror. In addition, we carry out our calculation by putting the noise operators associated with the vacuum reservoir in normal order. Thus, the noise operators will not have any effect on the dynamics of the cavity mode operators [7, 8]. We can therefore drop the noise operators and write the quantum Langevin equations for the operator $\widehat{a}$ as

$$\frac{d\widehat{a}}{dt} = -\frac{\kappa}{2}\widehat{a} - i\left[\widehat{a}, \widehat{H}\right], \tag{9}$$

where κ is the cavity damping constant. Then, in view of Eq. (6), we see that

$$\frac{d\widehat{a}}{dt} = -\frac{\kappa}{2}\widehat{a} - g\left(\widehat{\sigma}_a^k + \widehat{\sigma}_b^k\right) - \varepsilon a\wedge^{\dagger}. \tag{10}$$

We see that Eqs. (A.4)-(A.8) are nonlinear differential equations and hence it is not possible to find exact time-dependent solutions of these equations. We intend to overcome this problem by applying the large-time approximation [7, 8, 24, 25, 27]. Therefore, employing this approximation scheme, we get from Eq. (10) the approximately valid relation.

$$\widehat{a} = -\frac{2g}{\kappa}\left(\widehat{\sigma}_a^k + \widehat{\sigma}_b^k\right) - \frac{2\varepsilon}{\kappa}a\wedge^{\dagger}. \tag{11}$$

Evidently, this turns out to be exact relation at steady state. Employing the adjoint of this equation into Eq.(10), one easily verify that

$$\frac{d\widehat{a}}{dt} = -\frac{1}{2}\left(\frac{\kappa^2 - 4\varepsilon^2}{\kappa}\right)\widehat{a} - g\left(\widehat{\sigma}_a^k + \widehat{\sigma}_b^k\right) - \frac{2\varepsilon g}{\kappa}\left(\widehat{\sigma}_a^{\dagger k} + \widehat{\sigma}_b^{\dagger k}\right). \tag{12}$$

The solution of this equation is

$$\widehat{a} = -\frac{4\varepsilon g}{\kappa^2 - 4\varepsilon^2}\left(\widehat{\sigma}_a^k + \widehat{\sigma}_b^k\right) - \frac{2g\kappa}{\kappa^2 - 4\varepsilon^2}\left(\widehat{\sigma}_a^{\dagger k} + \widehat{\sigma}_b^{\dagger k}\right). \tag{13}$$

In the presence of N three-level atoms, we rewrite Eq. (12) as

$$\frac{d\widehat{a}}{dt} = -\frac{1}{2}\left(\frac{\kappa^2 - 4\varepsilon^2}{\kappa}\right)\widehat{a} + \lambda'\left(\widehat{m}_a + \widehat{m}_b\right) + \lambda''\left(\widehat{m}_a^{\dagger} + \widehat{m}_b^{\dagger}\right). \tag{14}$$

in which λ' and λ'' are constants whose values remain to be fixed. Then, using the definition $\widehat{m} = \widehat{m}_a + \widehat{m}_b$ [27], we obtain

$$\frac{d\widehat{a}}{dt} = -\frac{1}{2}\left(\frac{\kappa^2 - 4\varepsilon^2}{\kappa}\right)\widehat{a} + \lambda'\widehat{m} + \lambda'' m\wedge^{\dagger}. \tag{15}$$

Moreover, employing Eq. (13), the commutation relations of the cavity mode operators are

$$\left[\widehat{a}, a\wedge^{\dagger}\right]_k = \frac{\gamma_c\kappa}{\kappa^2 - 4\varepsilon^2}\left[\kappa^2\left[\widehat{\eta}_c^k - \widehat{\eta}_a^k\right] + 4\varepsilon^2\left[\widehat{\eta}_a^k - \widehat{\eta}_c^k\right]\right], \tag{16}$$

and on summing over all atoms, we have

$$\left[\widehat{a}, a\wedge^{\dagger}\right] = \frac{\gamma_c\kappa}{\kappa^2 - 4\varepsilon^2}\left[\kappa^2\left[\widehat{N}_c - \widehat{N}_a\right] + 4\varepsilon^2\left[\widehat{N}_a - \widehat{N}_c\right]\right], \tag{17}$$

where $\left[\widehat{a}, a\wedge^{\dagger}\right] = \sum_{k=1}^{N}\left[\widehat{a}, a\wedge^{\dagger}\right]_k$. We note that Eq. (17) stands for the commutators $\widehat{a}$ and $a\wedge^{\dagger}$ when the cavity mode is interacting with all the N three-level atoms. On the other hand, using the steady-state solution of Eq. (15), one can easily verify that

$$\left[\widehat{a}, a\wedge^{\dagger}\right] = \frac{4\lambda'^2\kappa^2 N}{\left(\kappa^2 - 4\varepsilon^2\right)}\left[\widehat{N}_c - \widehat{N}_a\right] + \frac{4\lambda''^2\kappa^2 N}{\left(\kappa^2 - 4\varepsilon^2\right)}\left[\widehat{N}_a - \widehat{N}_c\right]. \tag{18}$$

Upon comparing Eqs. (17) and (18), one can see that

$$\lambda' = \pm\frac{g}{\sqrt{N}}, \lambda'' = \pm\frac{2g\varepsilon}{\kappa\sqrt{N}}. \tag{19}$$

Hence, in view of these results, the equation of evolution of the cavity mode operator given by Eq. (15) can be written as

$$\frac{d\widehat{a}}{dt} = -\frac{1}{2}\left(\frac{\kappa^2 - 4\varepsilon^2}{\kappa}\right)\widehat{a} + \frac{g}{\sqrt{N}}\widehat{m} + \frac{2g\varepsilon}{\kappa\sqrt{N}}m\wedge^{\dagger}. \tag{20}$$

The steady-state solution of Eq. (20) is

$$\widehat{a} = \frac{2g\kappa}{\sqrt{N}\left(\kappa^2 - 4\varepsilon^2\right)}\widehat{m} + \frac{4g\varepsilon}{\sqrt{N}\left(\kappa^2 - 4\varepsilon^2\right)}m\wedge^{\dagger}. \tag{21}$$

The expectation value of the solution the annihilation operator for the cavity mode evolves in time according to the quantum Langevin equation given by Eq. (20) can be expressed as

$$\begin{aligned}\langle\widehat{a}(t)\rangle = \langle\widehat{a}(0)\rangle e^{-\eta t/2} + \frac{g}{\sqrt{N}}e^{-\eta t/2}\int_0^t e^{\eta t'/2}\left\langle\widehat{m}\left(t'\right)\right\rangle dt' \\ + \frac{2g\varepsilon}{\kappa\sqrt{N}}e^{-\eta t/2}\int_0^t e^{\eta t'/2}\left\langle m\wedge^{\dagger}\left(t'\right)\right\rangle dt',\end{aligned} \tag{22}$$

where $\eta = (\kappa^2 - 4\varepsilon^2)/\kappa$. Thus, applying the large-time approximation scheme, we find the adjoint solution of Eq. (A.10) to be

$$\left\langle\widehat{m}_b^{\dagger}(t)\right\rangle = -\frac{\zeta_+}{\nu}\langle\widehat{m}_a(t)\rangle. \tag{23}$$

Now, on substituting Eq. (23) into Eq. (A.9), it is not difficult to see that

$$\frac{d}{dt}\langle\widehat{m}_a(t)\rangle = -\frac{1}{2}\eta_0\langle\widehat{m}_a(t)\rangle, \tag{24}$$

where $\eta_0 = (2\nu^2 - \zeta_-\zeta_+)/\nu$. With the atoms considered to be initially in the bottom level, the solution of Eq. (24) is found to be

$$\langle \widehat{m}_a(t)\rangle = \langle \widehat{m}_b(t)\rangle = 0. \tag{25}$$

In view of these results together with $\widehat{m} = \widehat{m}_a + \widehat{m}_b$, one can see that

$$\langle \widehat{m}(t)\rangle = 0. \tag{26}$$

With the help of Eq. (26) and the assumption that the cavity light is initially in a vacuum state, Eq. (22) turns out to be

$$\langle \widehat{a}(t)\rangle = 0. \tag{27}$$

In view of the linear equation described by Eq. (20) along with (27), we claim that $\widehat{a}(t)$ is a Gaussian variable with zero mean. Finally, the steady-state solutions of the atomic operators are found to be

$$\langle \widehat{m}_c\rangle_{ss} = \left[\frac{2\nu(\xi+\Omega)}{4\nu^2 + 2\Gamma(2\xi+\Omega) + (2\Omega+\xi)\zeta_+}\right]N, \tag{28}$$

$$\langle \widehat{N}_a\rangle_{ss} = \left[\frac{\zeta_+(\xi+\Omega)}{4\nu^2 + 2\Gamma(2\xi+\Omega) + (2\Omega+\xi)\zeta_+}\right]N, \tag{29}$$

$$\langle \widehat{N}_b\rangle_{ss} = \left[\frac{2\Gamma\nu(\xi+\Omega)}{4\nu^2 + 2\Gamma(2\xi+\Omega) + (2\Omega+\xi)\zeta_+}\right]N, \tag{30}$$

$$\langle \widehat{N}_c\rangle_{ss} = N - \frac{(\zeta_+ + 2\Gamma\nu)(\xi+\Omega)N}{4\nu^2 + 2\Gamma(2\xi+\Omega) + (2\Omega+\xi)\zeta_+}, \tag{31}$$

where *ss* stands for steady state and

$$\Gamma = \frac{\zeta_+(\nu-\gamma) - 4\xi\nu}{2\nu^2}. \tag{32}$$

3. Quadrature Squeezing

The squeezing properties of the cavity light are described by two quadrature operators defined by

$$\widehat{a}_+ = a\wedge^\dagger + \widehat{a}, \tag{33}$$

$$\widehat{a}_- = i\left(a\wedge^\dagger - \widehat{a}\right), \tag{34}$$

where $\widehat{a}_+$ and $\widehat{a}_-$ are Hermitian operators representing the physical quantities called plus and minus quadrature. With the aid of Eqs. (33) and (34) along with (21), the two quadrature operators satisfy the commutation relation

$$[\widehat{a}_-, \widehat{a}_+] = 2i\frac{\gamma_c}{k}\left[\frac{\kappa^2}{\kappa^2 - 4\varepsilon^2}\right]\left[\widehat{N}_a - \widehat{N}_c\right]. \tag{35}$$

An interesting application of the commutator algebra is to derive a relation giving the uncertainties product of two operators $\widehat{A}$ and $\widehat{B}$, i.e, $\Delta A\Delta B \geq 1/2|\langle[\widehat{A},\widehat{B}]\rangle|$. Hence, in view of this, the uncertainty relation of the two quadrature operators can be written as

$$\Delta a_+\Delta a_- \geq \frac{\gamma_c}{k}\left[\frac{\kappa^2}{\kappa^2 - 4\varepsilon^2}\right]\left|\langle \widehat{N}_a\rangle - \langle \widehat{N}_c\rangle\right|. \tag{36}$$

On account of Eqs. (29) and (31), Eq. (36) takes the form

$$\Delta a_+\Delta a_- \geq \frac{\gamma_c}{k}\left[\frac{\kappa^2}{\kappa^2 - 4\varepsilon^2}\right]N \times \left|1 - \frac{(\zeta_+ + \xi + 2\Gamma\nu)(\xi+\Omega)}{4\nu^2 + 2\Gamma(2\xi+\Omega) + (2\Omega+\xi)\zeta_+}\right|. \tag{37}$$

It is interesting to consider some special cases. We first inspect the case in which the nonlinear crystal is removed from the cavity. Thus, upon setting $\beta = 0$ in Eq. (37), we get

$$\Delta a_+\Delta a_- \geq \frac{\gamma_c}{\kappa}N\left|\frac{\delta^3}{\delta^3 + (\gamma_c + 2\delta)\Omega^2}\right|, \tag{38}$$

where $\delta = \gamma + \gamma_c$.

In addition, we consider the case in which the top and bottom levels of the atoms do not coupled by the pump mode. Hence, upon setting $\Omega = 0$ in Eq. (38), we see that

$$\Delta a_+\Delta a_- \geq \frac{\gamma_c}{k}N, \tag{39}$$

which is the minimum uncertainty relation for vacuum state.

Next, we proceed to calculate the quadrature variance of the cavity light. The variance of the plus and minus quadrature operators of the cavity light are defined by

$$\Delta a_\pm^2 = \langle \widehat{a}_\pm^2\rangle - \langle a\wedge_\pm\rangle^2. \tag{40}$$

It then follows that

$$\Delta a_\pm^2 = \langle \widehat{a}a\wedge^\dagger\rangle + \langle a\wedge^\dagger\widehat{a}\rangle \pm \langle a\wedge^2\rangle \pm \langle a\wedge^{\dagger 2}\rangle. \tag{41}$$

Therefore, with the help of Eq. (21), one can readily establish that

$$\langle a\wedge^\dagger\widehat{a}\rangle = \frac{\gamma_c}{k}\left[(\nu-\gamma)^2\left[\langle \widehat{N}_a\rangle + \langle \widehat{N}_b\rangle + 4\varepsilon\langle \widehat{m}_c\rangle\right] + \left(\frac{2\xi}{\gamma_c}\right)^2\left[\langle \widehat{N}_b\rangle + \langle \widehat{N}_c\rangle\right]\right], \tag{42}$$

$$\langle \widehat{a}a\wedge^\dagger\rangle = \frac{\gamma_c}{k}\left[(\nu-\gamma)^2\left[\langle \widehat{N}_b\rangle + \langle \widehat{N}_c\rangle + 4\varepsilon\langle \widehat{m}_c\rangle\right] + \left(\frac{2\xi}{\gamma_c}\right)^2\left[\langle \widehat{N}_a\rangle + \langle \widehat{N}_b\rangle\right]\right], \tag{43}$$

$$\langle a\wedge^2\rangle = \frac{\gamma_c}{k}\left[\left[(\nu-\gamma)^2 + 4\xi^2\right]\langle \widehat{m}_c\rangle + \left(\frac{2\xi}{\gamma_c}\right)^2\left[N + \langle \widehat{N}_b\rangle\right]\right]. \tag{44}$$

Furthermore, on account of Eqs. (42)–(44), the quadrature variances takes the form

$$\begin{aligned}\Delta a_\pm^2 = \frac{\gamma_c}{k}\Bigg[&(\nu-\gamma)^2\left[N + \langle \widehat{N}_b\rangle + 8\varepsilon\langle \widehat{m}_c\rangle \pm 2\langle \widehat{m}_c\rangle\right] \\ &+ \left(\frac{2\xi}{\gamma_c}\right)^2\left[N + \langle \widehat{N}_b\rangle\right](1\pm 2) \pm 8\xi^2\langle \widehat{m}_c\rangle\Bigg]\end{aligned} \tag{45}$$

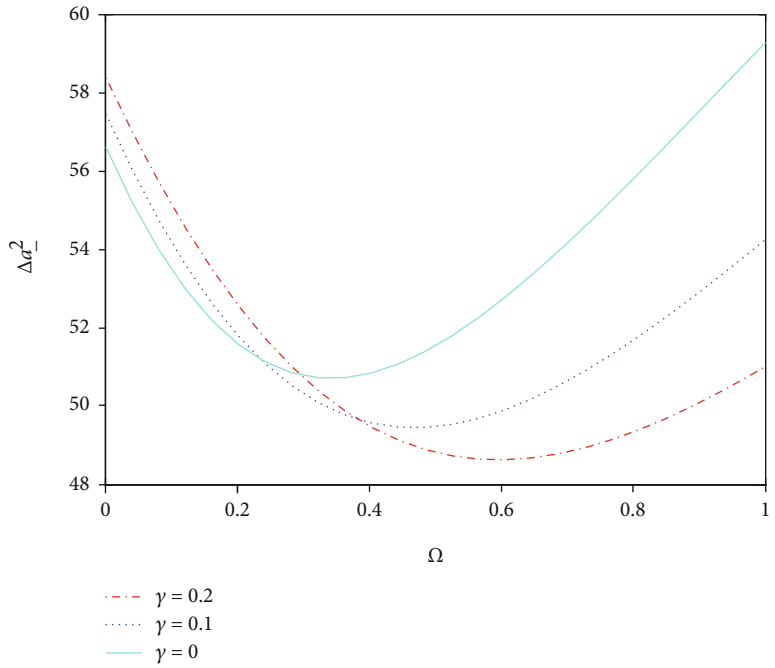

FIGURE 2: Plot of Δa_-^2 at steady state for Eq. (45) versus Ω for $\gamma_c = 0.4$, $k = 0.8$, $N = 50$, and for different values of γ.

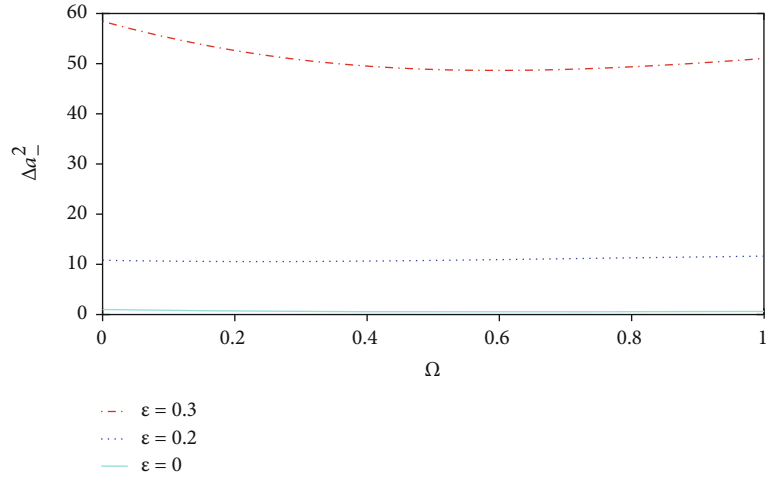

FIGURE 3: Plot of Δa_-^2 at steady state for [Eq. (45)] versus Ω for $\gamma_c = 0.4$, $k = 0.8$, $N = 50$, and for different values of γ.

It is indicated in Figure 2 that squeezing exhibits in a different manner from a single cavity radiation, for values of Ω between 0 and 1, with differing degree of squeezing. Moreover, it is possible to realize that the degree of squeezing increases with the spontaneous emission decay constant, γ. Hence, one can observe that a light produced by a degenerate three-level laser with a parametric amplifier can exhibit different degrees of squeezing when, for example, compared to the light generated by a three-level laser in which the three-level atoms available in a closed cavity are pumped to the top level by means of electron bombardment [24, 25] as well as by coherent light [7, 8].

In Figure 3, we plot the intracavity quadrature variance of the cavity light vs. Ω for $\gamma = 0.2$, $\gamma_c = 0.4$, $\kappa = 0.8$, $N = 50$, and for different values of the amplitude of the pump mode that drives the NLC, ε. This figure indicates that the system under consideration exhibits a single-mode squeezing, and the degree of squeezing increases with the parameter ε. In this figure, the presence of parametric amplifier decreases the degree of squeezing. Furthermore, it is vividly presented in Figures 2 and 3 that the degree of squeezing is significantly degraded by the decreasing of spontaneous emission (γ) and the increasing of the amplitude of the driving light on the parametric amplifier (ε).

4. The Mean Photon Number

To learn about the brightness of the generated light, it is necessary to study the mean photon number of the cavity

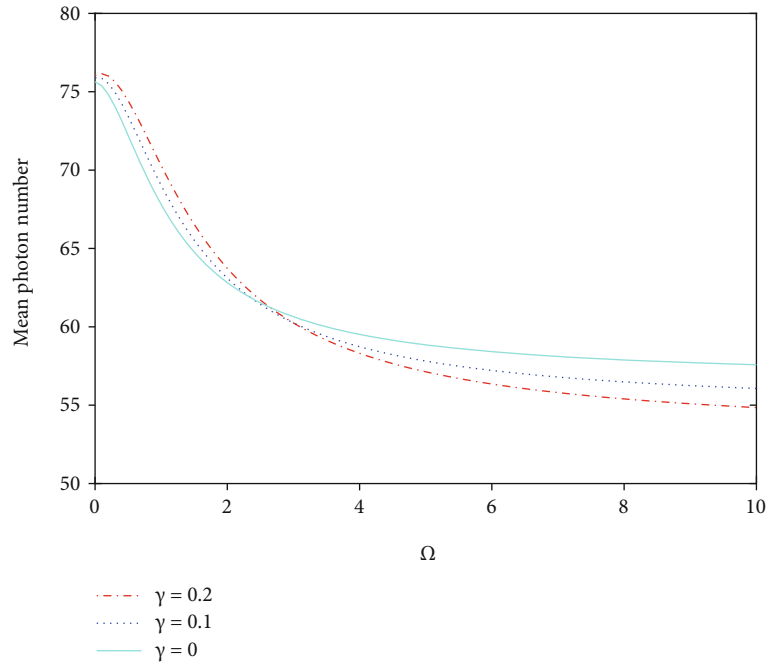

FIGURE 4: Plots of the steady-state mean photon number versus Ω for $\gamma_c = 0.4$, $\kappa = 0.8$, $N = 50$, $\varepsilon = 0.3$, and for different values of γ.

radiation that can be defined as

$$\bar{n} = \left\langle a\wedge^{\dagger}\hat{a}\right\rangle. \tag{46}$$

Hence, using Eq. (21) together with Eqs. (29) and (30), Eq. (46) takes the form

$$\bar{n} = \frac{\gamma_c N}{k}\left\{(\nu-\gamma)^2\left[\frac{(2\Gamma\nu+\zeta_+ + 8\varepsilon\nu)(\xi+\Omega)}{4\nu^2+2\Gamma(2\xi+\Omega)+(2\Omega+\xi)\zeta_+}\right] + \left(\frac{2\xi}{\gamma_c}\right)^2\left[1-\frac{\zeta_+(\xi+\Omega)}{4\nu^2+2\Gamma(2\xi+\Omega)+(2\Omega+\xi)\zeta_+}\right]\right\}. \tag{47}$$

Next, we consider the case in which the nonlinear crystal is removed from the cavity. Thus, upon setting $\beta = 0$ in Eq. (47), we get

$$\bar{n} = \left(\frac{\gamma_c}{k}N\right)\left[\frac{\Omega^2(\gamma_c+\delta)}{\delta^3+(\gamma_c+2\delta)\Omega^2}\right]. \tag{48}$$

This result is the same as the result found by Abebe [7].

In Figure 4, we plot the mean photon number of a cavity mode light versus Ω in the absence and presence of the spontaneous emission, γ. We observe from the plots in figure that the mean photon number of the cavity light beam is greater when $\gamma \neq 0$ than when $\gamma = 0$ for $0 \leq \Omega \leq 2.3$. This implies that the mean photon number increases when γ increases. It is easy to see from this figure that the presence of the spontaneous emission increases the mean photon number in region where there is strong squeezing. Hence, this system generates a bright and highly squeezed light.

In Figure 5, we plot the stead-state mean photon number versus Ω for $\gamma_c = 0.4$, $\kappa = 0.8$, $N = 50$, $\gamma = 0.2$, and for different values of ε. When we see these plots that the mean photon number increases as the parametric amplifier increases for Ω is small. Hence, the presence of parametric amplifier enhances the brightness of the cavity light.

5. The Q Function

We now consider a two-mode cavity light beams represented by the operators $\hat{a}$ and $a\wedge^{\dagger}$ subject to the commutation relations

$$\left[\hat{a}, a\wedge^{\dagger}\right] = \lambda, \tag{49}$$

where

$$\lambda = \frac{\gamma_c}{k}\left[\frac{\kappa^2}{\kappa^2-4\varepsilon^2}\right]\left[\left\langle\hat{N}_c\right\rangle - \left\langle\hat{N}_a\right\rangle\right] \tag{50}$$

is a constant c number. Then, the Q function for a cavity light is expressible as [24]

$$Q(\alpha^*,\alpha) = \frac{\lambda}{\pi^2}\int d^2z\phi_a(z^*,z)\exp\left[z^*\alpha - z\alpha^*\right], \tag{51}$$

in which

$$\phi_a(z^*,z) = Tr\left(\hat{\rho}e^{-z^*a\wedge(t)}e^{za\wedge^{\dagger}(t)}\right) \tag{52}$$

is the antinormally ordered characteristic function. Using the identity

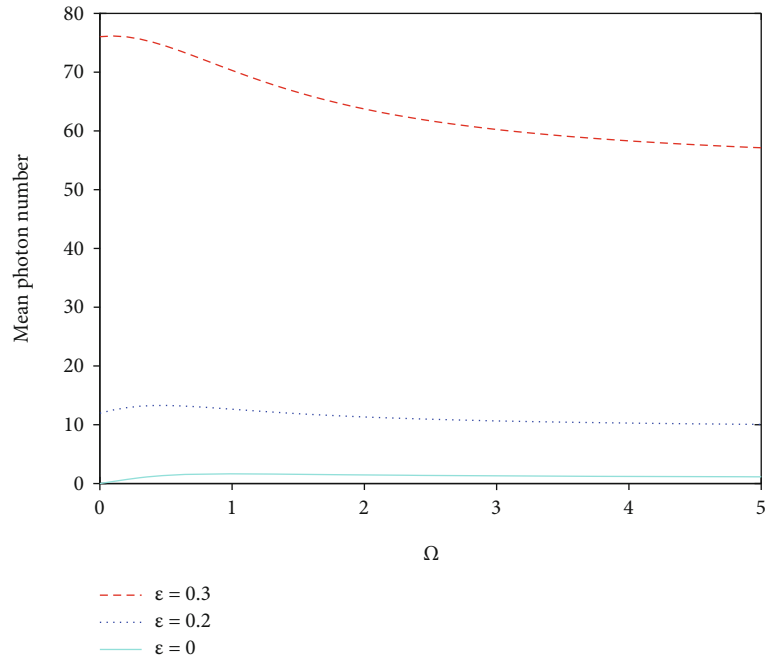

FIGURE 5: Plots of the steady-state mean photon number versus Ω, for $\gamma_c = 0.4$, $\kappa = 0.8$, $N = 50$, $\gamma = 0.2$, and for different values of ε.

$$e^{A\wedge}e^{B\wedge} = e^{A\wedge+B\wedge+\frac{1}{2}[A\wedge,B\wedge]} \tag{53}$$

along with Eqs. (49), one can put Eq. (52) in the form

$$\phi_a(z^*, z) = e^{-\frac{\lambda}{2}z^*z}\left\langle e^{\left[za\wedge^\dagger(t)-z^*a\wedge(t)\right]}\right\rangle. \tag{54}$$

Since $\widehat{a}(t)$ is a Gaussian variable with zero mean, we can rewrite Eq. (54) as

$$\phi_a(z^*, z) = \exp\left(-\frac{z^*z}{2}\left[\lambda + \left\langle a\wedge^\dagger(t)\widehat{a}(t)\right\rangle + \left\langle \widehat{a}(t)a\wedge^\dagger(t)\right\rangle\right] + \frac{z^2}{2}\left\langle a\wedge^{\dagger 2}(t)\right\rangle + \frac{z^{*2}}{2}\left\langle a\wedge^2(t)\right\rangle\right). \tag{55}$$

On account of Eqs. (42)-(44), and (50), we see that

$$\phi_a(z^*, z) = \exp\left[\frac{-az^*z + b\left(z^{*2} + z^2\right)}{2}\right], \tag{56}$$

where

$$a = \frac{\gamma_c}{k}\left\{\left(\frac{\nu-\gamma}{\gamma_c}\right)\left[\left\langle\widehat{N}_c\right\rangle - \left\langle\widehat{N}_a\right\rangle\right] + \left[\frac{2\xi(\nu-\gamma)}{\gamma_c^2}\right]\left\langle\widehat{m}_c\right\rangle + \left[\frac{(\nu-\gamma)^2 + 2(\zeta_+ - \Omega)}{\gamma_c^2}\right]\left[N + \left\langle\widehat{N}_b\right\rangle\right]\right\}, \tag{57}$$

$$b = \frac{\gamma_c}{k}\left\{\left[\frac{2(\nu-\gamma)(\zeta_+ - \Omega)}{\gamma_c^2}\right]\left[N + \left\langle\widehat{N}_b\right\rangle\right] + \left[\frac{(\nu-\gamma)^2 + 2(\zeta_+ - \Omega)}{\gamma_c^2}\right]\left\langle\widehat{m}_c\right\rangle\right\}. \tag{58}$$

Now, by substituting Eq. (56) into Eq. (51), we have

$$Q(\alpha^*, \alpha) = \frac{\lambda}{\pi^2}\int d^2z \exp\left[-az^*z + z^*\alpha - z\alpha^* + b\left[\frac{z^{*2}}{2} + \frac{z^2}{2}\right]\right]. \tag{59}$$

Carrying out the integration using the relation [24].

$$\int \frac{d^2z}{\pi} e^{-az^*z+bz+cz^*+Az^2+Bz^{*2}} = \left[\frac{1}{a^2-4AB}\right]^2 \times \exp\left[\frac{abc + Ac^2 + Bb^2}{a^2-4AB}\right], a > 0, \tag{60}$$

one can easily verify that

$$Q(\alpha^*, \alpha, t) = \frac{\chi}{\pi}\exp\left[-p\alpha^*\alpha + q\left(\frac{\alpha^{*2}}{2} + \frac{\alpha^2}{2}\right)\right], \tag{61}$$

where $\chi = \lambda/\sqrt{a^2 - b^2}$, $p = a/(a^2 - b^2)$, and $q = \mathrm{b}/(a^2 - b^2)$.

6. The Photon Number Distribution

The photon number distribution for a single-mode light defined by

$$P(n,t) = \left\langle n \mid \widehat{\rho}\left(a\wedge^{\dagger}, \widehat{a}\right) \mid n \right\rangle \tag{62}$$

is expressible in terms of the Q function as [17, 24, 26].

$$P(n,t) = \frac{\pi}{n!}\frac{\partial^{2n}}{\partial\alpha^{*n}\partial\alpha^{n}}\left[Q(\alpha^{*},\alpha,t)\,\exp\left[\alpha^{*}\alpha\right]\right]_{\alpha^{*}=\alpha=0}. \tag{63}$$

On account of Eq. (61), we see that

$$P(n,t) = \frac{\lambda}{n!}\left(p^{2}-q^{2}\right)^{1/2}\frac{\partial^{2n}}{\partial\alpha^{*n}\partial\alpha^{n}} \times \exp \cdot\left[(1-p)\alpha^{*}\alpha + q\left(\frac{\alpha^{*2}}{2}+\frac{\alpha^{2}}{2}\right)\right]\Bigg|_{\alpha^{*}=\alpha=0}. \tag{64}$$

Moreover, on expanding the exponential in power series

$$e^{(1-p)\alpha^{*}\alpha} = \sum_{k}^{\infty}\frac{(1-p)^{k}}{k!}\alpha^{*k}\alpha^{k}, \tag{65}$$

$$e^{\frac{q\alpha^{*2}}{2}} = \sum_{l}^{\infty}\frac{q^{l}}{2^{l}l!}\alpha^{*2l}, \tag{66}$$

$$e^{\frac{q^{*}\alpha^{2}}{2}} = \sum_{m}^{\infty}\frac{q^{*m}}{2^{m}m!}\alpha^{2m}, \tag{67}$$

expression (64) can be put in the form

$$P(n,t) = \frac{\lambda}{n!}\left(p^{2}-q^{2}\right)^{1/2}\sum_{k,l,m}\frac{(1-p)^{k}}{k!}\frac{q^{*l}}{l!}\frac{q^{m}}{m!}\frac{\partial^{n}}{\partial\alpha^{n}}\alpha^{k+2l}\times\frac{\partial^{n}}{\partial\alpha^{*n}}\alpha^{*k+2m}\Bigg|_{\alpha^{*}=\alpha=0}. \tag{68}$$

Upon carrying out the differentiation with the help of the relation

$$\frac{\partial^{m}}{\partial x^{n}} = \frac{n!}{(n-m)!}\delta_{n,m}, \tag{69}$$

we get

$$P(n,t) = \frac{\lambda}{n!}\left(p^{2}-q^{2}\right)^{1/2}\sum_{k,l,m}\frac{(1-p)^{k}}{k!}\frac{q^{*l}}{l!}\frac{q^{m}}{m!} \times\frac{(k+2l)!}{(k+2l-n)!}\frac{(k+2m)!}{(k+2m-n)!}\times\delta_{k+2l,n}\delta_{k+2m,n}. \tag{70}$$

Now, applying the property of the Kronecker delta, $l = m = (n-k)/2$, the photon number distribution for the signal mode can be written as

$$P(n,t) = \lambda\left(p^{2}-q^{2}\right)^{1/2}\sum_{k=0}^{n} n!\frac{(1-p)^{k}q^{*(n-k/2)}q^{(n-k/2)}}{(k!)^{2}\left[(n-k/2)!\right]^{2}}, \tag{71}$$

where $[n] = n/2$ for even n and $[n] = (n-1)/2$ for odd n [26]. From this result, we note that there is a finite probability of finding odd number of signal photons. This is due to the fact that, although the signal photons are generated in pairs, there is a possibility for an odd number of signal photons to leave the cavity via the port mirror. This must be then the reason for the possibility to observe an odd number of signal photons inside the cavity.

7. Conclusion

In this paper, we have studied the squeezing and statistical properties of the light produced by the coherently driven degenerate three-level laser with an open cavity and coupled to a two-mode vacuum reservoir via a single-port mirror. We have carried out our analysis by putting the vacuum noise operators in normal order and applying the large-time approximation scheme. Applying the solutions of the equations of evolution for the expectation values of the atomic operators and the quantum Langevin equations for the cavity mode operators, we have determined the mean photon number and the quadrature squeezing.

We have found that the light generated by the three-level laser is in a squeezed state, and the squeezing occurs in the minus quadrature. We have seen that the presence of spontaneous emission increases the degree of squeezing of the cavity light. On the other hand, the brightness of the cavity light enhanced in the presence of both the spontaneous emission and the parametric amplifier. The maximum mean photon number occurs for both cases at Ω near to zero. Finally, we have calculated with the aid of the Q function, the photon number distribution for the cavity light beams. Therefore, there is a finite probability of finding odd number of signal photons. This is due to the fact that, although the signal photons are generated in pairs, there is a possibility for an odd number of photons to leave the cavity through the port mirror.

Appendix

A.1. Equations of Evolution of the Atomic Operators

Here, we seek to obtain the equations of evolution of the expectation values of the atomic operators by applying the master equation and the large-time approximation scheme. To this end, making use of the master equation described by Eq. (8) for any operator $\widehat{A}$ and the fact that

$$\frac{d}{dt}\left\langle\widehat{A}\right\rangle = Tr\left(\frac{d\widehat{\rho}(t)}{dt}\widehat{A}\right), \tag{A.1}$$

it is not difficult to verify that

$$\begin{aligned}\frac{d}{dt}\left\langle\widehat{\sigma}_a^k\right\rangle = gTr\Big[&\widehat{\sigma}_a^{\dagger k}\widehat{a}\widehat{\rho}\widehat{\sigma}_a^k - a\wedge^{\dagger}\widehat{\sigma}_a^k\widehat{\rho}\widehat{\sigma}_a^k + \widehat{\sigma}_b^{\dagger k}\widehat{a}\widehat{\rho}\widehat{\sigma}_a^k\\ &- a\wedge^{\dagger}\widehat{\sigma}_b^k\widehat{\rho}\widehat{\sigma}_a^k - \widehat{\rho}\widehat{\sigma}_a^{\dagger k}\widehat{a}\widehat{\sigma}_a^k + \widehat{\rho}a\wedge^{\dagger}\widehat{\sigma}_a^k\widehat{\sigma}_a^k\\ &- \widehat{\rho}\widehat{\sigma}_b^{\dagger k}\widehat{a}\widehat{\sigma}_a^k + \widehat{\rho}a\wedge^{\dagger}\widehat{\sigma}_b^k\widehat{\sigma}_a^k\Big]\\ &+ \frac{\gamma}{2}Tr\left[2\widehat{\sigma}_a^k\widehat{\rho}\widehat{\sigma}_a^{\dagger k}\widehat{\sigma}_a^k - \widehat{\sigma}_a^{\dagger k}\widehat{\sigma}_a^k\widehat{\rho}\widehat{\sigma}_a^k - \widehat{\rho}\widehat{\sigma}_a^{\dagger k}\widehat{\sigma}_a^k\widehat{\sigma}_a^k\right]\\ &+ \frac{\gamma}{2}Tr\left[2\widehat{\sigma}_b^k\widehat{\rho}\widehat{\sigma}_b^{\dagger k}\widehat{\sigma}_a^k - \widehat{\sigma}_b^{\dagger k}\widehat{\sigma}_b^k\widehat{\rho}\widehat{\sigma}_a^k - \widehat{\rho}\widehat{\sigma}_b^{\dagger k}\widehat{\sigma}_b^k\widehat{\sigma}_a^k\right]\\ &+ \frac{\varepsilon}{2}Tr\left[a\wedge^2\widehat{\rho}\widehat{\sigma}_a^k - \widehat{\rho}a\wedge^2\widehat{\sigma}_a^k + \widehat{\rho}a\wedge^{\dagger 2}\widehat{\sigma}_a^k - a\wedge^{\dagger 2}\widehat{\rho}\widehat{\sigma}_a^k\right]\\ &+ \frac{\Omega}{2}Tr\left[\widehat{\sigma}_c^{\dagger k}\widehat{\rho}\widehat{\sigma}_a^k - \widehat{\sigma}_c^k\widehat{\rho}\widehat{\sigma}_a^k + \widehat{\rho}\widehat{\sigma}_c^{\dagger k}\widehat{\sigma}_a^k - \widehat{\rho}\widehat{\sigma}_c^k\widehat{\sigma}_a^k\right].\end{aligned} \tag{A.2}$$

Now, applying the cyclic property of the trace operation on the above equation results in

$$gTr\left(\widehat{\rho}\widehat{\sigma}_a^k\widehat{\sigma}_a^{\dagger k}\widehat{a}\right) = g\left\langle\widehat{\eta}_b^k\widehat{a}\right\rangle. \tag{A.3}$$

Following the same procedure on the remaining terms, one can readily establish that

$$\frac{d}{dt}\left\langle\widehat{\sigma}_a^k\right\rangle = g\left(\left\langle\widehat{\eta}_b^k\widehat{a}\right\rangle - \left\langle\widehat{\eta}_a^k\widehat{a}\right\rangle + \left\langle a\wedge^{\dagger}\widehat{\sigma}_c^k\right\rangle\right) + \frac{\Omega}{2}\left\langle\widehat{\sigma}_b^{\dagger k}\right\rangle - \gamma\left\langle\widehat{\sigma}_a^k\right\rangle, \tag{A.4}$$

$$\frac{d}{dt}\left\langle\widehat{\sigma}_b^k\right\rangle = g\left(\left\langle\widehat{\eta}_c^k\widehat{a}\right\rangle - \left\langle a\wedge^{\dagger}\widehat{\sigma}_c^k\right\rangle - \left\langle\widehat{\eta}_b^k\widehat{a}\right\rangle\right) - \frac{\Omega}{2}\left\langle\widehat{\sigma}_a^{\dagger k}\right\rangle - \frac{\gamma}{2}\left\langle\widehat{\sigma}_a^k\right\rangle, \tag{A.5}$$

$$\frac{d}{dt}\left\langle\widehat{\sigma}_c^k\right\rangle = g\left(\left\langle\widehat{\sigma}_b^k\widehat{a}\right\rangle - \left\langle\widehat{\sigma}_a^k\widehat{a}\right\rangle\right) + \frac{\Omega}{2}\left[\left\langle\widehat{\eta}_c^k\right\rangle - \left\langle\widehat{\eta}_a^k\right\rangle\right] - \frac{\gamma}{2}\left\langle\widehat{\sigma}_c^k\right\rangle, \tag{A.6}$$

$$\frac{d}{dt}\left\langle\widehat{\eta}_a^k\right\rangle = g\left(\left\langle\widehat{\sigma}_a^{\dagger k}\widehat{a}\right\rangle + \left\langle a\wedge^{\dagger}\widehat{\sigma}_a^k\right\rangle\right) + \frac{\Omega}{2}\left[\left\langle\widehat{\sigma}_c^k\right\rangle + \left\langle\widehat{\sigma}_c^{\dagger k}\right\rangle\right] - \gamma\left\langle\widehat{\eta}_a^k\right\rangle, \tag{A.7}$$

$$\frac{d}{dt}\left\langle\widehat{\eta}_b^k\right\rangle = g\left(\left\langle\widehat{\sigma}_b^{\dagger}\widehat{a}\right\rangle - \left\langle\widehat{\sigma}_a^{\dagger k}\widehat{a}\right\rangle - \left\langle a\wedge^{\dagger}\widehat{\sigma}_a^k\right\rangle + \left\langle a\wedge^{\dagger}\widehat{\sigma}_b^k\right\rangle\right) - \gamma\left\langle\widehat{\eta}_b^k\right\rangle, \tag{A.8}$$

where $\widehat{\eta}_a^k = |a\rangle_{kk}\langle a|$, $\widehat{\eta}_b^k = |b\rangle_{kk}\langle b|$, and $\widehat{\eta}_c^k = |c\rangle_{kk}\langle c|$ are the probabilities of the atoms on the top, middle, and bottom levels, respectively.

Now, introducing Eq. (19) into Eqs. (A.4)-(A.8) and sum over the N three-level atoms, we get

$$\frac{d}{dt}\langle\widehat{m}_a\rangle = -\nu\langle\widehat{m}_a\rangle - \frac{1}{2}\zeta_-\left\langle\widehat{m}_b^{\dagger}\right\rangle, \tag{A.9}$$

$$\frac{d}{dt}\langle\widehat{m}_b\rangle = -\frac{\nu}{2}\langle\widehat{m}_b\rangle - \frac{1}{2}\zeta_+\left\langle\widehat{m}_a^{\dagger}\right\rangle, \tag{A.10}$$

$$\frac{d}{dt}\langle\widehat{m}_c\rangle = -\frac{\nu}{2}\langle\widehat{m}_c\rangle + \xi\left[\left\langle\widehat{N}_c\right\rangle - \left\langle\widehat{N}_b\right\rangle\right] + \frac{\Omega}{2}\left[\left\langle\widehat{N}_c\right\rangle - \left\langle\widehat{N}_a\right\rangle\right], \tag{A.11}$$

$$\frac{d}{dt}\left\langle\widehat{N}_a\right\rangle = -\nu\left\langle\widehat{N}_a\right\rangle + \frac{1}{2}\zeta_+\left[\langle\widehat{m}_c\rangle + \left\langle\widehat{m}_c^{\dagger}\right\rangle\right], \tag{A.12}$$

$$\frac{d}{dt}\left\langle\widehat{N}_b\right\rangle = -\nu\left\langle\widehat{N}_b\right\rangle - \xi\left[\langle\widehat{m}_c\rangle + \left\langle\widehat{m}_c^{\dagger}\right\rangle\right] + [\nu-\gamma]\left\langle\widehat{N}_a\right\rangle, \tag{A.13}$$

where $\gamma_c = 4g^2/\kappa$ is the stimulated emission decay constant, whereas

$$\nu = \gamma + \frac{\gamma_c\kappa^2}{\kappa^2 - 4\varepsilon^2}, \tag{A.14}$$

$$\zeta_{\pm} = \frac{2\gamma_c\varepsilon\kappa}{\kappa^2 - 4\varepsilon^2} \pm \Omega, \tag{A.15}$$

$$\xi = \frac{\gamma_c\varepsilon\kappa}{\kappa^2 - 4\varepsilon^2}. \tag{A.16}$$

For N number of atoms, we see that $\widehat{m}_j = \sum_{k=1}^N \widehat{\sigma}_j^k$ and $\widehat{N}_j = \sum_{k=1}^N \widehat{\eta}_j^k$, (where $j = a, b, c$). Hence, the operators $\widehat{N}_a$, $\widehat{N}_b$, and $\widehat{N}_c$ represent the number of atoms in the top, middle, and bottom levels, respectively. In addition, employing the completeness relation

$$\widehat{\eta}_a^k + \widehat{\eta}_b^k + \widehat{\eta}_c^k = \widehat{I}, \tag{A.17}$$

we easily arrive at

$$\left\langle\widehat{N}_a\right\rangle + \left\langle\widehat{N}_b\right\rangle + \left\langle\widehat{N}_c\right\rangle = N. \tag{A.18}$$

Furthermore, using the definition $\widehat{\sigma}_a^k = |b\rangle_{kk}\langle a|$ and setting for any k, $\widehat{\sigma}_a^k = |b\rangle\langle a|$, we have $\widehat{m}_a = N|b\rangle\langle a|$. Following the same procedure, one can also easily establish that $\widehat{m}_b = N|c\rangle\langle b|$, $\widehat{m}_c = N|c\rangle\langle a|$, $\widehat{N}_a = N|a\rangle\langle a|$, $\widehat{N}_b = N|b\rangle\langle b|$, and $\widehat{N}_c = N|c\rangle\langle c$. Using the definition $\widehat{m} = \widehat{m}_a + \widehat{m}_b$, [27] it can be readily established that

$$\begin{cases} m\wedge^{\dagger}\widehat{m} = N\left(\widehat{N}_a + \widehat{N}_b\right),\\ \widehat{m}m\wedge^{\dagger} = N\left(\widehat{N}_b + \widehat{N}_c\right),\\ m\wedge^2 = N\widehat{m}_c. \end{cases} \tag{A.19}$$

Data Availability

The data used to findings the study are included within the article.

Conflicts of Interest

The authors declare that there is no conflict of interest regarding the publication of this paper.

Acknowledgments

It is our pleasure to thank Jimma University, College of Natural Sciences Research and Postgraduate Coordination Office for all they did for us, their help, encouragement, and financial support during our research.

References

[1] C. W. Gardiner, "Inhibition of atomic phase decays by squeezed light: a direct effect of squeezing," *Physical Review Letters*, vol. 56, no. 18, pp. 1917–1920, 1986.

[2] S. Qamar, S. Qamar, and M. S. Zubairy, "Effect of phase fluctuations on entanglement generation in a correlated emission laser with injected coherence," *Optics communications*, vol. 283, no. 5, pp. 781–785, 2010.

[3] T. Abebe, "Enhancement of squeezing and entanglement in a non-degenerate three-level cascade laser with coherently driven cavity," *Ukrainian Journal of Physics*, vol. 63, no. 8, pp. 733–739, 2018.

[4] E. Alebachew, "Enhanced squeezing and entanglement in a non-degenerate three-level cascade laser with injected squeezed light," *Optics Communication*, vol. 280, no. 1, pp. 133–141, 2007.

[5] S. Tesfa, "Effect of dephasing on quantum features of the cavity radiation of an externally pumped correlated emission laser," *Physical Review A*, vol. 79, no. 6, article 063815, 2009.

[6] N. A. Ansari, J. G. Banacloche, and M. S. Zubairy, "Phase-sensitive amplification in a three-level atomic system," *Physical Review A*, vol. 41, no. 9, pp. 5179–5186, 1990.

[7] T. Abebe, "The quantum analysis of nondegenerate three-level laser with spontaneous emission and noiseless vacuum reservoir," *Ukrainian Journal of Physics*, vol. 63, no. 11, pp. 969–978, 2018.

[8] T. Abebe, "Coherently driven nondegenerate three-level laser with noiseless vacuum reservoir," *Bulgarian Journal of Physics*, vol. 45, no. 4, pp. 357–373, 2018.

[9] H. Xiong, M. O. Scully, and M. S. Zubairy, "Correlated spontaneous emission laser as an entanglement amplifier," *Physical Review Letters*, vol. 94, no. 2, article 023601, 2005.

[10] C. Gashu, E. Mosisa, and T. Abebe, "Entanglement quantification of correlated photons generated by three-level laser with parametric amplifier and coupled to a two-mode vacuum reservoir," *Advances in Mathematical Physics*, vol. 2020, 14 pages, 2020.

[11] C. Gashu and T. Abebe, "Externally induced entanglement amplification in a coherently pumped emission of laser with parametric amplifier and coupled to squeezed vacuum reservoir," *Physica Scripta*, vol. 95, no. 7, p. 075105, 2020.

[12] T. Abebe, N. Gemechu, C. Gashu, K. Shogile, S. Hailemariam, and S. Adisu, "The quantum analysis of nonlinear optical parametric processes with thermal reservoirs," *International Journal of Optics*, vol. 2020, 11 pages, 2020.

[13] T. Abebe, N. Gemechu, K. Shogile, S. Hailemariam, C. Gashu, and S. Adisu, "Entanglement quantification using various inseparability criteria for correlated photons," *Romanian Journal of Physics*, vol. 65, no. 3-4, p. 107, 2020.

[14] J. Anwar and M. S. Zubairy, "Quantum-statistical properties of noise in a phase-sensitive linear amplifier," *Physical Review A*, vol. 49, no. 1, pp. 481–484, 1994.

[15] C. A. Blockley and D. F. Walls, "Intensity fluctuations in a frequency down-conversion process with three-level atoms," *Physical Review A*, vol. 43, no. 9, pp. 5049–5056, 1991.

[16] N. Lu, F. X. Zhao, and J. Bergou, "Nonlinear theory of a two-photon correlated-spontaneous-emission laser: a coherently pumped two-level-two-photon laser," *Physical Review A*, vol. 39, no. 10, pp. 5189–5208, 1989.

[17] B. Daniel and K. Fesseha, "The propagator formulation of the degenerate parametric oscillator," *Optics Communication*, vol. 151, no. 4-6, pp. 384–394, 1998.

[18] F. Kassahun, *Fundamental of Quantum Optics*, Lulu, North Carolina, 2008.

[19] S. Tesfa, "Continuous variable entanglement in a coherently pumped correlated emission laser," *Journal of Physics B: Atomic, Molecular and Optical Physics*, vol. 41, no. 5, article 055503, 2008.

[20] G. New, *Introduction to Nonlinear Optics*, Cambridge University Press, New York, 2011.

[21] W. H. Louisell, *Quantum Statistical Properties of Radiation*, Wiley, New York, 1973.

[22] E. Alebachew and K. Fesseha, "A degenerate three-level laser with a parametric amplifier," *Optics Communication*, vol. 265, no. 1, pp. 314–321, 2006.

[23] S. Tesfa, "Entanglement amplification in a nondegenerate three-level cascade laser," *Physical Review A*, vol. 74, no. 4, article 043816, 2006.

[24] F. Kassahun, *Refined Quantum Analysis of Light*, Create Space Independent Publishing Platform, United States, 2014.

[25] F. Kassahun, *Three-Level Laser Dynamics with the Atoms Pumped by Electron Bombardment*, 2012, https://arxiv.org/abs/1105.1438v3.

[26] B. Teklu, "Parametric oscillation with the cavity mode driven by coherent light and coupled to a squeezed vacuum reservoir," *Optics Communication*, vol. 261, no. 2, pp. 310–321, 2006.

[27] F. Kassahun, "Stimulated emission by two-level atoms pumped to the upper level," *Optics Communication*, vol. 284, no. 5, pp. 1357–1363, 2011.

Hindawi
Advances in Mathematical Physics
Volume 2020, Article ID 3758353, 17 pages
https://doi.org/10.1155/2020/3758353

Research Article

Mechanical Solving a Few Fractional Partial Differential Equations and Discussing the Effects of the Fractional Order

Kai Fan [1,2,3,4] **and Cunlong Zhou** [1,2,3]

[1]*Engineering Research Center of Heavy Machinery Ministry of Education, Taiyuan University of Science and Technology, Taiyuan 030024, China*
[2]*Mechanical Engineering College, Taiyuan University of Science and Technology, Taiyuan 030024, China*
[3]*Shanxi Provincial Key Laboratory of Metallurgical Device Design Theory and Technology, Taiyuan University of Science and Technology, Taiyuan 030024, China*
[4]*Applied Science College, Taiyuan University of Science and Technology, Taiyuan 030024, China*

Correspondence should be addressed to Kai Fan; 2014279@tyust.edu.cn and Cunlong Zhou; zcunlong@tyust.edu.cn

Received 26 May 2020; Revised 31 July 2020; Accepted 6 September 2020; Published 30 September 2020

Academic Editor: Zhi-Yuan Sun

With the help of Maple, the precise traveling wave solutions of three fractal-order model equations related to water waves, including hyperbolic solutions, trigonometric solutions, and rational solutions, are obtained by using function expansion method. An isolated wave solution is selected from the solution of each nonlinear dispersive wave model equation, and the influence of fractional order change on these isolated wave solutions is discussed. The results show that the fractional derivatives can modulate the waveform, local periodicity, and structure of the isolated solutions of the three model equations. We also point out the construction rules of the auxiliary equations of the extended (G'/G)-expansion method. In the "The Explanation and Discussion" section, a more generalized auxiliary equation is used to further emphasize the rules, which has certain reference value for the construction of the new auxiliary equations. The solutions of fractional-order nonlinear partial differential equations can be enriched by selecting other solvable equations as auxiliary equations.

1. Introduction

Because of many phenomena, integer-order differential equations cannot be well described, which makes fractional nonlinear differential equations have research significance. As an effective mathematical modeling tool, it is widely used in the mathematical modeling of nonlinear phenomena in biology, physics, signal processing, control theory, system recognition, and other scientific fields [1–4]. In order to better understand the mechanism behind the phenomena described by nonlinear fractional partial differential equations, it is necessary to obtain the exact solution, which also provides a reference for the accuracy and stability of the numerical solution. With the rapid development of computer algebraic system-based nonlinear sciences like Mathematica or Maple, divers' effective methods have been pulled out to acquire precise solutions to nonlinear fractional-order partial differential equations, such as the fractional first integral method [5, 6], the fractional simplest equation method [7, 8], the improved fractional subequation method [9], the Kudryashov method [10], the fractional subequation method [11, 12], the generalised Kudryashov method [13], the fractional exp-function method [14–19], the sech-tanh function expansion method [20, 21], the fractional (G'/G)-expansion method [22–29], the generalized Sinh-Gorden expansion method [30], the fractional functional variable method [31], the rational (G'/G)-expansion method [32], the modified Khater method [33–36], and the fractional modified trial

equation method [37, 38]. Many of these methods are constructed by fractional complex transform [39, 40] and use of the solutions of some solvable differential equations. However, there is no one way to solve all kinds of nonlinear problems, and for the same nonlinear differential equation, different methods will give you different forms of solutions. There are many articles about solving different equations by different methods, but the effect of fractional order on the solution is rarely discussed.

The first model equation we want to solve is the fractional-order Boussinesq equation in space and time, which is suitable for studying the propagation of water in heterogeneous porous media [41].

$$D_t^{2\alpha}u(x,t) + AD_x^{2\beta}[u(x,t)]^2 + BD_x^{2\beta}u(x,t) + ED_x^{4\beta}u(x,t) = 0, \quad 0 < \alpha, \beta \le 1, t > 0, \tag{1}$$

for the case of $\beta = \alpha$ [42]:

$$D_t^{2\alpha}u(x,t) + AD_x^{2\alpha}[u(x,t)]^2 + BD_x^{2\alpha}u(x,t) + ED_x^{4\alpha}u(x,t) = 0. \tag{2}$$

where $u(x,t)$ represents displacement. A, B, and E are constant coefficients. α and β are fractional derivatives. When $\alpha = \beta = 1$, equation (1) curtails to the Boussinesq equation of the form

$$u_{tt} + A\left(u^2\right)_{xx} + Bu_{xx} + Eu_{xxxx} = 0. \tag{3}$$

Equation (3) was first derived by Boussinesq when he studied the propagation of nonviscous shallow water waves [43–45]. Darvishi et al. obtained solitary wave solutions of some equations similar to Boussinesq in literature [46]. Combined with fractional complex transformation, we obtain multiple traveling wave solutions of equation (2) using extended (G'/G)-expansion method and show the effect of fractional order parameters on the waveform of an isolated wave solution of these solutions.

The second model equation we solved was a diffusion model describing shallow water waves (the time fractional-order Boussinesq-Burgers equation) [47].

$$\begin{aligned} D_t^{\alpha}u(x,t) - \frac{1}{2}v_x(x,t) + 2u_x(x,t) &= 0, \\ D_t^{\alpha}v(x,t) - \frac{1}{2}u_{xxx}(x,t) + 2(uv)_x(x,t) &= 0, \\ 0 < \alpha \le 1. \end{aligned} \tag{4}$$

There are several ways to solve this equation. For example, Javeed et al. solved it by the first integral method [47], and Kumar et al. solved it by the residual power series method [48].

Combined with fractional complex transformation, we obtain multiple traveling wave solutions of equation (4) using (G'/G)-expansion method and show the effect of fractional order parameters on the waveform of an isolated wave solution of these solutions.

Finally, the third model equation that we want to solve can simulate the propagation of surface water waves with a depth far less than the horizontal scale, which is the fractional coupled Boussinesq equations in space and time [49].

$$\begin{aligned} D_t^{\alpha}u(x,t) + D_x^{\beta}v(x,t) &= 0, \\ D_t^{\alpha}v(x,t) + AD_x^{\beta}\left(u^2(x,t)\right) - ED_{xxx}^{3\beta}u(x,t) &= 0, \\ 0 < \alpha, \beta \le 1. \end{aligned} \tag{5}$$

There are several ways to solve this system of equations. For example, Yaslan and Girgin solved it by the first integral method [49], Hosseini and Ansari obtained its solution by the modified Kudryashov method [50], and Hoseini et al. solved it by the $\exp(-\phi(\varepsilon))$-expansion method [51]. Combined with fractional complex transformation, we obtain multiple traveling wave solutions of equation (5) using extended (G'/G)-expansion method and show the effect of fractional order parameters on the waveform of an isolated wave solution of these solutions.

Given a function $f : [0,\infty] \longrightarrow R$. Then, the conformable fractional derivative of f of order $0 < \alpha < 1$ is defined as [52]

$$D_x^{\alpha}(f)(x) = \lim_{\varepsilon \to 0} \frac{f\left(x + \varepsilon x^{1-\alpha}\right) - f(x)}{\varepsilon}. \tag{6}$$

The derivative has the following properties [53].

$$\begin{cases} D_x^{\alpha}C = 0, \\ D_x^{\alpha}x^{\gamma} = \gamma x^{\gamma-\alpha}, \quad \text{for all } \gamma \in R, \\ (u(x)v(x))^{(\alpha)} = u^{(\alpha)}(x)v(x) + u(x)v^{(\alpha)}(x), \\ (f[u(x)])^{(\alpha)} = x^{1-\alpha}f'_u(u)u'(x). \end{cases} \tag{7}$$

2. The (G'/G)-Expansion Method Combined with Fractional Complex Transformation and Its Extension Method

Consider nonlinear fractional partial differential equations

$$P\left(u, D_t^{\alpha}u, D_x^{\beta}u, D_t^{\alpha}D_t^{\alpha}u, D_x^{\beta}D_t^{\alpha}u, D_x^{\beta}D_x^{\beta}u, , \cdots\right) = 0, \quad 0 < \alpha, \beta \le 1, \tag{8}$$

where u is the unsolved function of the variables x and t. P is a polynomial function, which consists of u and its fractional derivatives.

The fractional (G'/G)-expansion method and extended fractional (G'/G)-expansion method are used to solve equation (8); the steps are listed as follows:

Step 1. Under the fractional complex transform,

$$u(x,t) = U(\xi), \quad \xi = \frac{x^\beta}{\beta} - \frac{ct^\alpha}{\alpha}, \tag{9}$$

where c is a constant, and it cannot be zero. When $\alpha = \beta = 1$, equation (9) is the usual travelling wave variation.

In the complex fraction transformation, we get

$$\begin{aligned} D_t^\alpha(\cdot) &= -c\frac{d(\cdot)}{d\xi}, \\ D_x^\beta(\cdot) &= \frac{d(\cdot)}{d\xi}, \\ D_{xx}^{2\alpha}(\cdot) &= c^2\frac{d^2(\cdot)}{d\xi^2}, \\ D_x^\beta D_x^\alpha(\cdot) &= -c\frac{d^2(\cdot)}{d\xi^2}, \\ D_{xx}^{2\beta}(\cdot) &= \frac{d^2(\cdot)}{d\xi^2}\cdots. \end{aligned} \tag{10}$$

Substituting (9) and (10) into (8), a nonlinear ordinary differential equation is formulated

$$P\left(U, -cU', U', c^2U'', -cU'', U'', \cdots\right) = 0, \tag{11}$$

where $^{\cdot}U'^{\cdot} = dU/d\xi$. If the form of equation (11) allows, we can integrate first and set the integral constant to zero, which will help simplify the following calculation.

Step 2. For the fractional (G'/G)-expansion method, we assume that equation (11) has a quasisolution of equation (11) of the following form

$$U(\xi) = \sum_{i=0}^{m} a_i \left(\frac{G'}{G}\right)^i. \tag{12}$$

For the extended fractional (G'/G)-expansion method, we assume that equation (11) has a quasisolution of the following form

$$U(\xi) = \sum_{i=0}^{m} a_i \left(\frac{G'}{G}\right)^i + \sum_{i=1}^{m} b_i \left(\frac{G}{G'}\right)^i, \tag{13}$$

where $a_i (i = 0, 1, \cdots, m)$ and $b_i (i = 1, 2, \cdots, m)$ are undetermined constants. In combination with the form of equation (12) or (13), the highest derivative term and the nonlinear term in equation (11) are balanced by the homogeneous equilibrium principle, and the value of the positive integer in equation (12) or (13) can be obtained. Let us say that the degree of $U(\xi)$ is $D(U(\xi)) = m$, and then, we can easily derive the degrees of other forms of terms as follows:

$$D\left(\frac{d^qU}{d\xi^q}\right) = m + q, D\left[U^p\left(\frac{d^qU}{d\xi^q}\right)^s\right] = pm + s(m+q). \tag{14}$$

Thus, the value of m in equation (12) or equation (13) can be determined. The $G = G(\xi)$ appearing in equation (12) or (13) is the solution of the second-order differential equation below.

$$G'' + \lambda G' + \mu G = 0, \tag{15}$$

where λ and μ are undetermined constants. In addition, the derivative of (G'/G) is

$$\frac{d}{\xi}\left(\frac{G'}{G}\right) = \frac{G''G - \left(G'\right)^2}{G^2} = \frac{G''G}{G^2} - \left(\frac{G'}{G}\right)^2. \tag{16}$$

Equation (16) reveals that we can set the ordinary differential equation (15) to the following form or some other ordinary differential equation can make equation (11) in polynomial form of (G'/G) [54].

$$G''G = \lambda\left(G'\right)^2 + \mu GG' + \omega G^2, \tag{17}$$

where λ, μ, and ω are undetermined constants.

Step 3. Substitute equation (12) or (13) into equation (11), use ordinary differential equation (15) concerning (G'/G) to combine the same power terms of (G'/G), then set the coefficients of all powers of (G'/G) to zero, we get a nonlinear algebraic system of equations concerning the unknowns a_i, b_i, λ, μ, and c.

Step 4. We can use Maple to solve the equations obtained in the third step. By substituting the obtained results into equation (12) or (13) and using the general solutions of equation (15) in different situations, multiple exact solutions of different types of equation (8) can be obtained.

The solutions of equation (15) under different conditions are shown below.

$$\left(\frac{G'}{G}\right)=\begin{cases}\dfrac{\sqrt{\lambda^2-4\mu}}{2}\left(\dfrac{C_1\sinh\left(\left(\sqrt{\lambda^2-4\mu}/2\right)\xi\right)+C_2\cosh\left(\left(\sqrt{\lambda^2-4\mu}/2\right)\xi\right)}{C_1\cosh\left(\left(\sqrt{\lambda^2-4\mu}/2\right)\xi\right)+C_2\sinh\left(\left(\sqrt{\lambda^2-4\mu}/2\right)\xi\right)}\right)-\dfrac{\lambda}{2}, & \lambda^2-4\mu>0,\\ \dfrac{\sqrt{4\mu-\lambda^2}}{2}\left(\dfrac{-C_1\sin\left(\left(\sqrt{4\mu-\lambda^2}/2\right)\xi\right)+C_2\cos\left(\left(\sqrt{4\mu-\lambda^2}/2\right)\xi\right)}{C_1\cos\left(\left(\sqrt{4\mu-\lambda^2}/2\right)\xi\right)+C_2\sin\left(\left(\sqrt{4\mu-\lambda^2}/2\right)\xi\right)}\right)-\dfrac{\lambda}{2}, & \lambda^2-4\mu<0,\\ \dfrac{C_2}{C_1+C_2\xi}-\dfrac{\lambda}{2}, & \lambda^2-4\mu=0,\end{cases}\tag{18}$$

where C_1 and C_2 are free constants.

When C_1 and C_2 satisfy different conditions, these results can be further written in simpler forms.

$$\left(\frac{G'}{G}\right)=\begin{cases}\dfrac{\sqrt{\lambda^2-4\mu}}{2}\tanh\left(\dfrac{\sqrt{\lambda^2-4\mu}}{2}\xi+\xi_0\right)-\dfrac{\lambda}{2}, & \lambda^2-4\mu>0,\ \tanh(\xi_0)=\dfrac{C_2}{C_1},\ \left|\dfrac{C_2}{C_1}\right|<1,\\ \dfrac{\sqrt{\lambda^2-4\mu}}{2}\coth\left(\dfrac{\sqrt{\lambda^2-4\mu}}{2}\xi+\xi_0\right)-\dfrac{\lambda}{2}, & \lambda^2-4\mu>0,\ \coth(\xi_0)=\dfrac{C_2}{C_1},\ \left|\dfrac{C_2}{C_1}\right|>1,\\ \dfrac{\sqrt{4\mu-\lambda^2}}{2}\cot\left(\dfrac{\sqrt{4\mu-\lambda^2}}{2}\xi+\xi_0\right)-\dfrac{\lambda}{2}, & \lambda^2-4\mu<0,\ \cot(\xi_0)=\dfrac{C_2}{C_1},\\ \dfrac{C_2}{C_1+C_2\xi}-\dfrac{\lambda}{2}, & \lambda^2-4\mu=0.\end{cases}\tag{19}$$

The solutions of equation (17) under different conditions are shown below.

$$\left(\frac{G'}{G}\right)=\begin{cases}\dfrac{\sqrt{\mu^2+4\omega-4\lambda\omega}}{2(1-\lambda)}\left(\dfrac{C_1\sinh\left(\left(\sqrt{\mu^2+4\omega-4\lambda\omega}/2\right)\xi\right)+C_2\cosh\left(\left(\sqrt{\mu^2+4\omega-4\lambda\omega}/2\right)\xi\right)}{C_1\cosh\left(\left(\sqrt{\mu^2+4\omega-4\lambda\omega}/2\right)\xi\right)+C_2\sinh\left(\left(\sqrt{\mu^2+4\omega-4\lambda\omega}/2\right)\xi\right)}\right)+\dfrac{\mu}{2(1-\lambda)}, & \left(\mu^2-4(\lambda-1)\,\omega>0,\lambda\neq1\right),\\ \dfrac{\sqrt{4\lambda\omega-4\omega-\mu^2}}{2(1-\lambda)}\left(\dfrac{-C_1\sin\left(\left(\sqrt{4\lambda\omega-4\omega-\mu^2}/2\right)\xi\right)+C_2\cos\left(\left(\sqrt{4\lambda\omega-4\omega-\mu^2}/2\right)\xi\right)}{C_1\cos\left(\left(\sqrt{4\lambda\omega-4\omega-\mu^2}/2\right)\xi\right)+C_2\sin\left(\left(\sqrt{4\lambda\omega-4\omega-\mu^2}/2\right)\xi\right)}\right)+\dfrac{\mu}{2(1-\lambda)}, & \left(\mu^2-4(\lambda-1)\,\omega<0,\lambda\neq1\right),\\ \dfrac{1}{1-\lambda}\left(\dfrac{C_1}{C_1\xi+C_2}+\dfrac{\mu}{2}\right) & \left(\mu^2-4(\lambda-1)\,\omega=0,\lambda\neq1\right).\end{cases}\tag{20}$$

3. Applications of Fractional (G'/G)-Expansion Method and Its Extended Methods

3.1. Precise Solutions of the Fractional Boussinesq Equation in Space and Time with Generalised Fractional (G'/G)-Expansion Method. Equation (2) is written as follows.

$$D_t^{2\alpha}u(x,t) + AD_x^{2\alpha}[u(x,t)]^2 + BD_x^{2\alpha}u(x,t) + ED_x^{4\alpha}u(x,t) = 0. \tag{21}$$

Under the fractional complex transform,

$$u(x,t) = U(\xi), \quad \xi = \frac{x^\alpha}{\alpha} - \frac{ct^\alpha}{\alpha}. \tag{22}$$

Substituting (22) into (21), we convert our problem into a nonlinear ordinary differential equation.

$$c^2U'' + A\left(U^2\right)'' + BU'' + EU'''' = 0, \tag{23}$$

where $''U'''' = dU/d\xi$. By integrating twice with respect to travelling wave variable factor ξ and setting the constant from the integral to 0, you get the following equation.

$$\left(c^2 + B\right)U + AU^2 + EU'' = 0. \tag{24}$$

Applying the homogeneous equilibrium principle to equation (24), we get $2 + m = 2m \Longrightarrow m = 2$. By taking m to be 2 in equation (13), we get the form of the proposed solution of equation (24) as follows.

$$U(\xi) = a_0 + a_1\frac{G'}{G} + a_2\left(\frac{G'}{G}\right)^2 + b_1\left(\frac{G'}{G}\right)^{-1} + b_2\left(\frac{G'}{G}\right)^{-2}. \tag{25}$$

By using equation (15), from equation (25), we have

$$\begin{aligned} U^2(\xi) = {} & {b_2}^2\left(\frac{G'}{G}\right)^{-4} + 2b_1\left(\frac{G'}{G}\right)^{-3}b_2 + \left(2a_0b_2 + {b_1}^2\right)\left(\frac{G'}{G}\right)^{-2} \\ & + \left(2a_0b_1 + 2a_1b_2\right)\left(\frac{G'}{G}\right)^{-1} + {a_0}^2 + 2a_1b_1 + 2a_2b_2 \\ & + \left(2a_0a_1 + 2a_2b_1\right)\left(\frac{G'}{G}\right)^{1} + \left(2a_0a_2 + {a_1}^2\right)\left(\frac{G'}{G}\right)^{2} \\ & + 2a_1a_2\left(\frac{G'}{G}\right)^{3} + {a_2}^2\left(\frac{G'}{G}\right)^{4}, \end{aligned} \tag{26}$$

$$\begin{aligned} U''(\xi) = {} & 6b_2\mu^2\left(\frac{G'}{G}\right)^{-4} + \left(2b_1\mu^2 + 10b_2\lambda\mu\right)\left(\frac{G'}{G}\right)^{-3} \\ & + \left(3b_1\lambda\mu + 4b_2\lambda^2 + 8b_2\mu\right)\left(\frac{G'}{G}\right)^{-2} \\ & + \left(b_1\lambda^2 + 2b_1\mu + 6b_2\lambda\right)\left(\frac{G'}{G}\right)^{-1} \\ & + 2a_2\mu^2 + a_1\lambda\mu + b_1\lambda + 2b_2 \\ & + \left(6a_2\lambda\mu + a_1\lambda^2 + 2a_1\mu\right)\left(\frac{G'}{G}\right)^{1} \\ & + \left(4a_2\lambda^2 + 8a_2\mu + 3a_1\lambda\right)\left(\frac{G'}{G}\right)^{2} \\ & + \left(10a_2\lambda + 2a_1\right)\left(\frac{G'}{G}\right)^{3} + 6a_2\left(\frac{G'}{G}\right)^{4}. \end{aligned} \tag{27}$$

Equations (25), (26), and (27) are substituted into equation (24), and then, we can rearrange and combine equation (24) with respect to (G'/G) and set the coefficients of all powers of (G'/G) to be zero. The resulting nonlinear algebraic system with respect to the unknowns a_0, a_1, a_2, b_1, b_2, and c is as follows.

$$\left(\frac{G'}{G}\right)^{-4}: 6E\mu^2b_2 + Ab_2^2 = 0,$$

$$\left(\frac{G'}{G}\right)^{-3}: 2E\mu^2b_1 + 10E\mu\lambda b_2 + 2Ab_1b_2 = 0,$$

$$\left(\frac{G'}{G}\right)^{-2}: 3E\mu\lambda b_1 + 4E\lambda^2b_2 + 2Aa_0b_2 + Ab_1^2 + 8E\mu b_2 + c^2b_2 + Bb_2 = 0,$$

$$\left(\frac{G'}{G}\right)^{-1}: 2Aa_1b_2 + c^2b_1 + 2Aa_0b_1 + 6Eb_2\lambda + Bb_1 + Eb_1\lambda^2 + 2Eb_1\mu = 0,$$

$$\left(\frac{G}{G'}\right)^{0}: 2Eb_2 + c^2a_0 + Ba_0 + 2Ea_2\mu^2 + Ea_1\lambda\mu + 2Aa_2b_2 + 2Aa_1b_1 + Aa_0^2 + Eb_1\lambda = 0,$$

$$\frac{G'}{G}: 2Ea_1\mu + 2Aa_2b_1 + c^2a_1 + Ba_1 + 6Ea_2\lambda\mu + Ea_1\lambda^2 + 2Aa_0a_1 = 0,$$

$$\left(\frac{G'}{G}\right)^2 : 4E\lambda^2 a_2 + 2Aa_0a_2 + Aa_1^2 + 8E\mu a_2 + 3E\lambda a_1 + c^2 a_2 + Ba_2 = 0,$$

$$\left(\frac{G'}{G}\right)^3 : 2Aa_1a_2 + 10E\lambda a_2 + 2Ea_1 = 0,$$

$$\left(\frac{G'}{G}\right)^4 : Aa_2^2 + 6Ea_2 = 0. \tag{28}$$

The nonlinear algebraic equations were solved by using Maple symbol computing system, and the following solutions were obtained.

Case 1.

$$\left\{c = \pm\sqrt{-E\lambda^2 + 4E\mu - B}, a_0 = -\frac{6E\mu}{A}, a_1 = -\frac{6E\lambda}{A}, a_2 = -\frac{6E}{A}, b_1 = 0, b_2 = 0\right\}. \tag{29}$$

Case 2.

$$\left\{c = \pm\sqrt{E\lambda^2 - 4E\mu - B}, a_0 = -\frac{E\left(\lambda^2 + 2\mu\right)}{A}, a_1 = -\frac{6E\lambda}{A}, a_2 = -\frac{6E}{A}, b_1 = 0, b_2 = 0\right\}. \tag{30}$$

Substituting the values from (29) or (30) and equation (18) into (25), the exact solutions of equation (21) in different forms can be obtained under different parameter constraints.

Case 1. When λ^2-$4\mu > 0$, the exact solution of equation (21) in hyperbolic form is as follows.

$$U_{1,2}^1(\xi) = -\frac{6E}{A}\left[\mu + \lambda\left[-\frac{\lambda}{2} + \eta_1\left(\frac{C_1\sinh(\eta_1\xi) + C_2\cosh(\eta_1\xi)}{C_1\cosh(\eta_1\xi) + C_2\sinh(\eta_1\xi)}\right)\right] + \left[-\frac{\lambda}{2} + \eta_1\left(\frac{C_1\sinh(\eta_1\xi) + C_2\cosh(\eta_1\xi)}{C_1\cosh(\eta_1\xi) + C_2\sinh(\eta_1\xi)}\right)\right]^2\right], \tag{31}$$

where $\xi = (x^\alpha/\alpha) \mp (\sqrt{-E\lambda^2 + 4E\mu - B}t^\alpha/\alpha)$, and $\eta_1 = 1/2\sqrt{\lambda^2 - 4\mu}$. C_1 and C_2 are constants that can take any number.

If $C_1 \neq 0$, and $C_2 = 0$, then $U_{1,2}^1(\xi)$ become

$$u_{1,2}^1(x,t) = U_{1,2}^1(\xi) = -\frac{6E}{A}\left[\mu + \lambda\left[-\frac{\lambda}{2} + \eta_1\tanh(\eta_1\xi)\right] + \left[-\frac{\lambda}{2} + \eta_1\tanh(\eta_1\xi)\right]^2\right]. \tag{32}$$

Again, using (19), the general solutions for $U_{1,2}^1(\xi)$ in simplified forms are written as

$$\dot{U}_{1,2}^1(\xi) = -\frac{6E}{A}\left[\mu + \lambda\left[-\frac{\lambda}{2} + \eta_1\tanh(\eta_1\xi + \xi_0)\right] + \left[-\frac{\lambda}{2} + \eta_1\tanh(\eta_1\xi + \xi_0)\right]^2\right], \tag{33}$$

when $|C_2/C_1| < 1$, and $\xi_0 = \tanh^{-1}(C_2/C_1)$.

$$\ddot{U}_{1,2}^1(\xi) = -\frac{6E}{A}\left[\mu + \lambda\left[-\frac{\lambda}{2} + \eta_1\coth(\eta_1\xi + \xi_0)\right] + \left[-\frac{\lambda}{2} + \eta_1\coth(\eta_1\xi + \xi_0)\right]^2\right], \tag{34}$$

when $|C_2/C_1| > 1$, and $\xi_0 = \coth^{-1}(C_2/C_1)$.

When λ^2-$4\mu < 0$, the exact solution of equation (21) in trigonometric form is as follows.

$$U_{3,4}^1(\xi) = -\frac{6E}{A}\left[\mu + \lambda\left[-\frac{\lambda}{2} + \eta_2\left(\frac{-C_1\sin(\eta_2\xi) + C_2\cos(\eta_2\xi)}{C_1\cos(\eta_2\xi) + C_2\sin(\eta_2\xi)}\right)\right] + \left[-\frac{\lambda}{2} + \eta_2\left(\frac{-C_1\sin(\eta_2\xi) + C_2\cos(\eta_2\xi)}{C_1\cos(\eta_2\xi) + C_2\sin(\eta_2\xi)}\right)\right]^2\right], \tag{35}$$

where $\xi = (x^\alpha/\alpha) \mp (\sqrt{-E\lambda^2 + 4E\mu - B}t^\alpha/\alpha)$, and $\eta_2 = 1/2\sqrt{4\mu - \lambda^2}$. C_1 and C_2 are constants that can take any number.

In particular, if $C_1 \neq 0$, and $C_2 = 0$, then $U_{3,4}^1(\xi)$ become

$$u_{3,4}^1(x,t) = U_{3,4}^1(\xi) = -\frac{6E}{A}\left[\mu - \lambda\left[\frac{\lambda}{2} + \eta_2\tan(\eta_2\xi)\right] + \left[\frac{\lambda}{2} + \eta_2\tan(\eta_2\xi)\right]^2\right]. \tag{36}$$

When λ^2-$4\mu = 0$, the exact solution of equation (21) in rational form is as follows.

$$U_{5,6}^1(\xi) = -\frac{6E}{A}\left[\mu + \lambda\left[-\frac{\lambda}{2} + \frac{C_2}{C_1 + C_2\xi}\right] + \left[-\frac{\lambda}{2} + \frac{C_2}{C_1 + C_2\xi}\right]^2\right], \tag{37}$$

where $\xi = (x^\alpha/\alpha) \mp (\sqrt{-E\lambda^2 + 4E\mu - B}t^\alpha/\alpha)$. C_1 and C_2 are constants that can take any number.

Case 2. When λ^2-$4\mu > 0$, the exact solution of equation (21) in hyperbolic form is as follows.

$$U_{1,2}^2(\xi) = -\frac{6E}{A}\left[\frac{(\lambda^2+2\mu)}{6} + \lambda\left[-\frac{\lambda}{2} + \eta_1\left(\frac{C_1\sinh(\eta_1\xi) + C_2\cosh(\eta_1\xi)}{C_1\cosh(\eta_1\xi) + C_2\sinh(\eta_1\xi)}\right)\right] + \left[-\frac{\lambda}{2} + \eta_1\left(\frac{C_1\sinh(\eta_1\xi) + C_2\cosh(\eta_1\xi)}{C_1\cosh(\eta_1\xi) + C_2\sinh(\eta_1\xi)}\right)\right]^2\right], \tag{38}$$

where $\xi = (x^\alpha/\alpha) \mp (\sqrt{E\lambda^2 - 4E\mu - B}t^\alpha/\alpha)$, and $\eta_1 = 1/2\sqrt{\lambda^2 - 4\mu}$. C_1 and C_2 are constants that can take any number.

If $C_1 \neq 0$, and $C_2 = 0$, then $U_{1,2}^2(\xi)$ become

$$u_{1,2}^2(x,t) = U_{1,2}^2(\xi) = -\frac{6E}{A}\left[\frac{(\lambda^2+2\mu)}{6} + \lambda\left[-\frac{\lambda}{2} + \eta_1\tanh(\eta_1\xi)\right] + \left[-\frac{\lambda}{2} + \eta_1\tanh(\eta_1\xi)\right]^2\right]. \tag{39}$$

Again, using (19), the general solutions for $U_{1,2}^2(\xi)$ in simplified forms are written as

$$\dot{U}_{1,2}^2(\xi) = -\frac{6E}{A}\left[\frac{(\lambda^2+2\mu)}{6} + \lambda\left[-\frac{\lambda}{2} + \eta_1\tanh(\eta_1\xi + \xi_0)\right] + \left[-\frac{\lambda}{2} + \eta_1\tanh(\eta_1\xi + \xi_0)\right]^2\right], \tag{40}$$

when $|C_2/C_1| < 1$, and $\xi_0 = \tanh^{-1}(C_2/C_1)$.

$$\ddot{U}_{1,2}^2(\xi) = -\frac{6E}{A}\left[\frac{(\lambda^2+2\mu)}{6} + \lambda\left[-\frac{\lambda}{2} + \eta_1\coth(\eta_1\xi + \xi_0)\right] + \left[-\frac{\lambda}{2} + \eta_1\coth(\eta_1\xi + \xi_0)\right]^2\right], \tag{41}$$

when $|C_2/C_1| > 1$, and $\xi_0 = \coth^{-1}(C_2/C_1)$.

When λ^2-$4\mu < 0$, the exact solution of equation (21) in trigonometric form is as follows.

$$U_{3,4}^2(\xi) = -\frac{6E}{A}\left[\frac{(\lambda^2+2\mu)}{6} + \lambda\left[-\frac{\lambda}{2} + \eta_2\left(\frac{-C_1\sin(\eta_2\xi) + C_2\cos(\eta_2\xi)}{C_1\cos(\eta_2\xi) + C_2\sin(\eta_2\xi)}\right)\right] + \left[-\frac{\lambda}{2} + \eta_2\left(\frac{-C_1\sin(\eta_2\xi) + C_2\cos(\eta_2\xi)}{C_1\cos(\eta_2\xi) + C_2\sin(\eta_2\xi)}\right)\right]^2\right], \tag{42}$$

where $\xi = (x^\alpha/\alpha) \mp (\sqrt{E\lambda^2 - 4E\mu - B}t^\alpha/\alpha)$, and $\eta_2 = 1/2\sqrt{4\mu - \lambda^2}$. C_1 and C_2 are constants that can take any number.

In particular, if $C_1 \neq 0$, and $C_2 = 0$, then $U_{3,4}^2(\xi)$ become

$$u_{3,4}^2(x,t) = U_{3,4}^2(\xi) = -\frac{6E}{A}\left[\frac{(\lambda^2+2\mu)}{6} - \lambda\left[\frac{\lambda}{2} + \eta_2\tan(\eta_2\xi)\right] + \left[\frac{\lambda}{2} + \eta_2\tan(\eta_2\xi)\right]^2\right]. \tag{43}$$

When λ^2-$4\mu = 0$, the exact solution of equation (21) in rational form is as follows.

$$U_{5,6}^2(\xi) = -\frac{6E}{A}\left[\frac{(\lambda^2+2\mu)}{6} + \lambda\left[-\frac{\lambda}{2} + \frac{C_2}{C_1 + C_2\xi}\right] + \left[-\frac{\lambda}{2} + \frac{C_2}{C_1 + C_2\xi}\right]^2\right], \tag{44}$$

where $\xi = (x^\alpha/\alpha) \mp (\sqrt{E\lambda^2 - 4E\mu - B}t^\alpha/\alpha)$. C_1 and C_2 are constants that can take any number.

Similarly, if the auxiliary equation (17) and its solution (20) are used in the process of solving, we should also be able to get exact solutions, which we can prove later.

3.2. Precise Solutions of the Fractional Coupled Boussinesq-Burger Equation with Fractional (G'/G)-Expansion Method. Equation (4) is written as follows.

$$D_t^\alpha u(x,t) - \frac{1}{2}v_x(x,t) + 2u_x(x,t) = 0, \tag{45a}$$

$$D_t^\alpha v(x,t) - \frac{1}{2}u_{xxx}(x,t) + 2(uv)_x(x,t) = 0. \tag{45b}$$

Under the fractional complex transformations,

$$u(x,t) = U(\xi), \tag{46}$$

$v(x,t) = V(\xi)$,
$\xi = x - ct^\alpha/\alpha$.
We get the following output.

$$D_t^\alpha(\cdot) = -c\frac{d(\cdot)}{d\xi}, \quad \frac{\partial(\cdot)}{\partial x} = \frac{d(\cdot)}{d\xi}, \quad \frac{\partial^2(\cdot)}{\partial x^2} = \frac{d^2(\cdot)}{d\xi^2}, \tag{47}$$

$\partial^3(\cdot)/\partial x^3 = d^3(\cdot)/d\xi^3$.

Substituting (46) and (47) into (45a) and (45b), we convert our problem into nonlinear ordinary differential equations:

$$-cU' - \frac{1}{2}V' + 2UU' = 0, \tag{48a}$$

$$-cV' - \frac{1}{2}U''' + 2(UV)' = 0, \tag{48b}$$

where $''U'''' = dU/d\xi$. By integrating once with respect to travelling wave variable factor ξ and setting the constant from the integral to 0, you get the following equation.

$$-cU - \frac{1}{2}V + U^2 = 0, \tag{49a}$$

$$-cV - \frac{1}{2}U'' + 2UV = 0. \tag{49b}$$

From equation (49a), we get

$$V = 2\left(U^2 - cU\right). \tag{50}$$

Surrogating equation (50) in equation (49b)

$$-\frac{1}{2}U'' + 4U^3 - 6cU^2 + 2c^2U = 0. \tag{51}$$

Applying the homogeneous equilibrium principle to equation (51), we get $2 + m = 3m \Longrightarrow m = 1$. By taking m to be 1 in equation (12), we get the form of the proposed solution of equation (51) as follows.

$$U(\xi) = a_0 + a_1\frac{G'}{G}. \tag{52}$$

By using equations (15) and (52), from equation (51), we have

$$\begin{aligned} &4{a_0}^3 - 6c{a_0}^2 - 1/2a_1\lambda\mu + 2c^2a_0 + \left(12{a_0}^2a_1 + 2c^2a_1 - 1/2a_1\lambda^2\right.\\ &\left. - 12ca_0a_1 - a_1\mu\right)\frac{G'}{G} + \left(12a_0{a_1}^2 - 6c{a_1}^2 - 3/2a_1\lambda\right)\left(\frac{G'}{G}\right)^2\\ &+ \left(4{a_1}^3 - a_1\right)\left(\frac{G'}{G}\right)^3 = 0. \end{aligned} \tag{53}$$

The coefficients before all powers of (G'/G) in equation (53) are set as 0, and the resulting nonlinear algebraic system with respect to the unknowns a_0, a_1, and c is as follows.

$$\left(\frac{G}{G'}\right)^0 : 4{a_0}^3 - 6c{a_0}^2 - \frac{1}{2}a_1\lambda\mu + 2c^2a_0 = 0,$$

$$\frac{G'}{G} : 12{a_0}^2a_1 + 2c^2a_1 - \frac{1}{2}a_1\lambda^2 - 12ca_0a_1 - a_1\mu = 0,$$

$$\left(\frac{G'}{G}\right)^2 : 12a_0{a_1}^2 - 6c{a_1}^2 - \frac{3}{2}a_1\lambda = 0,$$

$$\left(\frac{G'}{G}\right)^3 : 4{a_1}^3 - a_1 = 0. \tag{54}$$

The symbolic computing system Maple was used to solve the nonlinear algebraic equations, and four sets of solutions were obtained.

Case 1.

$$\left\{c = -\frac{1}{2}\sqrt{\lambda^2 - 4\mu}, a_0 = -\frac{1}{4}\lambda - \frac{1}{4}\sqrt{\lambda^2 - 4\mu}, \quad a_1 = -\frac{1}{2}\frac{\lambda^2\left(\lambda + \sqrt{\lambda^2 - 4\mu}\right)}{\left(\lambda^2 - 4\mu\right)^{3/2} + \lambda^3 + 4\sqrt{\lambda^2 - 4\mu}\mu}\right\}. \tag{55}$$

Case 2.

$$\left\{c = -\frac{1}{2}\sqrt{\lambda^2 - 4\mu}, a_0 = \frac{1}{4}\lambda - \frac{1}{4}\sqrt{\lambda^2 - 4\mu}, \quad a_1 = \frac{1}{2}\frac{\lambda^2\left(-\lambda + \sqrt{\lambda^2 - 4\mu}\right)}{\left(\lambda^2 - 4\mu\right)^{3/2} - \lambda^3 + 4\sqrt{\lambda^2 - 4\mu}\mu}\right\}. \tag{56}$$

Case 3.

$$\left\{c = \frac{1}{2}\sqrt{\lambda^2 - 4\mu}, a_0 = -\frac{1}{4}\lambda + \frac{1}{4}\sqrt{\lambda^2 - 4\mu}, \quad a_1 = -\frac{1}{2}\frac{\lambda^2\left(-\lambda + \sqrt{\lambda^2 - 4\mu}\right)}{\left(\lambda^2 - 4\mu\right)^{3/2} - \lambda^3 + 4\sqrt{\lambda^2 - 4\mu}\mu}\right\}. \tag{57}$$

Case 4.

$$\left\{c = \frac{1}{2}\sqrt{\lambda^2 - 4\mu}, a_0 = \frac{1}{4}\lambda + \frac{1}{4}\sqrt{\lambda^2 - 4\mu}, \quad a_1 = \frac{1}{2}\frac{\lambda^2\left(\lambda + \sqrt{\lambda^2 - 4\mu}\right)}{\left(\lambda^2 - 4\mu\right)^{3/2} + \lambda^3 + 4\sqrt{\lambda^2 - 4\mu}\mu}\right\}. \tag{58}$$

Substituting the values from (55), (56), (57), or (58) and equation (18) into (52), the exact solutions of equations (45a) and (45b) in different forms can be obtained under different parameter constraints.

Case 1. When λ^2-$4\mu > 0$, the exact solution of equations (45a) and (45b) in hyperbolic form is as follows.

$$U_7^1(\xi) = -\frac{1}{4}\lambda - \frac{1}{4}\sqrt{\lambda^2-4\mu} - \frac{1}{2}\frac{\lambda^2\left(\lambda+\sqrt{\lambda^2-4\mu}\right)}{\left(\lambda^2-4\mu\right)^{3/2}+\lambda^3+4\sqrt{\lambda^2-4\mu}\mu} \cdot \left[-\frac{\lambda}{2}+\eta_1\left(\frac{C_1\sinh(\eta_1\xi)+C_2\cosh(\eta_1\xi)}{C_1\cosh(\eta_1\xi)+C_2\sinh(\eta_1\xi)}\right)\right],$$
$$V_7^1 = 2\left(\left(U_7^1(\xi)\right)^2 - cU_7^1(\xi)\right), \tag{59}$$

where $\xi = x + (1/2)(\sqrt{\lambda^2-4\mu}t^\alpha/\alpha)$, $\eta_1 = 1/2\sqrt{\lambda^2-4\mu}$, and C_1 and C_2 are constants that can take any number.

If $C_1 \neq 0$, and $C_2 = 0$, then $U_7^1(\xi)$ become

$$u_7^1(x,t) = U_7^1(\xi) = -\frac{1}{4}\lambda - \frac{1}{4}\sqrt{\lambda^2-4\mu} - \frac{1}{2}\frac{\lambda^2\left(\lambda+\sqrt{\lambda^2-4\mu}\right)}{\left(\lambda^2-4\mu\right)^{3/2}+\lambda^3+4\sqrt{\lambda^2-4\mu}\mu} \cdot \left[-\frac{\lambda}{2}+\eta_1\tanh(\eta_1\xi)\right], \tag{60a}$$

$$v_7^1(x,t) = V_7^1 = 2\left(\left(u_7^1(x,t)\right)^2 - cu_7^1(x,t)\right). \tag{60b}$$

Again, using (19), the general solutions for $U_7^1(\xi)$ in simplified forms are written as

$$\dot{U}_7^1(\xi) = -\frac{1}{4}\lambda - \frac{1}{4}\sqrt{\lambda^2-4\mu} - \frac{1}{2}\frac{\lambda^2\left(\lambda+\sqrt{\lambda^2-4\mu}\right)}{\left(\lambda^2-4\mu\right)^{3/2}+\lambda^3+4\sqrt{\lambda^2-4\mu}\mu} \cdot \left[-\frac{\lambda}{2}+\eta_1\tanh(\eta_1\xi+\xi_0)\right],$$
$$\dot{V}_7^1 = 2\left(\left(\dot{U}_7^1(\xi)\right)^2 - c\dot{U}_7^1(\xi)\right), \tag{61}$$

when $|C_2/C_1| < 1$, and $\xi_0 = \tanh^{-1}(C_2/C_1)$.

$$\ddot{U}_7^1(\xi) = -\frac{1}{4}\lambda - \frac{1}{4}\sqrt{\lambda^2-4\mu} - \frac{1}{2}\frac{\lambda^2\left(\lambda+\sqrt{\lambda^2-4\mu}\right)}{\left(\lambda^2-4\mu\right)^{3/2}+\lambda^3+4\sqrt{\lambda^2-4\mu}\mu} \cdot \left[-\frac{\lambda}{2}+\eta_1\coth(\eta_1\xi+\xi_0)\right],$$
$$\ddot{V}_7^1 = 2\left(\left(\ddot{U}_7^1(\xi)\right)^2 - c\ddot{U}_7^1(\xi)\right), \tag{62}$$

when $|C_2/C_1| > 1$, and $\xi_0 = \coth^{-1}(C_2/C_1)$.

When λ^2-$4\mu < 0$, the exact solution of equation (45a) and (45b) in trigonometric form is as follows.

$$U_8^1(\xi) = -\frac{1}{4}\lambda - \frac{1}{4}\sqrt{\lambda^2-4\mu} - \frac{1}{2}\frac{\lambda^2\left(\lambda+\sqrt{\lambda^2-4\mu}\right)}{\left(\lambda^2-4\mu\right)^{3/2}+\lambda^3+4\sqrt{\lambda^2-4\mu}\mu} \cdot \left[-\frac{\lambda}{2}+\eta_2\left(\frac{-C_1\sin(\eta_2\xi)+C_2\cos(\eta_2\xi)}{C_1\cos(\eta_2\xi)+C_2\sin(\eta_2\xi)}\right)\right],$$
$$V_8^1 = 2\left(\left(U_8^1(\xi)\right)^2 - cU_8^1(\xi)\right), \tag{63}$$

where $\xi = x + (1/2)(\sqrt{\lambda^2-4\mu}t^\alpha/\alpha)$, $\eta_2 = 1/2\sqrt{4\mu-\lambda^2}$, and C_1 and C_2 are free constants that can take any number.

If $C_1 \neq 0$, and $C_2 = 0$, then $U_{3,4}^1(\xi)$ become

$$u_8^1(x,t) = U_8^1(\xi) = -\frac{1}{4}\lambda - \frac{1}{4}\sqrt{\lambda^2-4\mu} - \frac{1}{2}\frac{\lambda^2\left(\lambda+\sqrt{\lambda^2-4\mu}\right)}{\left(\lambda^2-4\mu\right)^{3/2}+\lambda^3+4\sqrt{\lambda^2-4\mu}\mu} \cdot \left[-\frac{\lambda}{2}-\eta_2\tan(\eta_2\xi)\right], \tag{64}$$

$v_8^1(x,t) = V_8^1 = 2((u_8^1(x,t))^2 - cu_8^1(x,t))$.

When λ^2-$4\mu = 0$, the exact solution of equation (45a) and (45b) in rational form is as follows.

$$U_9^1(\xi) = -\frac{1}{4}\lambda - \frac{1}{4}\sqrt{\lambda^2-4\mu} - \frac{1}{2}\frac{\lambda^2\left(\lambda+\sqrt{\lambda^2-4\mu}\right)}{\left(\lambda^2-4\mu\right)^{3/2}+\lambda^3+4\sqrt{\lambda^2-4\mu}\mu} \cdot \left[-\frac{\lambda}{2}+\frac{C_2}{C_1+C_2\xi}\right],$$
$$V_9^1 = 2\left(\left(U_9^1(\xi)\right)^2 - cU_9^1(\xi)\right), \tag{65}$$

where $\xi = x + (1/2)(\sqrt{\lambda^2-4\mu}t^\alpha/\alpha)$, and C_1 and C_2 are free constants.

For Case 2, Case 3, and Case 4, we can similarly obtain the exact solutions of equations (45a) and (45b). For simplicity, they are unnecessary to repeat. If the auxiliary equation (17) and its solution (20) are used in the process of solving, we should also be able to get exact solutions, which we can prove later.

3.3. Precise Solutions of the Fractional Coupled Boussinesq Equations in Space and Time with Generalised Fractional (G'/G)-Expansion Method. Equation (5) is written as follows.

$$\begin{aligned} D_t^{\alpha}u(x,t) + D_x^{\beta}v(x,t) &= 0,\\ D_t^{\alpha}v(x,t) + AD_x^{\beta}\left(u^2(x,t)\right) - ED_{xxx}^{3\beta}u(x,t) &= 0, \end{aligned} \tag{66}$$

$0 < \alpha, \beta \le 1$.

Under the fractional complex transformations:

$$\begin{aligned} u(x,t) &= U(\xi),\\ v(x,t) &= V(\xi),\\ \xi &= \frac{x^{\beta}}{\beta} - \frac{ct^{\alpha}}{\alpha}, \end{aligned} \tag{67}$$

where c is a nonzero constant. We get the following output.

$$D_t^{\alpha}(\cdot) = -c\frac{d(\cdot)}{d\xi}, \tag{68}$$

$D_x^{\beta}(\cdot) = d(\cdot)/d\xi$,
$D_{xxx}^{3\beta}(\cdot) = d^3(\cdot)/d\xi^3$.

Substituting (67) and (68) into (66), we convert our problem into nonlinear ordinary differential equations

$$-cU' + V' = 0, \tag{69a}$$

$$-cV' + A\left(U^2\right)' - EU''' = 0, \tag{69b}$$

where $''U'''' = dU/d\xi$. By integrating once with respect to travelling wave variable factor ξ and taking the integral constant to be zero, we get

$$-cU + V = 0, \tag{70a}$$

$$-cV + AU^2 - EU'' = 0. \tag{70b}$$

From equation (70a), we get

$$V = cU. \tag{71}$$

Surrogating equation (71) in equation (70b)

$$-c^2U + AU^2 - EU'' = 0. \tag{72}$$

Applying the homogeneous equilibrium principle to equation (72), we get $2 + m = 2m \Longrightarrow m = 2$. By taking m to be 2 in equation (13), we get the form of the proposed solution of equation (72) as follows.

$$U(\xi) = a_0 + a_1\frac{G'}{G} + a_2\left(\frac{G'}{G}\right)^2 + b_1\frac{G}{G'} + b_2\left(\frac{G}{G'}\right)^2. \tag{73}$$

By substituting equations (73) and (15) into ordinary differential equation (72), we can rearrange and combine equation (72) with respect to (G'/G) and set the coefficients before all powers of (G'/G) to be 0. The resulting nonlinear algebraic system with respect to the unknowns a_0, a_1, a_2, b_1, b_2, and c is as follows.

$$\begin{aligned} \left(\frac{G'}{G}\right)^{-4} &: -6E\mu^2b_2 + Ab_2^2 = 0,\\ \left(\frac{G'}{G}\right)^{-3} &: -2E\mu^2b_1 - 10E\mu\lambda b_2 + 2Ab_1b_2 = 0,\\ \left(\frac{G'}{G}\right)^{-2} &: -3E\mu\lambda b_1 - 4E\lambda^2b_2 + 2Aa_0b_2 + Ab_1^2\\ &\quad - 8E\mu b_2 - c^2b_2 = 0,\\ \left(\frac{G'}{G}\right)^{-1} &: -E\lambda^2b_1 + 2Aa_0b_1 + 2Aa_1b_2 - 2E\mu b_1\\ &\quad - 6E\lambda b_2 - c^2b_1 = 0,\\ \left(\frac{G}{G'}\right)^{0} &: -2Eb_2 + Aa_0^2 - 2Ea_2\mu^2 + 2Aa_1b_1 - Eb_1\lambda - Ea_1\lambda\mu\\ &\quad + 2Aa_2b_2 - c^2a_0 = 0,\\ \frac{G'}{G} &: -6E\mu\lambda a_2 - E\lambda^2a_1 + 2Aa_0a_1 + 2Aa_2b_1\\ &\quad - 2E\mu a_1 - c^2a_1 = 0,\\ \left(\frac{G'}{G}\right)^{2} &: -4E\lambda^2a_2 + 2Aa_0a_2 + Aa_1^2 - 8E\mu a_2\\ &\quad - 3E\lambda a_1 - c^2a_2 = 0,\\ \left(\frac{G'}{G}\right)^{3} &: 2Aa_1a_2 - 10E\lambda a_2 - 2Ea_1 = 0,\\ \left(\frac{G'}{G}\right)^{4} &: Aa_2^2 - 6Ea_2 = 0. \end{aligned} \tag{74}$$

The nonlinear algebraic equations were solved by using Maple symbol computing system, and the following solutions were obtained.

Case 1.

$$\left\{c = \pm\sqrt{E\lambda^2 - 4E\mu}, a_0 = \frac{E\left(\lambda^2 + 2\mu\right)}{A}, a_1 = \frac{6E\lambda}{A}, a_2 = \frac{6E}{A}, b_1 = 0, b_2 = 0\right\}. \tag{75}$$

Case 2.

$$\left\{c = \pm\sqrt{-E\lambda^2 + 4E\mu}, a_0 = \frac{6E\mu}{A}, a_1 = \frac{6E\lambda}{A}, \quad a_2 = \frac{6E}{A}, b_1 = 0, b_2 = 0\right\}. \tag{76}$$

Substituting the values from (75) or (76) and equation (18) into (73), the exact solutions of equation (66) in different forms can be obtained under different parameter constraints.

Case 1. When $\lambda^2 - 4\mu > 0$, the exact solution of equation (66) in hyperbolic form is as follows.

$$U^1_{10,11}(\xi) = \frac{6E}{A}\left[\frac{(\lambda^2 + 2\mu)}{6} + \lambda\left[-\frac{\lambda}{2} + \eta_1\left(\frac{C_1\sinh(\eta_1\xi) + C_2\cosh(\eta_1\xi)}{C_1\cosh(\eta_1\xi) + C_2\sinh(\eta_1\xi)}\right)\right] + \left[-\frac{\lambda}{2} + \eta_1\left(\frac{C_1\sinh(\eta_1\xi) + C_2\cosh(\eta_1\xi)}{C_1\cosh(\eta_1\xi) + C_2\sinh(\eta_1\xi)}\right)\right]^2\right], \tag{77}$$

where $\xi = (x^\beta/\beta) \mp (\sqrt{E\lambda^2\text{-}4E\mu}t^\alpha/\alpha)$, $\eta_1 = 1/2\sqrt{\lambda^2 - 4\mu}$, and C_1 and C_2 are constants that can take any number.

If $C_1 \neq 0$, and $C_2 = 0$, then $U^1_{10,11}(\xi)$ become

$$u^1_{10,11}(x,t) = U^1_{10,11}(\xi) = \frac{6E}{A}\left[\frac{(\lambda^2 + 2\mu)}{6} + \lambda\left[-\frac{\lambda}{2} + \eta_1\tanh(\eta_1\xi)\right] + \left[-\frac{\lambda}{2} + \eta_1\tanh(\eta_1\xi)\right]^2\right]. \tag{78}$$

Again, using (19), the general solutions for $U^1_{10,11}(\xi)$ in simplified forms are written as

$$\dot{U}^1_{10,11}(\xi) = \frac{6E}{A}\left[\frac{(\lambda^2 + 2\mu)}{6} + \lambda\left[-\frac{\lambda}{2} + \eta_1\tanh(\eta_1\xi + \xi_0)\right] + \left[-\frac{\lambda}{2} + \eta_1\tanh(\eta_1\xi + \xi_0)\right]^2\right], \tag{79}$$

when $|C_2/C_1| < 1$, and $\xi_0 = \tanh^{-1}(C_2/C_1)$.

$$\ddot{U}^1_{10,11}(\xi) = \frac{6E}{A}\left[\frac{(\lambda^2 + 2\mu)}{6} + \lambda\left[-\frac{\lambda}{2} + \eta_1\coth(\eta_1\xi + \xi_0)\right] + \left[-\frac{\lambda}{2} + \eta_1\coth(\eta_1\xi + \xi_0)\right]^2\right], \tag{80}$$

when $|C_2/C_1| > 1$, and $\xi_0 = \coth^{-1}(C_2/C_1)$.

When $\lambda^2 - 4\mu < 0$, the exact solution of equation (66) in trigonometric form is as follows.

$$U^1_{12,13}(\xi) = \frac{6E}{A}\left[\frac{(\lambda^2 + 2\mu)}{6} + \lambda\left[-\frac{\lambda}{2} + \eta_2\left(\frac{-C_1\sin(\eta_2\xi) + C_2\cos(\eta_2\xi)}{C_1\cos(\eta_2\xi) + C_2\sin(\eta_2\xi)}\right)\right] + \left[-\frac{\lambda}{2} + \eta_2\left(\frac{-C_1\sin(\eta_2\xi) + C_2\cos(\eta_2\xi)}{C_1\cos(\eta_2\xi) + C_2\sin(\eta_2\xi)}\right)\right]^2\right], \tag{81}$$

where $\xi = (x^\beta/\beta) \mp (\sqrt{E\lambda^2 - 4E\mu}t^\alpha/\alpha)$, $\eta_2 = 1/2\sqrt{4\mu - \lambda^2}$, and C_1 and C_2 are constants that can take any number.

If $C_1 \neq 0$, and $C_2 = 0$, then $U^1_{12,13}(\xi)$ become

$$u^1_{12,13}(x,t) = U^1_{12,13}(\xi) = \frac{6E}{A}\left[\frac{(\lambda^2 + 2\mu)}{6} - \lambda\left[\frac{\lambda}{2} + \eta_2\tan(\eta_2\xi)\right] + \left[\frac{\lambda}{2} + \eta_2\tan(\eta_2\xi)\right]^2\right]. \tag{82}$$

When $\lambda^2\text{-}4\mu = 0$, the exact solution of equation (66) in rational form is as follows.

$$U^1_{14}(\xi) = -\frac{6E}{A}\left[\frac{(\lambda^2 + 2\mu)}{6} + \lambda\left[-\frac{\lambda}{2} + \frac{C_2}{C_1 + C_2\xi}\right] + \left[-\frac{\lambda}{2} + \frac{C_2}{C_1 + C_2\xi}\right]^2\right], \tag{83}$$

where $\xi = (x^\beta/\beta) \mp (\sqrt{E\lambda^2\text{-}4E\mu}t^\alpha/\alpha)$, and C_1 and C_2 are constants that can take any number.

Using the obtained result formula (76), we can similarly obtain the exact solution of equation (66). For simplicity, they are unnecessary to repeat. If the auxiliary equation (17) and its solution (20) are used in the process of solving, we should also be able to get exact solutions, which we can prove later.

4. The Explanation and Discussion

By calculating the operation of Maple software, we obtained the exact travelling wave solutions of three fractional-order equations. Literature [34] uses the simplest Riccati equation of a fractional order as an auxiliary function, directly solving space-time fractional Boussinesq equation, and the coefficients and functions in the obtained solution contained fractional order, which was quite different from the solution obtained by using complex transformation. In addition, literature [34] only obtained a set of solutions of algebraic equations composed of quasisolution coefficients, and we obtained four sets of solutions. For equation (4), literature

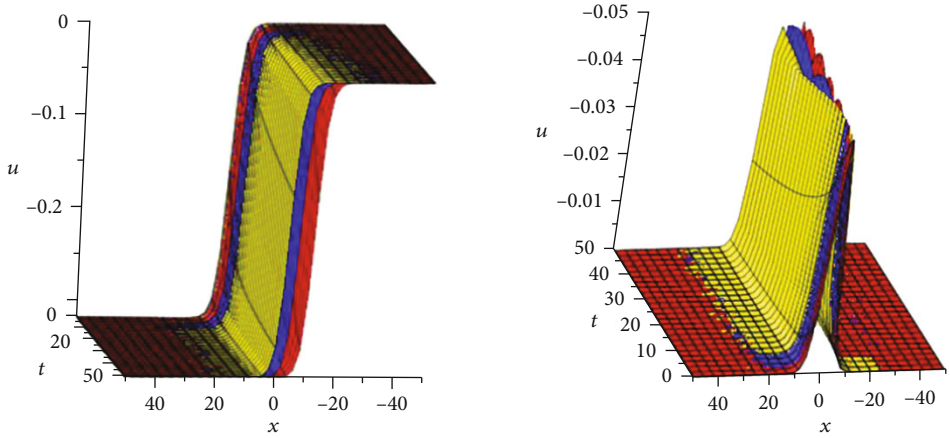

Solution (60a) red: $\alpha = 0.9$, blue: $\alpha = 0.7$, yellow: $\alpha = 0.3$ Solution (60b) red: $\alpha = 0.9$, blue: $\alpha = 0.7$, yellow: $\alpha = 0.3$

FIGURE 1: 3D plot of solutions (60a) and (60b) for various values of α, and $c = 1/2\sqrt{\lambda^2 - 4\mu}, \lambda - \sqrt{2}, \mu = 0.4$.

[40] uses the first integral method to obtain its two sets of solutions, both of which are kinked in the image, which is similar to the solution shown in Figure 1. We obtain four sets of solutions of algebraic equations, each of which contains three types of solutions, one kink, one period, and one rational function. For equation (5), reference [42] obtained a set of solutions of algebraic equations by using the exp-function method, which was illustrated as bell-shaped isolated waves. We obtain four sets of solutions of algebraic equations, each containing three types of solutions, one of which is the kink solution shown in Figure 2 or 3.

In general, there are many solutions to nonlinear partial differential equations, only some of which can be obtained in different ways, and our work enriches the solutions to these equations. The three model equations we studied are all water wave-related models, which are nonlinear dispersive wave equations. We are more concerned with the isolated wave solutions resulting from the equilibrium of the nonlinear and dispersion effects, so we select an isolated wave solution from each equation we study to discuss the effect of fractional order on its waveform. The results are shown in Figures 1, 2, 3, 4, and 5. Figure 4 shows the isolated wave solution of the first model equation. Figures 1 and 5 are the isolated wave solutions of the second model equation. Figures 2 and 3 are the isolated wave solutions of the third model equation. Let us look at each of these results in more details.

Solution (32) of equation (2) represents bell-type soliton solutions, which is the result of the equilibrium between the nonlinear term and the dispersion term in equation (2). When $c = +\sqrt{-E\lambda^2 + 4E\mu - B}$, $A = 3$, $B = -1$, $E = 0.5$, $\lambda = \sqrt{2}$, and $\mu = 0.4$, the graphical form of solution (32) changing with α is shown in Figure 4. After setting values for other parameters, Figure 4 explains the perspective view of solution (32), when the values of α are 0.9, 0.8, 0.7, 0.6, 0.5, and 0.4 in turn. You can see in Figure 4 that with the decrease of α, the width of the waveform is increasing, and the waveform surface is gradually transitioning from concave to convex. We might conclude that the fractional order modulates the waveforms of the isolated waves of this equation.

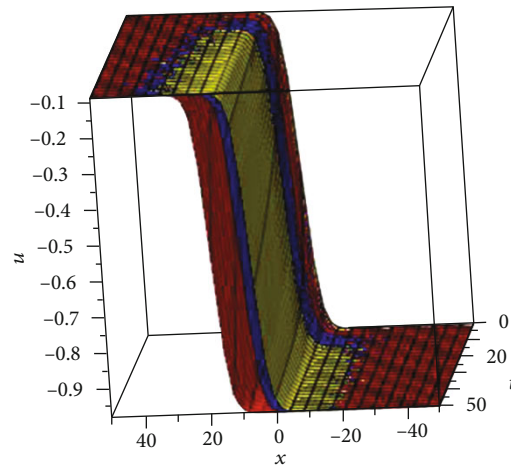

$\beta = 1$; solution (78) red: $\alpha = 0.9$, blue: $\alpha = 0.6$, yellow: $\alpha = 0.3$

FIGURE 2: 3D plot of solution (78) for various values of α, and $\beta = 1$, $c = \sqrt{E\lambda^2 - 4E\mu}, \lambda\sqrt{2}, \mu = 0.4$, $A = 3$, $E = 0.5$.

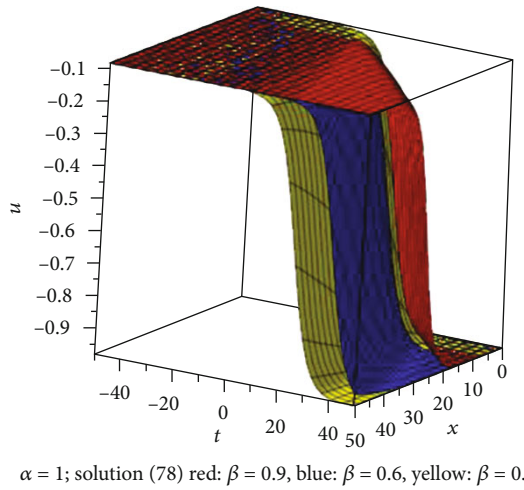

$\alpha = 1$; solution (78) red: $\beta = 0.9$, blue: $\beta = 0.6$, yellow: $\beta = 0.3$

FIGURE 3: 3D plot of solution (78) for various values of β, and $\alpha = 1$, $c = \sqrt{E\lambda^2 - 4E\mu}, \lambda\sqrt{2}, \mu = 0.4$, $A = 3$, $E = 0.5$.

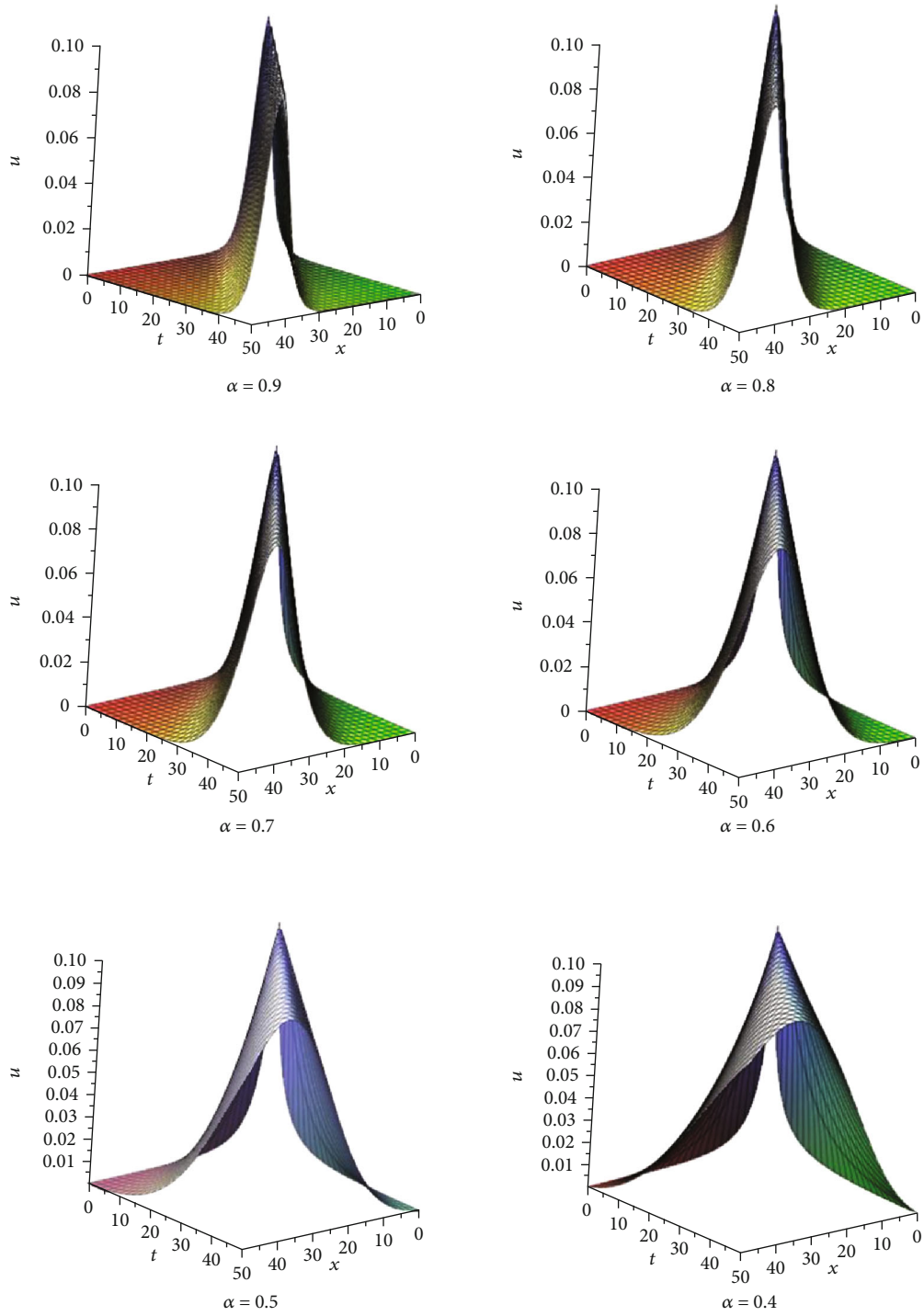

FIGURE 4: Snapshots of solution (32) for various values of α, and $c = +\sqrt{-E\lambda^2 + 4E\mu - B}$, $A = 3$, $B = -1$, $E = 0.5$, $\lambda = \sqrt{2}$, $\mu = 0.4$.

When $c = -1/2\sqrt{\lambda^2 - 4\mu}$, $\lambda = \sqrt{2}$, and $\mu = 0.4$, the graphical form of solutions (60a) and (60b) of equation (4) changing with α is shown in Figure 1. Solution (60a) in Figure 1 represents kink soliton solutions. Solution (60b) in Figure 1 represents bell-type soliton solutions. They are the result of the balance between the nonlinear term and the dispersion term in equation (4). The detailed expansion of the graphical form of solution (60b) is shown in Figure 5. After setting values for other parameters, Figure 5 explains the perspective view of the Solution (60b), when the values of α are 0.1, 0.5, 0.7, and 0.9 in turn. As you can see from Figure 5, the waveform of the solution changes from the form of an isolated wave to the form of a local period, which shows that for some solutions, fractional-order changes can change the structure of the waveform. In other words, the fractional order may modulate the local periodicity of some solutions.

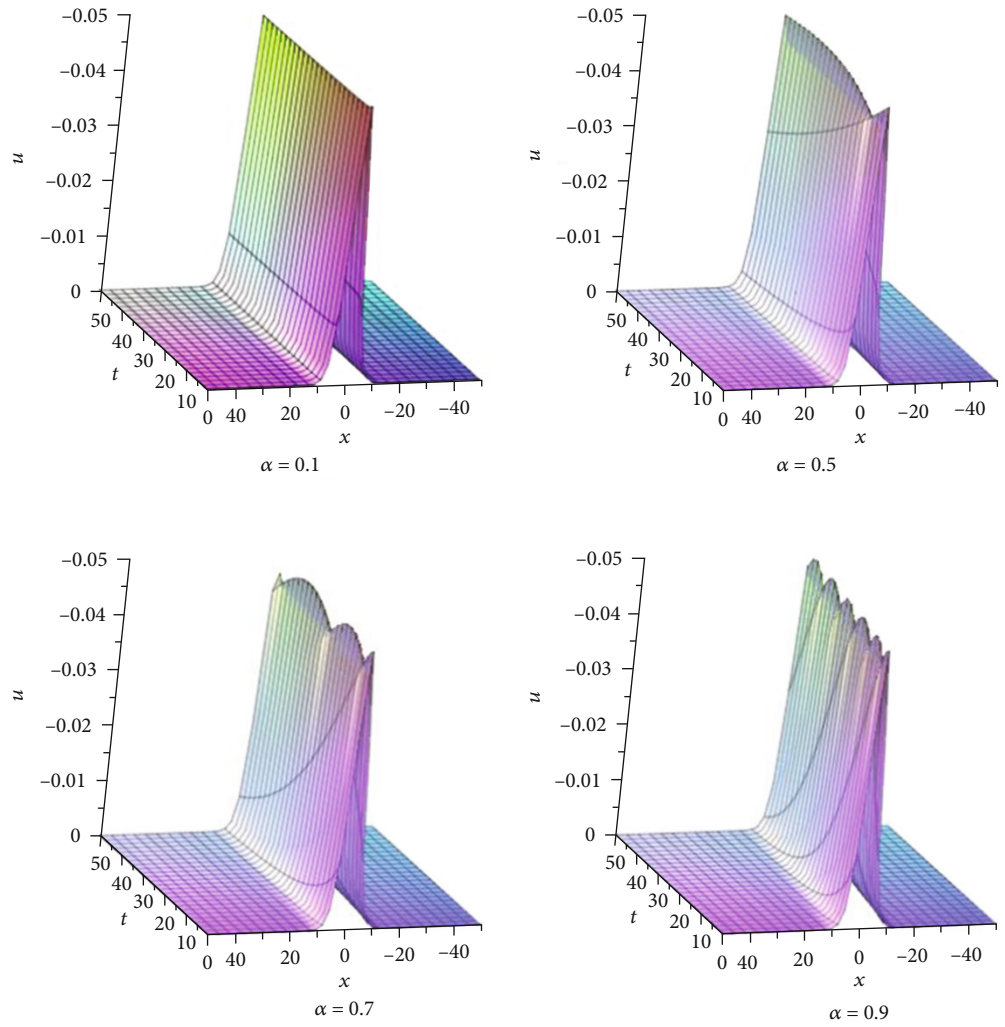

Figure 5: Snapshots of soliton solution to periodic solution of solution (60b) for various values of α, and $c = 1/2\sqrt{\lambda^2 - 4\mu}, \lambda = \sqrt{2}, \mu = 0.4$.

When $\beta = 1, c = \sqrt{E\lambda^2 - 4E\mu}, \lambda = \sqrt{2}, \mu = 0.4, A = 3$, and $E = 0.5$, the graphical form of solution (78) of equation (5) changing with α is shown in Figure 2. When $\alpha = 1, c = \sqrt{E\lambda^2 - 4E\mu}, \lambda = \sqrt{2}, \mu = 0.4, A = 3$, and $E = 0.5$, the graphical form of solution (78) of equation (5) changing with β is shown in Figure 3. Solution (78) in Figures 2 and 3 represent kink soliton solutions. For an equation with two fractional-order parameters, we fix one fractional-order parameter and then look at the effect of the other fractional-order parameter on the isolated wave solution waveform. For the case that the fractional-order parameter satisfies a certain relation, it needs further study in the future. The effect of fractional order on other solutions can be similarly graphically analysed.

Remark 1. When $G = G(\xi)$ satisfies equation (17), we have

$$\left(\frac{G'(\xi)}{G(\xi)}\right)' = \frac{G''(\xi)G(\xi) - \left(G'(\xi)\right)^2}{G^2(\xi)} = (\lambda - 1)\left(\frac{G'}{G}\right)^2 + \mu\left(\frac{G'}{G}\right) + \omega. \tag{84}$$

In this way, the Riccati equation satisfied by the extended (G'/G)-expansion method can be regarded as more generalised.

5. Conclusion

Combined with fractional complex transformation, the (G'/G)-expansion method and its extended generalised form are used to obtain abundant travelling wave solutions for three fractal-order model equations related to water waves. For the nonlinear dispersive wave model equations, we are more concerned about their soliton solutions, so we choose a soliton solution from the travelling wave solution of each model equation to illustrate and discuss the effect of fractional order parameters on it. The results show that the fractional derivatives can modulate the waveform, local periodicity, and structure of the isolated solutions of the three model equations. Of course, our discussion of fractional derivatives is not enough. For example, in the future, we will further discuss how to modulate the waveform of a soliton solution when multiple fractional parameters are coupled. With the further discussion of the influence of fractional

derivatives on the waveform of the solution of the equation, we may have a better understanding of the formation and properties of the waveform of the solution of the fractional equation. In addition, in this paper, we point out the rule that the auxiliary equation of the extended (G'/G)-expansion method should satisfy, that is, the result of the differential operation of (G'/G) should be in the polynomial form of (G'/G), which is the basis for the formation of algebraic equations by collecting (G'/G) power term coefficients later. According to the rules satisfied by the auxiliary equations, we can choose other solvable equations as auxiliary equations, which is also helpful to understand the selection of auxiliary equations in other methods.

Data Availability

No data were used to support this study.

Conflicts of Interest

The authors declare that they have no conflicts of interest.

Authors' Contributions

All authors conceived the study, participated in the sequence alignment, and read and approved the final manuscript.

Acknowledgments

The authors thank the anonymous reviewers for their improvements to the manuscript. This research was supported by Major Science and Technology Projects in Shanxi Province of China (20181101008), Major Science and Technology Projects in Shanxi Province of China (20181102015), and Supplementary Platform Project of "1331" Project in Shanxi Province in 2018.

References

[1] K. S. Miller and B. Ross, *An Introduction to the Fractional Calculus and Fractional Differential Equations*, Wiley, New York, NY, USA, 1993.

[2] I. Podlubny, *Fractional Differential Equations*, Academic Press, California, 1999.

[3] A. A. Kilbas, H. M. Srivastava, and J. J. Trujillo, *Theory and Applications of Fractional Differential Equations*, Elsevier, Amsterdam, 2006.

[4] J. F. Gómez Aguilar, T. Córdova-Fraga, J. Tórres-Jiménez, R. F. Escobar-Jiménez, V. H. Olivares-Peregrino, and G. V. Guerrero-Ramírez, "Nonlocal transport processes and the fractional Cattaneo-Vernotte equation," *Mathematical Problems in Engineering*, vol. 2016, Article ID 7845874, 15 pages, 2016.

[5] B. Lu, "The first integral method for some time fractional differential equations," *Journal of Mathematical Analysis and Applications*, vol. 395, no. 2, pp. 684–693, 2012.

[6] M. Eslami, B. Fathi Vajargah, M. Mirzazadeh, and A. Biswas, "Application of first integral method to fractional partial differential equations," *Indian Journal of Physics*, vol. 88, no. 2, pp. 177–184, 2014.

[7] J. Yu, D. S. Wang, Y. Sun, and S. Wu, "Modified method of simplest equation for obtaining exact solutions of the Zakharov–Kuznetsov equation, the modified Zakharov–Kuznetsov equation, and their generalized forms," *Nonlinear Dynamics*, vol. 85, no. 4, pp. 2449–2465, 2016.

[8] N. Taghizadeh, M. Mirzazadeh, M. Rahimian, and M. Akbari, "Application of the simplest equation method to some time-fractional partial differential equations," *Ain Shams Engineering Journal*, vol. 4, no. 4, pp. 897–902, 2013.

[9] S. Guo, L. Mei, Y. Li, and Y. Sun, "The improved fractional sub-equation method and its applications to the space–time fractional differential equations in fluid mechanics," *Physics Letters A*, vol. 376, no. 4, pp. 407–411, 2012.

[10] K. R. Raslan, T. S. el-Danaf, and K. K. Ali, "Exact solution of the space-time fractional coupled EW and coupled MEW equations," *The European Physical Journal Plus*, vol. 132, no. 7, pp. 1–11, 2017.

[11] B. Zheng and C. Wen, "Exact solutions for fractional partial differential equations by a new fractional sub-equation method," *Advances in Difference Equations*, vol. 2013, no. 1, 2013.

[12] B. Tang, Y. He, L. Wei, and X. Zhang, "A generalized fractional sub-equation method for fractional differential equations with variable coefficients," *Physics Letters A*, vol. 376, no. 38-39, pp. 2588–2590, 2012.

[13] M. M. A. Khater and D. Kumar, "New exact solutions for the time fractional coupled Boussinesq–Burger equation and approximate long water wave equation in shallow water," *Journal of Ocean Engineering and Science*, vol. 2, no. 3, pp. 223–228, 2017.

[14] S. Zhang, Q. A. Zong, D. Liu, and Q. Gao, "A generalized exp-function method for fractional Riccati differential equations," *Communications in Fractional Calculus*, vol. 1, pp. 48–51, 2010.

[15] A. Bekir, Ö. Güner, and A. C. Cevikel, "Fractional complex transform and exp-function methods for fractional differential equations," *Abstract and Applied Analysis*, vol. 2013, Article ID 426462, 8 pages, 2013.

[16] B. Zheng, "Exp-function method for solving fractional partial differential equations," *The Scientific World Journal*, vol. 2013, Article ID 465723, 8 pages, 2013.

[17] O. Guner and A. Bekir, "The Exp-function method for solving nonlinear space–time fractional differential equations in mathematical physics," *Journal of the Association of Arab Universities for Basic and Applied Sciences*, vol. 24, no. 1, pp. 277–282, 2018.

[18] Rahmatullah, R. Ellahi, S. T. Mohyud-Din, and U. Khan, "Exact traveling wave solutions of fractional order Boussinesq-like equations by applying Exp-function method," *Results in Physics*, vol. 8, pp. 114–120, 2018.

[19] A. Bekir, O. Guner, and A. Cevikel, "The exp-function method for some time-fractional differential equations," *Journal of Automatica Sinica*, vol. 4, no. 2, pp. 315–321, 2017.

[20] C. Park, M. M. A. Khater, A. H. Abdel-Aty et al., "Dynamical analysis of the nonlinear complex fractional emerging telecommunication model with higher–order dispersive cubic–quintic," *Alexandria Engineering Journal*, vol. 59, no. 3, pp. 1425–1433, 2020.

[21] M. M. A. Khater, B. Ghanbari, K. S. Nisar, and D. Kumar, "Novel exact solutions of the fractional Bogoyavlensky–Konopelchenko equation involving the Atangana-Baleanu-Riemann derivative," *Alexandria Engineering Journal*, 2020.

[22] B. Zheng, "(G'/G)-expansion method for solving fractional partial differential equations in the theory of mathematical physics," *Communications in Theoretical Physics*, vol. 58, no. 5, pp. 623–630, 2012.

[23] U. Khan, R. Ellahi, R. Khan, and S. T. Mohyud-Din, "Extracting new solitary wave solutions of Benny-Luke equation and Phi-4 equation of fractional order by using (G'/G)-expansion method," *Optical and Quantum Electronics*, vol. 49, no. 11, pp. 1–14, 2017.

[24] K. A. Gepreel and S. Omran, "Exact solutions for nonlinear partial fractional differential equations," *Chinese Physics B*, vol. 21, no. 11, p. 110204, 2012.

[25] A. Bekir, O. Guner, B. Ayhan, and A. C. Cevikel, "Exact solutions for fractional differential-difference equations by (G'/G)-expansion method with modified Riemann-Liouville derivative," *Advances in Applied Mathematics and Mechanics*, vol. 8, no. 2, pp. 293–305, 2016.

[26] A. Bekir and O. Guner, "Exact solutions of nonlinear fractional differential equations by (G'/G)-expansion method," *Chinese Physics B*, vol. 22, no. 11, article 110202, 2013.

[27] A. Biswas, A. Sonmezoglu, M. Ekici et al., "Optical soliton perturbation with fractional temporal evolution by extended G'/G-expansion method," *Optik*, vol. 161, pp. 301–320, 2018.

[28] A. Bekir, O. Guner, A. H. Bhrawy, and A. Biswas, "Solving nonlinear fractional differential equations using exp-function and (G/G') -expansion methods," *Romanian Journal of Physics*, vol. 60, pp. 3-4, 2015.

[29] A. Bekir and O. Guner, "The $G'G$-expansion method using modified Riemann–Liouville derivative for some space-time fractional differential equations," *Ain Shams Engineering Journal*, vol. 5, no. 3, pp. 959–965, 2014.

[30] M. M. A. Khater, R. A. M. Attia, A. H. Abdel-Aty, W. Alharbi, and D. Lu, "Abundant analytical and numerical solutions of the fractional microbiological densities model in bacteria cell as a result of diffusion mechanisms," *Chaos, Solitons and Fractals*, vol. 136, article 109824, 2020.

[31] W. Liu and K. Chen, "The functional variable method for finding exact solutions of some nonlinear time-fractional differential equations," *Indian Academy of Sciences*, vol. 81, no. 3, pp. 377–384, 2013.

[32] T. Islam, M. A. Akbar, and A. K. Azad, "Traveling wave solutions to some nonlinear fractional partial differential equations through the rational (G'/G)-expansion method," *Journal of Ocean Engineering and Science*, vol. 3, no. 1, pp. 76–81, 2018.

[33] M. M. A. Khater and D. Baleanu, "On abundant new solutions of two fractional complex models," *Advances in Difference Equations*, vol. 2020, no. 1, 2020.

[34] C. Yue, D. Lu, M. M. A. Khater, A. H. Abdel-Aty, W. Alharbi, and R. A. M. Attia, "On explicit wave solutions of the fractional nonlinear DSW system via the modified Khater method," *Fractals*, vol. 23, no. 47, 2020.

[35] A. H. Abdel-Aty, M. M. Khater, R. A. Attia, M. Abdel-Aty, and H. Eleuch, "On the new explicit solutions of the fractional nonlinear space-time nuclear model," *Fractals*, vol. 28, no. 8, article 2040035, 2020.

[36] H. Qin, M. M. A. Khater, and R. A. M. Attia, "Copious closed forms of solutions for the fractional nonlinear longitudinal strain wave equation in microstructured solids," *Mathematical Problems in Engineering*, vol. 2020, 8 pages, 2020.

[37] H. Bulut, H. M. Baskonus, and Y. Pandir, "The modified trial equation method for fractional wave equation and time fractional generalized Burgers equation," *Abstract and Applied Analysis*, vol. 2013, Article ID 636802, 8 pages, 2013.

[38] Y. Pandir, Y. Gurefe, and E. Misirli, "The extended trial equation method for some time fractional differential equations," *Discrete Dynamics in Nature and Society*, vol. 2013, Article ID 491359, 13 pages, 2013.

[39] Z. B. Li and J. H. He, "Fractional complex transform for fractional differential equations," *Mathematical and Computational Applications*, vol. 15, no. 5, pp. 970–973, 2010.

[40] Z. B. Li and J. H. He, "Application of the fractional complex transform to fractional differential equations nonlinear," *Nonlinear Science Letters A*, vol. 2, pp. 121–126, 2011.

[41] S. A. el-Wakil and E. M. Abulwafa, "Formulation and solution of space–time fractional Boussinesq equation," *Nonlinear Dynamics*, vol. 80, no. 1-2, pp. 167–175, 2015.

[42] H. Jafari, H. Tajadodi, and D. Baleanu, "Exact solutions of Boussinesq and KdV-mKdV equations by fractional subequation method," *Romanian Reports in Physics*, vol. 65, pp. 1119–1124, 2013.

[43] J. Boussinesq, "Théorie des ondes et des remous qui se propagent le long d'un canal rectangulaire horizontal en communiquant au liquide contenu dans ce canal des vitesses sensiblement pareilles de la surface au fond," *Journal de Mathématiques Pures et Appliquées*, vol. 17, pp. 55–108, 1872.

[44] J. Boussinesq, "Essai sur la théorie des eaux courantes," *Mém. Acad. Sci. Inst. Nat. France*, vol. 23, pp. 1–680, 1877.

[45] V. G. Makhankov, "Dynamics of classical solitons (in non-integrable systems)," *Physics Reports*, vol. 35, no. 1, pp. 1–128, 1978.

[46] M. T. Darvishi, M. Najafi, and A. M. Wazwaz, "Soliton solutions for Boussinesq-like equations with spatio-temporal dispersion," *Ocean Engineering*, vol. 130, pp. 228–240, 2017.

[47] S. Javeed, S. Saif, A. Waheed, and D. Baleanu, "Exact solutions of fractional mBBM equation and coupled system of fractional Boussinesq-Burgers," *Results in Physics*, vol. 9, pp. 1275–1281, 2018.

[48] S. Kumar, A. Kumar, and D. Baleanu, "Two analytical methods for time-fractional nonlinear coupled Boussinesq–Burger's equations arise in propagation of shallow water waves," *Nonlinear Dynamics*, vol. 85, no. 2, pp. 699–715, 2016.

[49] H. C. Yaslan and A. Girgin, "Exp-function method for the conformable space-time fractional STO, ZKBBM and coupled Boussinesq equations," *Arab Journal of Basic and Applied Sciences*, vol. 26, no. 1, pp. 163–170, 2019.

[50] K. Hosseini and R. Ansari, "New exact solutions of nonlinear conformable time-fractional Boussinesq equations using the modified Kudryashov method," *Wave Random Complex*, vol. 27, no. 4, pp. 628–636, 2017.

[51] K. Hoseini, A. Bekir, and R. Ansari, "Exact solutions of nonlinear conformable time-fractional Boussinesq equations using the $\exp(-\phi(\varepsilon))$ -expansion method," *Optimal Quants Electron*, vol. 49, pp. 1–11, 2017.

[52] R. Khalil, M. al Horani, A. Yousef, and M. Sababheh, "A new definition of fractional derivative," *Journal of Computational and Applied Mathematics*, vol. 264, pp. 65–70, 2014.

[53] T. Abdeljawad, "On conformable fractional calculus," *Journal of Computational and Applied Mathematics*, vol. 279, pp. 57–66, 2015.

[54] J. Manafian, M. F. Aghdaei, M. Khalilian, and R. Sarbaz Jeddi, "Application of the generalized (G'/G)-expansion method for nonlinear PDEs to obtaining soliton wave solution," *Optik*, vol. 135, pp. 395–406, 2017.

Hindawi
Advances in Mathematical Physics
Volume 2020, Article ID 5017893, 9 pages
https://doi.org/10.1155/2020/5017893

Research Article

Torus and Subharmonic Motions of a Forced Vibration System in 1:5 Weak Resonance

Yong Guo

School of Civil Engineering, Guizhou Institute of Technology, Guiyang, China

Correspondence should be addressed to Yong Guo; gy-gates@163.com

Received 27 April 2020; Revised 25 July 2020; Accepted 5 August 2020; Published 26 September 2020

Guest Editor: Yu-Hao Sun

The Neimark-Sacker bifurcation of a forced vibration system is considered in this paper. The series solution to the motion equation is obtained, and the Poincaré map is established. The fixed point of the Poincaré map is guaranteed by the implicit function theorem. The map is transformed into its normal form at the fifth-order resonance case. For some parameter values, there exists the torus T^1. Furthermore, the phenomenon of phase locking on the torus T^1 is investigated and the parameter condition under which there exists subharmonic motion on the torus T^1 is determined.

1. Introduction

In this article, we investigate the torus and subharmonic motions of the following system:

$$\begin{cases} \dot{y}_1 = -y_2, \\ \dot{y}_2 = y_1 + a_1\mu y_2 + by_2^2 + sy_1^3 + cy_2^3 + \varepsilon f((q+\delta)t) + \text{h.o.t.}, \end{cases} \tag{1}$$

where μ, ε, and δ are small parameters; f is a 2π periodic function; and a_1, s, b, and c are constants. $(q+\delta)$ is the frequency of the external force. If q is a positive integer with $q \geq 5$, we say that the system (1) is in $1:q$ weak resonance. For q being a positive integer satisfying $q \leq 4$, the system (1) is referred to as $1:q$ strong resonance. h.o.t. represents the "higher-order terms" than those that have been written out, and the same is true below. There are some mechanical models whose dynamical behaviors can be described by Equation (1), for example, the system shown in Figure 1, see Ref. [1] for more information. In this paper, we investigate abstractly system (1) and give a method for analyzing its Neimark-Sacker bifurcation. The value of relevant parameters and constants depends on some specific mechanical models whose dynamics can be described by Equation (1). Therefore, we do not introduce the given parameters or constants here, and only choose several sets of values for numerical simulations in Section 4.

For $\varepsilon = 0$, Equation (1) undergoes the Hopf bifurcation under certain conditions, and then, for $\varepsilon \neq 0$ and $|\varepsilon|$, sufficiently small torus or the qth order subharmonic motions can occur to Equation (1). The problem of $1:q$ resonance of a closed orbit in R^3 (or in $C \times S^1$) leads to the study of the Z_q-equivariant planar vector (see Refs. [2, 3]) whose versal unfolding has been studied for $q \neq 4$ and been conjectured for $q = 4$ by Arnold [2]. Bifurcation sequence inventory at $1:4$ resonance has been presented by Krauskopf [3]. Gambaudo [4] considered the general study of the periodic perturbation of a one family of autonomous differential equations in the plane satisfying conditions for a generic Hopf bifurcation. Iooss [5] investigated the subharmonic motion in the $1:3$ and $1:4$ resonance case. Wan [6] analyzed the Neimark-Sacker bifurcation in the $1:4$ strong resonance case for the planar map. The width of the resonance tongue at a distance σ from the unit circle given by Arnold [2, 7] is

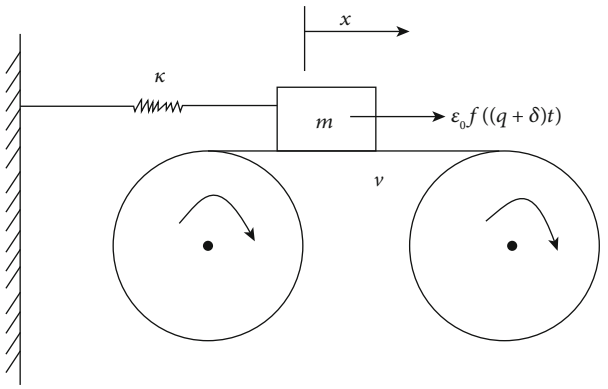

Figure 1: Schematic diagram of the dynamic model in Ref. [1].

of the order of $\sigma^{(q-2)/2}$. Shilnikov et al. [8] and Iooss [9] computed the Arnold tongue in weak resonance case for the planar map. The Neimark-Sacker bifurcation of an oscillator with dry friction was observed in Ref. [1]. Periodic-impact motions and bifurcations of vibroimpact systems near the 1 : 4 strong resonance point are considered in Ref. [10]. Results on other types of forced vibrations can be found in some literatures, see, for example, Refs. [11–16].

Judging from the above statement, we know that there is a lack of efficient criteria depending on the coefficients of the original differential equations, based on which we can talk about the asymptotic behaviors of trajectory. In this paper, we will restrict our attention to the case of 1 : 5 resonance, namely, $q = 5$ in Equation (1), and obtain criteria. For higher-order resonance, the procedure is essentially the same as this case but needs tedious computation.

This paper is organized as follows. In Section 2, the Poincaré map is established according to power series solution to Equation (1). The map is further transformed into its normal form. In Section 3, the Neimark-Sacker bifurcation is investigated. When there is a circle bifurcating from the fixed point, the phenomenon of phase locking on the invariant circle is studied and the parameter region in which subharmonic motion can occur is determined. In Section 4, choosing a set of parameters, the theoretical results stated above are verified by numerical simulations.

2. The Poincaré Map

Let $z = y_1 + iy_2$, Equation (1) takes the form

$$\dot{z} = iz + \frac{a_1\mu}{2}(z-\bar{z}) - \frac{ib}{4}(z-\bar{z})^2 + \frac{\mathrm{is}}{8}(z+\bar{z})^3 - \frac{c}{8}(z-\bar{z})^3 + i\varepsilon f((5+\delta)t) + \text{h.o.t.} \tag{2}$$

By the procedure applied in Ref. [1], the solution of Equation (2) satisfying $z(\eta, 0, \mu, \varepsilon) = \eta$ can be written as

$$z(\eta, t, \mu, \varepsilon) = z_0(\eta, t) + \mu z_{10}(\eta, t) + \varepsilon z_{01}(\eta, t) + \text{h.o.t.}, \tag{3}$$

where

$$\begin{cases} z_0 = L_{10}\eta + L_{01}\bar{\eta} + L_{20}\eta^2 + L_{11}\eta\bar{\eta} + L_{02}\bar{\eta}^2 + L_{30}\eta^3 + L_{21}\eta^2\bar{\eta} + L_{12}\eta\bar{\eta}^2 + L_{03}\bar{\eta}^3 + L_{04}\bar{\eta}^4, \\ z_{10} = \dfrac{a_1}{2}e^{it}\left[\eta t + \dfrac{i\bar{\eta}}{2}\left(1 - e^{-2it}\right)\right], \\ z_{01} = ie^{it}\displaystyle\int_0^t e^{-i\tau} f((5+\delta)\tau)\,d\tau, \end{cases}$$

$$L_{10} = e^{it},$$

$$L_{01} = 0,$$

$$L_{20} = \frac{b}{4}\left(-e^{2it} + e^{it}\right),$$

$$L_{11} = \frac{b}{2}\left(e^{it} - 1\right),$$

$$L_{02} = \frac{b}{12}\left(-e^{it} + e^{-2it}\right),$$

$$L_{30} = \left(\frac{b^2}{12} + \frac{s}{16} + \frac{ic}{16}\right)e^{3it} - \frac{b^2}{8}e^{2it} - \left(\frac{s}{16} + \frac{ic}{16}\right)e^{it} + \frac{b^2}{24},$$

$$L_{21} = -\frac{b^2}{4}e^{2it} + \left(\frac{3c}{8} + \frac{3si}{8} - \frac{b^2}{6}i\right)te^{it} + \frac{23b^2}{36}e^{it} - \frac{3}{8}b^2 - \frac{b^2}{72}e^{-2it},$$

$$L_{12} = \frac{b^2}{24}e^{2it} + \left(\frac{b^2}{6} + \frac{3s}{16} + \frac{3c}{16}i\right)e^{it} - \frac{3b^2}{8} + \left(\frac{b^2}{12} - \frac{3s}{16} - \frac{3c}{16}i\right)e^{-it} + \frac{b^2}{12}e^{-2it},$$

$$L_{03} = -\left(\frac{b^2}{24} - \frac{s}{32} + \frac{ic}{32}\right)e^{it} + \frac{b^2}{24} + \frac{b^2}{24}e^{-2it} - \left(\frac{b^2}{24} + \frac{s}{32} - \frac{ic}{32}\right)e^{-3it},$$

$$L_{04} = -\frac{b^3}{576}e^{2it} + \left(-\frac{7}{480}b^3 + \frac{23}{1920}bs - \frac{11}{480}bci\right)e^{it} + \left(\frac{b^3}{32} - \frac{bs}{64} + \frac{bci}{128}\right) + \left(-\frac{b^3}{144} + \frac{bs}{64} + \frac{bc}{64}i\right)e^{-it} + \left(\frac{b^3}{192} - \frac{bs}{96} + \frac{bc}{96}i\right)e^{-2it} + \left(-\frac{b^3}{32} - \frac{3bs}{128} + \frac{3bc}{128}i\right)e^{-3it} + \left(\frac{13b^3}{720} + \frac{7bs}{320} - \frac{11bc}{320}i\right)e^{-4it}. \tag{4}$$

Let $t = 2\pi/(5+\delta)$ [1] in (3), we can get the Poincaré map

$$\eta \longrightarrow z\left(\eta, \frac{2\pi}{5+\delta}, \mu, \varepsilon\right), \tag{5}$$

$$\begin{aligned} z\left(\eta, \frac{2\pi}{5+\delta}, \mu, \varepsilon\right) &= z_0\left(\eta, \frac{2\pi}{5+\delta}\right) + \mu z_{10}\left(\eta, \frac{2\pi}{5+\delta}\right) + \varepsilon z_{01}\left(\eta, \frac{2\pi}{5+\delta}\right) + \text{h.o.t.} \\ &= \lambda_0\left(1 - \frac{2\pi\delta}{25}i\right)\eta + \frac{\mu a_1}{2}\lambda_0\left[\frac{2\pi}{5}\eta + \frac{i\bar{\eta}}{2}\left(1 - \bar{\lambda}_0^{\,2}\right)\right] + \varepsilon i\lambda_0\int_0^{2\pi/5} e^{-i\tau} f((5+\delta)\tau)\,d\tau + \frac{g_{20}}{2}\eta^2 \\ &\quad + g_{11}\eta\bar{\eta} + \frac{g_{02}}{2}\bar{\eta}^2 + \frac{g_{30}}{6}\eta^3 + \frac{g_{21}}{2}\eta^2\bar{\eta} + \frac{g_{12}}{2}\eta\bar{\eta}^2 + \frac{g_{03}}{6}\bar{\eta}^3 + \frac{g_{04}}{24}\bar{\eta}^4 + \text{h.o.t.}, \end{aligned} \tag{6}$$

where $\lambda_0 = e^{(2\pi/5)i}$, $g_{20}/2$, g_{11}, $g_{02}/2$, $g_{30}/6$, $g_{21}/2$, $g_{12}/2$, $g_{03}/6$, and $g_{04}/24$ are given by L_{20}, L_{11}, L_{02}, L_{30}, L_{21}, L_{12}, L_{03}, and L_{04}, all of which are evaluated at $t = 2\pi/(5+\delta)$.

Because $z(0, 2\pi/5, 0, 0) = 0$, and

$$\left(D\left[z\left(\eta, \frac{2\pi}{5+\delta}, \mu, \varepsilon\right) - \eta\right]\Big|_{\eta=0,\delta=0,\mu=0,\varepsilon=0}\right)\varsigma = (\lambda_0 - 1)\varsigma, \tag{7}$$

$\lambda_0 - 1 \neq 0$, by the implicit function theorem, we know that (6) has a fixed point $F(\delta, \mu, \varepsilon)$ which depends on δ, μ, and ε continuously.

$F(\delta, \mu, \varepsilon) = F_1 + \text{h.o.t.}$ where $F_1 = (\varepsilon i\lambda_0/(1-\lambda_0))\int_0^{2\pi/5} e^{-i\tau} f((5+\delta)\tau)d\tau$.

Making a translation of coordinate $\xi = \eta - F(\delta, \mu, \varepsilon)$, map (6) becomes

$$\begin{aligned}\xi' = {} & \lambda_0\left(1 + \frac{\mu a_1\pi}{5} + \frac{g_{20}F_1 + g_{11}\bar{F}_1}{\lambda_0} - \frac{2\pi\delta}{25}i\right)\xi + c_1\bar{\xi} \\ & + \frac{g_{20}}{2}\xi^2 + g_{11}\xi\bar{\xi} + \frac{g_{02}}{2}\bar{\xi}^2 + \frac{g_{30}}{6}\xi^3 + \frac{g_{21}}{2}\xi^2\bar{\xi} + \frac{g_{12}}{2}\xi\bar{\xi}^2 \\ & + \frac{g_{03}}{6}\bar{\xi}^3 + \frac{g_{04}}{24}\bar{\xi}^4 + \text{h.o.t.}\end{aligned} \tag{8}$$

With a change of coordinate $\xi = (1 + O(\delta, \mu, \varepsilon))\zeta$, we can eliminate the linear term of $\bar{\xi}$ and not change the others in map (8). It follows that

$$\begin{aligned}\xi' = {} & \lambda_0\left(1 + \frac{\mu a_1\pi}{5} + \frac{g_{20}F_1 + g_{11}\bar{F}_1}{\lambda_0} - \frac{2\pi\delta}{25}i\right)\xi + \frac{g_{20}}{2}\xi^2 \\ & + g_{11}\xi\bar{\xi} + \frac{g_{02}}{2}\bar{\xi}^2 + \frac{g_{30}}{6}\xi^3 + \frac{g_{21}}{2}\xi^2\bar{\xi} + \frac{g_{12}}{2}\xi\bar{\xi}^2 + \frac{g_{03}}{6}\bar{\xi}^3 \\ & + \frac{g_{04}}{24}\bar{\xi}^4 + \text{h.o.t.}\end{aligned} \tag{9}$$

By the theory of a normal form for a map, we can cancel all of the nonresonant terms, and map (9) is equivalent to

$$\begin{aligned}\omega' = {} & \lambda_0\left(1 + \frac{\mu a_1\pi}{5} + \frac{g_{20}F_1 + g_{11}\bar{F}_1}{\lambda_0} - \frac{2\pi\delta}{25}i\right)\omega + \frac{g'_{21}}{2}\omega^2\bar{\omega} \\ & + \frac{g'_{04}}{24}\bar{\omega}^4 + \text{h.o.t.}\end{aligned} \tag{10}$$

The coefficients of $g'_{21}/2$ and $g'_{04}/24$ are determined by Iooss [5]

$$\begin{aligned}\frac{g'_{21}}{2} = {} & \frac{g_{21}}{2} - g_{20}\gamma_{11} - g_{11}\left(\bar{\gamma}_{11} + \frac{\gamma_{20}}{2}\right) - g_{02}\frac{\bar{\gamma}_{02}}{2} \\ & + \lambda\gamma_{20}(g_{11} - \lambda\gamma_{11}) + \gamma_{11}\bar{\lambda}\left(\frac{g_{20}}{2} - \frac{\lambda\gamma_{20}}{2}\right) \\ & + \gamma_{11}\lambda\left(\bar{g}_{11} - \bar{\lambda}\bar{\gamma}_{11}\right) + \gamma_{02}\bar{\lambda}\left(\frac{\bar{g}_{02}}{2} - \frac{\bar{\lambda}\bar{\gamma}_{02}}{2}\right) \\ & + \lambda\left[\gamma_{20}\gamma_{11} + \gamma_{11}\left(\frac{\gamma_{20}}{2} + \bar{\gamma}_{11}\right) + \frac{\gamma_{02}\bar{\gamma}_{02}}{2}\right], \frac{g'_{04}}{24} \\ = {} & -\lambda\gamma_{11}\left(\frac{\gamma_{11}\gamma_{02}}{2} + \frac{\gamma_{02}\bar{\gamma}_{20}}{2}\right) - \lambda\gamma_{02}\left(\frac{\bar{\gamma}^2{}_{20}}{2} + \frac{\bar{\gamma}_{11}\gamma_{02}}{2}\right) \\ & - \frac{\lambda\gamma_{20}}{2}\frac{\gamma_{02}^2}{4} - \lambda\gamma_{11}\frac{\gamma_{02}\bar{\gamma}_{20}}{4} - \frac{\lambda\gamma_{02}}{2}\frac{\bar{\gamma}^2{}_{20}}{4} + \frac{g_{20}}{2}\frac{\gamma_{02}^2}{4} \\ & + g_{11}\frac{\gamma_{02}}{2}\frac{\bar{\gamma}_{20}}{2} + \frac{g_{02}}{2}\frac{\bar{\gamma}_{20}^2}{4} + g_{11}\left(\frac{\gamma_{11}\gamma_{02}}{2} + \frac{\gamma_{02}\bar{\gamma}_{20}}{2}\right) \\ & + g_{02}\left(\frac{\bar{\gamma}^2{}_{20}}{2} + \frac{\bar{\gamma}_{11}\gamma_{02}}{2}\right) - \frac{g_{12}}{2}\frac{\gamma_{02}}{2} - \frac{g_{03}}{2}\frac{\bar{\gamma}_{20}}{2} \\ & + \frac{\gamma_{20}}{2}\left(\frac{g_{02}}{2} - \frac{\lambda\gamma_{02}}{2}\right)^2 + \gamma_{11}\left[\lambda\bar{\lambda}\left(\frac{\gamma_{11}\gamma_{02}}{2} + \frac{\gamma_{02}\bar{\gamma}_{20}}{2}\right)\right. \\ & - \bar{\lambda}g_{11}\frac{\gamma_{02}}{2} - \bar{\lambda}g_{02}\frac{\bar{\gamma}_{20}}{2} + \bar{\lambda}\frac{g_{03}}{6} + \frac{g_{02}\bar{g}_{20}}{4} - \bar{\lambda}\frac{g_{02}}{2}\frac{\bar{\gamma}_{20}}{2} \\ & \left. - \lambda\frac{\bar{g}_{20}}{2}\frac{\gamma_{02}}{2} + \lambda\bar{\lambda}\frac{\gamma_{02}}{2}\frac{\bar{\gamma}_{20}}{2}\right] + \frac{\gamma_{02}}{2}\left[2\bar{\lambda}^2\left(\frac{\bar{\gamma}^2{}_{20}}{2} + \frac{\bar{\gamma}_{11}\gamma_{02}}{2}\right)\right. \\ & - 2\bar{\lambda}\bar{g}_{20}\frac{\bar{\gamma}_{20}}{2} - 2\bar{\lambda}\bar{g}_{11}\frac{\gamma_{02}}{2} + \frac{\bar{\lambda}\bar{g}_{30}}{3} + \left(\frac{\bar{g}_{20}}{2}\right)^2 \\ & \left. + \bar{\lambda}^2\left(\frac{\bar{\gamma}_{20}}{2}\right)^2 - \bar{\lambda}\bar{g}_{20}\frac{\bar{\gamma}_{20}}{2}\right] + \frac{g_{04}}{24},\end{aligned} \tag{11}$$

where $\lambda = \lambda_0(1 + (\mu a_1\pi/5) + ((g_{20}F_1 + g_{11}\bar{F}_1)/\lambda_0) - (2\pi\delta/25)i)$, and

$$\begin{aligned}\gamma_{20} &= \frac{g_{20}}{\lambda - \lambda^2}, \\ \gamma_{11} &= \frac{g_{11}}{\lambda - \lambda\bar{\lambda}}, \\ \gamma_{02} &= \frac{g_{02}}{\lambda - \bar{\lambda}^2}.\end{aligned} \tag{12}$$

After computing straightly, we have

$$\begin{aligned}\frac{g'_{21}(0)}{2} &= \left(\frac{3c}{8} + \frac{3si}{8} - \frac{b^2i}{6}\right)\frac{2\pi}{5}\lambda_0, \\ \frac{g'_{04}(0)}{24} &= -\frac{bc}{128}i + \frac{bc}{128}i\lambda_0.\end{aligned} \tag{13}$$

3. Invariant Circle and Phase Locking

For convenience, let us write (10) as

$$\omega' = \lambda\omega + \alpha\omega^2\bar{\omega} + \gamma\bar{\omega}^4 + \text{h.o.t.}, \tag{14}$$

where $\alpha = g'_{21}/2$ and $\gamma = g'_{04}/24$. Let $\lambda = \lambda_0(1 + \tilde{\lambda}_1)$, $\alpha_0 = \alpha|_{\mu=\varepsilon=\delta=0}$, and $\gamma_0 = \gamma|_{\mu=\varepsilon=\delta=0}$.

As we know, the dynamic behavior of map (14) is corresponding to that of Equation (1). If $\text{Re}\,(\alpha_0\bar{\lambda}_0) \neq 0$ and the derivation of $\text{Re}\,(\tilde{\lambda}_1)$ with respect to parameters is nonzero, the Neimark-Sacker bifurcation takes place for map (14).

We further study the phenomenon of phase locking on an invariant circle bifurcating from the fixed point of map (14). By changing variables $\omega = re^{i\varphi}$ and $\omega' = Re^{i\Phi}$, map (14) is described by Shilnikov et al. [8]

$$R = \left[1 + \text{Re}\left(\tilde{\lambda}_1\right)\right] r + \text{Re}\left(\alpha_0\bar{\lambda}_0\right) r^3 + \text{Re}\left(\gamma_0\bar{\lambda}_0 e^{-5i\varphi}\right) r^4 + \text{h.o.t.}, \tag{15}$$

$$\Phi = \varphi + \theta + \text{Im}\left(\alpha_0\bar{\lambda}_0\right) r^2 + \text{Im}\left(\gamma_0\bar{\lambda}_0 e^{-5i\varphi}\right) r^3 + \text{h.o.t.}, \tag{16}$$

where $\theta = \arg(\lambda)$.

Let us note $l_1 = \text{Re}\,(\alpha_0\bar{\lambda}_0)$, $m_1 = \text{Im}\,(\alpha_0\bar{\lambda}_0)$, $A = \text{Re}\,(\gamma_0\bar{\lambda}_0)$, $B = \text{Im}\,(\gamma_0\bar{\lambda}_0)$, and $\psi = \arctan(A/B)$. Equations (15) and (16) can be written as

$$R = \left[1 + \text{Re}\left(\tilde{\lambda}_1\right)\right] r + l_1 r^3 + \sqrt{A^2 + B^2}\cos(5\varphi + \psi) r^4 + \text{h.o.t.}, \tag{17}$$

$$\Phi = \varphi + \theta + m_1 r^2 - \sqrt{A^2 + B^2}\sin(5\varphi + \psi) r^3 + \text{h.o.t.} \tag{18}$$

In order to find the fifth-order subharmonic solution, iterating Equations (17) and (18) five times, then we obtain

$$\begin{aligned} R &= \left[1 + 5\,\text{Re}\left(\tilde{\lambda}_1\right)\right] r + 5l_1 r^3 + 5\sqrt{A^2 + B^2}\cos(5\varphi + \psi) r^4 + \text{h.o.t.}, \\ \Phi &= \varphi + 5\theta + 5m_1 r^2 - 5\sqrt{A^2 + B^2}\sin(5\varphi + \psi) r^3 + \text{h.o.t.} \end{aligned} \tag{19}$$

Solutions of equations

$$\begin{cases} R = r, \\ \Phi = \varphi (\text{mod } 2\pi) \end{cases} \tag{20}$$

are corresponding to the period 5 points of map (14).

Solving the first equation of (20), we get

$$R = \sqrt{\frac{\text{Re}\left(\tilde{\lambda}_1\right)}{|l_1|} + \frac{\sqrt{A^2 + B^2}\,\text{Re}\left(\tilde{\lambda}_1\right)}{2l_1^2}\cos(5\varphi + \psi)} + \text{h.o.t.} \tag{21}$$

Substituting the second equation of (20) with (21), and considering that θ is close to $2\pi/5$, we have

$$\begin{aligned} \theta - \frac{2\pi}{5} + m_1 \frac{\text{Re}\left(\tilde{\lambda}_1\right)}{|l_1|} + \left[\frac{m_1}{|l_1|}\cos(5\varphi + \psi)\right. \\ \left. - \sin(5\varphi + \psi)\right] \left[\frac{\text{Re}\left(\tilde{\lambda}_1\right)}{|l_1|}\right]^{3/2} \sqrt{A^2 + B^2} + \text{h.o.t.} = 0. \end{aligned} \tag{22}$$

If for some $\varphi = \varphi_0$,

$$\begin{aligned} \theta - \frac{2\pi}{5} + \frac{\text{Re}\left(\tilde{\lambda}_1\right) m_1}{|l_1|} \\ + \frac{\sqrt{m_1^2 + l_1^2}\sqrt{A^2 + B^2}\left[\text{Re}\left(\tilde{\lambda}_1\right)\right]^{3/2}}{|l_1|^{5/2}} \sin(5\varphi_0 + \psi_1) = 0 \end{aligned} \tag{23}$$

together with $\sqrt{A^2 + B^2} \neq 0$, "h.o.t." in Equation (22) can be offset by adjusting φ near φ_0.

For the boundedness of sinusoidal function and $\theta = (2\pi/5) - (2\pi\delta/25)$, we assert that if

$$\left|\frac{\text{Re}\left(\tilde{\lambda}_1\right) m_1}{|l_1|} - \frac{2\pi\delta}{25}\right| < \frac{\sqrt{m_1^2 + l_1^2}\sqrt{A^2 + B^2}\left[\text{Re}\left(\tilde{\lambda}_1\right)\right]^{3/2}}{|l_1|^{5/2}}, \tag{24}$$

there exist two sets of values of φ denoted by $(\varphi_1^1, \varphi_2^1, \varphi_3^1, \varphi_4^1, \varphi_5^1)$ and $(\varphi_1^2, \varphi_2^2, \varphi_3^2, \varphi_4^2, \varphi_5^2)$ which satisfy Equation (22). Then, the second equation of (20) follows and map (14) possesses two sets of period 5 solutions, one of which is stable, another is unstable.

4. The Numerical Simulations

To illustrate the results stated above, numerical simulations will be presented in this section. As mentioned in the introduction, f is a 2π periodic function. For simplicity, let $f((5 + \delta)t) = \sin((5 + \delta)t)$ in Equation (1), which is a simple form of $f((5 + \delta)t)$. It follows from (6)–(14) that

$$\begin{aligned} \omega' = \lambda_0\left(1 + \frac{\mu a_1\pi}{5} - \frac{5b\varepsilon}{24}\sin\frac{2\pi}{5} - \frac{2\pi\delta}{25}i\right)\omega + \alpha\omega^2\bar{\omega} \\ + \gamma\bar{\omega}^4 + \text{h.o.t.} \end{aligned} \tag{25}$$

Furthermore, we take the set of parameters $a_1 = 2$, $b = 1$, $s = 0$, $c = -4$. We can calculate that $\text{Re}\,(\alpha_0\bar{\lambda}_0) = -1.8850 < 0$ and the derivation of $\text{Re}\,(\tilde{\lambda}_1)$ with respect to parameters μ and ε is nonzero, which means that the supercritical Neimark-Sacker bifurcation takes place for map (25) [17].

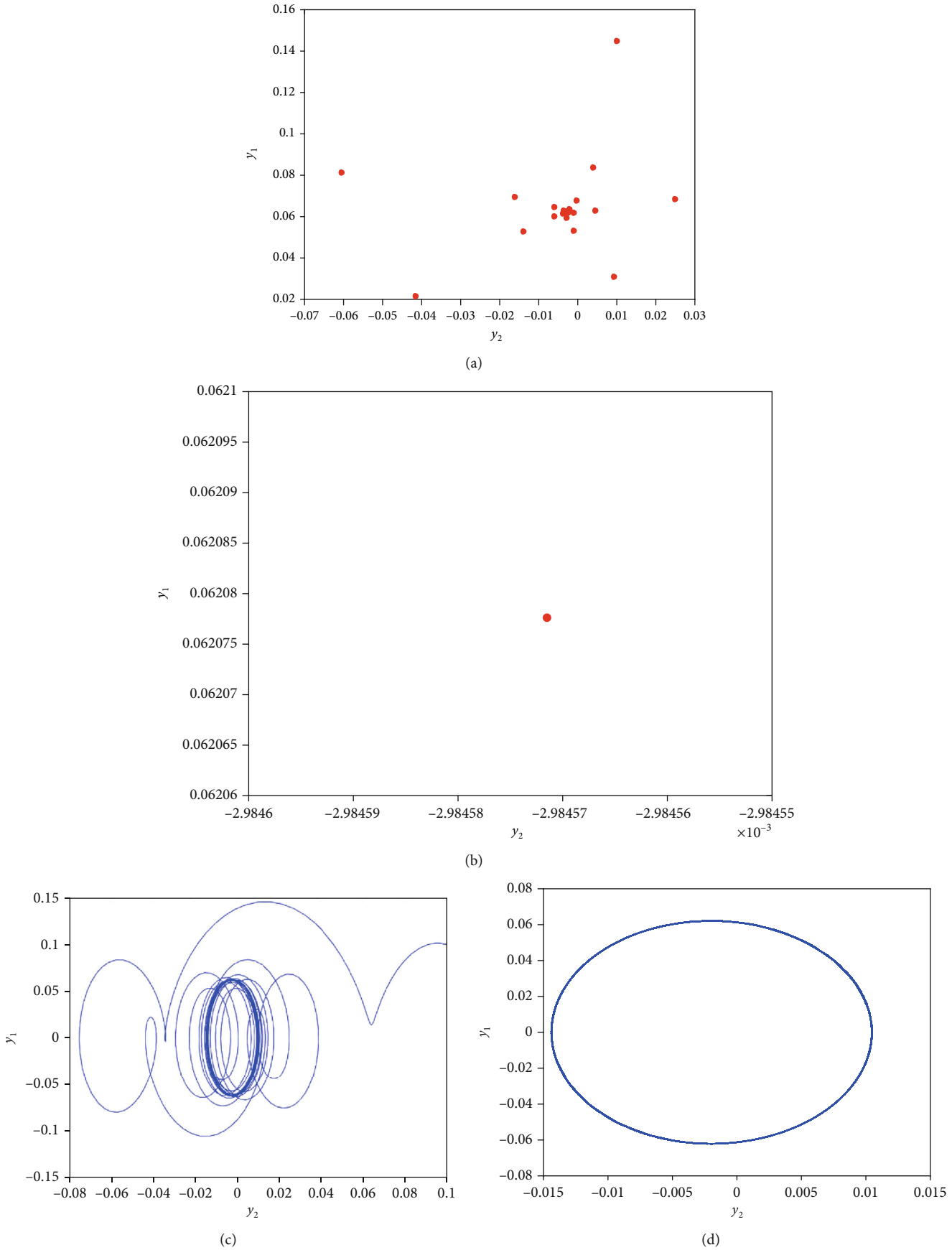

Figure 2: (a) Poincaré map; (b) Poincaré map (last 5000 points); (c) phase diagram; (d) phase diagram (last 10000 points).

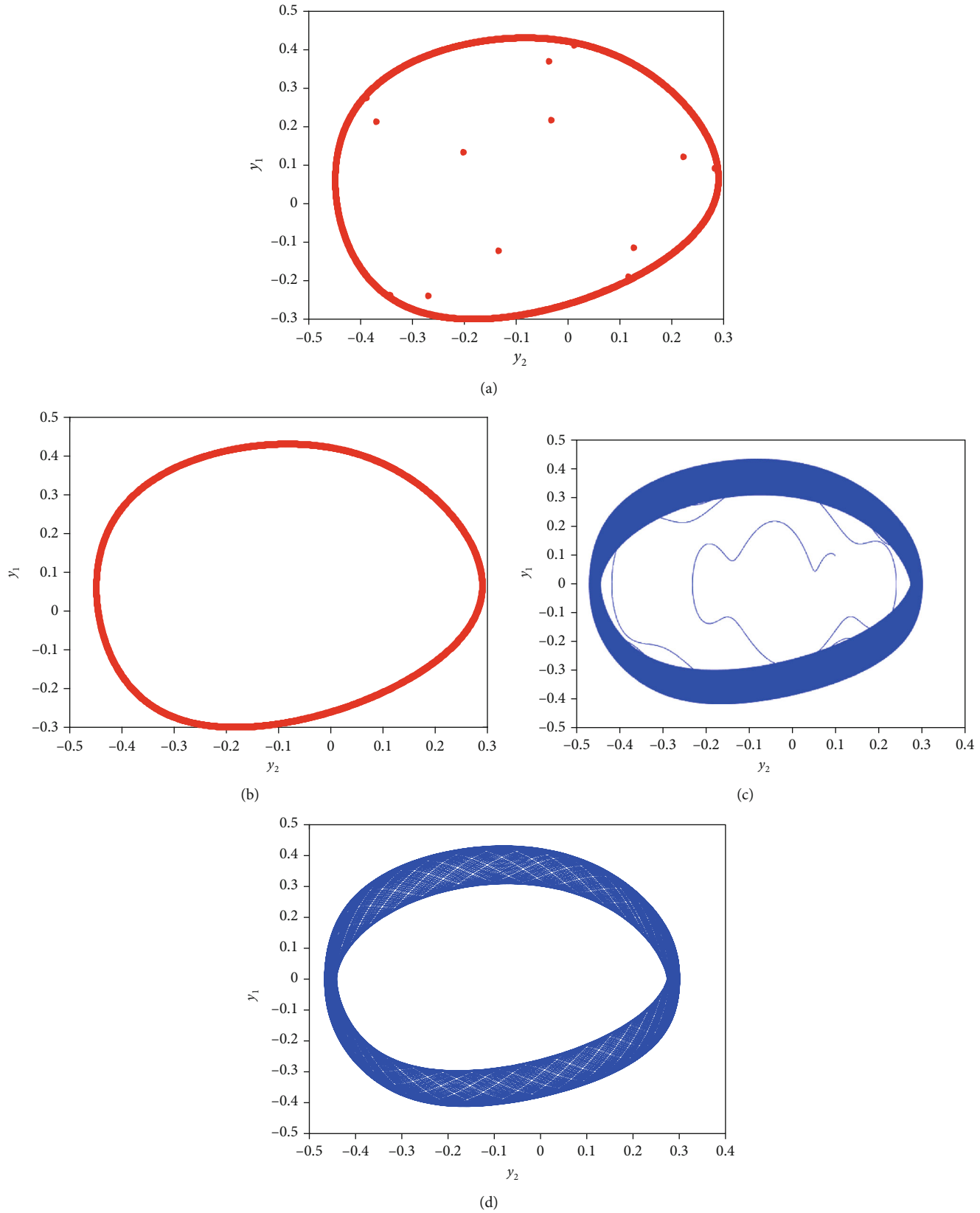

Figure 3: (a) Poincaré map; (b) Poincaré map (last 5000 points); (c) phase diagram; (d) phase diagram (last 10000 points).

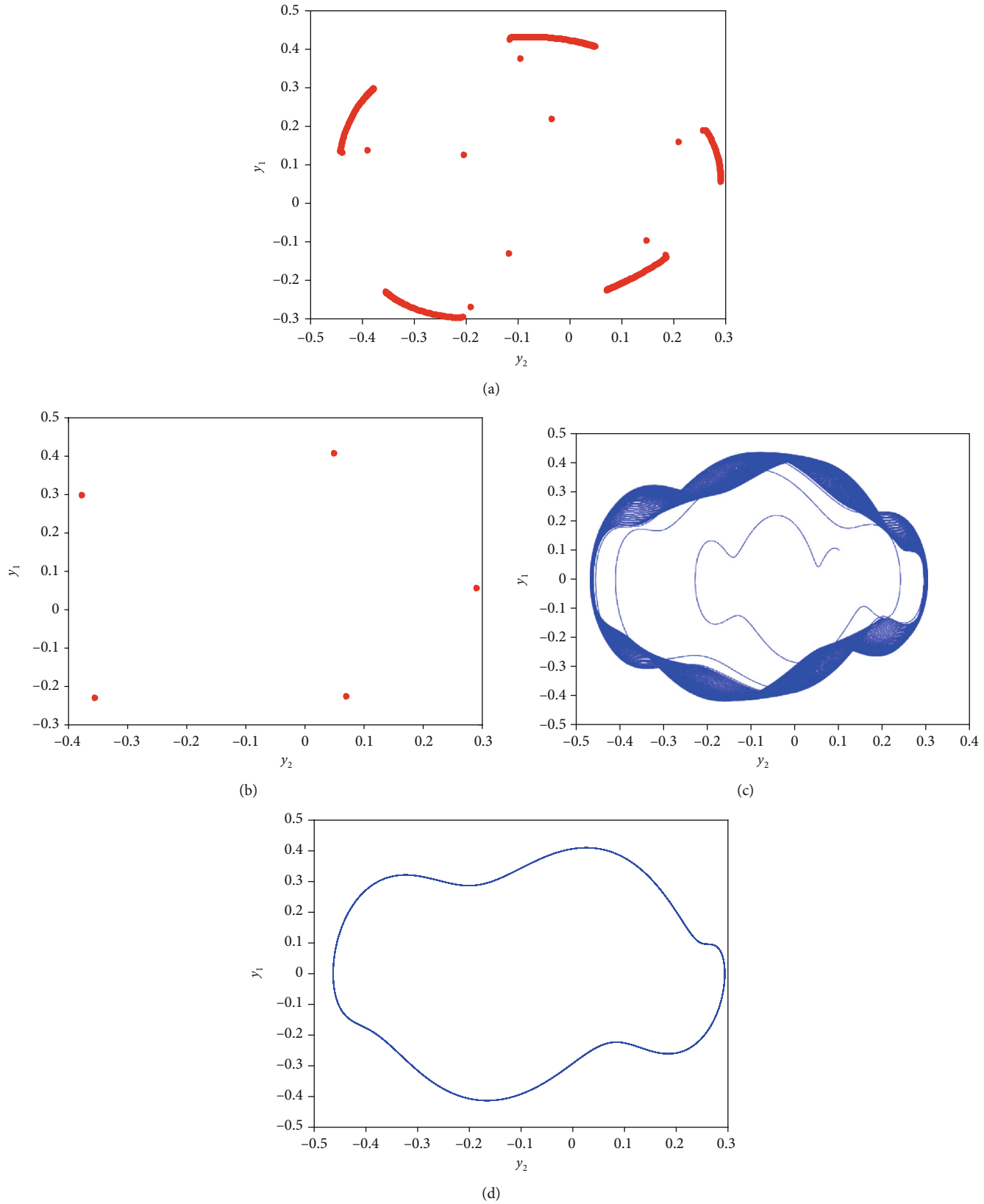

Figure 4: (a) Poincaré map; (b) Poincaré map (last 5000 points); (c) phase diagram; (d) phase diagram (last 10000 points).

Choosing $\varepsilon = -0.3$, $\mu = -0.2$, and $\delta = 0$, we get Re $(\tilde{\lambda}_1) = -0.1919$ and then assert that map (25) possesses a stable fixed point (see Figures 2(a) and 2(b)), namely, a stable periodic solution of Equation (1) (shown in Figures 2(c) and 2(d)). If the dynamic behaviors of the model in Figure 1 can be described by Equation (1) with the present parameters, the period of vibration of the mass body is the same as the external force.

Choosing $\varepsilon = -0.3$ and $\mu = 0.2$, we have Re $(\tilde{\lambda}_1) = 0.3108$ and then assert that map (25) possesses a stable invariant circle [17], namely, a stable torus motion of Equation (1). Because the limitation of map (25) on the stable invariant circle is a circle diffeomorphism, the trajectory on the torus is quasiperiodic or subharmonic motion, which depends on expression (24). As will be investigated below.

For $\delta = 0$, By straight computation, we obtain

$$\begin{aligned} &\frac{\mathrm{Re}\left(\tilde{\lambda}_1\right) m_1}{|l_1|} - \frac{2\pi\delta}{25} = -0.0345, \\ &\frac{\sqrt{m_1^2 + l_1^2}\sqrt{A^2 + B^2}\left[\mathrm{Re}\left(\tilde{\lambda}_1\right)\right]^{3/2}}{|l_1|^{5/2}} = 0.0025, \end{aligned} \tag{26}$$

which invalidate (24), there is no period 5 points for map (25) (see Figures 3(a) and 3(b)), and the solution of Equation (1) is quasiperiodic (shown in Figures 3(c) and 3(d)). If the dynamic behaviors of the model in Figure 1 can be described by Equation (1) with the present parameters, the vibration of the mass body is quasiperiodic, which is not periodic motion even though the external force is periodic.

For $\delta = -0.13$, calculation shows

$$\begin{aligned} &\frac{\mathrm{Re}\left(\tilde{\lambda}_1\right) m_1}{|l_1|} - \frac{2\pi\delta}{25} = -0.0019, \\ &\frac{\sqrt{m_1^2 + l_1^2}\sqrt{A^2 + B^2}\left[\mathrm{Re}\left(\tilde{\lambda}_1\right)\right]^{3/2}}{|l_1|^{5/2}} = 0.0025. \end{aligned} \tag{27}$$

Expression (24) follows, map (25) possesses period 5 points (see Figures 4(a) and 4(b)), and Equation (1) yields a subharmonic motion (shown in Figures 4(c) and 4(d)). If the dynamic behaviors of the model in Figure 1 can be described by Equation (1) with the present parameters, the vibration of the mass body is subharmonic, whose period is five times than that of the external force.

Because the analysis method of this paper is for system (1) with abstract coefficients, it can be applied in other mechanical models whose dynamics can be described by Equation (1), for example, the forced Van der Pol equations [6], the forced dry friction system [18], the vibration of railway bow net, and the forced vibration of cantilevered flow-conveying pipe.

5. Conclusions

In this paper, we study the Neimark-Sacker bifurcation of a forced vibration system by theoretical analysis and numerical simulations in the 1 : 5 resonance case. The Poincaré map is established by the analytical method. By means of analyzing the map, it is shown that there exist quasiperiodic and subharmonic solutions on the torus. Numerical simulations agreed with the theoretical results. It is certain that the method applied in this paper can be applied to some other analogous systems.

Data Availability

The data used to support the findings of this study are available from the corresponding author upon request.

Conflicts of Interest

The author declares that they have no conflicts of interest.

Acknowledgments

This work is supported by XJGC20190909.

References

[1] Y. Guo and J. H. Xie, "Neimark-Sacker (N-S) bifurcation of oscillator with dry friction in 1:4 strong resonance," *Applied Mathematics and Mechanics*, vol. 34, no. 1, pp. 27–36, 2013.

[2] V. I. Arnold, "Loss of stability of self-oscillations close to resonance and versal deformations of equivariant vector fields," *Functional Analysis and its Applications*, vol. 22, pp. 85–92, 1977.

[3] B. Krauskopf, "Bifurcation sequences at 1:4 resonance: an inventory," *Nonlinearity*, vol. 7, no. 3, pp. 1073–1091, 1994.

[4] J. M. Gambaudo, "Perturbation of a Hopf bifurcation by an external time-periodic forcing," *Journal of Differential Equations*, vol. 57, no. 2, pp. 172–199, 1985.

[5] G. Iooss, *Bifurcation of Maps and Applications*, North-Holland Publishing Company, Amsterdam. New York. Oxford, 1979.

[6] Y.-H. Wan, "Bifurcation into invariant tori at points of resonance," *Archive for Rational Mechanics Analysis*, vol. 68, no. 4, pp. 343–357, 1978.

[7] V. I. Arnold, *Geometrical Methods in the Theory of Ordinary Differential Equations*, Springe-Verlag, New York, 1983.

[8] L. P. Shilnikov, A. L. Shilnikov, D. V. Turaev, and L. O. Chua, *Methods of Qualitative Theory in Nonlinear Dynamics, Part II*, World Scientific, 2001.

[9] G. Iooss, *Bifurcation and transition to turbulence in hydrodynamics*, Springer, Berlin Heidelberg, Berlin, Heidelberg, 1984.

[10] G. Luo, Y. Zhang, J. Xie, and J. Zhang, "Periodic-impact motions and bifurcations of vibro-impact systems near 1:4 strong resonance point," *Communications in Nonlinear Science and Numerical Simulation*, vol. 13, no. 5, pp. 1002–1014, 2008.

[11] Y. Guo and A. C. J. Luo, "Periodic motions in a double-well Duffing oscillator under periodic excitation through discrete implicit mappings," *International Journal of Dynamics and Control*, vol. 5, pp. 223–238, 2015.

[12] T. S. Amer, M. A. Bek, and I. S. Hamada, "On the motion of harmonically excited spring pendulum in elliptic path near resonances," *Advances in Mathematical Physics*, vol. 2016, Article ID 8734360, 15 pages, 2016.

[13] Z. Hao, Q. Cao, and M. Wiercigroch, "Nonlinear dynamics of the quasi-zero-stiffness SD oscillator based upon the local and global bifurcation analyses," *Nonlinear Dynamics*, vol. 87, pp. 987–1014, 2016.

[14] A. C. J. Luo, "Periodic motions and chaos in nonlinear dynamical systems," *The European Physical Journal Special Topics*, vol. 228, no. 9, pp. 1745-1746, 2019.

[15] N. Hua and T. Li-Xin, "The existence of n periodic solutions on one element n-degree polynomial differential equation," *Advances in Mathematical Physics*, vol. 2020, Article ID 7034591, 7 pages, 2020.

[16] Y. Xu and A. C. J. Luo, "Frequency-amplitude characteristics of periodic motions in a periodically forced van der Pol oscillator," *The European Physical Journal Special Topics*, vol. 228, no. 9, pp. 1839–1854, 2019.

[17] Y. A. Kuznetsov, *Elements of Applied Bifurcation Theory*, Springer-Verlag, 2nd edition, 1998.

[18] R. I. Leine and H. Nijmeijer, *Dynamics and Bifurcations of Non-Smooth Mechanical Systems*, Springer, New York, 2004.

Hindawi
Advances in Mathematical Physics
Volume 2020, Article ID 5809289, 10 pages
https://doi.org/10.1155/2020/5809289

Research Article

On the Analytical and Numerical Solutions in the Quantum Magnetoplasmas: The Atangana Conformable Derivative (1 + 3)-ZK Equation with Power-Law Nonlinearity

Mostafa M. A. Khater,[1,2] **Yu-Ming Chu**,[3,4] **Raghda A. M. Attia**,[1,5] **Mustafa Inc**,[6,7] **and Dianchen Lu**[1]

[1]*Department of Mathematics, Faculty of Science, Jiangsu University, 212013 Zhenjiang, China*
[2]*Department of Mathematics, El Obour Institutes, 11828 Cairo, Egypt*
[3]*Department of Mathematics, Huzhou University, Huzhou 313000, China*
[4]*Hunan Provincial Key Laboratory of Mathematical Modeling and Analysis in Engineering, Changsha University of Science and Technology, Changsha 410114, China*
[5]*Department of Basic Science, Higher Technological Institute 10th of Ramadan City, El Sharqia 44634, Egypt*
[6]*Department of Mathematics, Science Faculty, Firat University, 23119 Elazig, Turkey*
[7]*Department of Medical Research, China Medical University Hospital, China Medical University, Taichung, Taiwan*

Correspondence should be addressed to Yu-Ming Chu; chuyuming@zjhu.edu.cn and Mustafa Inc; minc@firat.edu.tr

Received 10 June 2020; Accepted 31 July 2020; Published 23 September 2020

Guest Editor: Xiao-Ling Gai

In this research paper, our work is connected with one of the most popular models in quantum magnetoplasma applications. The computational wave and numerical solutions of the Atangana conformable derivative (1 + 3)-Zakharov-Kuznetsov (ZK) equation with power-law nonlinearity are investigated via the modified Khater method and septic-B-spline scheme. This model is formulated and derived by employing the well-known reductive perturbation method. Applying the modified Khater (mK) method, septic B-spline scheme to the (1 + 3)-ZK equation with power-law nonlinearity after harnessing suitable wave transformation gives plentiful unprecedented ion-solitary wave solutions. Stability property is checked for our results to show their applicability for applying in the model's applications. The result solutions are constructed along with their 2D, 3D, and contour graphical configurations for clarity and exactitude.

1. Introduction

In the existence of a magnetized e-p-i plasma [1], the ZK equation is one of the widely common methods to characterize the ion-acoustic solitary waves. The magnetized load-varying dusty plasma is the best location to look for alternate placed dust ion acoustic waves of nonthermal electrons with a vortex-like spread of velocity [2]. In a comprehensive computational analysis, the ZK method was used to spread the dust-acoustic waves in a magnetized dusty plasma [3] and to excite the electrostatic ion-acoustic lone wave in two dimensions of negative ion magnetoplasmas of superthermal electrons [4]. This plasma comprises of nonthermal ions and negatively charged mobile dust crystals, and q-distributed temperature electrons of distinct nonextensivity power [5]. The ZK equation's mathematical formula found by the well-known reductive disruption process [6] is given by

$$\mathscr{D}_t^{\alpha}\mathfrak{B} + \mathfrak{L}\,\mathfrak{B}\,\mathfrak{B}_z + \mathfrak{B}_{zzz} + \mathfrak{Q}\left(\mathfrak{B}_{xxz} + \mathfrak{B}_{yyz}\right) = 0, \quad (1)$$

where $\mathscr{D}_t^{\alpha} = d^{\alpha}/dt^{\alpha}, 0 < \alpha < 0, \mathfrak{B} = \mathfrak{B}(x, y, z, t)$, $\mathfrak{L} = 2$, $\mathfrak{Q} = 1 - (\mathfrak{H}_{\mathfrak{e}}^2/8)$, $\mathfrak{H}_{\mathfrak{e}} = (\mathscr{H}\sqrt{\omega_{ci}\omega_{ce}})/2\mathscr{K}_B\mathscr{T}_{Fe}$, $\mathscr{H} = 2\pi$, $\omega_{ci} = e\mathscr{B}_0/2\mathscr{K}_B\mathscr{T}_{Fe}$, and $\omega_{ce} = e\mathscr{B}_0/m_e, c$. Additionally, $\mathscr{H}$ is Planck's constant; $\sqrt{\omega_{ci}\omega_{ce}}$ is the lower-hybrid resonance frequency; $\omega_{ci} = e\mathscr{B}_0/\mathscr{M}_i c$, $\omega_{ce} = e\mathscr{B}_0/\mathscr{M}_e c$ are the ion

(electron) gyrofrequency; $\mathscr{M}_i$ is the ion mass; and c is the speed of light in vacuum.

Solving this kind of models has attracted many researchers in various areas, chemical physics [7], geochemistry [8], plasma physics [8], fluid mechanics [9], optical fiber [10], solid-state physics [11], and so on [12–15]. Consequently, constructing the exact solutions of these mathematical models is an indispensable tool for detecting novel properties of them that can be used in their various applications. However, finding the exact solutions of them are not easy to process but is also considered a hard and complex process where there is no unified computational or numerical technique that is able to be applied to all nonlinear evolution (NLE) equations. Almost all computational and numerical techniques depend on an auxiliary equation that is considered a pivot tool in these techniques where all obtained solutions via these schemes are special cases of its general solutions [16–24].

For the fractional models, many analytical and numerical methods with various fractional operators have been derived such as the exponential expansion method, Khater method, Kudryashov method, simplest equation method, (Ψ'/Ψ) -expansion method, Riccati expansion method, first integral method, tanh method, and the functional variable method [25–34].

This paper studies the analytical and numerical solutions of the Atangana conformable derivative (1 + 3)-ZK equation with power-law nonlinearity that is given by [35–38].

$$\mathscr{D}_t^{\alpha}\,\mathfrak{B} + a\,\mathfrak{B}^n\,\mathfrak{B}_x + b\left(\mathfrak{B}_{xxx} + \mathfrak{B}_{yyx} + \mathfrak{B}_{zzx}\right) = 0, \quad (2)$$

where a, b, respectively, represent the nonlinearity and dispersion real valued constants. Also, $\mathfrak{B}_t$ is the evolution term while n represents the power law nonlinearity parameter. Using the following wave transformation [39, 40] $[\mathfrak{B} = \mathfrak{B}(x, y, z, t) = \mathfrak{P}(\mathfrak{F}), \mathfrak{F} = x + y + z + (\lambda/\alpha)\,(t + (1/\Gamma(\alpha)))^{\alpha}]$ on Equation (1) where λ is an arbitrary constant yields

$$\lambda\,\mathfrak{P}' + \frac{a}{n+1}\,\mathfrak{P}^n\,\mathfrak{P}' + b\left(3\,\mathfrak{P}''\right) = 0. \quad (3)$$

Integrating Equation (3) once with zero constant of the integration leads to

$$\lambda\,\mathfrak{P} + \frac{a}{n+1}\,\mathfrak{P}^{n+1} + 3\,b\,\mathfrak{P}'' = 0. \quad (4)$$

Through the balancing principle, the terms $\mathfrak{P}^{n+1}$ and $\mathfrak{P}''$ force that $m = 2/n$. Thus, we employ another transformation $\mathfrak{P} = \mathfrak{U}^{2/n}$ on Equation (1) gives

$$\lambda\,\mathfrak{U}^2 + \frac{a}{n+1}\,\mathfrak{U}^4 + \frac{3\,b\,(4-2\,n)}{n^2}\,\mathfrak{U}'^2 + \frac{6\,b}{n}\,\mathfrak{U}\,\mathfrak{U}'' = 0. \quad (5)$$

Balancing between the terms of Equation (5) leads to $m = 1$.

The outline of this research paper is given as follows. Section 2 employs the mK method and septic B-spline scheme to get the abundant explicit wave and numerical solutions of the Atangana conformable derivative (1 + 3)-ZK equation with power-law nonlinearity. Section 3 investigates the stability of the results solutions. Section 4 shows and discusses the obtained results in our research paper. Section 5 gives the graphical demonstration of some of our solutions. Section 6 explains the conclusion of our study.

2. Implementation

In this section, we employ three recent analytical schemes to find the explicit wave solutions of the Atangana conformable derivative (1 + 3)-ZK equation with power-law nonlinearity.

2.1. Ion-Acoustic Solitary Waves Solutions. This section gives a transitory elucidation of the mK method. We now explore a nontrivial solution for Equation (5) in the form

$$\begin{aligned}\mathfrak{U} &= \sum_{i=1}^{m} a_i\,\mathscr{K}^{i\mathscr{F}(\mathfrak{F})} + \sum_{i=1}^{m} b_i\,\mathscr{K}^{-i\mathscr{F}(\mathfrak{F})} + a_0 \\ &= a_1\,\mathscr{K}^{\mathscr{F}(\mathfrak{F})} + a_0 + b_1\,\mathscr{K}^{-\mathscr{F}(\mathfrak{F})},\end{aligned} \quad (6)$$

where a_0, a_1, and b_1 are arbitrary constants while $\mathscr{F}(\mathfrak{F})$ is a function that satisfies the next ODE

$$\mathscr{F}'(\mathfrak{F}) = \frac{\mathrm{u}\,\mathscr{K}^{-\mathscr{F}(\mathfrak{F})} + \rho\,\mathscr{K}^{\mathscr{F}(\mathfrak{F})} + \delta}{\ln(\mathscr{K})}. \quad (7)$$

where u, ρ, and δ are arbitrary constants. Exchanging the values of $\mathfrak{U}, \mathfrak{U}''$ with Equation (6) along (7) and aggregation of all terms with the same power of $\mathscr{K}^{j\mathscr{F}(\mathfrak{F})}$, $(j = -4, -3, \cdots, 3, 4)$ then equating the gathering terms with zero lead to a system of equations. Solving this system yields

Family I

$$\begin{aligned} a_0 &\longrightarrow \frac{a_1\sqrt{\delta^2 - 4\rho\mathrm{u}} + a_1\delta}{2\rho}, \\ b_1 &\longrightarrow 0, \\ \lambda &\longrightarrow \frac{1}{4}(-3)\left(b\delta^2 - 4b\rho\mathrm{u}\right), \\ a &\longrightarrow -\frac{9b\rho^2}{4a_1^2}, \\ n &\longrightarrow -4. \end{aligned} \quad (8)$$

Family II

$$\begin{aligned} a_0 &\longrightarrow \frac{b_1\sqrt{\delta^2 - 4\rho\mathrm{u}} + b_1\delta}{2\mathrm{u}}, \\ a_1 &\longrightarrow 0, \\ \lambda &\longrightarrow \frac{1}{4}(-3)\left(b\delta^2 - 4b\rho\mathrm{u}\right), \\ a &\longrightarrow -\frac{9b\mathrm{u}^2}{4b_1^2}, \\ n &\longrightarrow -4. \end{aligned} \quad (9)$$

Family III

$$\begin{aligned} a_1 &\longrightarrow \frac{a_0\rho}{\delta},\\ b_1 &\longrightarrow \frac{a_0 \mathrm{u}}{\delta},\\ \lambda &\longrightarrow \frac{1}{4}(-3)\left(b\delta^2 - 4b\rho\mathrm{u}\right),\\ a &\longrightarrow -\frac{9b\delta^2}{4a_0^2},\\ n &\longrightarrow -4. \end{aligned} \tag{10}$$

Family IV

$$\begin{aligned} a_0 &\longrightarrow \frac{a_1\delta}{2\rho},\\ b_1 &\longrightarrow 0,\\ \lambda &\longrightarrow \frac{3}{2}\left(b\delta^2 - 4b\rho\mathrm{u}\right),\\ a &\longrightarrow -\frac{18b\rho^2}{a_1^2},\\ n &\longrightarrow 2. \end{aligned} \tag{11}$$

Family VI

$$\begin{aligned} a_0 &\longrightarrow \frac{b_1\delta}{2\mathrm{u}},\\ a_1 &\longrightarrow 0,\\ \lambda &\longrightarrow \frac{3}{2}\left(b\delta^2 - 4b\rho\mathrm{u}\right),\\ a &\longrightarrow -\frac{18b\mathrm{u}^2}{b_1^2},\\ n &\longrightarrow 2. \end{aligned} \tag{12}$$

Thus, using the above families leads to the new exact solitary wave solutions to the Atangana conformable derivative (1 + 3)-ZK equation with power-law nonlinearity in the next formulas.

For $\delta^2 - 4\rho\,\mathrm{u} < 0$, $\rho \neq 0$, we get

$$\begin{aligned}
\mathfrak{B}_{\mathrm{I},1}(x,t) &= \frac{\sqrt{2}}{\sqrt{\left(a_1\left(\sqrt{4\rho\mathrm{u}-\delta^2}\tan\left(\left(\sqrt{4\rho\mathrm{u}-\delta^2}\left(4\alpha\mathscr{H}-3b\phi\left(\delta^2-4\rho\mathrm{u}\right)\right)\right)/8\alpha\right)+\sqrt{\delta^2-4\rho\mathrm{u}}\right)\right)/\rho}},\\
\mathfrak{B}_{\mathrm{I},2}(x,t) &= \frac{\sqrt{2}}{\sqrt{\left(a_1\left(\sqrt{4\rho\mathrm{u}-\delta^2}\cot\left(\left(\sqrt{4\rho\mathrm{u}-\delta^2}\left(4\alpha\mathscr{H}-3b\phi\left(\delta^2-4\rho\mathrm{u}\right)\right)\right)/8\alpha\right)+\sqrt{\delta^2-4\rho\mathrm{u}}\right)\right)/\rho}},\\
\mathfrak{B}_{\mathrm{II},1}(x,t) &= \frac{\sqrt{2}}{\sqrt{b_1\left(\left(\left(\sqrt{\delta^2-4\rho\mathrm{u}}+\delta\right)/\mathrm{u}\right)-\left(4\rho/\left(\delta-\sqrt{4\rho\mathrm{u}-\delta^2}\tan\left(\left(\sqrt{4\rho\mathrm{u}-\delta^2}\left(4\alpha\mathscr{H}-3b\phi\left(\delta^2-4\rho\mathrm{u}\right)\right)\right)/8\alpha\right)\right)\right)\right)}},\\
\mathfrak{B}_{\mathrm{II},2}(x,t) &= \frac{\sqrt{2}}{\sqrt{b_1\left(\left(\left(\sqrt{\delta^2-4\rho\mathrm{u}}+\delta\right)/\mathrm{u}\right)-\left(4\rho/\left(\delta-\sqrt{4\rho\mathrm{u}-\delta^2}\cot\left(\sqrt{4\rho\mathrm{u}-\delta^2}\left(4\alpha\mathscr{H}-3b\phi\left(\delta^2-4\rho\mathrm{u}\right)\right)/8\alpha\right)\right)\right)\right)}},\\
\mathfrak{B}_{\mathrm{III},1}(x,t) &= \frac{1}{\sqrt{\left(a_0\left(\delta^2-4\rho\mathrm{u}\right)\right)/\left(\delta\left(-\sqrt{4\rho\mathrm{u}-\delta^2}\sin\left(\sqrt{4\rho\mathrm{u}-\delta^2}\left(\mathscr{H}-\left(3b\phi\left(\delta^2-4\rho\mathrm{u}\right)/4\alpha\right)\right)\right)+\delta\cos\left(\sqrt{4\rho\mathrm{u}-\delta^2}\left(\mathscr{H}-\left(3b\phi\left(\delta^2-4\rho\mathrm{u}\right)/4\alpha\right)\right)\right)+\delta\right)\right)}},\\
\mathfrak{B}_{\mathrm{III},2}(x,t) &= \frac{1}{\sqrt{-\left(a_0\left(\delta^2-4\rho\mathrm{u}\right)\right)/\left(\delta\left(\sqrt{4\rho\mathrm{u}-\delta^2}\sin\left(\sqrt{4\rho\mathrm{u}-\delta^2}\left(\mathscr{H}-\left(3b\phi\left(\delta^2-4\rho\mathrm{u}\right)/4\alpha\right)\right)\right)+\delta\cos\left(\sqrt{4\rho\mathrm{u}-\delta^2}\left(\mathscr{H}-\left(3b\phi\left(\delta^2-4\rho\mathrm{u}\right)/4\alpha\right)\right)\right)-\delta\right)\right)}},\\
\mathfrak{B}_{\mathrm{IV},1}(x,t) &= \frac{a_1\sqrt{4\rho\mathrm{u}-\delta^2}\tan\left(\left(\sqrt{4\rho\mathrm{u}-\delta^2}\left(3b\phi\left(\delta^2-4\rho\mathrm{u}\right)+2\alpha\mathscr{H}\right)\right)/4\alpha\right)}{2\rho},\\
\mathfrak{B}_{\mathrm{IV},2}(x,t) &= \frac{a_1\sqrt{4\rho\mathrm{u}-\delta^2}\cot\left(\left(\sqrt{4\rho\mathrm{u}-\delta^2}\left(3b\phi\left(\delta^2-4\rho\mathrm{u}\right)+2\alpha\mathscr{H}\right)\right)/4\alpha\right)}{2\rho},\\
\mathfrak{B}_{\mathrm{V},1}(x,t) &= \frac{1}{2}b_1\left(\frac{\delta}{\mathrm{u}}-\frac{4\rho}{\delta-\sqrt{4\rho\mathrm{u}-\delta^2}\tan\left(\left(\sqrt{4\rho\mathrm{u}-\delta^2}\left(3b\phi\left(\delta^2-4\rho\mathrm{u}\right)+2\alpha\mathscr{H}\right)\right)/4\alpha\right)}\right),\\
\mathfrak{B}_{\mathrm{V},2}(x,t) &= \frac{1}{2}b_1\left(\frac{\delta}{\mathrm{u}}-\frac{4\rho}{\delta-\sqrt{4\rho\mathrm{u}-\delta^2}\cot\left(\left(\sqrt{4\rho\mathrm{u}-\delta^2}\left(3b\phi\left(\delta^2-4\rho\mathrm{u}\right)+2\alpha\mathscr{H}\right)\right)/4\alpha\right)}\right).
\end{aligned} \tag{13}$$

For $\rho\delta^2 - 4\rho u < 0, \neq 0$, we get

$$\mathfrak{B}_{I,3}(x,t) = \frac{\sqrt{2}}{\sqrt{-\left(a_1\sqrt{\delta^2-4\rho u}\left(\tanh\left(\left(\sqrt{\delta^2-4\rho u}(4\alpha\mathscr{H}-3b\phi(\delta^2-4\rho u))\right)/8\alpha\right)-1\right)\right)/\rho}},$$

$$\mathfrak{B}_{I,4}(x,t) = \frac{\sqrt{2}}{\sqrt{-\left(a_1\sqrt{\delta^2-4\rho u}\left(\coth\left(\left(\sqrt{\delta^2-4\rho u}(4\alpha\mathscr{H}-3b\phi(\delta^2-4\rho u))\right)/8\alpha\right)-1\right)\right)/\rho}},$$

$$\mathfrak{B}_{II,3}(x,t) = \frac{\sqrt{2}}{\sqrt{b_1\left(\left(\left(\sqrt{\delta^2-4\rho u}+\delta\right)/u\right)-\left(4\rho/\left(\sqrt{\delta^2-4\rho u}\tanh\left(\left(\sqrt{\delta^2-4\rho u}(4\alpha\mathscr{H}-3b\phi(\delta^2-4\rho u))\right)/8\alpha\right)+\delta\right)\right)\right)}},$$

$$\mathfrak{B}_{II,4}(x,t) = \frac{\sqrt{2}}{\sqrt{b_1\left(\left(\left(\sqrt{\delta^2-4\rho u}+\delta\right)/u\right)-\left(4\rho/\left(\sqrt{\delta^2-4\rho u}\coth\left(\left(\sqrt{\delta^2-4\rho u}(4\alpha\mathscr{H}-3b\phi(\delta^2-4\rho u))\right)/8\alpha\right)+\delta\right)\right)\right)}},$$

$$\mathfrak{B}_{III,3}(x,t) = \frac{1}{\sqrt{(a_0(\delta^2-4\rho u))/\left(\delta\left(\sqrt{\delta^2-4\rho u}\sinh\left(\sqrt{\delta^2-4\rho u}(\mathscr{H}-(3b\phi(\delta^2-4\rho u)/4\alpha))\right)+\delta\cosh\left(\sqrt{\delta^2-4\rho u}(\mathscr{H}-(3b\phi(\delta^2-4\rho u)/4\alpha))\right)+\delta\right)\right)}},$$

$$\mathfrak{B}_{III,4}(x,t) = \frac{1}{\sqrt{-(a_0(\delta^2-4\rho u))/\left(\delta\left(\sqrt{\delta^2-4\rho u}\sinh\left(\sqrt{\delta^2-4\rho u}(\mathscr{H}-(3b\phi(\delta^2-4\rho u)/4\alpha))\right)+\delta\cosh\left(\sqrt{\delta^2-4\rho u}(\mathscr{H}-(3b\phi(\delta^2-4\rho u)/4\alpha))\right)-\delta\right)\right)}},$$

$$\mathfrak{B}_{IV,3}(x,t) = -\frac{a_1\sqrt{\delta^2-4\rho u}\tanh\left(\left(\sqrt{\delta^2-4\rho u}(3b\phi(\delta^2-4\rho u)+2\alpha\mathscr{H})\right)/4\alpha\right)}{2\rho},$$

$$\mathfrak{B}_{IV,4}(x,t) = -\frac{a_1\sqrt{\delta^2-4\rho u}\coth\left(\left(\sqrt{\delta^2-4\rho u}(3b\phi(\delta^2-4\rho u)+2\alpha\mathscr{H})\right)/4\alpha\right)}{2\rho},$$

$$\mathfrak{B}_{V,3}(x,t) = \frac{1}{2}b_1\left(\frac{\delta}{u}-\frac{4\rho}{\sqrt{\delta^2-4\rho u}\tanh\left(\left(\sqrt{\delta^2-4\rho u}(3b\phi(\delta^2-4\rho u)+2\alpha\mathscr{H})\right)/4\alpha\right)+\delta}\right),$$

$$\mathfrak{B}_{V,4}(x,t) = \frac{1}{2}b_1\left(\frac{\delta}{u}-\frac{4\rho}{\sqrt{\delta^2-4\rho u}\coth\left(\left(\sqrt{\delta^2-4\rho u}(3b\phi(\delta^2-4\rho u)+2\alpha\mathscr{H})\right)/4\alpha\right)+\delta}\right). \tag{14}$$

For $\rho u > 0, u \neq 0, \rho \neq 0, \delta = 0$, we get

$$\mathfrak{B}_{I,5}(x,t) = \frac{1}{\sqrt{\left(a_1\left(\sqrt{\rho u}\tan\left(\sqrt{\rho u}((3b\rho u\phi)/\alpha+\mathscr{H})\right)+\sqrt{\rho(-u)}\right)\right)/\rho}},$$

$$\mathfrak{B}_{I,6}(x,t) = \frac{1}{\sqrt{\left(a_1\left(\sqrt{\rho(-u)}-\sqrt{\rho u}\cot\left(\sqrt{\rho u}(((3b\rho u\phi)/\alpha)+\mathscr{H})\right)\right)\right)/\rho}},$$

$$\mathfrak{B}_{II,5}(x,t) = \frac{1}{\sqrt{\left(b_1\left(\sqrt{\rho u}\cot\left(\sqrt{\rho u}(((3b\rho u\phi)/\alpha)+\mathscr{H})\right)+\sqrt{\rho(-u)}\right)\right)/u}},$$

$$\mathfrak{B}_{II,6}(x,t) = \frac{1}{\sqrt{\left(b_1\left(\sqrt{\rho(-u)}-\sqrt{\rho u}\tan\left(\sqrt{\rho u}(((3b\rho u\phi)/\alpha)+\mathscr{H})\right)\right)\right)/u}},$$

$$\mathfrak{B}_{IV,5}(x,t) = \frac{a_1 u\tan\left(\sqrt{\rho u}(\mathscr{H}-((6b\rho u\phi)/\alpha))\right)}{\sqrt{\rho u}},$$

$$\mathfrak{B}_{IV,6}(x,t) = -\frac{a_1 u\cot\left(\sqrt{\rho u}(\mathscr{H}-((6b\rho u\phi)/\alpha))\right)}{\sqrt{\rho u}},$$

$$\mathfrak{B}_{V,5}(x,t) = \frac{b_1\rho\cot\left(\sqrt{\rho u}(\mathscr{H}-((6b\rho u\phi)/\alpha))\right)}{\sqrt{\rho u}},$$

$$\mathfrak{B}_{V,6}(x,t) = -\frac{b_1\rho\tan\left(\sqrt{\rho u}(\mathscr{H}-((6b\rho u\phi)/\alpha))\right)}{\sqrt{\rho u}}. \tag{15}$$

For $\rho\,\mathrm{u} < 0$, $\mathrm{u} \neq 0$, $\rho \neq 0$, $\delta = 0$, we get

$$\mathfrak{B}_{\mathrm{I},7}(x,t) = \frac{1}{\sqrt{\left(a_1\mathrm{u}\left(\tanh\left(\sqrt{\rho(-\mathrm{u})}((3b\rho\mathrm{u}\phi/\alpha)+\mathscr{H})\right)-1\right)\right)/\sqrt{\rho(-\mathrm{u})}}}, \tag{16}$$

$$\mathfrak{B}_{\mathrm{I},8}(x,t) = \frac{1}{\sqrt{\left(a_1\mathrm{u}\left(\coth\left(\sqrt{\rho(-\mathrm{u})}((3b\rho\mathrm{u}\phi/\alpha)+\mathscr{H})\right)-1\right)\right)/\sqrt{\rho(-\mathrm{u})}}}, \tag{17}$$

$$\mathfrak{B}_{\mathrm{II},7}(x,t) = \frac{1}{\sqrt{\left(b_1\sqrt{\rho(-\mathrm{u})}\left(\coth\left(\sqrt{\rho(-\mathrm{u})}((3b\rho\mathrm{u}\phi/\alpha)+\mathscr{H})\right)+1\right)\right)/\mathrm{u}}}, \tag{18}$$

$$\mathfrak{B}_{\mathrm{II},8}(x,t) = \frac{1}{\sqrt{\left(b_1\sqrt{\rho(-\mathrm{u})}\left(\tanh\left(\sqrt{\rho(-\mathrm{u})}((3b\rho\mathrm{u}\phi/\alpha)+\mathscr{H})\right)+1\right)\right)/\mathrm{u}}}, \tag{19}$$

$$\mathfrak{B}_{\mathrm{IV},7}(x,t) = \frac{a_1\mathrm{u}\tanh\left(\sqrt{\rho(-\mathrm{u})}(\mathscr{H}-(6b\rho\mathrm{u}\phi)/\alpha)\right)}{\sqrt{\rho(-\mathrm{u})}}, \tag{20}$$

$$\mathfrak{B}_{\mathrm{IV},8}(x,t) = \frac{a_1\mathrm{u}\coth\left(\sqrt{\rho(-\mathrm{u})}(\mathscr{H}-(6b\rho\mathrm{u}\phi)/\alpha)\right)}{\sqrt{\rho(-\mathrm{u})}}, \tag{21}$$

$$\mathfrak{B}_{\mathrm{V},7}(x,t) = \frac{b_1\sqrt{\rho}\cot\left(\sqrt{\rho}\sqrt{\mathrm{u}}(\mathscr{H}-(6b\rho\mathrm{u}\phi)/\alpha)\right)}{\sqrt{\mathrm{u}}}, \tag{22}$$

$$\mathfrak{B}_{\mathrm{V},8}(x,t) = \frac{b_1\sqrt{\rho(-\mathrm{u})}\tanh\left(\sqrt{\rho(-\mathrm{u})}(\mathscr{H}-\mathscr{H}-(6b\rho\mathrm{u}\phi)/\alpha)\right)}{\mathrm{u}}. \tag{23}$$

For $\delta = \mathrm{u}/2 = \kappa$, $\rho = 0$, we get

$$\mathfrak{B}_{\mathrm{II},9}(x,t) = \frac{2}{\sqrt{b_1\left(\left(4/\left(e^{\kappa\mathscr{H}-((3b\kappa^3\phi)/4\alpha)}-2\right)\right)+\left(\kappa/\sqrt{\kappa^2}\right)+1\right)}},$$

$$\mathfrak{B}_{\mathrm{III},9}(x,t) = \frac{1}{\sqrt{a_0\left(2/\left(e^{\kappa\mathscr{H}-((3b\kappa^3\phi)/4\alpha)}-2\right)+1\right)}},$$

$$\mathfrak{B}_{\mathrm{VI},9}(x,t) = \frac{1}{4}b_1\left(\frac{4}{e^{((3b\kappa^3\phi)/2\alpha)+\kappa\mathscr{H}}-2}+1\right). \tag{24}$$

For $\delta = \rho = \kappa$, $\mathrm{u} = 0$, we get

$$\mathfrak{B}_{\mathrm{I},10}(x,t) = \frac{\sqrt{2}}{\sqrt{a_1\left(\left(\kappa/\sqrt{\kappa^2}\right)-\coth\left((\kappa\mathscr{H}/2)-((3b\kappa^3\phi)/8\alpha)\right)\right)}},$$

$$\mathfrak{B}_{\mathrm{III},10}(x,t) = \frac{1}{\sqrt{-a_0/e^{\kappa\mathscr{H}-((3b\kappa^3\phi)/4\alpha)}-1}},$$

$$\mathfrak{B}_{\mathrm{IV},10}(x,t) = -\frac{1}{2}a_1\coth\left(\frac{3b\kappa^3\phi}{4\alpha}+\frac{\kappa\mathscr{H}}{2}\right). \tag{25}$$

For $\mathrm{u} = 0$, $\delta \neq 0$, $\rho \neq 0$, we get

$$\mathfrak{B}_{\mathrm{I},11}(x,t) = \frac{\sqrt{2}}{\sqrt{\left(a_1\left(\delta\left(-4/\left(\rho e^{\delta\mathscr{H}-\left(3b\delta^3\phi\right)/4\alpha}-2\right)-1\right)+\sqrt{\delta^2}\right)\right)/\rho}},$$

$$\mathfrak{B}_{\mathrm{III},10}(x,t) = \frac{1}{\sqrt{2}\sqrt{-a_0/\left(\rho e^{(\delta\mathscr{H}-((3b\delta\wedge 3\,3\,\phi)/4\alpha))}-2\right)}},$$

$$\mathfrak{B}_{\mathrm{IV},10}(x,t) = \frac{a_1\delta\left(4/\left(2-\rho e^{((3b\delta\wedge 3\,\phi)/2\alpha+\delta\mathscr{H})}\right)-1\right)}{2\rho}. \tag{26}$$

For $\delta = \rho = 0$, $\mathrm{u} \neq 0$, we get

$$\mathfrak{B}_{\mathrm{II},10}(x,t) = \frac{1}{\sqrt{b_1/\lambda t\mathrm{u}+x\mathrm{u}}},$$

$$\mathfrak{B}_{\mathrm{V},10}(x,t) = \frac{b_1}{\lambda t\mathrm{u}+x\mathrm{u}}. \tag{27}$$

For $\delta = 0$, $\mathrm{u} = \rho$, we get

$$\mathfrak{B}_{\mathrm{I},11}(x,t) = \frac{1}{\sqrt{a_1\left(\tan\left((3b\mathrm{u}^3\phi/\alpha)+C+\mathscr{H}u\right)+\left(\sqrt{-\mathrm{u}}/\sqrt{\mathrm{u}}\right)\right)}},$$

$$\mathfrak{B}_{\mathrm{II},11}(x,t) = \frac{1}{\sqrt{b_1\left(\cot\left((3b\mathrm{u}^3\phi/\alpha)+C+\mathscr{H}u\right)+\left(\sqrt{-\mathrm{u}}/\sqrt{\mathrm{u}}\right)\right)}},$$

$$\mathfrak{B}_{\mathrm{IV},11}(x,t) = \frac{1}{\sqrt{b_1\left(\cot\left((3b\mathrm{u}^3\phi/\alpha)+C+\mathscr{H}u\right)+\left(\sqrt{-\mathrm{u}}/\sqrt{\mathrm{u}}\right)\right)}},$$

$$\mathfrak{B}_{\mathrm{V},11}(x,t) = a_1\tan\left(-\frac{6b\mathrm{u}^3\phi}{\alpha}+C+\mathscr{H}u\right),$$

$$\mathfrak{B}_{\mathrm{VI},11}(x,t) = b_1\cot\left(-\frac{6b\mathrm{u}^3\phi}{\alpha}+C+\mathscr{H}u\right). \tag{28}$$

For $\rho = 0, \delta \neq 0, \mathrm{u} \neq 0$, we get

$$\mathfrak{B}_{\mathrm{II},12}(x,t) = \frac{1}{2}b_1\left(\frac{2\delta}{\delta e^{\delta\mathscr{H}-\left(3b\delta^3\phi/4\alpha\right)} - \mathrm{u}} + \frac{\sqrt{\delta^2}+\delta}{\mathrm{u}}\right),$$
$$\mathfrak{B}_{\mathrm{III},12}(x,t) = a_0\left(\frac{\mathrm{u}}{\delta e^{\delta\mathscr{H}-\left(3b\delta^3\phi/4\alpha\right)} - \mathrm{u}} + 1\right),$$
$$\mathfrak{B}_{\mathrm{VI},12}(x,t) = \frac{1}{2}b_1\delta\left(\frac{2}{\delta e^{\left(3b\delta^3\phi/2\alpha\right)+\delta\mathscr{H}} - \mathrm{u}} + \frac{1}{\mathrm{u}}\right). \tag{29}$$

where $\mathscr{H} = x + y + z, \phi = (t + (1/\Gamma(\alpha)))^{\alpha}$.

2.2. Numerical Solutions. Here, we use three different analytical solutions Equations (16), (19) and (20) to evaluate the numerical solutions of the Atangana conformable derivative (1 + 3)-ZK equation with power-law nonlinearity. Employing the septic spline technique to Equation (5) with the following conditions $a_1 = 3, a_0 = -6, a = -5/4, b = 5, b_1 = 0, \delta = 0, \lambda = -60, n = -4, \rho = -1, \mathrm{u} = 4\&a_0 = -25, a_1 = 0, a = -9/20, b_1 = 5, b = 2, \delta = 0, \lambda = -150, n = -4, \rho = 25, \mathrm{u} = -1\&a_1 = 3, a_0 = 0, a = -4, b = 2, b_1 = 0, \delta = 0, \lambda = 108, n = 2, \rho = -1$, and $\mathrm{u} = 9$ gives its numerical solutions in the next form

$$\mathfrak{B}(\mathfrak{F}) = \sum_{\mathfrak{T}=-1}^{\mathfrak{M}+1} \mathfrak{C}_{\mathfrak{M}}\, \mathscr{E}_{\mathfrak{M}}, \tag{30}$$

where $c_{\mathfrak{M}}, \mathscr{E}_{\mathfrak{M}}$ follow the next conditions, respectively:

$$\mathfrak{L}\,\mathfrak{B}(\mathfrak{F}) = \mathscr{F}(\mathfrak{F}_{\mathfrak{M}}, \mathfrak{B}(\mathfrak{F}_{\mathfrak{M}})) \text{ where } (\mathfrak{M} = 0, 1, \cdots, n)$$
$$\mathscr{E}_{\mathfrak{T}}(\mathfrak{F}) = \frac{1}{\mathscr{S}^5}\begin{cases} (\mathfrak{F}-\mathfrak{F}_{\mathfrak{T}-4})^7, & \mathfrak{F}\in[\mathfrak{F}_{\mathfrak{T}-4},\mathfrak{F}_{\mathfrak{T}-3}], \\ (\mathfrak{F}-\mathfrak{F}_{\mathfrak{T}-4})^7 - 8(\mathfrak{F}-\mathfrak{F}_{\mathfrak{T}-3})^7, & \mathfrak{F}\in[\mathfrak{F}_{\mathfrak{T}-3},\mathfrak{F}_{\mathfrak{T}-2}], \\ (\mathfrak{F}-\mathfrak{F}_{\mathfrak{T}-4})^7 - 8(\mathfrak{F}-\mathfrak{F}_{\mathfrak{T}-3})^7 + 28(\mathfrak{F}-\mathfrak{F}_{\mathfrak{T}-2})^7, & \mathfrak{F}\in[\mathfrak{F}_{\mathfrak{T}-2},\mathfrak{F}_{\mathfrak{T}-1}], \\ (\mathfrak{F}-\mathfrak{F}_{\mathfrak{T}-4})^7 - 8(\mathfrak{F}-\mathfrak{F}_{\mathfrak{T}-3})^7 + 28(\mathfrak{F}-\mathfrak{F}_{\mathfrak{T}-2})^7 + 56(\mathfrak{F}-\mathfrak{F}_{\mathfrak{T}-1})^7, & \mathfrak{F}\in[\mathfrak{F}_{\mathfrak{T}-1},\mathfrak{F}_{\mathfrak{T}}], \\ (\mathfrak{F}_{\mathfrak{T}+4}-\mathfrak{F})^7 - 8(\mathfrak{F}_{\mathfrak{T}+3}-\mathfrak{F})^7 + 28(\mathfrak{F}_{\mathfrak{T}+2}-\mathfrak{F})^7 + 56(\mathfrak{F}_{\mathfrak{T}+1}-\mathfrak{F})^7, & \mathfrak{F}\in[\mathfrak{F}_{\mathfrak{T}},\mathfrak{F}_{\mathfrak{T}+1}], \\ (\mathfrak{F}_{\mathfrak{T}+4}-\mathfrak{F})^7 - 8(\mathfrak{F}_{\mathfrak{T}+3}-\mathfrak{F})^7 + 28(\mathfrak{F}_{\mathfrak{T}+2}-\mathfrak{F})^7, & \mathfrak{F}\in[\mathfrak{F}_{\mathfrak{T}+1},\mathfrak{F}_{\mathfrak{T}+2}], \\ (\mathfrak{F}_{\mathfrak{T}+4}-\mathfrak{F})^7 - 8(\mathfrak{F}_{\mathfrak{T}+3}-\mathfrak{F})^7, & \mathfrak{F}\in[\mathfrak{F}_{\mathfrak{T}+2},\mathfrak{F}_{\mathfrak{T}+3}], \\ (\mathfrak{F}_{\mathfrak{T}+4}-\mathfrak{F})^7, & \mathfrak{F}\in[\mathfrak{F}_{\mathfrak{T}+3},\mathfrak{F}_{\mathfrak{T}+4}], \\ 0, & \text{otherwise.} \end{cases} \tag{31}$$

For $\mathfrak{T} \in [-3, \mathfrak{M}+3]$, we get

$$\mathfrak{B}_{\mathfrak{T}}(\mathfrak{F}) = \mathfrak{C}_{\mathfrak{T}-3} + 120\,\mathfrak{C}_{\mathfrak{T}-2} + 1191\,\mathfrak{C}_{\mathfrak{T}-1} + 2416\,\mathfrak{C}_{\mathfrak{T}} + 1191\,\mathfrak{C}_{\mathfrak{T}+1} + 120\,\mathfrak{C}_{\mathfrak{T}+2} + \mathfrak{C}_{\mathfrak{T}+3}. \tag{32}$$

Substituting Equation (32) into Equation (5) gives $(\mathfrak{M}+7)$ of equations. Resolving this system leads to the following values of exact, numerical, and absolute values or error.

3. Stability Characteristics

In this section, the stability property has been tested of the obtained results based on the Hamiltonian system characteristics. This system imposes a single condition to ensure the stability of the solution. This condition is given by

$$\left.\frac{\partial\mathscr{M}}{\partial\lambda}\right|_{\lambda=\mathscr{G}} > 0, \tag{33}$$

where $\mathscr{M} = (1/2)\int_{-\mathfrak{E}}^{\mathfrak{E}} \mathfrak{B}^2\, d\mathfrak{F}$ where $\mathfrak{E}$ is an arbitrary constants, λ is the frequency, and $\mathscr{G}$ is an arbitrary constant.

Applying the stability check of Equation (20) with the following values of the parameters $a_1 = 3, a_0 = 0, a = -4, b = 2, b_1 = 0, \delta = 0, \lambda = 108, n = 2, \rho = -1$, and $\mathrm{u} = 9$, leads to

$$\left.\frac{\partial\mathscr{M}}{\partial\lambda}\right|_{\lambda=6} = -2.3447910280083306 \times 10^{-13} < 0. \tag{34}$$

Consequently, this solution is not stable and applying the

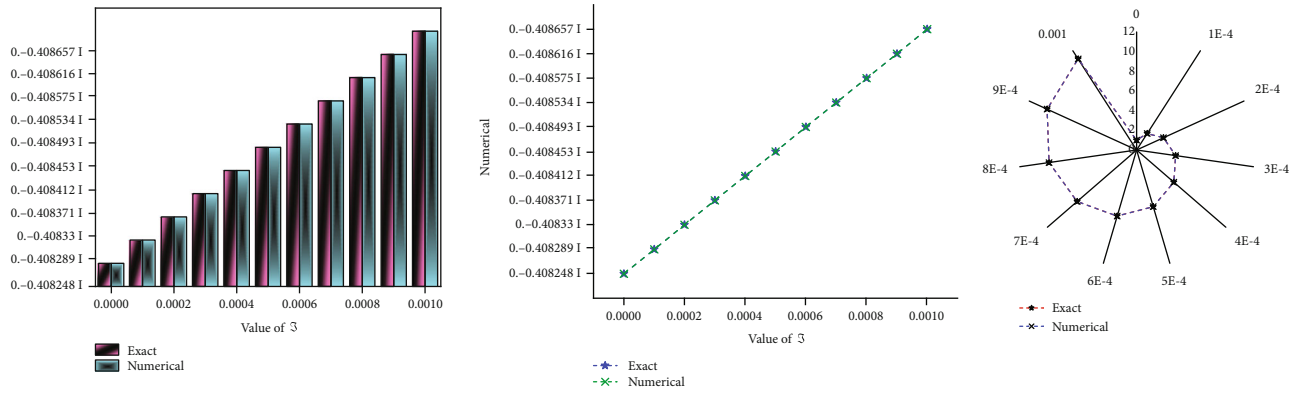

Figure 1: Exact, and numerical solutions based on the obtained analytical solution Equation (16) and septic B-spline scheme.

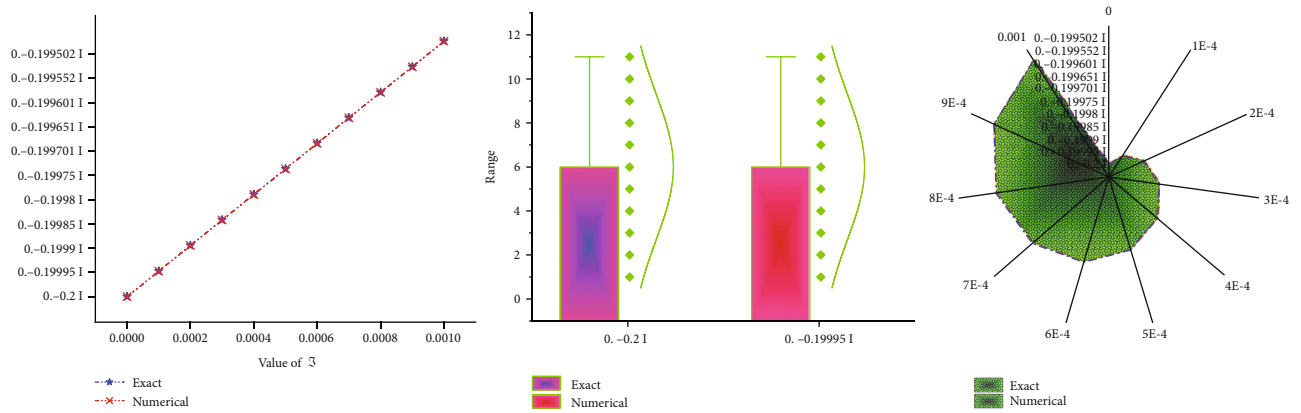

Figure 2: Exact and numerical solutions based on the obtained analytical solution Equation (19) and septic B-spline scheme.

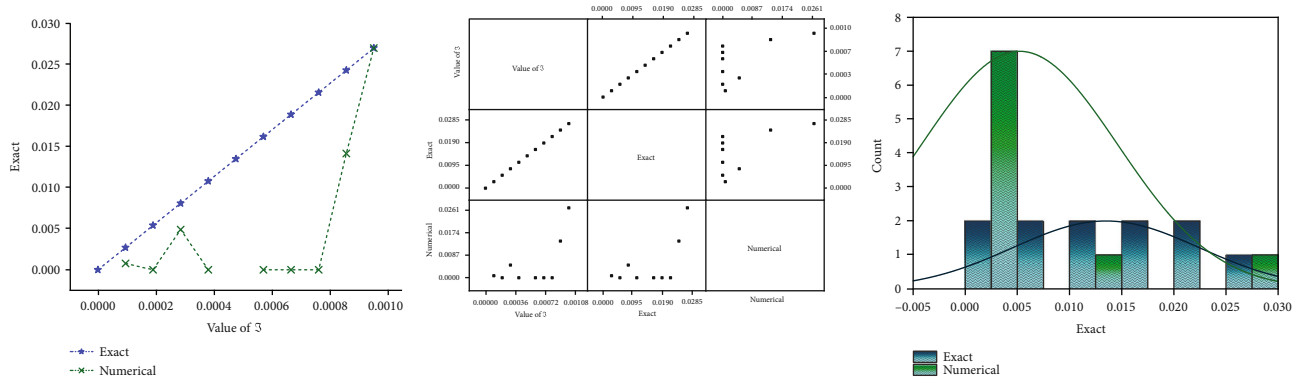

Figure 3: Exact and numerical solutions based on the obtained analytical solution Equation (20) and septic B-spline scheme.

same steps to other obtained solutions investigates their stability property.

4. Result and Discussion

Here, we discuss our obtained solutions of the Atangana conformable derivative (1 + 3)-ZK equation with power-law nonlinearity that have been obtained through one of the most recent computational schemes in nonlinear evolution equation field (the mK method) via two main axes which are a comparison between our obtained computational solutions and other previous obtained solutions, while the second axis of this discussion is studying our exact and numerical solutions.

(i) Computational solutions

(1) Applying the modified Khater method to the Atangana conformable derivative (1 + 3)-ZK equation with power-law nonlinearity has obtained sixty distinct traveling wave solutions

(2) The difference between our obtained solutions and that have been obtained in [41] by Aminikhah et al. who had used the functional variable method; however, they have just found three solutions and accurate in their and our solutions, we can figure out the complete difference between these solutions that thing makes our solutions are novel

(ii) Numerical solutions

(1) Applying the septic B-spline scheme to the Atangana conformable derivative (1 + 3)-ZK equation with power-law nonlinearity by using three of our obtained solutions in evaluating the initial and boundary conditions that give the ability of employing the septic B-spline scheme to the fractional model

5. Figure and Table Interpretation

This section illustrates our explained Figures 1–3 and Tables 1–3 with the abovementioned values of the parameters.

(i) Figure 1 and Table 1 show the value of the exact and numerical solutions and absolute error of Equation (5) with Equation (16) in three distinct types of sketches to explain the convergence between the two types of solutions

(ii) Figure 2 and Table 2 show the value of exact and numerical solutions and absolute error of Equation (5) with Equation (19) in three distinct types of sketches to illustrate the closer between the two types of solutions

(iii) Figure 3 and Table 3 explain the value of exact, numerical solutions and absolute error of Equation (5) with Equation (20) in three distinct types of sketches to show the matching between the two types of solutions

6. Conclusion

This paper has succeeded in the implementation of the mK method and septic B-spline scheme to the Atangana conformable derivative (1 + 3)-ZK equation with power-law nonlinearity. Sixty distinct novel computational solutions have been obtained. Three of these solutions have been used to evaluate the initial and boundary conditions that have allowed the application of the numerical scheme. Calculating the absolute value of error between the exact and numerical is the aim of our study. Moreover, the stability of our obtained solutions has been illustrated based on the Hamiltonian system characteristics. The effectiveness and power of our two used schemes have been verified, and all obtained solutions have been also verified by putting them back in the original equation via Mathematica 12 software.

Table 1: Exact and numerical value of the Atangana conformable derivative (1 + 3)-ZK equation with power-law nonlinearity through the obtained analytical solutions via the modified Khater method Equation (16) and septic B-spline scheme.

Value of $\mathfrak{F}$	Exact	Numerical	Absolute error
0	0. -0.408248 I	0. -0.0000110311 I	0.408237
0.0001	0. -0.408289 I	0. -8.37587×10^{-6} I	0.408281
0.0002	0. -0.40833 I	0. -5.50221×10^{-6} I	0.408324
0.0003	0. -0.408371 I	0. -2.53611×10^{-6} I	0.408368
0.0004	0. -0.408412 I	0. -1.13958×10^{-6} I	0.408411
0.0005	0. -0.408453 I	0. $+1.58999 \times 10^{-7}$ I	0.408453
0.0006	0. -0.408493 I	0. -1.01297×10^{-6} I	0.408492
0.0007	0. -0.408534 I	0. -2.41857×10^{-6} I	0.408532
0.0008	0. -0.408575 I	0. -5.26488×10^{-6} I	0.40857
0.0009	0. -0.408616 I	0. -7.96518×10^{-6} I	0.408608
0.001	0. -0.408657 I	0. -0.0000103138 I	0.408647

Table 2: Exact and numerical value of the Atangana conformable derivative (1 + 3)-ZK equation with power-law nonlinearity through the obtained analytical solutions via the modified Khater method Equation (19) and septic B-spline scheme.

Value of $\mathfrak{F}$	Exact	Numerical	Absolute error
0	0. -0.2 I	0. -0.0000794823 I	0.199921
0.0001	0. -0.19995 I	0. -0.0000595992 I	0.19989
0.0002	0. -0.1999 I	0. -0.0000399605 I	0.19986
0.0003	0. -0.19985 I	0. -0.0000214 I	0.199829
0.0004	0. -0.1998 I	0. -8.76169×10^{-6} I	0.199792
0.0005	0. -0.19975 I	0. $+1.47924 \times 10^{-6}$ I	0.199752
0.0006	0. -0.199701 I	0. -7.5007×10^{-6} I	0.199693
0.0007	0. -0.199651 I	0. -0.0000199929 I	0.199631
0.0008	0. -0.199601 I	0. -0.0000376969 I	0.199564
0.0009	0. -0.199552 I	0. -0.000056177 I	0.199495
0.001	0. -0.199502 I	0. -0.0000736582 I	0.199428

Table 3: Exact and numerical value of the Atangana conformable derivative (1 + 3)-ZK equation with power-law nonlinearity through the obtained analytical solutions via the modified Khater method Equation (20) and septic B-spline scheme.

Value of $\mathfrak{F}$	Exact	Numerical	Absolute error
0	0	3.46945×10^{-17}	3.46945×10^{-17}
0.0001	0.0027	0.000779236	0.00192076
0.0002	0.0054	-8.67362*E*-18	0.0054
0.0003	0.0081	0.00489544	0.00320455
0.0004	0.0108	0	0.0108
0.0005	0.0135	6.50521*E*-19	0.0135
0.0006	0.0162	0	0.0162
0.0007	0.0189	-4.33681*E*-19	0.0189
0.0008	0.0216	-8.67362*E*-19	0.0216
0.0009	0.0242999	0.0141565	0.0101435
0.001	0.0269999	0.0269999	3.46945×10^{-18}

Data Availability

No data were used to support this study.

Conflicts of Interest

The authors declare that there is no conflict of interests regarding the publication of this article.

Acknowledgments

The work was supported by the Natural Science Foundation of China (Grant Nos. 61673169, 11301127, 11701176, 11626101, and 11601485).

References

[1] A. Lotekar, A. Kakad, and B. Kakad, "Generation of ion acoustic solitary waves through wave breaking in superthermal plasmas," *Physics of Plasmas*, vol. 24, no. 10, 2017.

[2] K. Devi, A. Nag, J. Paul, and P. K. Karmakar, "Dynamics of sheath evolution in magnetized chargeuctuating dusty plasmas," *Chinese Journal of Physics*, vol. 65, pp. 405–411, 2020.

[3] P. Ankiewicz, "Perceptions and attitudes of pupils towards technology: In search of a rigorous theoretical framework," *International Journal of Technology and Design Education*, vol. 29, no. 1, pp. 37–56, 2019.

[4] M.-J. Lee, N. Ashikawa, and Y.-D. Jung, "Characteristics of ion-cyclotron surface waves in semi-bounded (r, q) distribution dusty plasmas," *Physics of Plasmas*, vol. 25, article 062110, no. 6, 2018.

[5] M. M. Hossen, M. S. Alam, S. Sultana, and A. Mamun, "Low frequency nonlinear waves in electron depleted magnetized nonthermal plasmas," *The European Physical Journal D*, vol. 70, no. 12, 2016.

[6] F. S. Khodadad, F. Nazari, M. Eslami, and H. Rezazadeh, "Soliton solutions of the conformable fractional Zakharov-Kuznetsov equation with dual-power law nonlinearity," *Optical and Quantum Electronics*, vol. 49, no. 11, 2017.

[7] M. M. Khater, R. A. Attia, A.-H. Abdel-Aty, W. Alharbi, and D. Lu, "Abundant analytical and numerical solutions of the fractional microbiological densities model in bacteria cell as a result of diffusion mechanisms," *Solitons & Fractals*, vol. 136, 2020.

[8] Z. Korpinar, M. Inc, and M. Bayram, "Theory and application for the system of fractional Burger equations with Mittag leffler kernel," *Applied Mathematics and Computation*, vol. 367, 2020.

[9] C. Park, M. M. Khater, A.-H. Abdel-Aty et al., "Dynamical analysis of the nonlinear complex fractional emerging telecommunication model with higher–order dispersive cubic–quintic," *Alexandria Engineering Journal*, vol. 59, no. 3, pp. 1425–1433, 2020.

[10] M. A. Abdelrahman, S. I. Ammar, K. M. Abualnaja, and M. Inc, "New solutions for the unstable nonlinear Schrödinger equation arising in natural science," *Aims Mathematics*, vol. 5, no. 3, pp. 1893–1912, 2020.

[11] M. M. Khater, B. Ghanbari, K. S. Nisar, and D. Kumar, "Novel exact solutions of the fractional Bogoyavlensky–Konopelchenko equation involving the Atangana-Baleanu-Riemann derivative," *Alexandria Engineering Journal*, 2020, In press.

[12] Z.-y. Zhang, Z.-h. Liu, X.-j. Miao, and Y.-z. Chen, "New exact solutions to the perturbed nonlinear Schrödinger's equation with kerr law nonlinearity," *Applied Mathematics and Computation*, vol. 216, no. 10, pp. 3064–3072, 2010.

[13] Z.-y. Zhang, Y.-x. Li, Z.-h. Liu, and X.-j. Miao, "New exact solutions to the perturbed nonlinear Schrodinger's equation with kerr law nonlinearity via modi_ed trigonometric function series method," *Communications in Nonlinear Science and Numerical Simulation*, vol. 16, no. 8, pp. 3097–3106, 2011.

[14] Z.-y. Zhang, Z.-h. Liu, X.-j. Miao, and Y.-z. Chen, "Qualitative analysis and traveling wave solutions for the perturbed nonlinear Schrödinger's equation with kerr law nonlinearity," *Physics Letters A*, vol. 375, no. 10, pp. 1275–1280, 2011.

[15] X.-j. Miao and Z.-y. Zhang, "The modified G'/G -expansion method and traveling wave solutions of nonlinear the perturbed nonlinear Schrödinger's equation with kerr law nonlinearity," *Communications in Nonlinear Science and Numerical Simulation*, vol. 16, no. 11, pp. 4259–4267, 2011.

[16] A.-H. Abdel-Aty, M. Khater, R. A. Attia, and H. Eleuch, "Exact traveling and nano-solitons wave solitons of the ionic waves propagating along microtubules in living cells," *Mathematics*, vol. 8, no. 5, 2020.

[17] J. Li, R. A. Attia, M. M. Khater, and D. Lu, "The new structure of analytical and semi-analytical solutions of the longitudinal plasma wave equation in a magneto-electro-elastic circular rod," *Modern Physics Letters B*, vol. 34, article 2050123, no. 12, 2020.

[18] M. M. Khater, R. A. Attia, S. S. Alodhaibi, and D. Lu, "Novel soliton waves of two uid nonlinear evolutions models in the view of computational scheme," *International Journal of Modern Physics B*, vol. 34, article 2050096, no. 10, 2020.

[19] H. Rezazadeh, D. Kumar, A. Neirameh, M. Eslami, and M. Mirzazadeh, "Applications of three methods for obtaining optical soliton solutions for the Lakshmanan–Porsezian–Daniel model with Kerr law nonlinearity," *Pramana*, vol. 94, no. 1, 2020.

[20] S. M. Mirhosseini-Alizamini, H. Rezazadeh, M. Eslami, M. Mirzazadeh, and A. Korkmaz, "New extended direct algebraic method for the Tzitzica type evolution equations arising in nonlinear optics," *Computational Methods for Differential Equations*, vol. 8, no. 1, pp. 28–53, 2020.

[21] Z.-Y. Zhang, X.-Y. Gan, and D.-M. Yu, "Bifurcation Behaviour of the Travelling Wave Solutions of the Perturbed Nonlinear Schrödinger Equation with Kerr Law Nonlinearity," *Zeitschrift für Naturforschung A*, vol. 66, no. 12, pp. 721–727, 2011.

[22] Z. Zhang, J. Huang, J. Zhong et al., "The extended (G'/G)-expansion method and travelling wave solutions for the perturbed nonlinear Schrödinger's equation with Kerr law nonlinearity," *Pramana*, vol. 82, no. 6, pp. 1011–1029, 2014.

[23] Z. Zai-Yun, G. Xiang-Yang, Y. De-Min, Z. Ying-Hui, and L. Xin-Ping, "A Note on Exact Traveling Wave Solutions of the Perturbed Nonlinear Schrödinger's Equation with Kerr Law Nonlinearity," *Communications in Theoretical Physics*, vol. 57, no. 5, p. 764, 2012.

[24] A. Korkmaz and K. Hosseini, "Exact solutions of a nonlinear conformable time-fractional parabolic equation with exponential nonlinearity using reliable methods," *Optical and Quantum Electronics*, vol. 49, no. 8, 2017.

[25] S. M. Mirhosseini-Alizamini, H. Rezazadeh, K. Srinivasa, and A. Bekir, "New closed form solutions of the new coupled Konno–Oono equation using the new extended direct algebraic method," *Pramana*, vol. 94, no. 1, 2020.

[26] C. Yue, A. Elmoasry, M. Khater et al., "On complex wave structures related to the nonlinear long-short wave interaction system: analytical and numerical techniques," *AIP Advances*, vol. 10, no. 4, 2020.

[27] M. M. Khater, R. A. Attia, and D. Lu, "Computational and numerical simulations for the nonlinear fractional Kolmogorov–Petrovskii–Piskunov (FKPP) equation," *Physica Scripta*, vol. 95, no. 5, 2020.

[28] N. A. Kudryashov, "Periodic and solitary waves of the Biswas–Arshed equation," *Optik*, vol. 200, 2020.

[29] M. Torvattanabun, P. Juntakud, A. Saiyun, and N. Khansai, "The new exact solutions of the new coupled Konno-Oono equation by using extended simplest equation method," *Applied Mathematical Sciences*, vol. 12, no. 6, pp. 293–301, 2018.

[30] M. Kaplan, A. Bekir, and A. Akbulut, "A generalized Kudryashov method to some nonlinear evolution equations in mathematical physics," *Nonlinear Dynamics*, vol. 85, no. 4, pp. 2843–2850, 2016.

[31] M. M. Khater, D. Lu, and E. H. Zahran, "Solitary Wave Solutions of the Benjamin-Bona- Mahoney-Burgers Equation with Dual Power-Law Nonlinearity," *Applied Mathematics & Information Sciences*, vol. 11, no. 5, pp. 1–5, 2017.

[32] K. Hosseini, E. Y. Bejarbaneh, A. Bekir, and M. Kaplan, "New exact solutions of some nonlinear evolution equations of pseudoparabolic type," *Optical and Quantum Electronics*, vol. 49, no. 7, 2017.

[33] H. Gündoğdu and Ö. F. Gözükızıl, "Applications of the decomposition methods to some nonlinear partial differential equations," *New Trends in Mathematical Sciences*, vol. 6, no. 3, pp. 57–66, 2018.

[34] O. A. Ilhan, A. Esen, H. Bulut, and H. M. Baskonus, "Singular solitons in the pseudo-parabolic model arising in nonlinear surface waves," *Results in Physics*, vol. 12, pp. 1712–1715, 2019.

[35] L. Á valos-Ruiz, J. Go´ mez-Aguilar, A. Atangana, and K. M. Owolabi, "On the dynamics of fractional maps with power-law, exponential decay and Mittag–Leffler memory," *Chaos, Solitons & Fractals*, vol. 127, pp. 364–388, 2019.

[36] M. N. Alam and C. Tunc, "Constructions of the optical solitons and other solitons to the conformable fractional Zakharov–Kuznetsov equation with power law nonlinearity," *Journal of Taibah University for Science*, vol. 14, no. 1, pp. 94–100, 2020.

[37] M. Osman, H. Rezazadeh, and M. Eslami, "Traveling wave solutions for (3+1) dimensional conformable fractional Zakharov-Kuznetsov equation with power law nonlinearity," *Nonlinear Engineering*, vol. 8, no. 1, pp. 559–567, 2019.

[38] Q. Jin, T. Xia, and J. Wang, "The Exact Solution of the Space-Time Fractional Modified Kdv-Zakharov-Kuznetsov Equation," *Journal of Applied Mathematics and Physics*, vol. 5, no. 4, pp. 844–852, 2017.

[39] H. Yépez-Martínez and J. F. Gómez-Aguilar, "Fractional sub-equation method for Hirota–Satsuma-coupled KdV equation and coupled mKdV equation using the Atangana's conformable derivative," *Waves in Random and Complex Media*, vol. 29, no. 4, pp. 678–693, 2019.

[40] H. Yepez-Martinez and J. Gomez-Aguilar, "Optical solitons solution of resonance nonlinear Schrödinger type equation with Atangana's-conformable derivative using sub-equation method," *Waves in Random and Complex Media*, pp. 1–24, 2019, In press.

[41] H. Aminikhah, B. P. Ziabary, and H. Rezazadeh, "Exact traveling wave solutions of partial differential equations with power law nonlinearity," *Nonlinear Engineering*, vol. 4, no. 3, 2015.

Hindawi
Advances in Mathematical Physics
Volume 2020, Article ID 7360794, 10 pages
https://doi.org/10.1155/2020/7360794

Research Article

Nonlinear Hydroelastic Interaction among a Floating Elastic Plate, Water Waves, and Exponential Shear Currents

Ping Wang[1], **Yongyan Wang**[2] **and Xintai Huo**[1]

[1]*School of Mathematics and Physics, Qingdao University of Science and Technology, Songling Road, Qingdao 266061, China*
[2]*College of Electromechanical Engineering, Qingdao University of Science and Technology, Songling Road, Qingdao 266061, China*

Correspondence should be addressed to Ping Wang; pingwang2003@126.com

Received 12 May 2020; Revised 8 July 2020; Accepted 30 July 2020; Published 26 August 2020

Guest Editor: Yu-Hao Sun

Nonlinear hydroelastic interaction among a floating elastic plate, a train of deepwater waves, and a current which decays exponentially with depth is studied analytically. We introduce a stream function to obtain the governing equation with the dynamic boundary condition expressing a balance among the hydrodynamic, the shear currents, elastic, and inertial forces. We use the Dubreil-Jacotin transformation to reformulate the unknown free surface as a fixed location in the calculations. The convergent analytical series solutions for the floating plate deflection are obtained with the aid of the homotopy analysis method (HAM). The effects of the shear current are discussed in detail. It is found that the phase speed decreases with the increase of the vorticity parameter in the opposing current, while the phase speed increases with the increase of the vorticity parameter in the aiding current. Larger vorticity tends to increase the horizontal velocity. In the opposing current, the horizontal velocity under the wave crest delays more quickly as the depth increases than that of waves under the wave trough, while in the aiding current case, there is the opposite effect. Furthermore, the larger vorticity can sharpen the hydroelastic wave crest and smooth the trough on an opposing current, while it produces an opposite effect on an aiding current.

1. Introduction

Hydroelastic interaction between a floating deformable plate and water flows has been a long-standing and hot issue under the rapidly growing demand for exploiting ocean resources and utilizing marine space. For example, hydroelastic interaction has become an indispensable factor during designing a very large floating structure (VLFS) as a storage facility, a mobile offshore base, or even an aircraft airport, which also is available to analyze the floating ice sheet in the polar region, ice-breaking with air-cushioned vehicles, and marine climate.

There is an extensive literature on the theory of nonlinear hydroelastic interaction between a floating elastic plate and the water waves. Most of the relevant research is under the hypothesis that there is no current in oceanic environments, such as Refs. [1–6]. In fact, there are various reasons such as wind, thermal, earth rotation, tidal effects, the vertical variation of water salinity, and temperature which frequently generate ocean currents. Some authors have considered the problem of hydroelastic waves propagating on a current. Schulkes et al. [7] first built the governing equation with the boundary conditions to research the effect of the uniform flow in the underlying water on a floating ice plate. It is found that the flow with constant velocity had an apposite influence slightly the dispersion at very short wavelengths and the ice profile was no longer aligned with the source velocity but rotated through an angle. Bhattacharjee and Sahoo [8] analyzed the interaction between current and flexural gravity waves generated due to a floating elastic plate under the assumptions of linearized theory and studied the effect of current on the wavelength, phase velocity, and group velocity of the flexural gravity waves in detail. Bhattacharjee and Sahoo [9] extended their study [8] to the generation of flexural gravity waves resulting from initial disturbances at a point and derived asymptotic depressions for the transient flexural gravity for large distances and times by the application of the method of the stationary phase. Mohanty et al. [10] studied a combined effect of the uniform current and compressive force on time-dependent flexural gravity wave

motion in both the cases of single and two-layer fluids and derived the integral forms of Greens function and the velocity potential by using the method of stationary phase. Lu and Yeung [11] studied unsteady hydroelastic waves generated by point loads in a uniform current and found the flexural gravity wave motion depended on the ratio of current speed to phase or group speeds. Wang et al. [12] considered nonlinear hydroelastic waves generated due to a floating elastic plate in an underlying uniform current and studied analytically the effects of the uniform current on the nonlinear hydroelastic waves.

All the aforementioned literatures were based on the assumption that the underlying current is uniform in the fluid and hence ignore the effects of the vorticity distribution. However, in many situations, the current velocity in the vertical direction is mostly nonuniform and the vorticity appears (e.g., wind-driven current and tidal current). Hydroelastic waves with a linear shear or constant-vorticity current were investigated by many authors. Bhattacharjee and Sahoo [13] analyzed the effect of a linear shear current on the propagation of flexural gravity waves is analyzed in the frame of linearized shallow-water theory and derived the reflection and transmission coefficients based on the conservation of energy flux and the continuity of the vertical deformation of the ice sheet. Gao et al. [14] studied hydroelastic solitary waves in the presence of a linear shear current in the limit of deep water, and traveling solitary waves on water of infinite depth were computed for different values of vorticity and new generalised solitary waves were discovered. Recently, Gao et al. [15] investigated hydroelastic waves on water of finite depth interacting with a linear shear current in inviscid flows and derive a nonlinear Schrodinger equation for quasimonochromatic wavetrains and discuss the various behaviors of the coefficient of the nonlinear term from the NLS at different parameter values by employing a conformal mapping technique.

It is noted that the homotopy analysis method (HAM) [16, 17], which does not rely on any small physical parameter, has been applied to solve analytically the problem of the nonlinear wave-current interaction. Cheng et al. [18] investigated a train of periodic deepwater waves propagating on a steady shear current with a vertical distribution of vorticity by using the HAM and analyzed the influences of an exponential shear current on a train of waves in detail. Cang et al. [19] extend Cheng et al.'s study [18] on the effect of a background shear flow on periodic water waves by introducing a new parameter which measures the depth of the background shear current, and the impact of the depth parameter on the wave phase speed, the velocity profiles, and the maximum wave height were given. These works encouraged us to apply the HAM to the complex nonlinear problem of hydroelastic interaction among a floating elastic plate, water waves, and exponential shear currents.

In this work, our aim is to obtain accurate analytic approximations of nonlinear hydroelastic waves generated due to a floating elastic plate in a current which decays exponentially with depth. The influences of the exponential shear current on the hydroelastic wave profile, the wave phase speed, and the horizontal velocity profile are investigated and discussed in detail with the aid of the HAM. The remainder of the paper is organized as follows: In Section 2, the mathematical model of nonlinear hydroelastic interaction among a floating elastic plate, water waves, and exponential shear currents is formulated, and the Dubreil-Jacotin transformation is introduced to reformulate the original moving boundary problem into a fixed one. In Section 3, we present the solution procedure and the approximation and iteration of solutions in the frame of the HAM. In Section 4, the results of numerical calculations and the influence of the shear current are shown. Finally, concluding remarks are given in Section 5.

2. Mathematical Description

Consider an incompressible flow of an inviscid but rotational fluid with a two-dimensioned case, we choose Cartesian coordinates oxz in which the x-axis coincides with the undisturbed fluid-plate interface, while the z-axis points vertically upward. The floating elastic plate extends to the infinity along the x-axis. When the traveling waves exist, we use the moving coordinates $(x - ct, z) \longrightarrow (x, z)$ to eliminate time from the fluid-plate region, where c is the wave speed. The conservation of mass for a two-dimensional incompressible fluid is

$$\frac{\partial(u + U - c)}{\partial x} + \frac{\partial v}{\partial y} = 0, \tag{1}$$

where (u, v) are the motions related to wave-current interaction in the (x, y) directions, U is the mean x-directed current, and the wave speed c appears as negative due to the translation of the coordinate axis. We introduced a stream function $\psi(x, z)$, which satisfies exactly

$$\begin{aligned} u + U - c &= -\frac{\partial \psi(x, z)}{\partial y}, \\ v &= \frac{\partial \psi(x, z)}{\partial x}. \end{aligned} \tag{2}$$

Substituting the stream function into the governing equation derived by Lamb [20], we denote the vorticity distribution Ω as

$$\frac{\partial v}{\partial x} - \frac{\partial(u + U - c)}{\partial y} = \nabla^2 \psi = -\Omega(\psi), \quad (z \le \zeta(x)). \tag{3}$$

Here, we study the shear current decay exponentially with depth, and let $\Omega(\psi) = \mu \exp(-\psi)$, where μ is a physical parameter determining the strength of the fluid vorticity. When $\mu < 0$, the current moves in the same direction of wave propagation and then is called the aiding current. When $\mu > 0$, the current is called the opposing current which moves in the opposing direction of wave propagation [21].

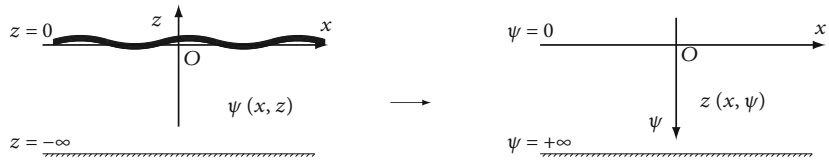

Figure 1: The coordinate transformation.

The impermeable bottom condition at deep water can be written as

$$\frac{\partial \psi}{\partial x} = 0, \quad (z = -\infty). \tag{4}$$

With the assumption that there is no cavitation between the fluid and the plate with on draft, the unknown fluid-plate interface $z = \zeta(x)$ is a streamline. Without loss of generality, the kinematic boundary conditions on $z = \zeta(x)$ can be written as

$$\psi = 0. \tag{5}$$

The nonlinear dynamic boundary conditions on the unknown fluid-plate interface streamline is described as

$$\frac{1}{2}|\nabla\psi|^2 + \frac{p_e}{\rho} + g\zeta = Q, \tag{6}$$

where p_e is the pressure on the plate-water interface, Q an unknown Bernoulli's constant on the fluid-plate interface streamline, ρ is the uniform densities of the fluid, and g is the gravitational acceleration.

As the surface pressure is equal to the pressure of the plate, we model the floating elastic plate as a linear Kirchhoff–Love plate [5].

$$p_e = D\frac{\partial^4 \zeta}{\partial x^4} + m_e g, \tag{7}$$

where the flexural rigidity of the plate is expressed by $D = Ed^3/[12(1-\nu^2)]$ with Young's modulus E, the constant thickness d, and Poisson's ratio ν of the plate, respectively. $m_e(= \rho_e d)$ is the mass of the plate in a unit length with the uniform densities ρ_e of an elastic plate. Substituting Equation (7) into Equation (6) yields the full form of the dynamic boundary condition as

$$\frac{1}{2}|\nabla\psi|^2 + g\zeta + \frac{1}{\rho}\left(D\frac{\partial^4 \zeta}{\partial x^4} + m_e g\right) = Q. \tag{8}$$

It is difficult to directly solve the above Equations (3), (4), (5), and (8) in which the boundary conditions (5) and (8) satisfy the unknown fluid-plate interface $z = \zeta(x)$. So we use the Dubreil-Jacotion transformation [18, 19, 21] to convert Cartesian coordinates oxz into Cartesian coordinates $ox\psi$ in which the z-axis points vertically downward, and then, the unknown interface $z = \zeta(x)$ is reformulated as the fixed location $\psi = 0$, as shown in Figure 1. Here, we consider that $z(x, \psi)$ is a periodic function in the x direction with the period 2π.

For the sake of clarity, we introduce the following dimensionless quantities

$$x^* = kx, z^* = kz, \psi^* = \frac{k}{c}\psi, \Omega^*(\psi) = \frac{\Omega(\psi)}{(kc)}, m_e^* = \frac{km_e}{\rho},$$
$$\rho_e^* = \frac{\rho_e}{\rho}, D^* = k^4\frac{D}{(\rho g)}, E^* = \frac{kE}{(\rho g)}, H^* = kH, \tag{9}$$

where variables with $*$ are dimensionless. By the Dubreil-Jacotion transformation and the nondimensionalization (9), Equations (3), (8), and (4) are reformulated as (after omitting the $*$)

$$\frac{\partial^2 z}{\partial x^2}\left(\frac{\partial z}{\partial \psi}\right)^2 - 2\frac{\partial z}{\partial x}\frac{\partial z}{\partial \psi}\frac{\partial^2 z}{\partial x \partial \psi} + \left[1 + \left(\frac{\partial z}{\partial x}\right)^2\right]\frac{\partial^2 z}{\partial \psi^2} = \left(\frac{\partial z}{\partial \psi}\right)^3 \Omega(\psi), \quad (\psi > 0), \tag{10}$$

$$\frac{1}{2}\delta\left[1 + \left(\frac{\partial z}{\partial x}\right)^2\right] + \left(z + D\frac{\partial^4 z}{\partial x^4} + m_e - \kappa\right)\left(\frac{\partial z}{\partial \psi}\right)^2 = 0, \quad (\psi = 0), \tag{11}$$

$$\frac{\partial z}{\partial x} = 0, \quad (\psi = +\infty), \tag{12}$$

respectively, where both $\delta = c^2/c_0^2$ and $\kappa = kQ/g$ are unknown constants, and $c_0^2 = g/k$ is known linear phase speed without any background current.

3. Analytical Approach Based on the HAM

3.1. Solution Expressions. From physical points of views, our hydroelastic problem is made of a train of deepwater hydroelastic waves, a uniform current due to the moving coordinates, and shear currents with exponential decay on depth. In case of the pure deepwater hydroelastic waves, the periodic wave deflection can be expressed by

$$z = \sum_{m=0}^{+\infty} \alpha_m \cos(mx), \tag{13}$$

where α_m is an unknown coefficient to be derived [5]. Considering the shear currents with vorticity distribution $\Omega(\psi) = \mu \exp(-\psi)$, Equation (10) contains the term $\exp(-\psi)$, so it is suitable that $z(x, \psi)$ should contain the term $\exp(-n\psi)$, where n is an integer. As hydroelastic wave deflections with shear currents are still periodic in the x direction, then $z(x, \psi)$ should also contain the term $\cos(mx)$. Besides, the uniform currents caused by the coming coordinates do not give rise to the interaction between the hydroelastic waves and the currents. So we consider the solution expression of the hydroelastic wave deflection as

$$z(x, \psi) = -\psi + \sum_{n=0}^{+\infty} \sum_{m=0}^{+\infty} \alpha_{m,n} \exp(-n\psi) \cos(mx), \quad (14)$$

where $\alpha_{m,n}$ is an unknown coefficient to be derived.

According to the solution expressions (14), we may construct the initial estimation of the hydroelastic wave deflection as

$$z_0(x, \psi) = -\psi + \frac{H}{2} \exp(-\psi) \cos(x), \quad (15)$$

where H is an unknown dimensionless wave height to be derived [18].

3.2. Deformation Equations. We construct three homotopies $Z(x, \psi; q)$, $\Delta(q)$, and $\Gamma(q)$. These homotopies are governed by the following zeroth-order deformation equations for the governing equation (10) and two boundary conditions (11) and (12) as

$$(1-q)\mathscr{L}_1[Z(x,\psi;q) - z_0(x,\psi)] = qc_0 N_1[Z(x,\psi;q)], \quad (\psi > 0), \quad (16)$$

$$(1-q)\mathscr{L}_2[Z(x,\psi;q) - z_0(x,\psi)] = qc_0 N_2[Z(x,\psi;q), \Delta(q), \Gamma(q)], \quad (\psi = 0), \quad (17)$$

$$\frac{\partial Z(x,\psi;q)}{\partial x} = 0, \quad (\psi = +\infty), \quad (18)$$

respectively, with the wave height

$$Z(0, 0; q) - Z(\pi, 0; q) = H. \quad (19)$$

where $q \in [0, 1]$ is the embedding parameter. When q increases from 0 to 1, $Z(x, \psi; q)$ varies continuously from its initial estimation $z_0(x, \psi)$ to the exact solution $z(x, \psi)$, $\Delta(q)$ deforms continuously from its initial estimation δ_0 to the exact solution δ, and $\Gamma(q)$ is from κ_0 to κ. c_0 is a nonzero convergence-control parameter. Based on the governing equation (10) and the boundary condition (11), $\mathscr{N}_1[\cdot]$ and $\mathscr{N}_2[\cdot]$ are the nonlinear operators defined by

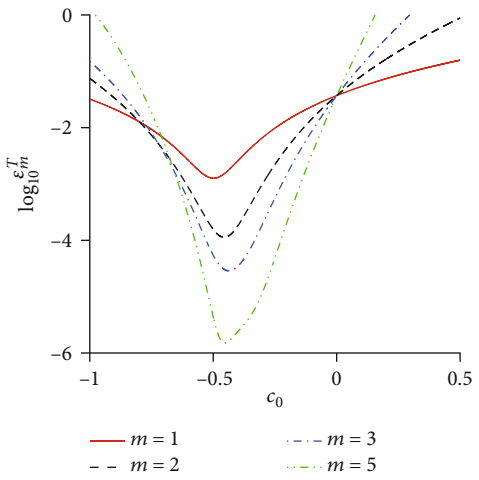

FIGURE 2: Residual squares of $\log_{10}\varepsilon_m^T$ of the mth order homotopy approximation c_0.

$$\mathscr{N}_1[Z(x,\psi;q)] = \frac{\partial^2 Z}{\partial x^2}\left(\frac{\partial Z}{\partial \psi}\right)^2 - \frac{\partial Z}{\partial x}\frac{\partial Z}{\partial \psi}\frac{\partial^2 Z}{\partial x \partial \psi} + \left[1 + \left(\frac{\partial Z}{\partial x}\right)^2\right]\frac{\partial^2 Z}{\partial \psi^2} - \left(\frac{\partial Z}{\partial \psi}\right)^3 \Omega(\psi),$$

$$\mathscr{N}_2[Z(x,\psi;q), \Delta(q), \Gamma(q)] = \frac{1}{2}\Delta\left[1 + \left(\frac{\partial Z}{\partial x}\right)^2\right] + \left(Z + D\frac{\partial^4 Z}{\partial x^4} + m_e - \Gamma\right)\left(\frac{\partial Z}{\partial \psi}\right)^2, \quad (20)$$

respectively.

If we only choose the unique linear term $\partial^2/\partial\psi^2$ in the equation (10) as the auxiliary linear operators $\mathscr{L}_1$, we would get a solution $z(x, \psi)$ in the power series of ψ which cannot satisfy the impermeable bottom condition (12). We can obey the solution expression (14) under the physical considerations to choose the following auxiliary linear operator

$$\mathscr{L}_1[u] = \frac{\partial^2 u}{\partial \psi^2} + \frac{\partial^2 u}{\partial x^2}, \quad (21)$$

where $\mathscr{L}_1[0] = 0$.

The nonlinear boundary condition (11) does not contain any linear term. Here, we still follow the solution expression (14) to choose another auxiliary linear operator

$$\mathscr{L}_2[u] = u + \frac{\partial u}{\partial \psi}, \quad (22)$$

where $\mathscr{L}_2[0] = 0$.

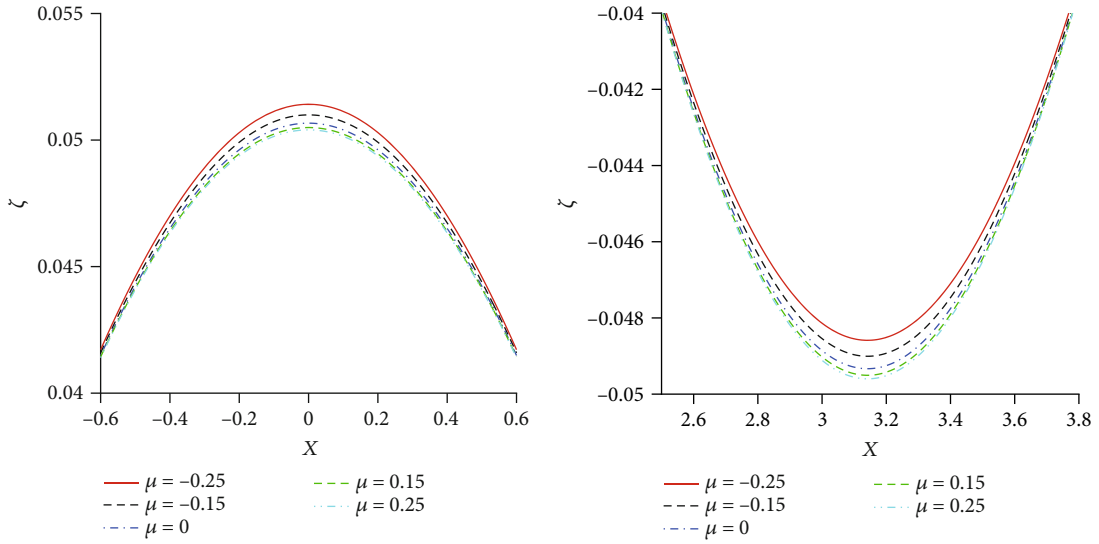

(a) Wave elevations near the crest

(b) Wave elevations near the trough

FIGURE 3: Variation of the hydroelastic wave profiles versus x for different vorticity parameter μ.

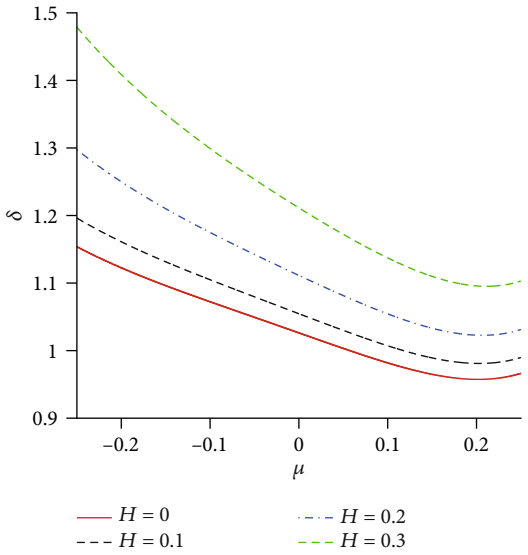

FIGURE 4: The influence of the vorticity parameter μ on the phase velocity $\delta(=c^2/c_0^2)$ for different wave amplitude H.

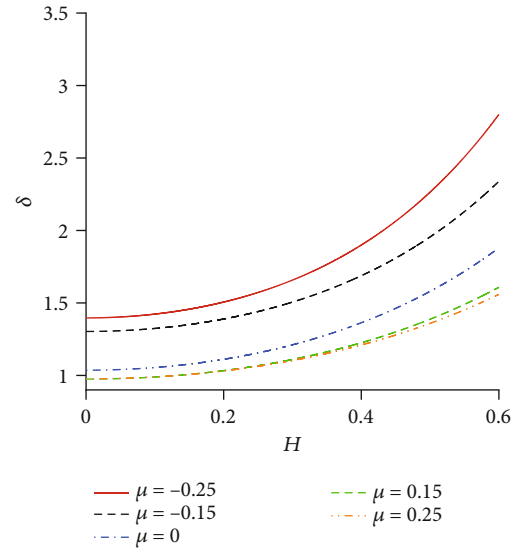

FIGURE 5: The influence of the wave amplitude H on the phase velocity $\delta(=c^2/c_0^2)$ for different vorticity parameter μ.

Expanding the unknown function $Z(x, \psi; q)$ and the two unknown constants $\Delta(q)$ and $\Gamma(q)$ into the Maclaurin series about q at $q = 0$,

$$Z(x, \psi; q) = \sum_{m=0}^{+\infty} z_m(x, \psi) q^m, \tag{23}$$

$$\Delta(q) = \sum_{m=0}^{+\infty} \delta_m q^m, \tag{24}$$

$$\Gamma(q) = \sum_{m=0}^{+\infty} \kappa_m q^m, \tag{25}$$

where

$$\{z_m(x, \psi), \delta_m, \kappa_m\} = \frac{1}{m!} \frac{\partial^m}{\partial q^m} \{Z(x, \psi; q), \Delta(q), \Gamma(q)\}|_{q=0}. \tag{26}$$

We substitute these series (23), (24), and (25) into the zeroth-order deformation equations (16) and (17) and differentiate the zero-order deformation equations m times about q, then divide them by $m!$. Setting $q = 0$, we can obtain the linear PDEs (i.e., high-order deformation equations in the

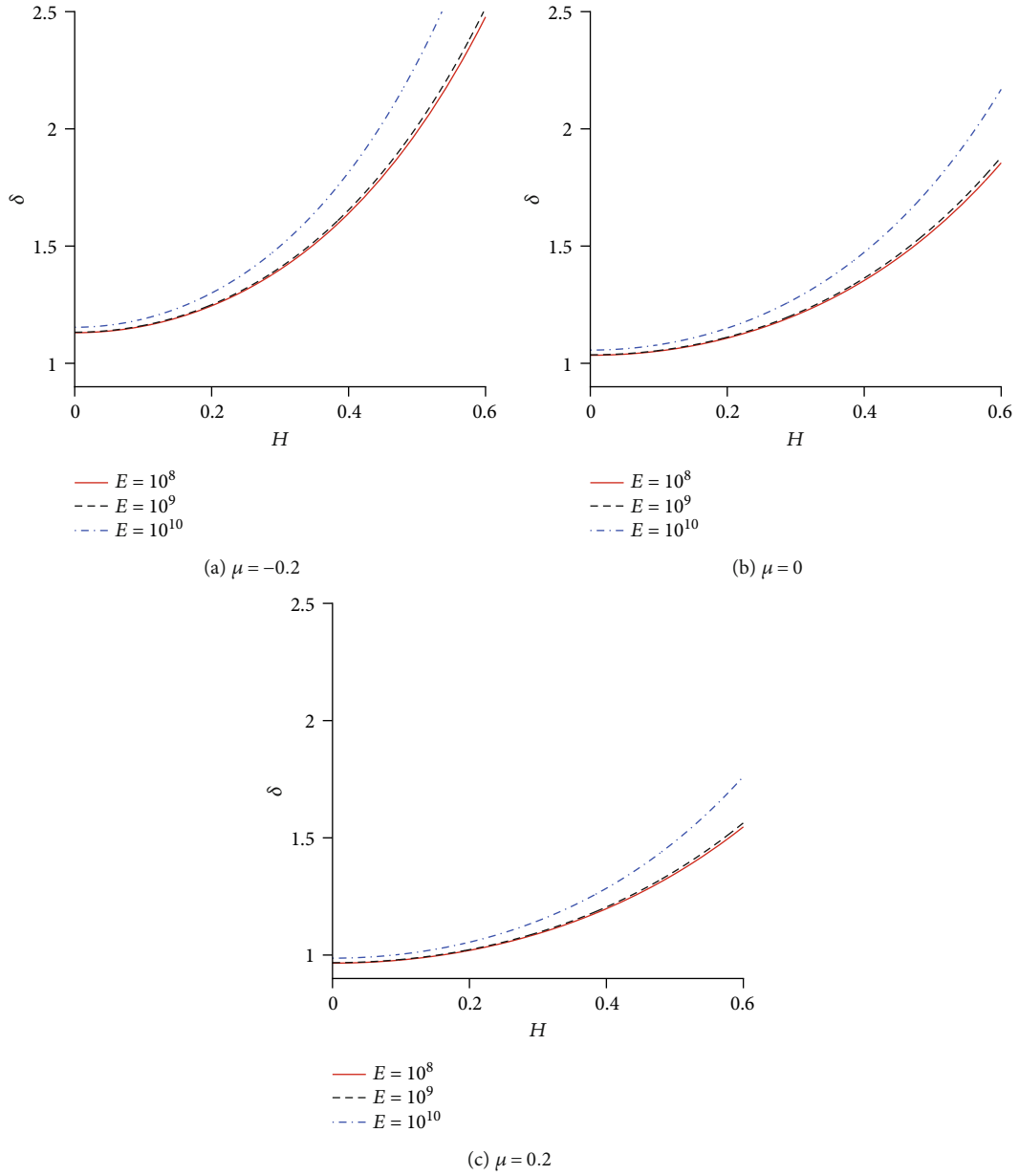

Figure 6: The influence of Young's modulus E on the phase velocity $\delta(=c^2/c_0^2)$ for different wave amplitude μ.

HAM) for the unknown function $z_m(x,\psi)$ and the unknown constants δ_m and κ_m. In order to make our equations closed, we consider

$$z_n(0,0) - z_n(\pi,0) = H, \quad (n \geq 0), \tag{27}$$

to relate the solutions and the wave height H.

3.3. Optimal Convergence-Control Parameters. To ensure the accuracy of our HAM-based series solutions, we define the total squared error ${\varepsilon^T}_m$ as follows:

$$\varepsilon_m^T = \varepsilon_{m,1} + \varepsilon_{m,2}, \tag{28}$$

where

$$\varepsilon_{m,1} = \frac{1}{(1+M)^2}\sum_{i=0}^{M}\sum_{j=0}^{M}\left(\mathcal{N}_1[Z(x,\psi;q)]\big|_{x=i\Delta x,\psi=j\Delta\psi}\right)^2,$$

$$\varepsilon_{m,2} = \frac{1}{1+M}\sum_{i=0}^{M}\left(\mathcal{N}_2[Z(x,\psi;q),\Delta(q),\Gamma(q)]\big|_{x=i\Delta x,\psi=0}\right)^2, \tag{29}$$

where $\varepsilon_{m,2}$ are the residual square errors of Equations (10) and (11), respectively. $\Delta x = \Delta\psi = \pi/M$. In this paper, we choose $M = 10$. The optimal convergence-control parameter c_0 can be acquired by the minimum value of ε_m^T in the residual plot as shown in Figure 2

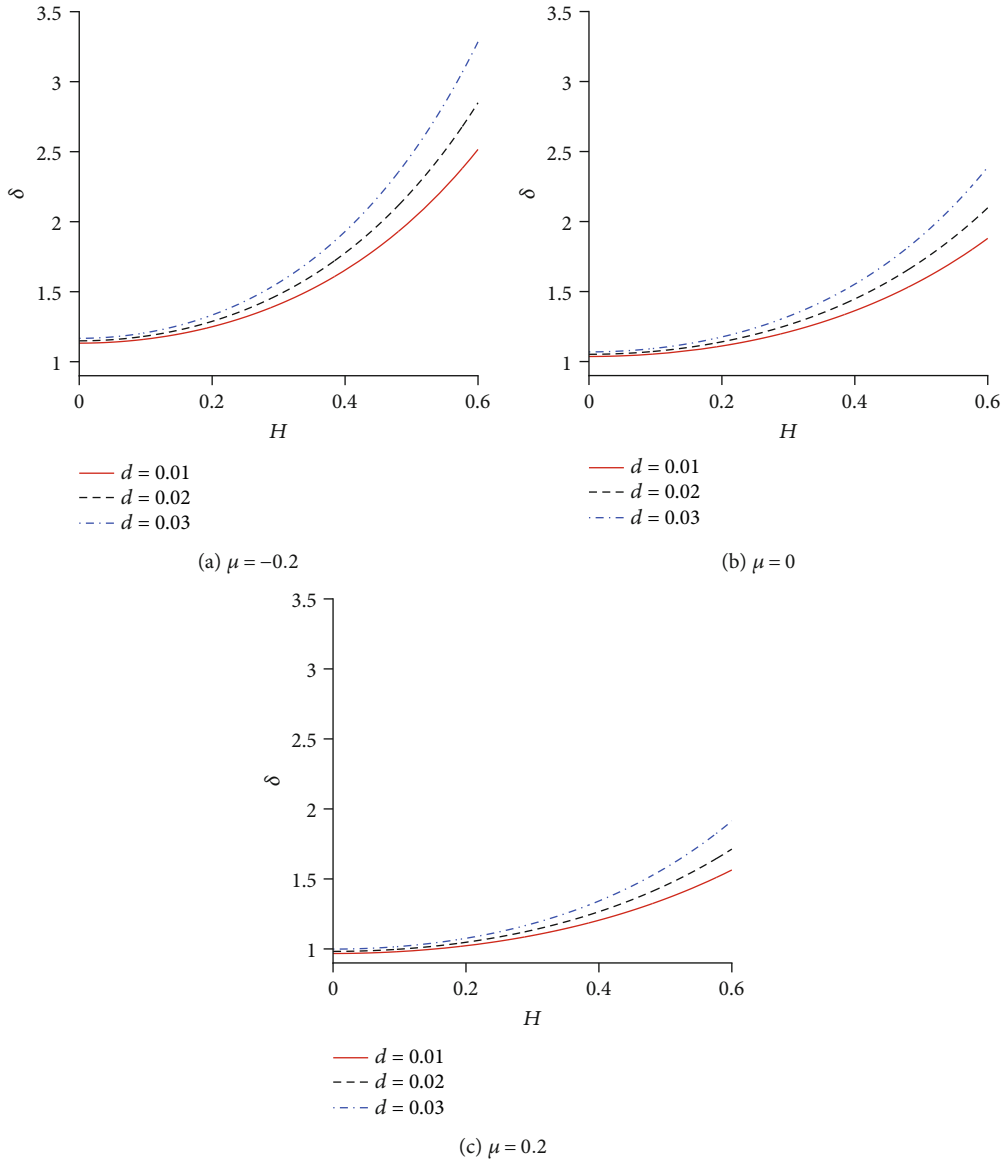

FIGURE 7: The influence of the plate's thickness d on the phase velocity $\delta(=c^2/c_0^2)$ for different wave amplitude μ.

3.4. Iteration of Solutions. Substituting the initial estimation of hydroelastic wave deflection (15) into the high-order deformation equations, we can obtain every order analytic solution from these deformation equations by performing symbolic computation using Mathematica 8.0. First, one-order solution for the unknown function $z(x, \psi)$ is acquired from the one-order deformation equations as follows:

$$\begin{aligned} z_1(x,\psi) = {} & \left[\mu \exp(-\psi) - \frac{1}{4}H^2 \exp(-2\psi) + \frac{3}{8}H^2\mu \exp(-3\psi)\right] c_0 \\ & + \left[\left(-1 - \frac{1}{2}D - \frac{1}{2}\delta_0 + \kappa_0 - \frac{3}{32}H^2 - \frac{3}{32}DH^2\right) \exp(-\psi)\right. \\ & - \frac{3}{2}\mu \exp(-2\psi) + \frac{1}{16}H^2 \exp(-3\psi) \\ & \left. - \frac{3}{32}H^2\mu \exp(-4\psi)\right] c_0 H \cos t(x) \\ & + \left[\left(-\frac{5}{24} - \frac{1}{8}D - \frac{1}{16}m_e - \frac{1}{32}\delta_0 + \frac{1}{16}\kappa_0\right)\right. \\ & \left. + \left(\frac{1}{24} - \frac{1}{8}\mu\right) \exp(-\psi) + \frac{1}{16} \exp(-2\psi)\right] c_0 H^2 \\ & \times \exp(-2\psi) \cos(2x) + \left[-\left(\frac{7}{384} + \frac{1}{96}D\right) - \frac{1}{256}\mu \exp(-\psi)\right. \\ & \left. + \frac{1}{384} \exp(-2\psi) + \frac{1}{768}\mu \times \exp(-3\psi)\right] c_0 H^3 \exp(-3\psi) \cos(3x), \end{aligned} \tag{30}$$

where the initial solutions δ_0 of δ and κ_0 of κ are still unknown. We use the relation (27) for the wave amplitude and the vertical displacement to determine δ_0 and κ_0 as follows:

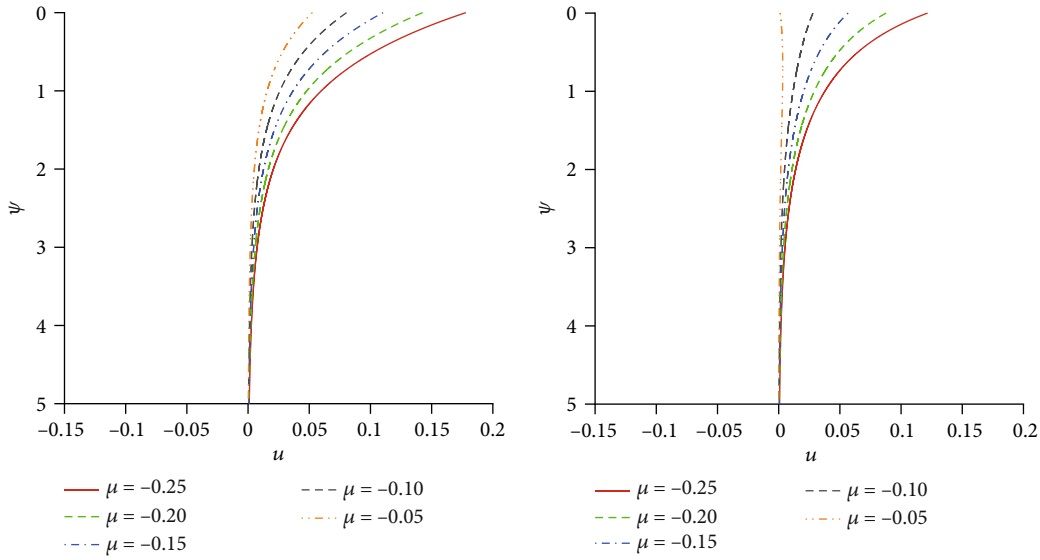

(a) Horizontal velocity u near the crest

(b) Horizontal velocity u near the trough

FIGURE 8: The influence of the aiding shear currents on horizontal velocity profile u of propagating periodic waves for different vorticity parameter μ by means of $c_0 = -0.4$. Solid line: $\mu = -0.25$; dashed line: $\mu = -0.20$; dash dot line: $\mu = -0.15$; long dash line: $\mu = -0.10$; dash dot dot: $\mu = -0.05$.

$$\delta_0 = 2 + \frac{1}{c_0} + D\left(1 - \frac{H^2}{6} + \frac{5H^4}{192}\right) + \mu\left(1 - \frac{35H^2}{192} + \frac{37H^4}{1536}\right) + \frac{3c_0 + 32}{256c_0}H^4 + \frac{11}{32}H^2,$$

$$\kappa_0 = 2 + \frac{1}{c_0} + D\left(1 - \frac{H^2}{48} + \frac{5H^4}{384}\right) + \mu\left(2 + \frac{H^2}{192} + \frac{37H^4}{3072}\right) + m_e\frac{7c_0 + 2}{32c_0}H^2 + \frac{3}{512}H^4, \tag{31}$$

respectively. Once the convergence control parameter c_0 and important physical parameters H, D, μ, and m_e are given, we can get the corresponding solutions for our hydroelastic problem. If we continue with the one-order approximations by utilizing the high-order deformation equations, the higher-order approximations can be acquired iteratively.

4. Result Analysis

First, we illustrate the total squared residual error ε_m^T of our solutions at several different orders versus c_0 with the case of $\mu = 0.1$, $H = 0.1$, $d = 0.01$, $\rho_e = 0.9$, $E = 12822.8$ (i.e., the dimensional $E = 109$ Pa), and $\nu = 0.33$ and take these data hereinafter for computation unless otherwise stated. As shown in Figure 2, we find that ε in Equation (28) decreases firstly and then increases in the interval $[-1.0, 0]$. And as the order m increases, ε decreases gradually about -0.4. Then, the optimal value of c_0 can be chosen as -0.4. This illustrates that our HAM-based series solutions are accurate and convergent for the nonlinear hydroelastic interaction.

The plate deflections at the crest and the trough in the case of $H = 0.1$ and $-0.25 \le \mu \le 0.25$ are shown in Figures 3(a) and 3(b), respectively. It is found that, for a given wave height H, the aiding exponential shear current ($\mu < 0$) tends to sharpen the crest and smoothen the trough, while the opposing shear current ($\mu > 0$) has the opposite effect. And the effect of the shear current on plate deformation is more obvious at the trough than at the crest. This might explain why the aiding exponential shear current tends to shorten the maximum wave height while the opposing one tends to enlarge it.

In Figure 4, we show a fourth-order dispersion relation for the phase speed $\delta(= c^2/c_0^2)$ as a function of the vorticity parameter μ with several given wave heights H. And Figure 5 shows the phase speed $\delta(= c^2/c_0^2)$ as a function of the wave heights H with several given vorticity parameter μ. It is found that, for both an opposing current and an aiding current, the larger value of the wave height increases the wave phase speed, while the phase speed decreases with the increase of the vorticity parameter in the opposing current, but the phase speed increases with the increase of the vorticity parameter in the aiding current. As shown in Figures 4 and 5, the phase speed δ is close to 1 when H is very small (linear waves) and μ (no current). It is demonstrated that our result is compatible with the dispersion relation in deep water $\delta = (1 + D)/(1 + m)$ [22] from the linearized theory of hydroelastic waves with no current.

The effects of Young's modulus of the plate are shown in Figure 6, from which we can see that for both an opposing current and an aiding current, the phase speed δ increases with increasing Young's modulus. The effects of the plate

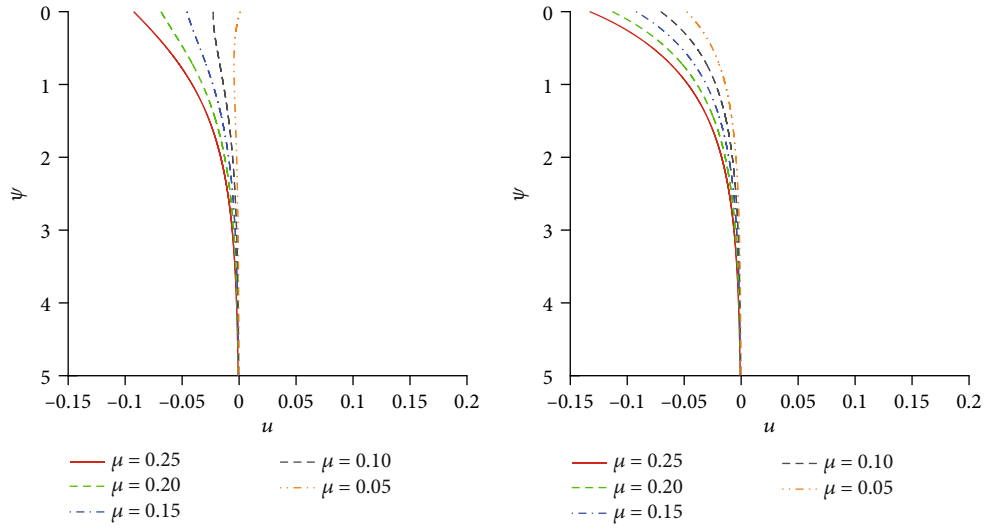

(a) Horizontal velocity u near the crest

(b) Horizontal velocity u near the trough

FIGURE 9: The influence of the opposing shear currents on the horizontal velocity profile u of propagating periodic waves for different vorticity parameter μ by means of $c_0 = -0.4$. Solid line: $\mu = 0.25$; dashed line: $\mu = 0.20$; dash dot line: $\mu = 0.15$; long dash line: $\mu = 0.10$; dash dot dot: $\mu = 0.05$.

thickness d on the phase speed δ are studied. Figure 7 shows that a larger d increases the phase speed, which is similar to effects for Young's modulus of the plate in Figure 6.

Figure 8 shows the horizontal velocity profiles $u(= 1 + z_\psi(x, \psi)^{-1})$ in the aiding shear currents for different vorticity parameters μ. We find that the horizontal velocity under the wave crest is in the same direction, while the horizontal velocity under the wave trough changes from the same direction into the opposing direction when the absolute value of μ decreases to about 0.05. Figure 9 shows the horizontal velocity profiles in the opposing shear currents for different vorticity parameters μ. We observe that the horizontal velocity under the wave trough is in the opposing direction, while the horizontal velocity under the wave crest changes from the opposing direction into the same direction when the value of μ decreases to about 0.05. As shown in Figures 8 and 9, we observe that for both an opposing current and an aiding current, a larger μ tends to increase the horizontal velocity u. Besides, in the opposing current, the horizontal velocity u under the wave crest delays more quickly as ψ increases than that of waves under the wave trough, while in the aiding current case, we observe the opposite effect.

5. Conclusions

In this work, we are concerned with nonlinear hydroelastic waves generated due to a floating elastic plate interacting with a shear current which decays exponentially with depth. We introduce a stream function to obtain the governing equation with the boundary conditions expressing a balance among the hydrodynamic, the shear currents, elastic, and inertial forces. In order to simplify the algorithm, we transfer the nonlinear boundary value problem from an unknown free surface into a known boundary by means of Dubreil-Jacotin transformation. In the frame of the HAM, we consider the solution expression of the hydroelastic wave deflection as a series with a set of base functions $\exp(-n\psi)\cos(mx)$ based on physical points of view. Numerical results demonstrate the validity and convergence of our HAM-based analytical solutions for the nonlinear hydroelastic interaction a wave-current coexisting fluid.

The effects of some important physical parameters on the plate deflections, the phase speed, and the horizontal velocity profiles are considered in detail. We find that a larger aiding shear current tends to sharpen the crest and smoothen the trough of the plate deflections, while the opposing shear current has the opposite effect, and both opposing and aiding current on plate deformation all have a more obvious effect on the trough than on the crest.

For both an opposing current and an aiding current, the larger wave height H increases the wave phase speed δ, while the aiding exponential shear currents tend to increase the wave phase velocity, but the opposing exponential shear currents tend to decrease it. It is noted that our result is compatible with the dispersion relation in deep water from the linearized theory of hydroelastic waves with no current.

The horizontal velocity under a shear current is in the same direction, while the velocity's direction changes as the value of vorticity parameters μ decreases. But in the case of an opposing current, the horizontal velocity under the wave crest delays more quickly as ψ increases than that of waves under the wave trough, while in the aiding current case, there is an opposite effect. All of those results obtained here can help us further understand hydroelastic interaction between a floating elastic plate and wave current in the real ocean.

Data Availability

All models generated or used during the study appear in the submitted article. All code generated or used during the study are available from the corresponding author by request (Ping Wang, Email: pingwang2003@126.com).

Conflicts of Interest

There is no any conflict of interests in our manuscript. The authors themselves program the symbolic computation software named Mathematica 8.0 independently to gain the approximate analytical solutions of the PDEs considered here.

Acknowledgments

This research was financially supported by the Natural Science Foundation of Shandong Province under Grant No. ZR2017MA014 and the National Natural Science Foundation of China under Grant No. 51674149. Qingdao Postdoctoral Applied Research Project No. 020022034 is also acknowledged.

References

[1] L. K. Forbes, "Surface waves of large amplitude beneath an elastic sheet. Part 1. Highorder series solution," *Journal of Fluid Mechanics*, vol. 169, no. 1, pp. 409–428, 1986.

[2] L. K. Forbes, "Surface waves of large amplitude beneath an elastic sheet. Part 2. Galerkin solution," *Journal of Fluid Mechanics*, vol. 188, pp. 491–508, 1988.

[3] J.-M. Vanden-Broeck and E. I. Părău, "Two-dimensional generalized solitary waves and periodic waves under an ice sheet," *Philosophical Transactions of the Royal Society A: Mathematical, Physical and Engineering Sciences*, vol. 369, no. 1947, pp. 2957–2972, 2011.

[4] P. A. Milewski, J. M. Vanden-Broeck, and Z. Wang, "Hydroelastic solitary waves in deep water," *Journal of Fluid Mechanics*, vol. 679, pp. 628–640, 2011.

[5] P. Wang and D. Q. Lu, "Analytic approximation to nonlinear hydroelastic waves traveling in a thin elastic plate floating on a fluid," *Science China Physics, Mechanics and Astronomy*, vol. 56, no. 11, pp. 2170–2177, 2013.

[6] P. Wang and D. Q. Lu, "Nonlinear hydroelastic waves traveling in a thin elastic plate floating on a two-layer fluid," *Applied Mathematics and Computation*, vol. 274, pp. 700–710, 2016.

[7] R. Schulkes, R. Hosking, and A. Sneyd, "Waves due to a steadily moving source on a floating ice plate. Part 2," *Journal of Fluid Mechanics*, vol. 180, no. 1, pp. 297–318, 1987.

[8] J. Bhattacharjee and T. Sahoo, "Interaction of current and flexural gravity waves," *Ocean Engineering*, vol. 34, no. 11-12, pp. 1505–1515, 2007.

[9] J. Bhattacharjee and T. Sahoo, "Flexural gravity wave generation by initial disturbances in the presence of current," *Journal of Marine Science and Technology*, vol. 13, no. 2, pp. 138–146, 2008.

[10] S. Mohanty, R. Mondal, and T. Sahoo, "Time dependent flexural gravity waves in the presence of current," *Journal of Fluids and Structures*, vol. 45, pp. 28–49, 2014.

[11] D. Q. Lu and R. W. Yeung, "Hydroelastic waves generated by point loads in a current," *International Journal of Offshore and Polar Engineering*, vol. 25, no. 1, pp. 8–12, 2015.

[12] P. Wang, Y. Wang, C. Su, and Y. Yang, "Nonlinear hydroelastic waves generated due to a floating elastic plate in a current," *Advances in Mathematical Physics*, vol. 2017, Article ID 2837603, 9 pages, 2017.

[13] J. Bhattacharjee and T. Sahoo, "Interaction of flexural gravity waves with shear current in shallow water," *Ocean Engineering*, vol. 36, no. 11, pp. 831–841, 2009.

[14] T. Gao, P. Milewski, and J.-M. vanden-Broeck, "Hydroelastic solitary waves with constant vorticity," *Wave Motion*, vol. 85, pp. 84–97, 2019.

[15] T. Gao, Z. Wang, and P. Milewski, "Nonlinear hydroelastic waves on a linear shear current at finite depth," *Journal of Fluid Mechanics*, vol. 876, pp. 55–86, 2019.

[16] S. J. Liao, *Beyond Perturbation: Introduction to the Homotopy Analysis Method*, CRC Press, Boca Raton, 2004.

[17] S. J. Liao, *Homotopy Analysis Method in Nonlinear Differential Equations*, Higher Education Press, Beijing, 2012.

[18] J. Cheng, J. Cang, and S. Liao, "On the interaction of deep water waves and exponential shear currents," *Zeitschrift für angewandte Mathematik und Physik*, vol. 60, no. 3, pp. 450–478, 2009.

[19] J. Cang, J. Cheng, and R. Grimshaw, "A short comment on the effect of a shear layer on nonlinear water waves," *Science China Physics, Mechanics & Astronomy*, vol. 54, no. 1, pp. 67–73, 2011.

[20] H. Lamb, *Hydrodynamics*, Dover Press, 6th edition, 1945.

[21] T. Wang and G. C. Li, "Effect of nonlinear wave-current interaction on flow fields and hydrodynamic forces," *Science in China Series A: Mathematics*, vol. 40, no. 6, pp. 622–632, 1997.

[22] F. Xu and D. Q. Lu, "An optimization of eigenfunction expansion method for the interaction of water waves with an elastic plate," *Journal of Hydrodynamics*, vol. 21, no. 4, pp. 526–530, 2009.

Hindawi
Advances in Mathematical Physics
Volume 2020, Article ID 4378691, 6 pages
https://doi.org/10.1155/2020/4378691

Research Article

Semiclassical Solutions for a Kind of Coupled Schrödinger Equations

Jinmei Fan, Yi-rong Jiang, and Qiongfen Zhang

College of Science, Guilin University of Technology, Guilin, Guangxi 541004, China

Correspondence should be addressed to Qiongfen Zhang; qfzhangcsu@163.com

Received 11 June 2020; Accepted 27 July 2020; Published 17 August 2020

Guest Editor: Xin Yu

In this paper, we are concerned with the following coupled Schrödinger equations $\begin{cases} -\lambda^2\Delta u + a_1(x)u = c(x)v + a_2(x)|u|^{p-2}u + a_3(x)|u|^{2^*-2}u, & x \in \mathbb{R}^N, \\ -\lambda^2\Delta v + b_1(x)v = c(x)u + b_2(x)|v|^{p-2}v + b_3(x)|v|^{2^*-2}v, & x \in \mathbb{R}^N, \end{cases}$ where $2 < p < 2^*, 2 < q < 2^*, 2^* = 2N/(N-2)$, and $N \geq 3$; $\lambda > 0$ is a parameter; and $a_1, a_2, a_3, b_1, b_2, b_3, c \in C(\mathbb{R}^N, \mathbb{R})$ and $u, v \in H^1(\mathbb{R}^N)$. Under some suitable conditions that $a_1^0 = \inf a_1 = 0$ or $b_1^0 = \inf b_1 = 0$ and $|c(x)|^2 \leq \vartheta a_1(x)b_1(x)$ with $\vartheta \in (0,1)$, the above coupled Schrödinger system possesses nontrivial solutions if $\lambda \in (0, \lambda_0)$, where λ_0 is related to $a_1, a_2, a_3, b_1, b_2, b_3$, and N.

1. Introduction

We consider the following coupled Schrödinger equations in this paper:

$$\begin{cases} -\lambda^2\Delta u + a_1(x)u = c(x)v + a_2(x)|u|^{p-2}u + a_3(x)|u|^{2^*-2}u, & x \in \mathbb{R}^N, \\ -\lambda^2\Delta v + b_1(x)v = c(x)u + b_2(x)|v|^{p-2}v + b_3(x)|v|^{2^*-2}v, & x \in \mathbb{R}^N, \end{cases} \tag{1}$$

where $2 < p < 2^*$, $2 < q < 2^*$, $N \geq 3$, and $2^* = 2N/(N-2)$ are the Sobolev critical exponent;$\lambda > 0$ is a parameter; and a_1, $a_2, a_3, b_1, b_2, b_3, c \in C(\mathbb{R}^N, \mathbb{R})$ and $u, v \in H^1(\mathbb{R}^N)$.

As it is known in [1], this type of systems arises in nonlinear optics. In the past years, under different kinds of assumptions on the potential V and the nonlinearity f, many authors [2–8] focus on the following kind of Schrödinger equation:

$$-\lambda^2\Delta u + V(x)u = f(x,u), \quad x \in \mathbb{R}^N. \tag{2}$$

As one knows, single-mode optical fibers are not really "single mode" but actually bimodal because of the presence of birefringence. So recently, the coupled Schrödinger systems are investigated by the authors [9–12]. For more related results and physical background on Schrödinger systems, please see [13–23] and references therein.

In [11], the authors investigated standing waves for the following kind of coupled Schrödinger equations:

$$\begin{cases} -\lambda^2\Delta u + a_1(x)u = cv + |u|^{p-2}u, & x \in \mathbb{R}^N, \\ -\lambda^2\Delta v + b_1(x)v = cu + |v|^{2^*-2}v, & x \in \mathbb{R}^N, \end{cases} \tag{3}$$

where $a_1, b_1 \in C(\mathbb{R}^N, \mathbb{R})$, $N \geq 3$, $u, v > 0$, $u, v \in H^1(\mathbb{R}^N)$, and $u(x), v(x) \to 0$ as $|x| \to \infty$. Under the following conditions,

(A0) there exist positive constants $a_1^0 > 0$ and $b_1^0 > 0$ such that $a_1(x) \geq a_1^0$, $b_1(x) \geq a_1^0$, and $0 < c \leq \sqrt{a_1^0 b_1^0}$; they obtained the existence of a positive solution for (3) if λ is sufficiently small. But, if $a_1^0 = \inf a_1 = 0$ or $b_1^0 = \inf b_1 = 0$, then $0 < c \leq \sqrt{a_1^0 b_1^0}$ cannot hold. So in the very recent paper [12], Peng et al. investigated the following coupled Schrödinger equations and generalize the result in [11]:

$$\begin{cases} -\lambda^2 \Delta u + a_1(x)u = c(x)v + |u|^{p-2}u, & x \in \mathbb{R}^N, \\ -\lambda^2 \Delta v + b_1(x)v = c(x)u + |v|^{q-2}v, & x \in \mathbb{R}^N, \end{cases} \tag{4}$$

where a_1, b_1 are the same as in (3), $N \geq 3$. Under the following conditions,

(A1) $a_1(x) \geq a_1(0) = 0$ and $b_1(x) \geq 0$, and there exist constants $a_1^0 > 0$ and $b_1^0 > 0$ such that the measure of the sets $A_{a_1^0} := \{x : a_1(x) < a_1^0\}$ and $B_{b_1^0} := \{x : b_1(x) < b_1^0\}$ are finite

(A2) there exists a constant $\vartheta \in (0, 1)$ such that $|c(x)|^2 \leq \vartheta a_1(x) b_1(x)$ for all $x \in \mathbb{R}^N$; Peng et al. proved that system (4) has at least one nontrivial solution. An interesting question is what will happen if the nonlinearity is also critical growth in system (4)? Motivated mainly by the abovementioned results, we will answer this question and prove that system (1), under conditions (A1) and (A2), and

(A3) there exist constants a_2^0, a_2^1, a_3^0, a_3^1, b_2^0, b_2^1, b_3^0, $b_3^1 > 0$ such that

$$\begin{aligned} &a_2^0 \leq a_2(x) \leq a_2^1, a_3^0 \leq a_3(x) \leq a_3^1, b_2^0 \leq b_2(x) \leq b_2^1, \\ &b_3^0 \leq b_3(x) \leq b_3^1, \quad \forall x \in \mathbb{R}^N, \end{aligned} \tag{5}$$

possesses nontrivial solutions if $\lambda \in (0, \lambda_0)$, where λ_0 is related to $a_1, a_2, a_3, b_1, b_2, b_3$, and N. As far as we know, similar results for system (1) with a critical exponent have not been investigated by variational methods in the literature. The following condition is similar to condition (A1):

(A1') $b_1(x) \geq b_1(0) = 0$ and $a_1(x) \geq 0$, and there exist constants $a_1^0 > 0$ and $b_1^0 > 0$ such that the measure of the sets $A_{a_1^0} := \{x \in \mathbb{R}^N : a_1(x) < a_1^0\}$ and $B_{b_1^0} := \{x \in \mathbb{R}^N : b_1(x) < b_1^0\}$ are finite.

Since $(q-2)N - 2q < 0$ and $(p-2)N - 2p < 0$, one can choose $d_0 \geq 1$ such that

$$C_1 a_2^1 \alpha^{(p-2)/p} + C_2 b_2^1 \beta^{(q-2)/q} + C_3 a_3^1 \alpha^{2/N} + C_4 b_3^1 \beta^{2/N} \leq \frac{1}{2}(1 - \vartheta), \tag{6}$$

where

$$\begin{aligned} \alpha &= \frac{\omega_N a_2^0 (p-2)}{2Np} \left\{ \frac{N^2 + 2(N+2)}{(N+2)\left(1 - 2^{-N}\right)^2} \right\}^{p/(p-2)} d_0^{[(p-2)N-2p]/(p-2)}, \\ \beta &= \frac{\omega_N b_2^0 (q-2)}{2Nq} \left\{ \frac{N^2 + 2(N+2)}{(N+2)\left(1 - 2^{-N}\right)^2} \right\}^{q/(q-2)} d_0^{[(q-2)N-2q]/(q-2)}, \\ C_1 &= \left[\frac{2p(\eta_0 \eta_{2^*})^N}{(p-2)a_2^0} \right]^{(p-2)/p} \left(a_1^0\right)^{[p(N-2)-2N]/2p}, \\ C_2 &= \left[\frac{2q(\eta_0 \eta_{2^*})^N}{(q-2)b_2^0} \right]^{(q-2)/q} \left(b_1^0\right)^{[q(N-2)-2N)]/2q}, \\ C_3 &= \left[\frac{22^*(\eta_0 \eta_{2^*})^N}{(2^*-2)a_3^0} \right]^{2/N}, \\ C_4 &= \left[\frac{22^*(\eta_0 \eta_{2^*})^N}{(2^*-2)b_3^0} \right]^{2/N}, \end{aligned} \tag{7}$$

η_0 and η_{2^*} are embedding constants and ω_N is the volume of the unit ball in $\mathbb{R}^N$. From (A1') and (A1), using $b_1(0) = 0$ and $a_1(0) = 0$, one can let $\mu_0 > 1$ such that

$$\sup_{\mu^{1/2}|x| \leq 2d_0} |b_1(x)| \leq d_0^{-2}, \quad \sup_{\mu^{1/2}|x| \leq 2d_0} |a_1(x)| \leq d_0^{-2}, \quad \forall \mu \geq \mu_0. \tag{8}$$

Let $w = (u, v)$ and $\lambda^{-2} = \mu$, then system (1) can be rewritten as

$$\begin{cases} -\Delta u + \mu a_1(x)u = \mu c(x)v + \mu a_2(x)|u|^{p-2}u + \mu a_3(x)|u|^{2^*-2}u, & x \in \mathbb{R}^N, \\ -\Delta v + \mu b_1(x)v = \mu c(x)u + \mu b_2(x)|v|^{p-2}v + \mu b_3(x)|v|^{2^*-2}v, & x \in \mathbb{R}^N, \end{cases} \tag{9}$$

and the functional of (9) is given by

$$\begin{aligned} S_\mu(w) = \frac{1}{2}\int_{\mathbb{R}^N} &\left[|\Delta u|^2 + |\Delta v|^2 + \mu a_1(x)|u|^2 + \mu b_1(x)|v|^2 \right] dx \\ &- \frac{\mu}{p}\int_{\mathbb{R}^N} a_2(x)|u|^p dx - \frac{\mu}{q}\int_{\mathbb{R}^N} b_2(x)|v|^q dx \\ &- \frac{\mu}{2^*}\int_{\mathbb{R}^N} a_3(x)|u|^{2^*} dx - \frac{\mu}{2^*}\int_{\mathbb{R}^N} b_3(x)|v|^{2^*} dx \\ &- \mu \int_{\mathbb{R}^N} c(x)uv dx. \end{aligned} \tag{10}$$

As is known, the solutions of (1) are the critical points of $S_{\lambda^{-1/2}}(w)$. The main results are the following.

Theorem 1. *Suppose that (A1)–(A3) or (A1')–(A3) hold. Then, (9) possesses at least one nontrivial solution $w_\mu = (u_\mu, v_\mu)$ such that $0 < S_\mu(w_\mu) \leq \beta \mu^{1-N/2}$ for $\mu \geq \mu_0$.*

Theorem 2. *Suppose that (A1)–(A3) or (A1')–(A3) hold. Then, (1) possesses at least one nontrivial solution $w_\lambda = (u_\lambda, v_\lambda)$ such that $0 < S_{\lambda^{-1/2}}(w_\lambda) \leq \beta \lambda^{N-2}$ for $0 < \lambda < \mu_0^{-1/2}$.*

Remark 3. Since the presence of the terms $a_2(x)|u|^{p-2}u$, $a_3(x)|u|^{2^*-2}u$, $b_2(x)|v|^{p-2}v$, and $b_3(x)|v|^{2^*-2}v$, system (1) is more general than (4), and it is more difficult to deal with the nontrivial solutions. In order to prove that system (1) has nontrivial solutions, we need to find some conditions to restrict $a_2(x)$, $a_3(x)$, $b_2(x)$, and $b_3(x)$. It seems that there is no literature considering system (1).

2. Preliminaries

Let

$$E = \left\{ (u, v) : \int_{\mathbb{R}^N} \left[a_1(x)|u|^2 + b_1(x)|v|^2 \right] dx < \infty, u, v \in H^1\left(\mathbb{R}^N\right) \right\}, \tag{11}$$

$$\|w\|_{\mu^\dagger} = \left\{ \int_{\mathbb{R}^N} \left[|\Delta u|^2 + |\Delta v|^2 + \mu a_1(x)|u|^2 + \mu b_1(x)|v|^2 \right] dx \right\}^{1/2}, \quad \forall \quad w = (u, v) \in E. \tag{12}$$

From Lemma 1 of [17], by (A1) or (A1') and the Sobolev inequality, there exists a positive constant $\eta_0 > 0$ independent of μ such that

$$\|w\|_{H^1} := \left\{ \int_{\mathbb{R}^N} \left[|\Delta u|^2 + |\Delta v|^2 + |u|^2 + |v|^2 \right] dx \right\}^{1/2} \le \eta_0 \|w\|_{\mu^\dagger}, \quad \forall w = (u, v) \in E, \mu \ge 1, \tag{13}$$

where $H^1 := H^1(\mathbb{R}^N)$. Then, $(E, \|\cdot\|_{\mu^\dagger})$ is a Banach space for $\mu \ge 1$ equipped with the norm given by (12). Moreover, for $s \in [2, 2^*]$, one has

$$\|w\|_s \le \eta_s \|w\|_{H^1} \le \eta_s \eta_0 \|w\|_{\mu^\dagger}, \quad \forall w \in E, \mu \ge 1, \tag{14}$$

where $\|w\|_s$ is the usual norm in space $L^s(\mathbb{R}^N)$. From (12), we rewrite S_μ as

$$\begin{aligned} S_\mu(w) = {} & \frac{1}{2}\|w\|_{\mu^\dagger}^2 - \frac{\mu}{p}\int_{\mathbb{R}^N} a_2(x)|u|^p dx - \frac{\mu}{q}\int_{\mathbb{R}^N} b_2(x)|v|^q dx \\ & - \frac{\mu}{2^*}\int_{\mathbb{R}^N} a_3(x)|u|^{2^*} dx - \frac{\mu}{2^*}\int_{\mathbb{R}^N} b_3(x)|v|^{2^*} dx \\ & - \mu\int_{\mathbb{R}^N} c(x)uv dx, \quad \forall w \in E. \end{aligned} \tag{15}$$

It is not difficult to see that $S_\mu \in C^1(E, \mathbb{R})$ and

$$\begin{aligned} \left\langle S'_\mu(w), \bar{w} \right\rangle = {} & \int_{\mathbb{R}^N} [\Delta u \cdot \bar{u} + \Delta v \cdot \bar{v} + \mu a_1(x)u\bar{u} + \mu b_1(x)v\bar{v}] dx \\ & - \mu\int_{\mathbb{R}^N} c(x)(u\bar{v} + v\bar{u}) dx - \mu\int_{\mathbb{R}^N} a_2(x)|u|^{p-2}u\bar{u} dx \\ & - \mu\int_{\mathbb{R}^N} b_2(x)|v|^{q-2}v\bar{v} dx - \mu\int_{\mathbb{R}^N} a_3(x)|u|^{2^*-2}u\bar{u} dx \\ & - \mu\int_{\mathbb{R}^N} b_3(x)|v|^{2^*-2}v\bar{v} dx, \quad \forall w = (u, v), \bar{w} = (\bar{u}, \bar{v}) \in E. \end{aligned} \tag{16}$$

As in [12, 22], let

$$\theta(x) = \begin{cases} \dfrac{1}{d_0}, & |x| \le d_0, \\ \dfrac{d_0^{N-1}}{1 - 2^{-N}} \left[|x|^{-N} - (2d_0)^{-N} \right], & d_0 < |x| \le 2d_0, \\ 0, & |x| > 2d_0. \end{cases} \tag{17}$$

Then, $\theta \in H^1(\mathbb{R}^N)$; moreover,

$$\|\nabla\theta\|_2^2 = \int_{\mathbb{R}^N} |\nabla\theta(x)|^2 dx \le \frac{N\omega_N d_0^{N-4}}{(N+2)\left(1 - 2^{-N}\right)^2}, \tag{18}$$

$$\|\theta\|_2^2 = \int_{\mathbb{R}^N} |\theta(x)|^2 dx \le \frac{2\omega_N d_0^{N-2}}{N\left(1 - 2^{-N}\right)^2}. \tag{19}$$

In the next section, we will prove the main results.

3. Proof of the Main Results

Proof of Theorem 1. The proof of Theorem 1 is divided into four steps.

Step 1. We first prove that for any $\mu \ge \mu_0 > 1$, one has

$$\begin{aligned} \sup\left\{ S_\mu(0, te_\mu) : t \ge 0 \right\} \le \beta\mu^{1-N/2}, \\ \sup\left\{ S_\mu(te_\mu, 0) : t \ge 0 \right\} \le \alpha\mu^{1-N/2}, \end{aligned} \tag{20}$$

where $e_\mu(x) = \theta(\mu^{1/2}x)$. From (8), (9), (17), (18), (19), and (A3), we have

$$\begin{aligned} S_\mu(0, te_\mu) = {} & \frac{t^2}{2}\int_{\mathbb{R}^N} \left[|\nabla e_\mu|^2 + \mu b_1(x)|e_\mu|^2 \right] dx - \frac{\mu}{q}\int_{\mathbb{R}^N} b_2(x)|te_\mu|^q dx \\ & - \frac{\mu}{2^*}\int_{\mathbb{R}^N} b_3(x)|te_\mu|^{2^*} dx = \mu^{1-N/2}\left[\frac{t^2}{2}\int_{\mathbb{R}^N} \left(|\nabla\theta|^2 + b_1(\mu^{-1/2}x)|\theta|^2 \right) dx \right. \\ & \left. - \frac{1}{q}\int_{\mathbb{R}^N} b_2(\mu^{-1/2}x)|t\theta|^q dx - \frac{1}{2^*}\int_{\mathbb{R}^N} b_3(\mu^{-1/2}x)|t\theta|^{2^*} dx \right] \\ \le {} & \mu^{1-N/2}\left[\frac{t^2}{2}\left(\|\nabla\theta\|_2^2 + \|\theta\|_2^2 \sup_{|x|\le 2d_0} |b_1(\mu^{-1/2}x))| \right) \right. \\ & \left. - \frac{1}{q}\int_{|x|\le d_0} b_2(\mu^{-1/2}x)\left|\frac{t}{d_0}\right|^q dx - \frac{1}{2^*}\int_{|x|\le d_0} b_3(\mu^{-1/2}x)\left|\frac{t}{d_0}\right|^{2^*} dx \right] \\ \le {} & \mu^{1-N/2}\left[\frac{t^2}{2}\left(\|\nabla\theta\|_2^2 + d_0^{-2}\|\theta\|_2^2 \right) - \frac{\omega_N b_2^0}{qN}t^q d_0^{N-q} - \frac{\omega_N b_3^0}{2^*N}t^{2^*} d_0^{N-2^*} \right] \\ \le {} & \mu^{1-N/2}\left[\frac{t^2}{2}\left(\|\nabla\theta\|_2^2 + d_0^{-2}\|\theta\|_2^2 \right) - \frac{\omega_N b_2^0}{qN}t^q d_0^{N-q} \right] \\ \le {} & \mu^{1-N/2}(q-2)\left(\|\nabla\theta\|_2^2 + d_0^{-2}\|\theta\|_2^2 \right)^{q/(q-2)}(2q)^{-1}\left(\frac{\omega_N b_2^0 d_0^{N-q}}{N} \right)^{-2/(q-2)} \\ \le {} & \mu^{1-N/2}\frac{\omega_N b_2^0(q-2)}{2Nq}\left\{ \frac{N^2 + 2(N+2)}{(N+2)\left(1 - 2^{-N}\right)^2} \right\}^{q/(q-2)} \\ & \cdot d_0^{[(q-2)N-2q]/(q-2)} := \beta\mu^{1-N/2}. \end{aligned} \tag{21}$$

Similarly, from (8), (9), (17), (18), (19), and (A3), we have

$$\begin{aligned} S_\mu(te_\mu, 0) \le {} & \mu^{1-N/2}\frac{\omega_N a_2^0(p-2)}{2Np}\left\{ \frac{N^2 + 2(N+2)}{(N+2)\left(1 - 2^{-N}\right)^2} \right\}^{p/(p-2)} \\ & \cdot d_0^{[(p-2)N-2p]/(p-2)} := \alpha\mu^{1-N/2}, \end{aligned} \tag{22}$$

which together with (21) implies that (20) holds.

Step 2. Let $c_\mu^* = \min\{S_\mu(te_\mu, 0), S_\mu(0, te_\mu)\}$, we should prove that there exists a constant $c_\mu \in (0, c_\mu^*]$ and a sequence $\{w_n\} \subset E$ satisfying

$$S_\mu(w_n) \to c_\mu,\ \left\|S'_\mu(w_n)\right\|_{E^*}\left(1 + \|w_n\|_{\mu^\dagger}\right), \quad \text{as } n \to \infty. \tag{23}$$

By a standard argument, one can obtain (23) by employing the mountain-pass lemma without the (PS) condition, so we omit the details here.

Step 3. We prove that any sequence $\{w_n\} \subset E$ satisfying (23) is bounded in E. From (A2) and Young's inequality, we have

$$\begin{aligned}\mu\int_{\mathbb{R}^3} |c(x)u_n v_n|dx &\le \mu\vartheta\int_{\mathbb{R}^3} \sqrt{a_1(x)b_1(x)}|u_n v_n|dx \\ &\le \frac{\vartheta}{2}\int_{\mathbb{R}^3}\left[\mu a_1(x)u_n^2 + \mu b_1(x)v_n^2\right]dx \\ &\le \frac{\vartheta}{2}\|w_n\|_{\mu^\dagger}^2.\end{aligned} \tag{24}$$

For $2 < p \le q < 2^*$, from (15), (16), (23), and (24), we have

$$\begin{aligned}c_\mu + o(1) = S_\mu(w_n) - \frac{1}{p}\left\langle S'_\mu(w_n), w_n\right\rangle &= \left(\frac{1}{2} - \frac{1}{p}\right)\|w_n\|_{\mu^\dagger}^2 \\ &+ \left(\frac{1}{p} - \frac{1}{q}\right)\mu\int_{\mathbb{R}^N} b_2(x)|v_n|^q dx \\ &+ \left(\frac{1}{p} - \frac{1}{2^*}\right)\mu\int_{\mathbb{R}^N} a_3(x)|u_n|^{2^*}dx \\ &- \left(1 - \frac{2}{p}\right)\mu\int_{\mathbb{R}^N} c(x)u_n v_n dx \\ &+ \left(\frac{1}{p} - \frac{1}{2^*}\right)\mu\int_{\mathbb{R}^N} b_3(x)|v_n|^{2^*}dx \\ &\ge \left(\frac{1}{2} - \frac{1}{p}\right)(1-\vartheta)\|w_n\|_{\mu^\dagger}^2.\end{aligned} \tag{25}$$

For $2 < q \le p < 2^*$, from (15), (16), (23), and (24), we obtain

$$\begin{aligned}c_\mu + o(1) = S_\mu(w_n) - \frac{1}{q}\left\langle S'_\mu(w_n), w_n\right\rangle &= \left(\frac{1}{2} - \frac{1}{q}\right)\|w_n\|_{\mu^\dagger}^2 \\ &+ \left(\frac{1}{q} - \frac{1}{p}\right)\mu\int_{\mathbb{R}^N} a_2(x)|v_n|^p dx + \left(\frac{1}{q} - \frac{1}{2^*}\right) \\ &\cdot \mu\int_{\mathbb{R}^N} a_3(x)|u_n|^{2^*}dx - \left(1 - \frac{2}{q}\right)\mu\int_{\mathbb{R}^N} c(x)u_n v_n dx \\ &+ \left(\frac{1}{q} - \frac{1}{2^*}\right)\mu\int_{\mathbb{R}^N} b_3(x)|v_n|^{2^*}dx \\ &\ge \left(\frac{1}{2} - \frac{1}{q}\right)(1-\vartheta)\|w_n\|_{\mu^\dagger}^2.\end{aligned} \tag{26}$$

It follows from (25) and (26) that $\{w_n\}$ is bounded in E.

Step 4. We show that there exists a nontrivial solution. By Steps 1–3, we know that there exists a bounded sequence $\{w_n\} \subset E$ satisfying (23) with

$$c_\mu \le c_\mu^*, \quad \forall \mu \ge \mu_0. \tag{27}$$

Passing to a subsequence, one can suppose that $w_n = (u_n, v_n) \rightharpoonup w_\mu = (u_\mu, v_\mu)$ in $(E, \|\cdot\|_{\mu^\dagger})$ and $S'_\mu(w_n) \to 0$, as $n \to \infty$. Now, we verify that $w_\mu \ne (0,0)$. Arguing by contradiction, assume that $w_\mu = (0,0)$, that is, $w_n \rightharpoonup (0,0)$ in E, so by [24], we have $w_n \to (0,0)$ in $L^s_{loc}(\mathbb{R}^N)$, $s \in [2, 2^*]$, and $w_n \to (0,0)$ a.e. on $\mathbb{R}^N$. Since $A_{a_1^0}$ and $B_{b_1^0}$ are sets with finite measure, we have

$$\begin{aligned}\|u_n\|_2^2 &= \int_{\mathbb{R}^N\setminus A_{a_1^0}} |u_n|^2 dx + \int_{A_{a_1^0}} |u_n|^2 dx = \int_{\mathbb{R}^N\setminus A_{a_1^0}} |u_n|^2 dx \\ &+ \int_{A_{a_1^0}} |u_n|^2 dx \le \int_{\mathbb{R}^N\setminus A_{a_1^0}} \frac{1}{\mu a_1^0}\mu a_1(x)|u_n|^2 dx \\ &+ \int_{A_{a_1^0}} |u_n|^2 dx \le \frac{1}{\mu a_1^0}\|w_n\|_{\mu^\dagger}^2 + o(1),\end{aligned} \tag{28}$$

$$\begin{aligned}\|v_n\|_2^2 &= \int_{\mathbb{R}^N\setminus B_{b_1^0}} |v_n|^2 dx + \int_{B_{b_1^0}} |v_n|^2 dx = \int_{\mathbb{R}^N\setminus B_{b_1^0}} |v_n|^2 dx \\ &+ \int_{B_{b_1^0}} |v_n|^2 dx \le \int_{\mathbb{R}^N\setminus B_{b_1^0}} \frac{1}{\mu b_1^0}\mu b_1(x)|v_n|^2 dx \\ &+ \int_{B_{b_1^0}} |v_n|^2 dx \le \frac{1}{\mu b_1^0}\|w_n\|_{\mu^\dagger}^2 + o(1).\end{aligned} \tag{29}$$

Similar to [12], from (14), (28), (29), and the Hölder inequality, we obtain

$$\begin{aligned}\|u_n\|_s^s &= \int_{\mathbb{R}^N} |u_n|^s dx \le \left(\int_{\mathbb{R}^N} |u_n|^{2(2^*-s)/(2^*-2)} dx\right) \\ &\cdot \left(\int_{\mathbb{R}^N} |u_n|^{2^*(s-2)/(2^*-2)} dx\right) \le \left(\eta_0\eta_{2^*}\right)^{2^*(s-2)/(2^*-2)} \\ &\cdot \left(\mu a_1^0\right)^{-(2^*-s)/(2^*-2)}\|w_n\|_{\mu^\dagger}^s + o(1), \quad s \in (2, 2^*)\end{aligned} \tag{30}$$

$$\begin{aligned}\|v_n\|_s^s &= \int_{\mathbb{R}^N} |v_n|^s dx \le \left(\int_{\mathbb{R}^N} |v_n|^{2(2^*-s)/(2^*-2)} dx\right) \\ &\cdot \left(\int_{\mathbb{R}^N} |v_n|^{2^*(s-2)/(2^*-2)} dx\right) \le \left(\eta_0\eta_{2^*}\right)^{2^*(s-2)/(2^*-2)} \\ &\cdot \left(\mu b_1^0\right)^{-(2^*-s)/(2^*-2)}\|w_n\|_{\mu^\dagger}^s + o(1), \quad s \in (2, 2^*).\end{aligned} \tag{31}$$

It follows from (15), (16), (23), and (A3) that

$$\begin{aligned} c_\mu + o(1) &= S_\mu(w_n) - \frac{1}{2}\left\langle S'_\mu(w_n), w_n\right\rangle \\ &= \left(\frac{1}{2}-\frac{1}{p}\right)\mu\int_{\mathbb{R}^N} a_2(x)|u_n|^p dx + \left(\frac{1}{2}-\frac{1}{q}\right)\mu\int_{\mathbb{R}^N} b_2(x)|v_n|^q dx \\ &\quad + \left(\frac{1}{2}-\frac{1}{2^*}\right)\mu\int_{\mathbb{R}^N} a_3(x)|u_n|^{2^*} dx + \left(\frac{1}{2}-\frac{1}{2^*}\right) \\ &\quad \cdot \mu\int_{\mathbb{R}^N} b_3(x)|v_n|^{2^*} dx \geq \frac{(p-2)\mu a_2^0}{2p}\|u_n\|_p^p + \frac{(q-2)\mu b_2^0}{2q}\|v_n\|_q^q \\ &\quad + \frac{(2^*-2)\mu a_3^0}{22^*}\|u_n\|_{2^*}^{2^*} + \frac{(2^*-2)\mu b_3^0}{22^*}\|v_n\|_{2^*}^{2^*}. \end{aligned} \tag{32}$$

From (14), (30), (31), and (32), we have

$$\begin{aligned} \mu\|u_n\|_p^p &= \mu\|u_n\|_p^{p-2}\|u_n\|_p^2 \leq \mu\left(\mu a_1^0\right)^{-2(2^*-p)/[p(2^*-2)]} \\ &\quad \cdot \left(\eta_0\eta_{2^*}\right)^{22^*(p-2)/[p(2^*-2)]}\left[\frac{2pc_\mu}{\mu a_2^0(p-2)}\right]^{(p-2)/p}\|w_n\|_{\mu^\dagger}^2 \\ &\quad + o(1) \coloneqq C_1\left[\mu^{(N-2)/2}c_\mu\right]^{(p-2)/p}\|w_n\|_{\mu^\dagger}^2 + o(1), \end{aligned} \tag{33}$$

$$\begin{aligned} \mu\|v_n\|_q^q &= \mu\|u_n\|_q^2\|v_n\|_q^{q-2} \leq \mu\left(\mu b_1^0\right)^{-2(2^*-q)/[q(2^*-2)]} \\ &\quad \cdot \left(\eta_0\eta_{2^*}\right)^{22^*(q-2)/[q(2^*-2)]}\left[\frac{2qc_\mu}{\mu b_2^0(q-2)}\right]^{(q-2)/q}\|w_n\|_{\mu^\dagger}^2 \\ &\quad + o(1) \coloneqq C_2\left[\mu^{(N-2)/2}c_\mu\right]^{(q-2)/q}\|w_n\|_{\mu^\dagger}^2 + o(1). \end{aligned} \tag{34}$$

From (14) and (32), we have

$$\begin{aligned} \mu\|u_n\|_{2^*}^{2^*} &= \mu\|u_n\|_{2^*}^2\|u_n\|_{2^*}^{2^*-2} \leq \mu(\eta_0\eta_2)^2\left[\frac{22^*c_\mu}{(2^*-2)\mu a_3^0}\right]^{(2^*-2)/2^*} \\ &\quad \cdot \|w_n\|_{\mu^\dagger}^2 + o(1) = (\eta_0\eta_2)^2\left[\frac{22^*c_\mu}{(2^*-2)a_3^0}\right]^{(2^*-2)/2^*} \\ &\quad \cdot \left[\mu^{(N-2)/N}c_\mu\right]^{2/N}\|w_n\|_{\mu^\dagger}^2 + o(1) \\ &\coloneqq C_3\left[\mu^{(N-2)/N}c_\mu\right]^{2/N}\|w_n\|_{\mu^\dagger}^2 + o(1), \end{aligned} \tag{35}$$

$$\begin{aligned} \mu\|v_n\|_{2^*}^{2^*} &= \mu\|v_n\|_{2^*}^2\|v_n\|_{2^*}^{2^*-2} \leq \mu(\eta_0\eta_2)^2\left[\frac{22^*c_\mu}{(2^*-2)\mu b_3^0}\right]^{\frac{2^*-2}{2^*}} \\ &\quad \cdot \|w_n\|_{\mu^\dagger}^2 + o(1) = (\eta_0\eta_2)^2\left[\frac{22^*c_\mu}{(2^*-2)b_3^0}\right]^{\frac{2^*-2}{2^*}} \\ &\quad \cdot \left[\mu^{\frac{N-2}{N}}c_\mu\right]^{\frac{2}{N}}\|w_n\|_{\mu^\dagger}^2 + o(1) \coloneqq C_4\left[\mu^{\frac{N-2}{N}}c_\mu\right]^{\frac{2}{N}}\|w_n\|_{\mu^\dagger}^2 + o(1). \end{aligned} \tag{36}$$

It follows from (6), (16), (20), (33), (34), (35), and (36) that

$$\begin{aligned} o(1) &= \left\langle S'_\mu(w_n), w_n\right\rangle = \|w_n\|_{\mu^\dagger}^2 - \mu\int_{\mathbb{R}^N} a_2(x)|u_n|^p dx \\ &\quad - \mu\int_{\mathbb{R}^N} b_2(x)|v_n|^q dx - \mu\int_{\mathbb{R}^N} a_3(x)|u_n|^{2^*} dx \\ &\quad - \mu\int_{\mathbb{R}^N} b_3(x)|v_n|^{2^*} dx - 2\mu\int_{\mathbb{R}^N} c(x)u_n v_n dx \\ &\geq (1-\vartheta)\|w_n\|_{\mu^\dagger}^2 - \left\{C_1 a_2^1\left[\mu^{(N-2)/2}c_\mu\right]^{(p-2)/p}\right. \\ &\quad + C_2 b_2^1\left[\mu^{(N-2)/2}c_\mu\right]^{(q-2)/q} + C_3 a_3^1\left[\mu^{(N-2)/N}c_\mu\right]^{2/N} \\ &\quad \left. + C_4 b_3^1\left[\mu^{(N-2)/N}c_\mu\right]^{2/N}\right\}\|w_n\|_{\mu^\dagger}^2 + o(1) \\ &\geq (1-\vartheta)\|w_n\|_{\mu^\dagger}^2 - \left[C_1 a_2^1\alpha^{(p-2)/p} + C_2 b_2^1\beta^{(q-2)/q}\right. \\ &\quad \left. + C_3 a_3^1\alpha^{2/N} + C_4 b_3^1\beta^{2/N}\right]\|w_n\|_{\mu^\dagger}^2 + o(1) \\ &\geq \frac{1-\vartheta}{2}\|w_n\|_{\mu^\dagger}^2 + o(1). \end{aligned} \tag{37}$$

Hence, we obtain

$$\lim_{n\to\infty}\|w_n\|_{\mu^\dagger}^2 = 0. \tag{38}$$

From (15), (23), and (38), we have

$$0 < c_\mu = \lim_{n\to\infty} S_\mu(w_n) \leq \frac{1}{2}\|w_n\|_{\mu^\dagger}^2 = 0, \tag{39}$$

a contradiction, which implies that $w_\mu \neq (0,0)$. We can easily check that $S'_\mu(w_n) = 0$ and $S_\mu(w_n) \leq c_\mu$ by a standard argument. Hence, w_μ is a nontrivial solution for (9).

It is easy to see that Theorem 2 is a direct consequence of Theorem 1.

Data Availability

No data were used to support this study.

Conflicts of Interest

No potential conflict of interest was reported by the authors.

Acknowledgments

This work is supported by the National Natural Science Foundation of China (No. 11961014 and No. 61563013) and Guangxi Natural Science Foundation (2016GXNSFAA380082, 2018GXNSFBA281019, and 2018GXNSFAA281021).

References

[1] N. Akhmediev and A. Ankiewicz, "Novel soliton states and bifurcation phenomena in nonlinear fiber couplers," *Physical Review Letters*, vol. 70, no. 16, pp. 2395–2398, 1993.

[2] Y. Y. Li, "On a singularly perturbed elliptic equation," *Advances in Differential Equations*, vol. 2, pp. 955–980, 1997.

[3] A. Ambrosetti, A. Malchiodi, and W. M. Ni, "Singularly perturbed elliptic equations with symmetry: existence of solutions concentrating on spheres, part I," *Communications in Mathematical Physics*, vol. 235, no. 3, pp. 427–466, 2003.

[4] A. Ambrosetti, A. Malchiodi, and W. M. Ni, "Singularly perturbed elliptic equations with symmetry: existence of solutions concentrating on spheres, part II," *Indiana University Mathematics Journal*, vol. 53, no. 2, pp. 297–330, 2004.

[5] A. Pomponio, "Coupled nonlinear Schrödinger systems with potentials," *Journal of Differential Equations*, vol. 227, no. 1, pp. 258–281, 2006.

[6] Y. H. Ding and F. H. Lin, "Solutions of perturbed Schrödinger equations with critical nonlinearity," *Calculus of Variations and Partial Differential Equations*, vol. 30, no. 2, pp. 231–249, 2007.

[7] Y. H. Ding and J. C. Wei, "Semiclassical states for nonlinear Schrodinger equations with sign-changing potentials," *Journal of Functional Analysis*, vol. 251, no. 2, pp. 546–572, 2007.

[8] W. N. Huang and X. H. Tang, "Semi-classical solutions for the nonlinear Schrödinger-Maxwell equations," *Journal of Mathematical Analysis and Applications*, vol. 415, no. 2, pp. 791–802, 2014.

[9] Z. J. Chen and W. M. Zou, "On coupled systems of Schrödinger equations," *Advances in Differential Equations*, vol. 16, pp. 755–800, 2011.

[10] Z. J. Chen and W. M. Zou, "Ground states for a system of Schrödinger equations with critical exponent," *Journal of Functional Analysis*, vol. 262, no. 7, pp. 3091–3107, 2012.

[11] Z. J. Chen and W. M. Zou, "Standing waves for linearly coupled Schrodinger equations with critical exponent," *Annales de l'Institut Henri Poincare (C) Non Linear Analysis*, vol. 31, no. 3, pp. 429–447, 2014.

[12] J. Y. Peng, S. T. Chen, and X. H. Tang, "Semiclassical solutions for linearly coupled Schrödinger equations without compactness," *Complex Variables and Elliptic Equations*, vol. 64, pp. 548–556, 2018.

[13] X. H. Tang, "New super-quadratic conditions for asymptotically periodic Schrödinger equations," *Canadian Mathematical Bulletin*, vol. 60, no. 2, pp. 422–435, 2017.

[14] X. H. Tang, X. Y. Lin, and J. S. Yu, "Nontrivial solutions for Schrödinger equation with local super-quadratic conditions," *Journal of Dynamics and Differential Equations*, vol. 31, no. 1, pp. 369–383, 2019.

[15] X. H. Tang, "Non-Nehari manifold method for superlinear Schrödinger equation," *Taiwanese Journal of Mathematics*, vol. 18, no. 6, pp. 1957–1979, 2014.

[16] X. H. Tang, "Non-Nehari manifold method for asymptotically linear Schrödinger equation," *Journal of the Australian Mathematical Society*, vol. 98, no. 1, pp. 104–116, 2015.

[17] B. Sirakov, "Standing wave solutions of the nonlinear Schrödinger equations in $\mathbb{R}^N$," *Annali di Matematica Pura ed Applicata*, vol. 183, no. 4, pp. 73–83, 2002.

[18] G. F. Che and H. B. Chen, "Existence of multiple nontrivial solutions for a class of quasilinear Schrödinger equations on $\mathbb{R}^N$," *Bulletin of the Belgian Mathematical Society - Simon Stevin*, vol. 25, no. 1, pp. 39–53, 2018.

[19] X. Y. Lin, Y. B. He, and X. H. Tang, "Existence and asymptotic behavior of ground state solutions for asymptotically linear Schrödinger equation with inverse square potential," *Communications on Pure and Applied Analysis*, vol. 18, no. 3, pp. 1547–1565, 2019.

[20] J. H. Chen, X. H. Tang, and B. T. Cheng, "Existence of ground state solutions for a class of quasilinear Schrödinger equations with general critical nonlinearity," *Communications on Pure and Applied Analysis*, vol. 18, no. 1, pp. 493–517, 2019.

[21] D. D. Din, X. H. Tang, and Q. F. Wu, "Ground states of nonlinear Schrödinger systems with periodic or non-periodic potentials," *Communications on Pure and Applied Analysis*, vol. 18, no. 3, pp. 1261–1280, 2019.

[22] X. Y. Lin and X. H. Tang, "Semiclassical solutions of perturbed p-Laplacian equations with critical nonlinearity," *Journal of Mathematical Analysis and Applications*, vol. 413, no. 1, pp. 438–449, 2014.

[23] L. B. Wang, X. Y. Zhang, and H. Fang, "Existence of ground state solutions for a class of quasilinear elliptic systems in Orlicz-Sobolev spaces," *Boundary Value Problems*, vol. 2017, no. 1, p. 106, 2017.

[24] M. Willem, *Minimax Theorems*, Birkhäuser, Boston, 1996.

Hindawi
Advances in Mathematical Physics
Volume 2020, Article ID 4596050, 8 pages
https://doi.org/10.1155/2020/4596050

Research Article

The Theory and Demonstration of the Solid-Fluid Transformation of Ice Water

Yong-Yan Wang,[1] **Xi-Yan Fan**,[1,2] **Nan Qin**,[1] **Jian-Guang Li**,[1] **and Chuan-Qi Su**[1]

[1]*Mechanics Center of Qingdao University of Science and Technology, Qingdao 266061, China*
[2]*State Key Laboratory of Coal Resources and Safe Mining, China Mining University, Beijing 100083, China*

Correspondence should be addressed to Yong-Yan Wang; wangyongyan168@163.com

Received 21 May 2020; Accepted 15 July 2020; Published 8 August 2020

Guest Editor: Zhi-Yuan Sun

In this paper, a mathematical model for describing the solid-fluid transformation of ice water is put forward based on the special geometry cases. The correctness of the obtained model is verified through comparison with numerical analysis and experiments. The good agreement indicates that the obtained model is available for the study of the solid-fluid transformation of ice water. The theory derived in this paper lays a foundation for the research of solid-fluid transformation phenomena of other materials and may have important applications in engineering areas such as rheology, creep, and instability of materials.

1. Introduction

The phenomena of solid-fluid transformation exist in the processes of ice melting, metal melting, rheology, and so on [1–7]. On September 11, 2001, the secondary collapse of the world trade center in the terrorist attack is a typical problem of creep under the action of thermal flow. The metals and concrete supports of the building crept under the action of thermal flow after a period of time, which led to the strength loss and collapse. Although the rheology and creep of materials have been hot topics in the engineering science, the mathematical aspect of the solid-fluid transformation has not been pointed out clearly. Starting from the Newton's law of cooling, the theory of the solid-fluid transformation of ice water will be derived in this paper. That can be a theoretical foundation for the solid-fluid transformation problem and may have important applications in the field of engineering science.

2. The Mathematical Model for the Ice Water's Solid-Fluid Transformation

Firstly, we take the ice ball as a special example to facilitate the deduction. Assume the radius of the ice ball as r, then the surface area of the ball as $4\pi r^2$. Newton's law of cooling states that the rate of heat loss of a body is directly proportional to the difference between its own temperature and the temperature of its surroundings [8]. Therefore, the heat transferred through the surface of the ball within Δt time can be expressed as follows:

$$\Delta Q = 4\pi r^2 \kappa (T - T_0)\Delta t, \tag{1}$$

where κ is the heat transfer coefficient, T_0 is the temperature of ice ball, and T is the temperature of its surroundings. It should be noted that we assume T_0 and T are both constant and $T_0 < 0^\circ\mathrm{C} < T$. Within Δt time, there are ΔV volumes of ice melting into water:

$$\Delta V = 4\pi r^2 \Delta r. \tag{2}$$

Dividing the both sides of the above equation by Δt and taking the limit, we have

$$\lim_{\Delta t \to 0} \frac{\Delta V}{\Delta t} = 4\pi r^2 \lim_{\Delta t \to 0} \frac{\Delta r}{\Delta t}. \tag{3}$$

The above equation can be rewritten as

$$\frac{dV}{dt} = 4\pi r^2 \frac{dr}{dt}. \quad (4)$$

The density of ice is set to be ρ; then the quality of melted ice is $\Delta m = -\rho \Delta V$, where the negative sign signifies that the quality of ice ball decreases. The heat needed to convert T_0 ice to 0°C ice is

$$\Delta Q_1 = c\Delta m(0 - T_0) = -\rho c \Delta V\,(0 - T_0) = 4\pi r^2 \rho c \Delta r T_0, \quad (5)$$

where c denotes the specific heat of ice, namely, the heat needed to raise 1°C per unit mass of ice. The heat needed to melt 0°C ice to 0°C water can be calculated as follows:

$$\Delta Q_2 = \gamma \Delta m = -\rho \gamma \Delta V = -4\pi r^2 \rho \gamma \Delta r, \quad (6)$$

where γ is the latent heat per unit mass of ice. Thus, the total amount of heat is

$$\Delta Q = \Delta Q_1 + \Delta Q_2 = 4\pi r^2 \rho (cT_0 - \gamma)\Delta r. \quad (7)$$

By combining Equations (1) and (7), we have

$$4\pi r^2 \rho (cT_0 - \gamma)\Delta r = 4\pi r^2 \kappa (T - T_0)\Delta t. \quad (8)$$

When $\Delta t \to 0$, the following differential equation could be derived:

$$\frac{dr}{dt} = \frac{\kappa (T - T_0)}{\rho (cT_0 - \gamma)}. \quad (9)$$

In order to integrate the above equation, we assume that the thermal parameters c and γ are both constant. Thus, we have

$$r = \frac{\kappa (T - T_0)t}{\rho (cT_0 - \gamma)} + C, \quad (10)$$

with C as a constant of integration. When $t = 0$, $r = r_0$, thus, we have $C = r_0$. When the ice ball is completely melted, i.e., $r = 0$, the time of melting can be expressed as

$$t = \frac{\rho (cT_0 - \gamma)}{\kappa (T - T_0)} r_0. \quad (11)$$

The denominator in the above equation is positive because $T > T_0$, while the numerator is negative because $T_0 < 0$°C. Therefore, the time of melting t is positive.

In fact, Equation (11) can also be obtained by the calculus relations. We assume that the thickness of ice ball melted within dt time is dr; then the mass of ice melted is $dm = -\rho dV = -4\pi r_2 \rho dr$. The heat of melting needed is

$$dQ = \beta dm = -4\pi r^2 \rho \beta dr, \quad (12)$$

where β is the heat of melting needed per unit mass of ice, with the unit J/kg. Based on Newton's law of cooling, the heat transferred through the surface of the ball within dt time is

$$dQ = 4\pi r^2 \kappa (T - T_0) dt. \quad (13)$$

The following equation can be derived according to the conservation of energy:

$$dQ = -4\pi r^2 \rho \beta dr = 4\pi r^2 \kappa (T - T_0) dt. \quad (14)$$

Then, the decreasing rate for the ice ball's radius with time t is

$$\frac{dr}{dt} = \frac{\kappa (T - T_0)}{\rho \beta}. \quad (15)$$

The reduced surface area of ice ball within dt time can be calculated as

$$dS = 4\pi \left[(r + dr)^2 - r^2\right] = 4\pi \left(2rdr + dr^2\right). \quad (16)$$

By ignoring the two-order infinitesimal, Equation (16) could be simplified as

$$dS = 8\pi r dr. \quad (17)$$

By dividing both sides of the above equation by dt, we can get the decreasing rate for the ice ball's surface area with time t:

$$\frac{dS}{dt} = 8\pi r \frac{dr}{dt}. \quad (18)$$

Substituting Equation (15) into Equation (18), the following equation can be obtained:

$$\frac{dS}{dt} = -8\pi r \frac{\kappa (T - T_0)}{\rho \beta}. \quad (19)$$

Although Equations (11), (15), and (19) are derived from the melting process of ice ball, they could apply to the general melting cases. For the cylinder, cone, and other shapes of ice, the corresponding equations can be derived in a similar way. In the following, we will take the ice cylinder as another example to derive the corresponding equations. Assume that the height of the ice cylinder is h and the radius is r, then the surface area of the cylinder is $2\pi r^2 + 2\pi rh$. The heat transferred through the surface of the cylinder within dt time can be expressed as

$$dQ = \kappa \left(2\pi r^2 + 2\pi rh\right)(T - T_0) dt. \quad (20)$$

Within dt time, there are dV volumes of ice melting into water:

$$dV = 2\pi rh dr + \pi r^2 dh. \quad (21)$$

The heat needed to convert T_0 ice to 0°C ice is

$$dQ_1 = cdm(0 - T_0) = -\rho cdV(0 - T_0) = \rho c\left(2\pi rhdr + \pi r^2 dh\right)T_0. \quad (22)$$

The heat needed to melt 0°C ice to 0°C water can be calculated as

$$dQ_2 = \gamma dm = -\rho\gamma\left(2\pi rhdr + \pi r^2 dh\right). \quad (23)$$

Thus, the total amount of heat is

$$dQ = dQ_1 + dQ_2. \quad (24)$$

By combining Equations (20), (22), (23), and (24), we have

$$\kappa\left(2\pi r^2 + 2\pi rh\right)(T - T_0)dt = 2\pi rh\rho(cT_0 - \gamma)dr + \pi r^2\rho(cT_0 - \gamma)dh. \quad (25)$$

The above mathematical relationships can be used as a unified theory of the solid-fluid transformation of ice water. That can be a theoretical foundation for the solid-fluid transformation problem and may have important applications in the field of engineering science.

3. Experimental Results on Ice Water's Solid-Fluid Transformation

Ice melting is an unsteady heat transfer process, including not only heat conduction, convection, and radiation but also phase transformation. As for the influence factors regarding ice melting, the external influence factors such as environment temperature, humidity, pressure, convective heat transfer coefficient, and thermal radiation field play important roles, while the internal factors such as the temperature, shape, and size of ice also have nonnegligible effects [9]. The melting experiments were carried out by testing ice of different sizes and shapes in a RPH-80 thermotank, in which the environment temperature was set to be 25°C. Specimens were prepared by pouring purified water into containers of different shapes and sizes, and then the containers were put in the freezer for 24 hours. The initial temperature of ice is set at -18°C. Table 1 shows the records of melting time of the ice with different shapes and sizes under the same experimental conditions.

Table 1: The melting time for three kinds of shapes.

Shape	Diameter (mm)	Height (mm)	Time of melting (min)
Cylinder	25	100	77
	35		96
	45		120
	55		155
	65		179
Circular truncated cone	25 (Φ1), 40 (Φ2)	100	91
	35 (Φ1), 50 (Φ2)		116
	45 (Φ1), 60 (Φ2)		144
	55 (Φ1), 70 (Φ2)		175
	65 (Φ1), 80 (Φ2)		215
Ball	25		42
	35		63
	45		81
	55		101
	65		125

4. Comparison between the Mathematical Models with Experimental Results

By processing the experimental data using Origin software, the linear fitting curves (as shown in Figure 1) and nonlinear (quadratic function) fitting curves (as shown in Figure 2) for the three types of specimens can be obtained, respectively. It can be seen that the experimental data agree well with the melting time of ice predicted through Equation (11). The melting time and diameter have similar relationship for three types of specimens, which further shows that Equation (11) also works for the cases of the cylinder and circular truncated cone. The differences on slopes and curvatures of fitting curves show that the heat transfer coefficient is a comprehensive parameter, which changes with the shape and size of specimen. Two kinds of fitting are analyzed by the way of comparative error analysis, as shown in Figure 3, from which it can be seen that the nonlinear fitting error is smaller than the linear fitting case for the relationship between the melting time and the diameter of the ice ball cylinder and circular truncated cone. The heat transfer coefficients for the ice ball, cylinder, and circular truncated cone are unrelated to their diameters.

5. Numerical Analysis on the Solid-Fluid Transformation of Ice Water

In the following, ANSYS and fluent analyses will be employed to study the process of ice melting numerically [10, 11]. The mesh size used in the software is 3 mm, and the number of nodes for the ice ball is 1766, the ice cylinder is 5888, and the ice circular truncated cone is 8014.

5.1. ANSYS Numerical Simulation Analysis. Ice melting is a process related to the phase transformation. The latent heat must be taken into consideration when the phase transformation is involved, because the latent heat is defined from the concept of enthalpy, which will be taken as an attribute definition of material. The curve that enthalpy changes with temperature can be obtained. According to the definition, solid temperature (T_s) and fluid temperature (T_l) will divide the enthalpy curve into three areas, i.e., the solid area $(T < T_s)$, phase-transition area $(T_s < T < T_l)$, and fluid area $(T_l < T)$. The phases can be distinguished by the temperatures in different time. The temperature of ice for phase transformation is 0°C in the atmospheric circumstances.

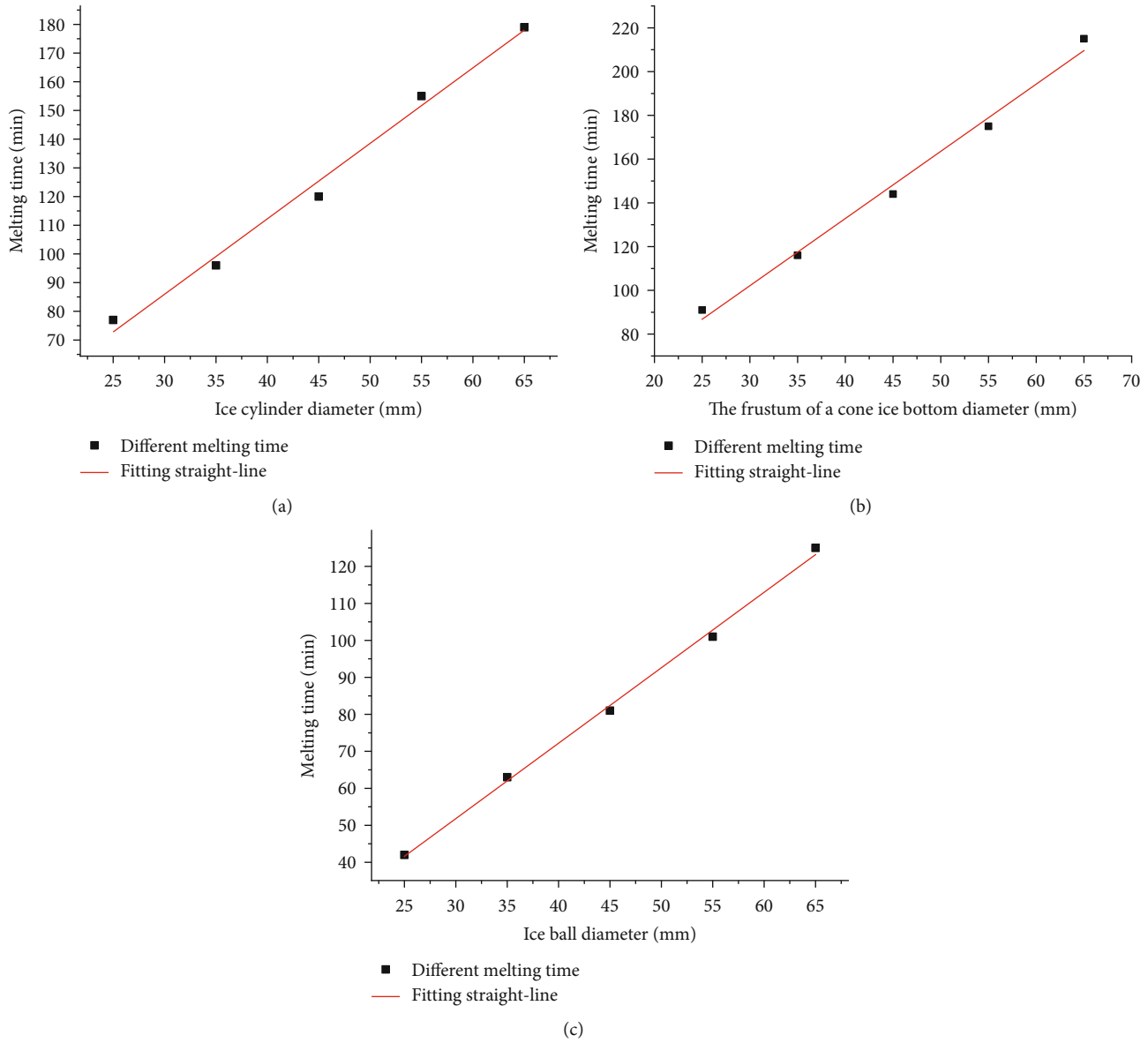

Figure 1: The linear fit between the melting time and diameter: (a) ice cylinder, (b) ice circular truncated cone, and (c) ice ball.

When the temperature is higher than 0°C, the material will melt from ice to water [10].

The melting process of ice in the thermotank is mainly influenced by the heat convection and radiation. Typical parameters for the thermotank wall are shown in Table 2. The temperature is set to be 25°C in the thermotank, and the initial temperature of ice is −18°C. Considering the heating principle and the heat transfer process of ice in thermotank, we set the mixed boundary condition on the surface of ice that contacts with air and selects the convective heat transfer coefficient as 20 W/(m^2·K) [10].

From the numerical simulation results worked by ANSYS, we find that the temperature of ice ball reduces from the external to the inner on the melting nephogram at 60 min, which agrees perfectly with the experimental results in the thermotank. The temperature of the ice cylinder and circular truncated cone also reduces from the external to the inner part on the melting nephogram at 60 min, and the temperature at the edges and angles remains the highest, indicating that the melting process starts from the edges and angles to the inner gradually. The results of the numerical simulation also agree well with that of the corresponding experiments in the thermotank. Table 3 shows the melting time in the numerical simulation and the thermotank experiment, respectively. It can be seen from Table 3 that the agreement degree between numerical and experimental results on the melting time for ice ball, cylinder, and circular truncated cone reaches 92.6%, 92.5%, and 95.3%, respectively. The melting time for the numerical simulation is shorter than that for the experiment, which can be attributed to the loss of heat during the experiment.

5.2. Fluent Numerical Simulation Analysis. In order to further verify the correctness of the theoretical model and make

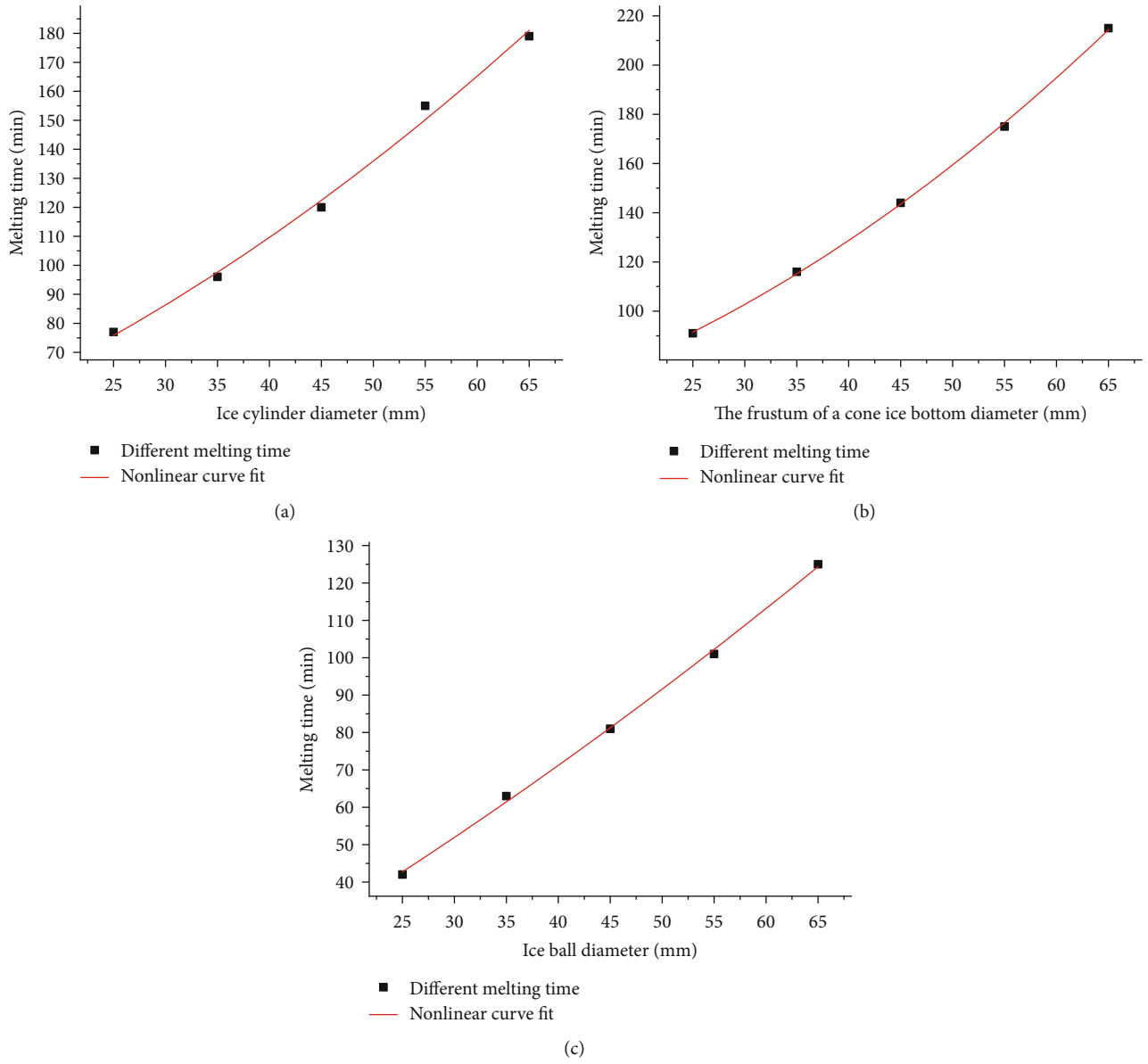

Figure 2: The nonlinear fit between the melting time and diameter: (a) ice cylinder, (b) ice circular truncated cone, and (c) ice ball.

a comparison with the results of ANSYS simulation, fluent analysis is employed to simulate the melting process of ice. The air medium in the box is set to be ideal gas, and environmental pressure is set as a standard atmospheric pressure. The latent heat of ice medium is 333146 J/kg, and the melting point of ice and freezing point of water are the same (273.15 K) [11].

Fluent analysis uses the heat enthalpy technology to handle with the melting and solidification processes. The melting process is characterized by the changing of the liquid fraction without tracing on the interface [11]. The simulation results are shown in Figure 4 and Table 4, from which it can be seen that the melting processes start from the corners, then carry on from the outside to the inside. The simulation results by fluent analysis also agree well with experiments and are consistent with the results worked out by ANSYS.

It can be seen from Table 4 that the melting time for the ice ball, cylinder, and circular truncated cone by the Fluent simulation is less than that by the experiments and the rates of agreement reach 91.4%, 95.8%, and 97.2% for the ice ball, cylinder, and circular truncated cone, respectively. The reason for this phenomenon is that in the numerical simulation, the boundary conditions and material properties are in the ideal conditions and there is no heat loss.

6. Conclusion

In this paper, the theory of the solid-fluid transformation of ice water with special shapes such as the ball, cylinder, and circular truncated cone has been derived and the mathematical relationships of ice water's solid-fluid transformation have been presented. The unified theory and formulas of

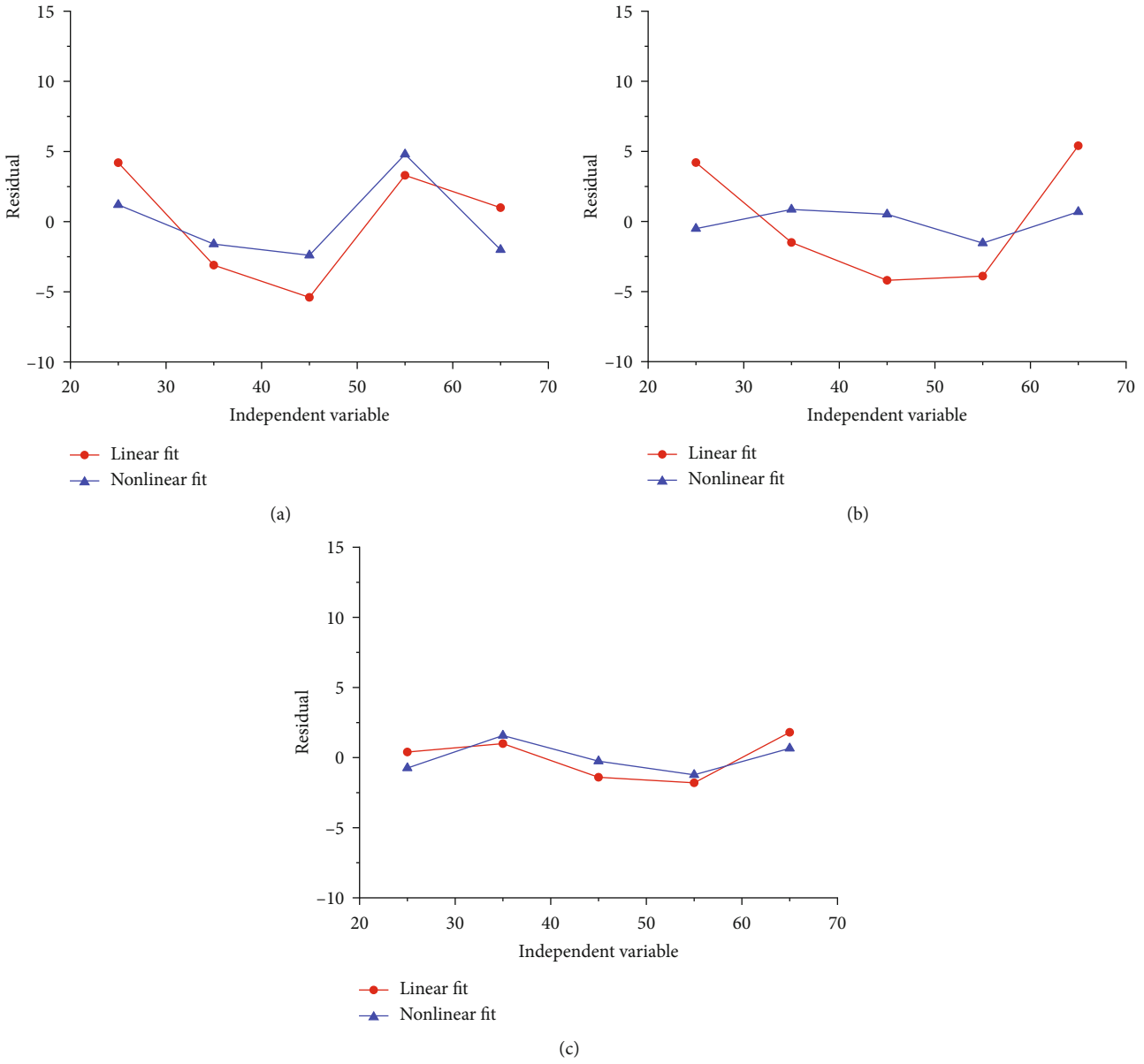

Figure 3: The comparative error analysis for the two kinds of fitting: (a) ice cylinder, (b) ice circular truncated cone, and (c) ice ball.

Table 2: Typical parameters for the thermotank wall.

Coefficient of thermal conductivity [W/(m·K)]	Density (kg/m^3)	Modulus of elasticity (Pa)	Poisson's ratio (1)	Specific heat capacity [J/(kg·K)]
60.64	7850	2e11	0.3	96

Table 3: The comparison of melting time between ANSYS simulation and experimental results.

Shape	Size (mm)		ANSYS (min)	Experiment (min)	Difference (%)
Ball	Diameter	45	75	81	7.4
Cylinder	Diameter	45	111	120	7.5
	Height	100			
Circular	Top	45			
Truncated	Root	60	137	144	4.7
Cone	Height	100			

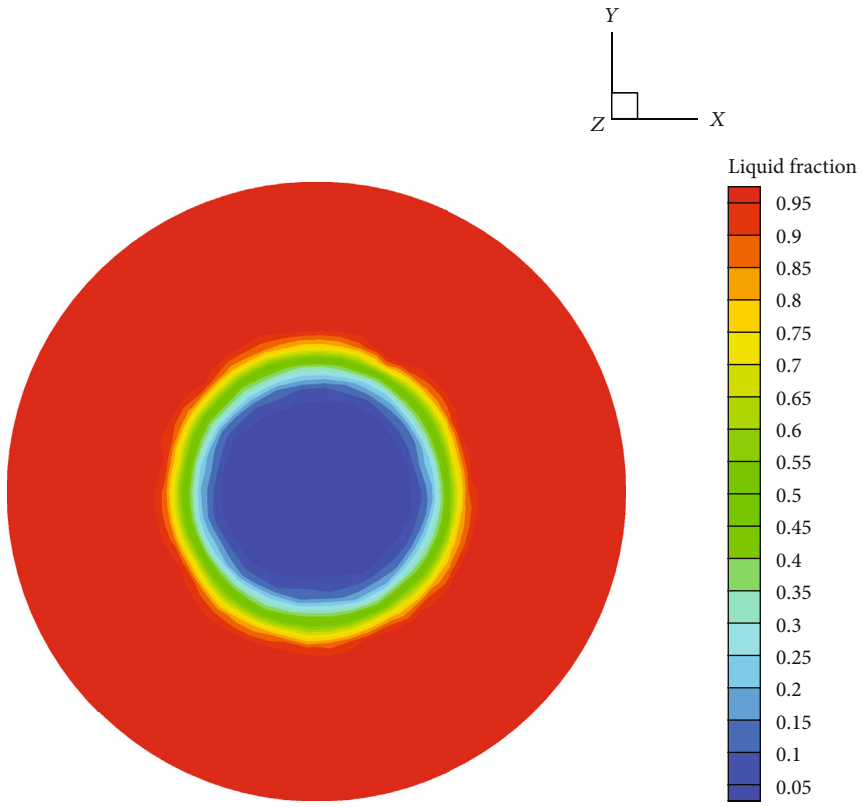

Figure 4: The simulation result for the ice ball by fluent analysis at 60 min.

Table 4: The comparison of melting time between fluent simulation and experimental results.

Shape	Size (mm)		Fluent (min)	Experiment (min)	Difference (%)
Ball	Diameter	45	74	81	8.6
Cylinder	Diameter	45	115	120	4.2
	Height	100			
Circular	Top	45			
Truncated	Root	60	140	144	2.8
Cone	Height	100			

ice water's solid-fluid transformation are validated through simulation analysis and corresponding experiments. It is expected that the theory derived in this paper could lay a foundation for the research of solid-fluid transformation phenomena of other materials and may have important applications in engineering areas.

Data Availability

The data used to support the findings of this study are available from the corresponding author upon request.

Conflicts of Interest

The authors declare that they have no conflicts of interest.

Acknowledgments

We express our sincere thanks to the editors, reviewers, and all the members of our discussion group for their valuable comments. This work has been supported by the National Natural Science Foundation of China under Grant No. 51674149, Open Research Fund of the State Key Laboratory of Coal Resources and Safe Mining under Grant No. SKLCRSM20KF006 and Natural Science Foundation of Shandong Province under Grant No. ZR2019MEE082.

References

[1] W. K. Heidug, "Intergranular solid-fluid phase transformations under stress: the effect of surface forces," *Journal of Geophysical Research: Solid Earth*, vol. 100, no. B4, pp. 5931–5940, 1995.

[2] J. Ghoussoub and Y. M. Leroy, "Solid-fluid phase transformation within grain boundaries during compaction by pressure solution," *Journal of the Mechanics and Physics of Solids*, vol. 49, no. 10, pp. 2385–2430, 2001.

[3] J. I. D. Alexander and W. C. Johnson, "Thermomechanical equilibrium in solid-fluid systems with curved interfaces," *Journal of Applied Physics*, vol. 58, no. 2, pp. 816–824, 1985.

[4] A. Putnis and C. V. Putnis, "The mechanism of reequilibration of solids in the presence of a fluid phase," *Journal of Solid State Chemistry*, vol. 180, no. 5, pp. 1783–1786, 2007.

[5] A. S. Dogonchi, M. Hatami, and G. Domairry, "Motion analysis of a spherical solid particle in plane Couette Newtonian fluid flow," *Powder Technology*, vol. 274, pp. 186–192, 2015.

[6] J. Yu, X. Chen, H. Li, J. W. Zhou, and Y. Y. Cai, "Effect of freeze-thaw cycles on mechanical properties and permeability of red sandstone under triaxial compression," *Journal of Mountain Science*, vol. 12, no. 1, pp. 218–231, 2015.

[7] G. Wang, X. Qin, J. Shen, Z. Zhang, D. Han, and C. Jiang, "Quantitative analysis of microscopic structure and gas seepage characteristics of low-rank coal based on CT three-dimensional reconstruction of CT images and fractal theory," *Fuel*, vol. 256, p. 115900, 2019.

[8] S. M. Yang and W. Q. Tao, *Heat Transfer*, Higher Education Press, Beijing, 2006.

[9] M. E. Grainger and H. Lister, "Wind speed, stability and eddy viscosity over melting ice surfaces," *Journal of Glaciology*, vol. 6, no. 43, pp. 101–127, 1966.

[10] W. T. Xin, Z. Z. Li, and R. X. Hu, *ANSYS13.0 Thermodynamic Finite Element Analysis*, Machinery Industry Press, Beijing, 2011.

[11] J. P. Tang, *FLUENT 14.0 Super Learning Manual*, The Posts and Telecommunications Press, Beijing, 2013.